

# Raman spectroscopic investigation of the effects of heat-treatment and Al, Ce or Eu doping concentration on TiO<sub>2</sub> powder crystallization

Oualid Berkani<sup>a</sup>, Hicham El Hamzaoui<sup>b</sup>, Khelil Latrous<sup>a</sup>, Bruno Capoen<sup>b</sup> and Mohamed Bouazaoui<sup>b</sup>

<sup>a</sup> *Laboratoire des Composants Actifs et Matériaux,*

*Université Larbi Ben M'hidi d'Oum El-Bouaghi, Algérie*

<sup>b</sup> *Univ-Lille, CNRS, UMR 8523 - PhLAM - Physique des Lasers Atomes et Molécules,*

*CERLA/IRCICA, F-59000 Lille, France*

Received date: April 09, 2016; revised date: October 03, 2016; accepted date: December 01, 2016

---

## Abstract

*In this paper, we study the effects of various doping elements (Aluminum, Cerium or Europium) with different contents and of heat-treatment on the structural properties of TiO<sub>2</sub> nano-crystalline powders. The sol-gel technique was used to prepare the doped and undoped TiO<sub>2</sub> powders. The structures of the obtained samples were investigated using Raman spectroscopy, which allowed to monitor the formation of anatase and rutile crystalline phases as a function of the annealing temperature. We have shown that all the doping elements contribute to stabilize anatase phase at high calcination temperature. Furthermore, doping with Europium was found to be the most efficient anatase phase stabilizer.*

### Key words:

*Doped TiO<sub>2</sub> powder, Aluminum, Cerium, Europium, Raman spectroscopy, sol-gel, anatase, rutile.*

---

## 1. Introduction

Recently, TiO<sub>2</sub> powders doped with diverse elements have been investigated for many applications, among which photocatalytic activity is the most important [1-6]. For instance, TiO<sub>2</sub> powders doped with cerium were analysed for photocatalytic activity [7-9]. As another example, nano-powders of Aluminum-doped TiO<sub>2</sub> were used to make thick films-based gas sensors exhibiting a good selectivity and sensitivity to CO and O<sub>2</sub> gases. These Al-doped TiO<sub>2</sub> powders showed stable anatase phase up to 800°C [10]. Besides, the properties of TiO<sub>2</sub> nanoparticles doped with Europium have been studied for optical applications [11-14]. Hence, the impact of such dopants on the structural properties of titanium dioxide is of crucial importance for these various applications.

In this paper, we report on the crystallization of sol-gel-derived TiO<sub>2</sub> powders as a function of heat-treatment temperature and of doping contents ranging between 1 and 7 (mol.%), with different elements (Al, Ce or Eu). The crystal phase was studied using micro-Raman spectroscopy.

## 2. Materials and methods

### 2.1. Synthesis of TiO<sub>2</sub> powders

All chemical products have been purchased from Aldrich and used as-received. A TiO<sub>2</sub> sol was prepared using titanium isopropoxide (Ti(O<sup>i</sup>Pr)<sub>4</sub>), isopropanol (PrOH) and acetic acid (AcOH) with a molar ratio

AcOH/Ti = 6. The obtained mixture was diluted with methanol. The solution was slowly evaporated at room temperature to yield a powder. Then, the residual solvents (isopropanol, acetic acid and methanol) were eliminated by heating the obtained product at 120°C for 48 h. The resulting powder was ground using an automatic crusher.

Furthermore, for the preparation of doped powders with 1%, 2%, 5% and 7% of Europium, Cerium or Aluminum, the as-synthesized sol of TiO<sub>2</sub> was doped with europium (III) nitrate pentahydrate Eu(NO<sub>3</sub>)<sub>3</sub>·5H<sub>2</sub>O, Cerium(III) nitrate hexahydrate Ce(NO<sub>3</sub>)<sub>3</sub>·6H<sub>2</sub>O and Aluminum nitrate nonahydrate Al(NO<sub>3</sub>)<sub>3</sub>·9H<sub>2</sub>O respectively.

To investigate the effect of the calcination temperature on the structural properties of the obtained powders, they have been heat-treated for 1 hour in air at a temperature ranging from 400°C to 1100°C.

### 2.2. Characterisation

The Raman spectra were obtained in a confocal configuration using a triple-grating spectrometer (Jobin-Yvon T64000) and the 514.5 nm line of an Ar<sup>+</sup> laser as the excitation source with a power of 0.2 W on the sample. The absence of any phase change under the continuous laser irradiation has been carefully checked prior to the data acquisitions. All Raman spectra were recorded at room temperature in the wavenumber range 50-700 cm<sup>-1</sup>.

### 3. Results and discussion

In the corresponding Raman spectra of the pure  $\text{TiO}_2$  sample annealed at different temperatures ranging between 400 and 1100°C (Fig. 1), the formation of anatase phase appears at from the lower temperature 400°C, while the rutile phase begins to be observed at 700°C. Considering that the Raman scattering cross-section is constant for the anatase phase and that the spectra acquisitions have been performed in almost the same conditions, the increasing intensity of each peak in Fig. 1 may be attributed to the increasing crystallinity of the powder, due to the heat-treatment. Moreover, Fig. 1 shows the complete and rapid phase conversion from anatase to rutile for heat-treatment temperatures between 600 and 800°C. The observed Raman frequencies for  $\text{TiO}_2$  products at different calcination temperatures are listed in Table 1.

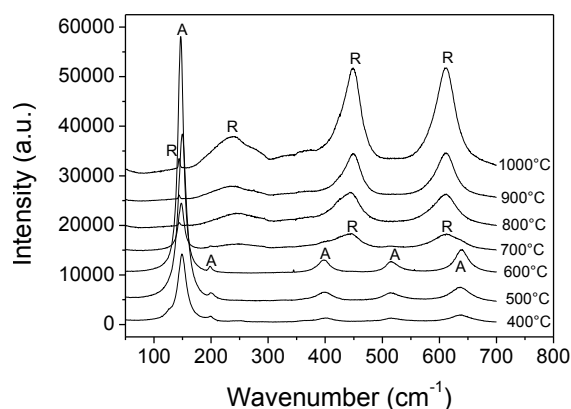


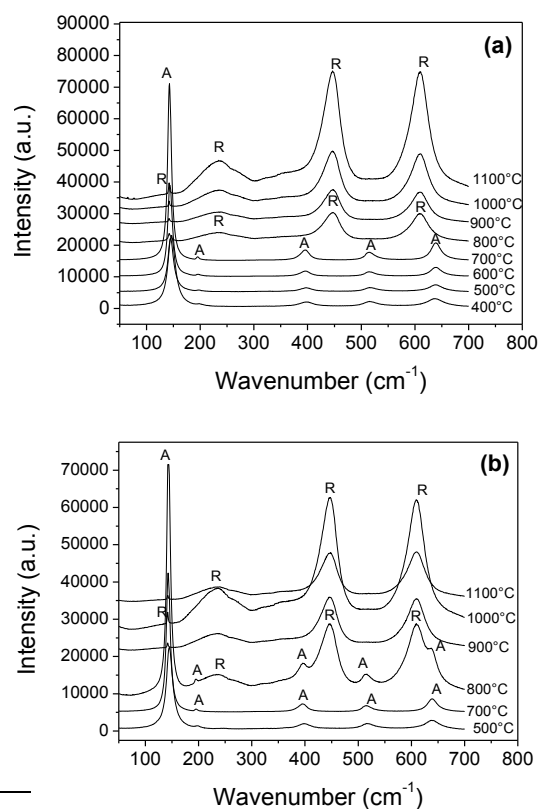
Fig. 1. Raman spectra of a pure  $\text{TiO}_2$  powder annealed at different temperatures for 1 hour.

**Table 1**

Observed Raman frequencies ( $\text{cm}^{-1}$ ) and their assignments in pure and doped  $\text{TiO}_2$  powders annealed at different temperature.

	$\text{TiO}_2$ (600°C)	$\text{TiO}_2$ - 1%Eu (900°C)	$\text{TiO}_2$ - 5%Al (800°C)	$\text{TiO}_2$ - 1%Ce (800°C)	Assignment
<b>Anatase</b>					
$\nu_1$	147	144	143	145	$E_{g1}$
$\nu_2$	197	195	196	197	$E_{g2}$
$\nu_3$	397	395	395	395	$B_{1g}$
$\nu_4$	515	512	513	512	$A_{1g}$
$\nu_5$	515	512	513	512	$B_{1g}$
$\nu_6$	640	636	638	637	$E_{g3}$
<b>Rutile</b>					
	(700°C)	(1000°C)	(900°C)	(900°C)	
	144	142	142	143	$B_{1g}$
	237	238	237	239	Multi- phonon process
	449	447	446	444	$E_g$
	612	609	610	610	$A_{1g}$

Fig. 2 shows the Raman spectra of  $\text{TiO}_2$  powders doped by Aluminum with 1%, 2%, 5% and 7% contents. For sample doped with 1% Al and heat-treated from 400°C to 700°C, the vibration bands have been clearly attributed to the anatase phase while the rutile phase bands were observed from 800°C to 1100°C. For 2% Al-doped sample, at 800°C the characteristic vibration bands of both phases were observed and the complete polymorph conversion from anatase to rutile was achieved at 900°C. For the higher Aluminum contents (5% and 7%), only the anatase phase is obtained for temperatures up to 800°C. For all contents in Al, the rutile phase was completed at 900°C and above.



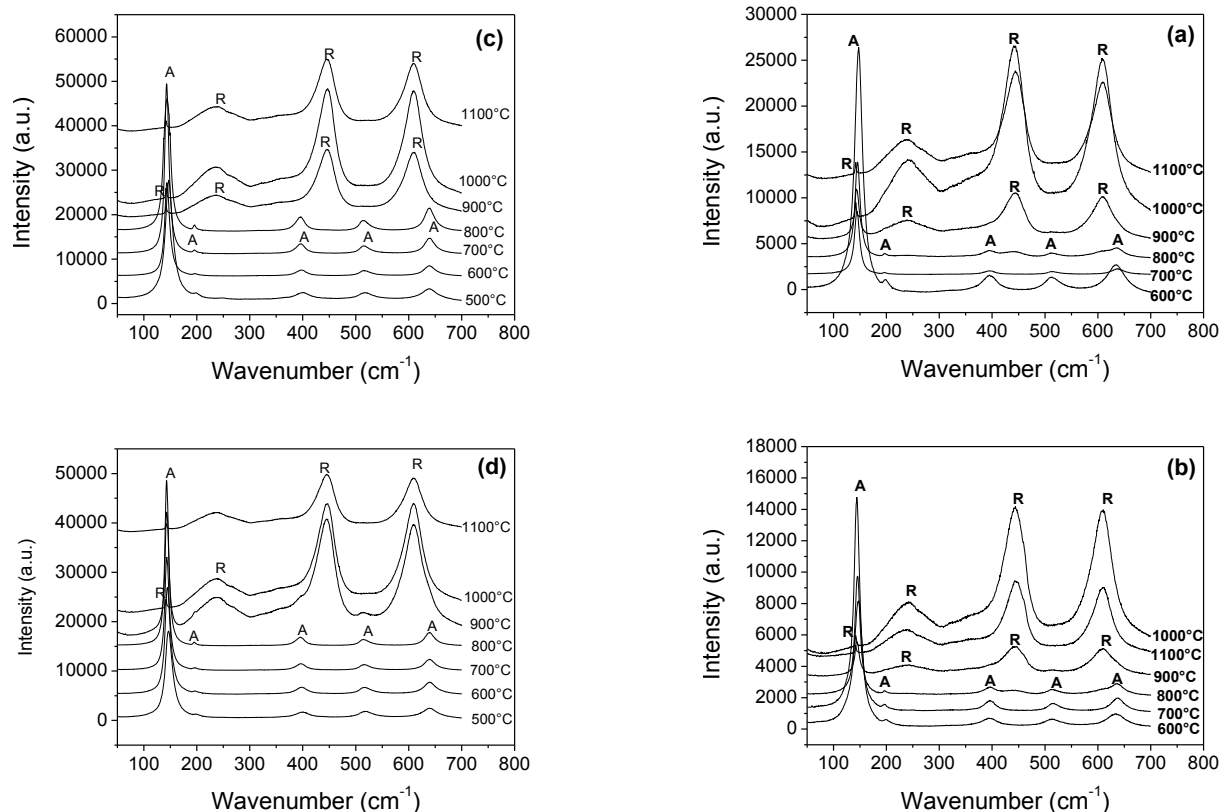


Fig. 2. Raman spectra of  $\text{TiO}_2$  powders doped with different Al contents  
(a) 1%, (b) 2%, (c) 5% and (d) 7%.

Fig. 3 shows the Raman spectra of  $\text{TiO}_2$  powders doped with 1%, 2%, 5% and 7% Cerium contents. At all Cerium contents, the anatase phase was observed for temperatures up to 800°C. Furthermore, when the calcination temperature became higher than 800°C, the rutile phase was the only observed phase. One can also note, for high Ce concentrations (5 and 7%), the presence of Raman band around 460  $\text{cm}^{-1}$ . This band could be attributed to the triply degenerate Raman-active mode of cubic fluorite-type crystallizing  $\text{CeO}_2$ . This mode, assigned to  $F_{2g}$  symmetry, can be viewed as a symmetric breathing mode of the oxygen atoms around cerium ions [15, 16].

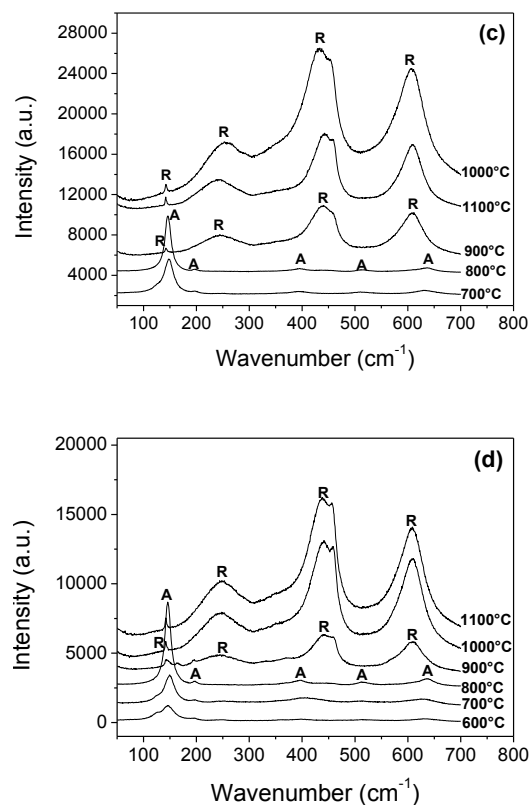


Fig. 3. Raman spectra of  $\text{TiO}_2$  powders doped with different Ce contents  
(a) 1%, (b) 2%, (c) 5% and (d) 7%.

Fig. (4) presents Raman spectra of 1%, 2%, 5% and 7% Eu-doped  $\text{TiO}_2$  powders annealed at different temperatures for 1 hour. As it can be seen, anatase phase appears at 400°C for all samples, while the rutile is observed at 1000°C. This result corresponds to tremendous influence of Europium on the crystallization of  $\text{TiO}_2$ . Indeed, rutile phase was observed at 700°C for pure  $\text{TiO}_2$  powders and at 800°C or 900°C for  $\text{TiO}_2$  powder doped with Cerium or Aluminum, depending on their concentration, while in the case of Eu-doped  $\text{TiO}_2$  powders, rutile phase appeared at 1000°C and the phase transition was even not completed at this temperature for the highest Eu concentration. This result demonstrates that  $\text{Eu}^{3+}$  plays the role of anatase phase stabilizer, much better than other doping elements. It can be noted that only a few amount of europium (1%) is sufficient to stabilize the anatase phase up to 900°C.

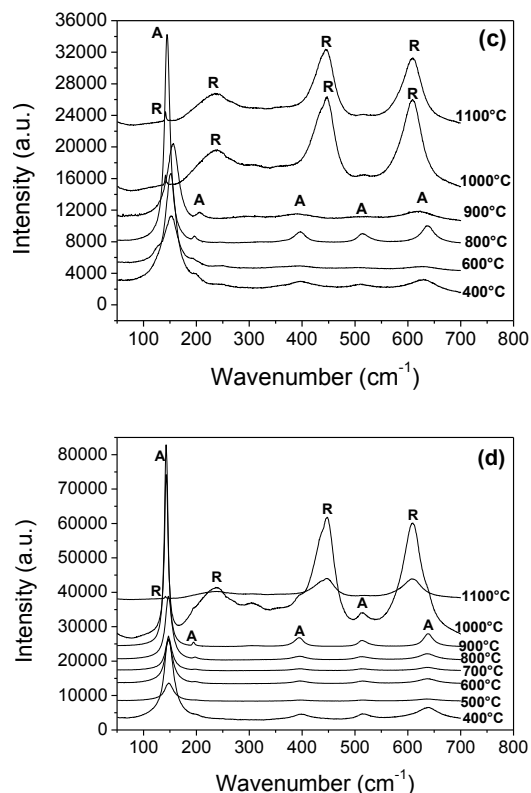
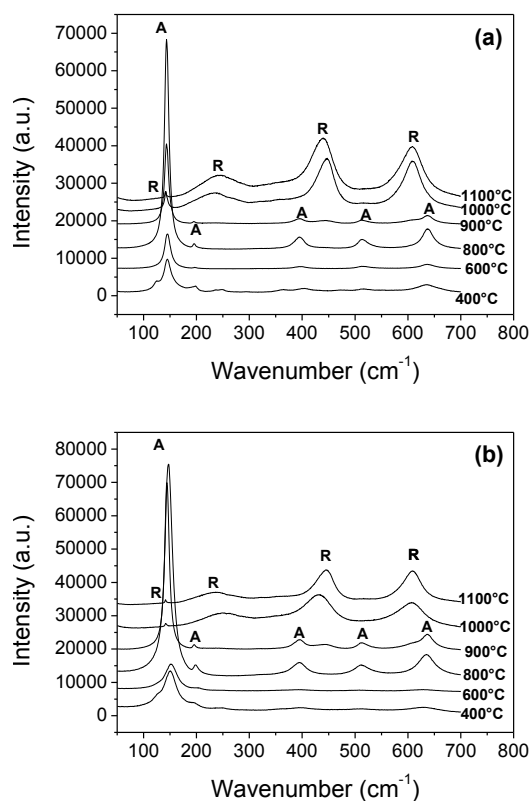


Fig. 4. Raman spectra of  $\text{TiO}_2$  powders doped with different Eu contents (a) 1%, (b) 2%, (c) 5% and (d) 7%.

Raman spectra can also be used to evaluate the crystallite size. Indeed, a phonon confinement model has been reported [17], expressing the relation between the size of  $\text{TiO}_2$  anatase nanocrystals and the full-width at half-maximum (FWHM) of the  $E_g$  Raman mode around  $147\text{ cm}^{-1}$ . Fig. 5 shows that the mean crystallite size, derived using this phonon confinement model, remained between 4 and 8 nm for the non-doped  $\text{TiO}_2$  powder, increasing with the calcination temperature. Furthermore, it increased from 3 nm to 10 nm for the samples doped with Cerium and from 5 nm to 13 nm for those doped with Aluminum. For the Eu-doped samples, it increased from 4 nm to 14 nm. Furthermore, for a given temperature, the mean crystallite size of samples doped with Aluminum was found to be the largest. Hence, it is shown that a relative control of the mean crystallite size (between 3 and 14 nm) can be performed by acting either on the doping or on the heat-treatment temperature.

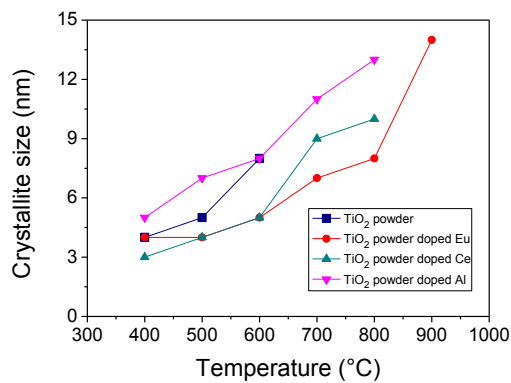


Fig. 5. TiO<sub>2</sub> anatase crystallite size, determined using the FWHM of E<sub>g(1)</sub> Raman mode and the phonon confinement model [17] and reported as a function of the heat-treatment temperature.

#### 4. Conclusion

Nanocrystalline TiO<sub>2</sub> powders doped with Aluminum, Cerium and Europium at several concentrations were prepared by the sol-method. These powders were heat-treated at different temperatures ranging from 400°C to 1100°C and their structure was studied by Raman spectroscopy. Raman analysis of pure and doped TiO<sub>2</sub> powders demonstrated that doping the TiO<sub>2</sub> matrix with aluminum, cerium or europium improves anatase phase stability at high temperature. It was shown that the Europium is the most efficient dopant for anatase phase stabilization up to 900 °C (instead of 600°C for the undoped sample). Moreover, the mean crystallite size increased with the annealing temperature and could be controlled between 3 and 14 nm, depending on the doping species.

#### Acknowledgements

This work has been realized inside the Centre d'Etudes et de Recherches Lasers et Applications (CERLA), which is supported by the Ministère Chargé de la Recherche, the Région Nord/Pas de Calais and the Fonds Européens de Développement Economique des Régions.

#### References

[1] M. Crişan, M. Răileanu, N. Drăgan, D. Crişan, A. Ianculescu, I. Niţoi, P. Oancea, S. Şomărescu, N.

- Stănică, B. Vasile, C. Stan, *Appl. Catal. A-Gen.* 504 (2015) 130.
- [2] R. Klaysri, S. Wichaidit, T. Tubchareon, S. Nokjan, S. Piticharoenphun, O. Mekasuwandumrong, P. Praserthdam, *Ceram. Int.* 41 (2015) 11409.
- [3] J. Reszczyńska, T. Grzyb, Z. Wei, M. Klein, E. Kowalska, B. Ohtani, A. Zaleska-Medynska, *Appl. Catal. B-Environ.* 181 (2016) 825.
- [4] L. Elsellami, H. Lachheb, A. Houas, *Mater. Sci. Semicon. Proc.* 36 (2015) 103.
- [5] D. Kapusuz, J. Park, A. Ozturk, *J. Phys. Chem. Solids* 74 (2013) 1026.
- [6] V.D. Binas, K. Sambani, T. Maggos, A. Katsanaki, G. Kiriakidis, *Appl. Catal. B-Environ.* 113-114 (2012) 79.
- [7] M. Myilsamy, V. Murugesan, M. Mahalakshmi, *Appl. Catal. A-Gen.* 492 (2015) 212.
- [8] Q.-Z. Yan, X.-T. Su, Z.-Y. Huang, C.-C. Ge, *J. Eur. Ceram. Soc.* 26 (2006) 915.
- [9] C. Fan, P. Xue, Y. Sun, *J. Rare Earths* 24 (2006) 309.
- [10] Y. J. Choi, Z. Seeley, A. Bandyopadhyay, S. Bose, S. A. Akbar, *Sensors and Actuators B: Chemical*. Volume 124, Issue 1, 10 June 2007, Pages 111-117.
- [11] Marko G. Nikolić, Željka Antić, Sanja Čulubrk, Jovan M. Nedeljković, Miroslav D. Dramićanin, *Sensor. Actuat. B-Chem.* 201 (2014) 46.
- [12] C. Leostean, M. Stefan, O. Pana, A.I. Cadis, R.C. Suciuc, T.D. Silipas, E. Gautron, *J. Alloy. Compd.* 575 (2013) 29
- [13] M. Ikeda, J.-G. Li, N. Kobayashi, Y. Moriyoshi, H. Hamanaka, T. Ishigaki, *Thin Solid Films* 516 (2008) 6640.
- [14] L. Diamandescu, F. Vasiliu, D. Tarabasanu-Mihaila, M. Feder, A.M. Vlaicu, C.M. Teodorescu, D. Macovei, I. Enculescu, V. Parvulescu, E. Vasile, *Mate. Chem. Phys.* 112 (2008) 146.
- [15] B.M. Reddy, A. Khan, Y. Yamada, T. Kobayashi, S. Lorient, J.C. Volta, *J. Phys. Chem. B*, 107 (2003) 5162.
- [16] V. Rico-Pérez, A. Bueno-López, *Appl. Sci.* 4 (2014), 468.
- [17] K.-R. Zhu, M.-S. Zhang, Q. Chena, Z. Yina, *Phys. Lett. A* 340 (2005) 220.

# Enhancement of characteristics of a functionalized oligophenylene by acid hydrolysis modification

S. Ben. Amor<sup>a,c</sup>, S. Belkhiria<sup>b</sup>, A. Haj. Said<sup>e</sup> and S. Roudesli<sup>c</sup>

<sup>a</sup>Faculté des sciences et techniques Sidi Bouzid, B.P.380, Université de Kairouan, 9100 Tunisie

<sup>b</sup>Faculté des sciences, Université de Monastir, 5000, Tunisie

<sup>c</sup>Laboratoire Polymères, Biopolymères, Matériaux Organiques, Faculté des sciences, Université de Monastir, 5000, Tunisie

Corresponding author: email: sarra\_ben\_amor77@yahoo.fr

Received date: April 09, 2016; revised date: November 02, 2016; accepted date: December 04, 2016

## Abstract

New modified oligophenylene was prepared by acid hydrolysis of a functionalized oligophenylene (OMPA). The latter was obtained by (4-methoxy phenyl) acetonitrile electrochemical oxidation. The resulting modified oligomer (OAC) was characterized by various spectroscopic techniques: NMR, FTIR and UV. The thermal study showed that the modified material exhibited a higher thermal stability compared with OMPA. Further, the optical study revealed that in solution, the emission was blue-shifted when compared with the non-modified oligomer emission and that the optical gap changed from 3.1 eV to 2.75eV. In chloroform solution, photoluminescence was again blue-shifted by 90 nm, which is probably due to an interaction between the oligomer chains.

**Keywords:** oligophenylene, optical gap, cyclic voltammetry, photoluminescence;

## 1. Introduction

Conjugated polymers have attracted and still attract much attention due to their promising electrochemical, electronic and opto-electronic properties. These kind of polymers are applicable in various technological fields such as electroluminescent displays, field-effect transistors, the elaboration of photovoltaic devices, super capacitors, active thin layer of different sensing devices, etc. [1-4].

In nowadays, compared with inorganic semiconductors, semiconducting polymers have many advantages. In fact, they offer a greater adaptability and flexibility, simple manufacturing techniques and a low cost of production. Moreover, they allow a better and an easier modification polymer's physical and chemical properties when making small structural changes in the monomer [4-12]. Indeed, not only the polymeric backbone influences these properties but also those depend on the nature of the presence of covalently attached functional groups. In fact, the attachment of functional groups onto the polymer backbone or the modification of the monomer repeat unit in a post-polymerization step can be used to achieve molecular level control of the structure and the properties of the polymer. And then, it will be possible to (a) give new functionalities to the polymer (b) enhance the delocalization of electrons through the  $\pi$ -conjugation on the polymer (c) reduce the polymer's band gap by the control of the HOMO-LUMO energy level (d) improve the optical and electrical properties [4-15].

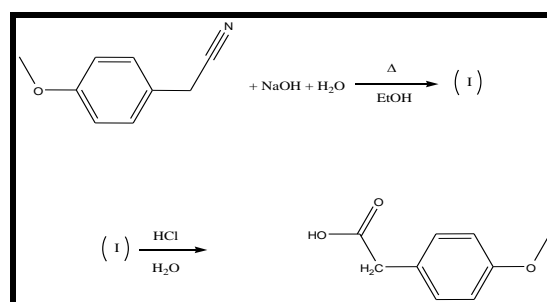
In this frame, one significant design approach towards low band gap polymers is to introduce alternating donor and acceptor units along the polymer backbone [16-19].

In this study, we report the synthesis and the physico-chemical characterization of a new conjugated oligomer prepared by acid hydrolysis modification of a functionalized oligophenylene (OMPA). The obtained material can be described as an oligophenylene backbone with carboxylic pendent chains. Finally, a structural and an optical study of the elaborated material will be described.

## 2. Results and Discussion

### 2.1. Synthesis and characterization

We synthesized the oligomer (OMPA) by the electrolysis of (4-methoxy phenyl) acetonitrile at a controlled potential of 1.8 V as described in the experimental section. The results of gel permeation chromatography analyses and osmometry indicated that the average chain length was about 5 units [20]. Afterward, OMPA was subjected to a chemical modification via acid hydrolysis modification (Scheme 1). The resulting material was analyzed by NMR and FTIR spectroscopy. To analyse the recorded spectra and to assign different signals we prepared the **monomer** (AC) which will serve as a model.



Scheme 1. OAC synthesis

Figures 1 and 2 give us the  $^{13}\text{C}$  NMR spectra of AC and OAC, respectively. They revealed that OMPA was partially modified by acidic hydrolysis reaction. In fact, the signal appearing at 40 ppm in the OAC spectrum corresponds to the deblinded benzylic carbons resulting from the chemical modification. On the other hand, the presence of a signal at 180 ppm (Fig.2), corresponding to the new carboxylic carbons, evidenced the complete modification. It should be noted that signals located around 111 ppm and 130 ppm, were assigned to the quaternary carbons resulting from the C-C inter-ring bond in the oligophenylene structure.

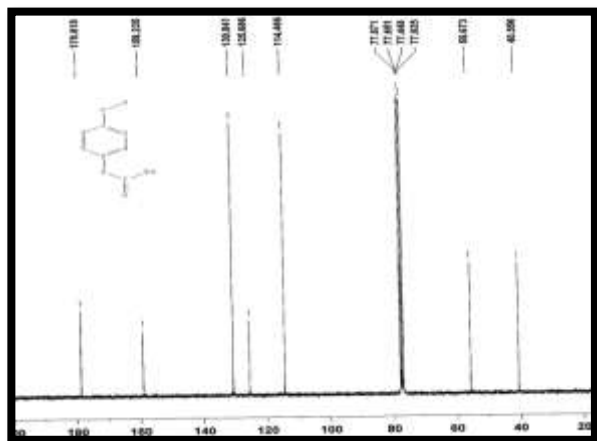


Figure 1.  $^{13}\text{C}$  NMR spectra of AC.

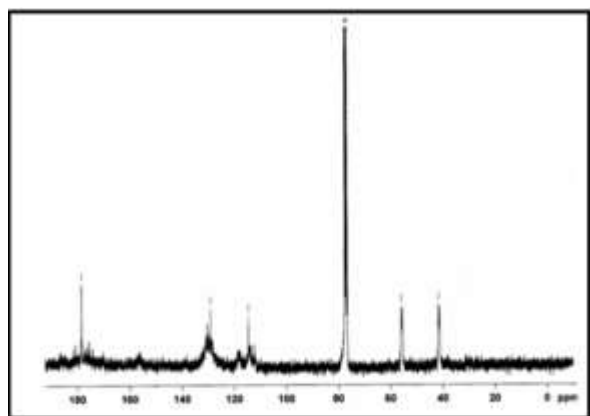


Figure 2.  $^{13}\text{C}$  NMR spectra of OAC.

In the  $^1\text{H}$  NMR spectra of OAC, given in figure 3, we detected three broad signals. The first appeared around 3.8 ppm and corresponded to methoxylic and benzylic protons, the second signal, recorded between 6.8 and 8 ppm, was assigned to aromatic protons and the third, having a low intensity, appears at 12 ppm and corresponds to the mobile hydrogen of carboxylic function.

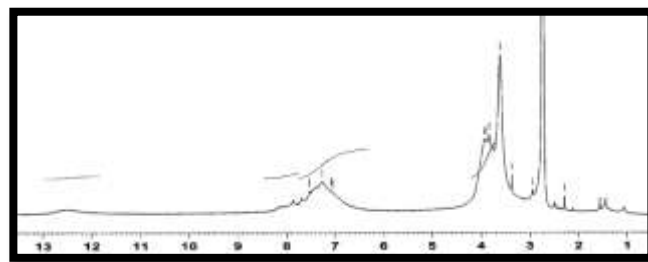


Figure 3.  $^1\text{H}$  NMR spectra of OAC.

The recorded FTIR spectra for OMPA, AC and OAC are illustrated in figure 4. It can be noted that both spectra possess almost the same absorption bands. The most important bands are grouped in Table 1.

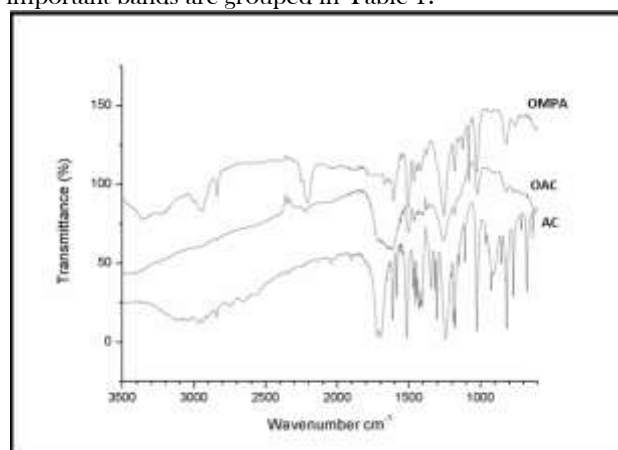


Figure 4. FTIR spectra of OMPA (top), OAC (middle) and AC (bottom).

Table 1. Group frequency assignment for the main infrared band observed in OMPA, AC and OAC spectra.

Vibration	Aromatic ring C-H stretching	Methyl group C-H stretching	Aromatic ring C=C stretching	Methoxy C-O-C
$\nu(\text{cm}^{-1})$	3100	2900	1609, 1512, ,1470	1250, 1029

However, we detected the most important modifications in OA and OAC spectrum. In fact, the band appearing at  $2258\text{ cm}^{-1}$ , typical of the nitrile stretching disappears both spectra of AC and OAC and we note a formation of a new and intense band at  $1700\text{ cm}^{-1}$  characteristic of C=O carboxylic.

## 2.2. Electrochemical Study

Measurements of cyclic voltammetry were performed using a three-electrode cell setup, the supporting electrolyte, tetrabutylammonium tetrafluoroborate ( $\text{Bu}_4\text{NBF}_4$ ), has a concentration of 0.1M in degassed acetonitrile. The electrochemical behaviour of the oligomers was studied to understand their electrochemical stability in p and n-doped states. Figures 5 and 6 illustrate the cyclic voltammograms of AC and OAC, respectively. During the first anodic scan

(fig.5), AC exhibits an irreversible oxidation peak at around 1.7 V which is almost the same than that of MPA [20], clearly indicating that both of MPA and AC have the same donor unit. In the other hand, we note that, like the MPA [20], there isn't a reduction peak. The peaks irreversibility, indicate the short lifetime of the formed radical ions during electrochemical processes. The cyclic voltammogram of OAC exhibits irreversible anodic and, unlike AC, a cathodic responses. However, no clear peaks were recorded. This result could be explained by a slow electron transfer processes and by the presence of oligomer chains with different lengths. Nevertheless, the electrochemical gap, related to the highest occupied (HOMO) and lowest unoccupied (LUMO) molecular orbitals, can be estimated by calculating the difference between the onset of electron and hole injections under the experimental conditions. We note that both anodic and cathodic processes occur at lower potentials than for AC. In fact, the extension of the electronic delocalization, over the molecular structure of the modified oligomer, stabilizes the electrogenerated radical ions. The calculated electrochemical band gap of OAC was found to be 2.41 eV.

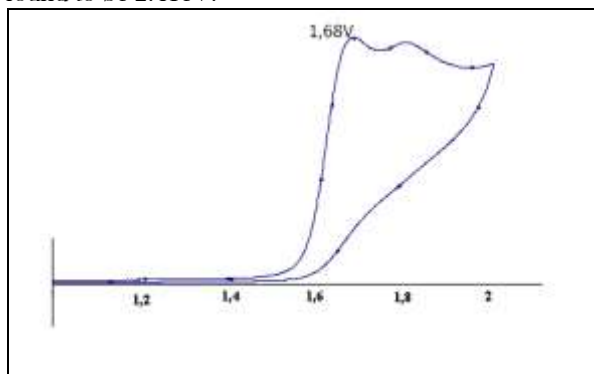


**Figure 5.** Oxidation voltammogram of AC performed in acetonitrile,  $\text{NBu}_4\text{BF}_4$  0.1 M;  $C=10^{-3}$  M;  $\nu=100\text{mVs}^{-1}$  on platinum disc ( $d = 2\text{mm}$ ).

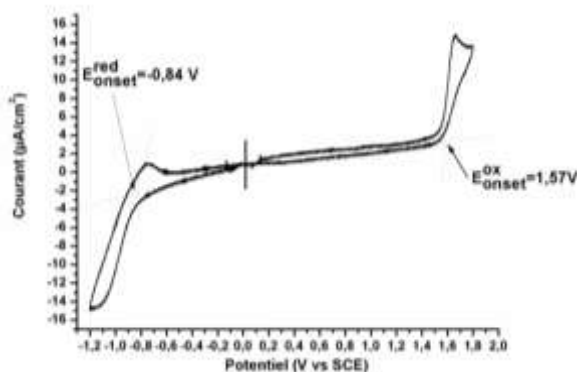


**Figure 6.** Oxidation and reduction voltammogram of OAC performed in acetonitrile,  $\text{NBu}_4\text{BF}_4$  0.1 M;  $C=10^{-3}$  M;  $\nu=20\text{mVs}^{-1}$  on platinum disc ( $d = 2\text{mm}$ ).

Besides, we calculated the HOMO and the LUMO energies as described in the experimental section. We estimated  $E_{\text{HOMO}}$  and  $E_{\text{LUMO}}$  to be -5.8 and -3.39 eV, respectively.

### 2.3. Thermal study

OAC thermal stability was investigated by TGA and DTA. The obtained results are shown in Fig. 7. It should be noted that a small weight loss (<10%), most probably related to evaporation of the residual solvents used during the oligomer preparation and purification, was observed from 80 °C to 120 °C. The results of differential thermal analysis showed that a slow exothermic phenomenon took place from 150°C to 250°C when an accentuated peak was observed. The corresponding weight loss exceeded 30%. This phenomenon could be attributed to the degradation of carboxylic pendant chains. This assumption was supported by the higher thermal stability of the modified oligomer relatively to OMPA [20]. Finally, a faster degradation was observed from 370 °C corresponding to the polyphenylene backbone degradation as previously described [21].

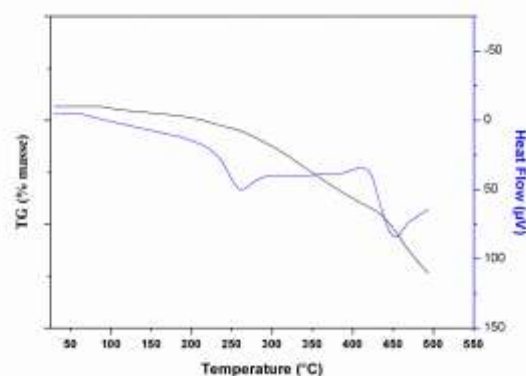


**Figure 7.** TGA and TDA thermograms of OAC under Nitrogen.

### 2.4. Optical properties

The optical absorption spectroscopy enables us to provide fundamental information on the properties of absorption, especially in the case of molecules very absorbing in the UV-Visible as well as in conjugated polymers.

#### 2.4.1. Optical absorption

The optical absorption spectrum performed on OAC in chloroform solution is shown in Figure 8. From this spectrum we can immediately deduce that the solution of OAC absorbs in UV and near UV ranges with a strong absorption band located at 290 nm.

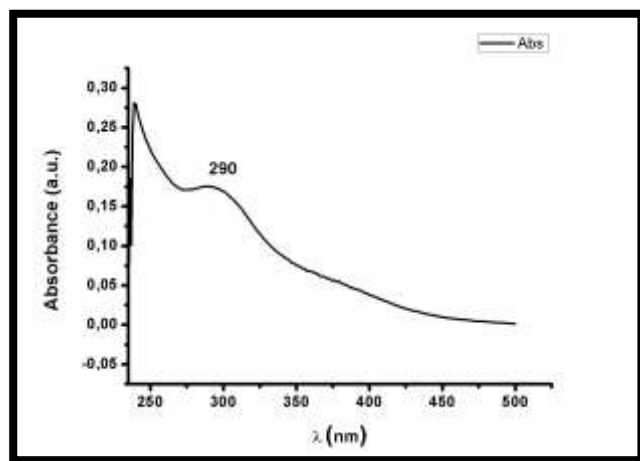


**Figure 8.** UV-vis absorption spectra of OAC in chloroform solution

When compared to the OMPA spectrum, band is blue-shifted at 290 nm. This displacement can be explained by the extension of the electronic delocalization over the oligomer after the chemical modification. The onset  $\lambda_{onset}$  of the OAC optical absorption spectrum (Figure 8) is estimated to be at 450 nm (2.75 eV). This indicates the band gap of OAC is smaller compared to that reported for the unmodified oligomer (400 nm; 3.1 eV) [20]. Note that this value is different from the electrochemical gap previously obtained. This result could be explained by the fact that the optical electron transition leads to the formation of excited states whereas electrochemical reduction/oxidation are reactions generating species in a ground states. Indeed, the electro-generation of radical anion or radical cation in solution involves other kinetic and affects thermodynamic (salvation...). In fact, it is expected that the onsets potential will be lowered owing to fast chemical reactions following electron transfer inducing kinetic instability of the primarily generated radical ions.

#### 2.4.2. Photoluminescence

The steady state PL is widely used to provide fundamental information on the photophysical properties. Figure 9 displays the steady state PL spectra carried out on an OAC in chloroform solution. When compared with spectrum of OMPA in chloroform solution [20], the PL spectrum of OAC in solution (Figure 9) presents two maxima emission at 380 and 485 nm. It presents a maximum emission blue shifted of 90 nm with respect to OMPA in solution because of the presence 4-methoxy cyanostyryl pendant chains in OMPA. These groups increase the degree of delocalization of  $\pi$ -electrons on the carbon atoms of the oligomer backbone which are responsible for the conjugation. This case shows how the chemical nature of the substituent group can impact the conjugation of polymer.

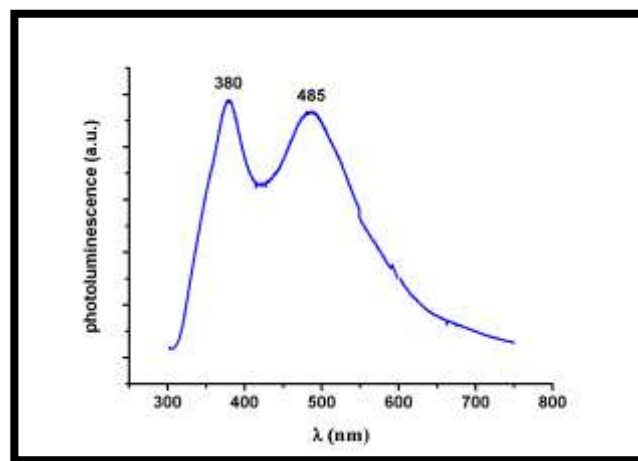


**Figure 9.** Steady state PL spectra of OAC in  $\text{CHCl}_3$  solution; (excitation wavelength 320 nm).

### 3. Experimental Section

#### 3.1. Chemicals

4-Methoxyphenyl acetonitrile, 4-methoxybenzaldehyde and tetraethyl ammonium tetrafluoroborate were from ACROS. Chloroform and dichloromethane were from PROLABO. Diethyl ether, ethanol, petroleum ether and acetonitrile were from PANREAC. Chemicals were used as received.

#### 3.2. Analysis

##### 3.2.1 Spectroscopic Analysis

FTIR analysis was performed with a Bruker Vector 22. The spectra were obtained with KBr pressed pellets.  $^1\text{H}$  NMR and  $^{13}\text{C}$  NMR spectral data were obtained on a Bruker AV 300 spectrometer in  $\text{CDCl}_3$  as solvent. UV-Vis spectrophotometric measurements were performed with a Shimadzu spectrophotometer.

##### 3.2. 2. Gel permeation chromatography (GPC) and osmometry analysis.

The oligomer's chain length was determined by Gel permeation chromatography (GPC) and osmometry. A  $\mu$  styragel 500 A-15  $\mu\text{m}$  column (length 300 mm and diameter 7.8 mm) was used in GPC. The temperature was 30°C. The solvent was tetrahydrofuran with a flow rate of 0.85 mL/min. Polystyrene was used as a standard for the column calibration. For the osmometry study, a Knauer thermoelectric apparatus was used with the (4-methoxy phenyl) acetonitrile as standard.

##### 3.2.3. Thermal Study

A METTLER DSC was used for the thermal study. The samples were analyzed between ambient temperature and 500°C with a heating rate of 10 °C/min. The dynamic thermogravimetric analysis was carried out in a Perkin-Elmer TGS-1 thermal balance with a Perkin-Elmer UV-1 temperature program control. The samples were placed in a platinum sample holder and the thermal degradation measurements were carried out between 30 and 550°C at a speed rate of 10°C/min under Nitrogen atmospheres.

### 3.2.4. Photoluminescence Study

Optical density measurements were carried out at room temperature (RT) using a Cary 2300 spectrophotometer, in the range 200 to 2200 nm. Steady-state photoluminescence emission (PL) was carried out on a Jobin-Yvon Fluorolog 3 spectrometer using a Xenon lamp (500 W) at RT and sample degradation.

The transient PL was spectrally dispersed into an ORIEL MS260i imaging spectrograph (150 grooves/mm, f=1/4) designed to minimize stray light with high spectral resolution.

### 3.2.5. Electrochemical Techniques

The voltammetric study was performed with a Voltalab10 apparatus from Radiometer driven by the Volta Master software. The working electrode was a 2mm diameter platinum disk; the reference electrode was a SCE (Tacussel SR110) and the counter electrode was a platinum wire. The preparative electrolyses were carried out in a two-compartment cell, under nitrogen, at a controlled potential versus a SCE (Tacussel C12). The potentiostat and the current integrator were Tacussel (PRT 1-100 and IG 5 respectively). The working electrode and the counter electrode were a 4 cm<sup>2</sup> and a 0.25 cm<sup>2</sup> platinum gaze, respectively. The separation between cell compartments was realized by a number 4 glass frit.

The  $E_{\text{HOMO}}$  and the  $E_{\text{LUMO}}$  were calculated according the empirical method [22, 23] where:

$E_{\text{HOMO}}$  (eV) =  $-(E_{\text{onset}}^{\text{oxi}} + 4.4)$  and  $E_{\text{LUMO}}$  (eV) =  $-(E_{\text{onset}}^{\text{red}} + 4.4)$  with the onset potentials were measured vs an ECS electrode.

## 3.3. Synthesis

### 3.3.1. OMPA synthesis

OMPA was prepared by preparative electrolyses carried out at a constant potential of 1.8 V. The supporting electrolyte used was tetraethyl ammonium tetrafluoroborate (NEt<sub>4</sub>BF<sub>4</sub>) and the (4-methoxy phenyl) acetonitrile (MPA) concentration was about 0.1M. Homogenization of the solution was assured by a mechanical stirring. The electrolyses were stopped after consumption of 2 F/mole of the starting material. The electrolysis solutions were evaporated under vacuum until elimination of the major part of acetonitrile, then 50 ml of water was added and an extraction with dichloromethane was performed to eliminate

the supporting salt. The organic phase, containing the electrolysis products, was concentrated and then precipitated in diethyl ether. OMPA was collected by filtration as a brown powder. The weight ratio of the powder to the starting material ( $m_0/m$ ) was around 0.3.

### 3.3.2. Synthesis of monomer (AC)

A 50 ml reaction vessel was equipped with a magnetic stirrer, reflux condenser, gas inlet and a rubber septum. It was charged with 1mmol of MPA dissolved in 20 ml of anhydrous ethanol. To this mixture was added drop-wise, with stirring, 2 ml of a solution of sodium hydroxide (2M) and heated to reflux for twenty-four hours. The reaction was controlled by thin layer chromatography. Then the medium is acidified with a concentrated HCl solution, that's when it appears a white precipitate that will be filtered through a sintered porosity 4. The reaction yield is 65%. mp 77 ° C

<sup>1</sup>H NMR (300 Hz, CDCl<sub>3</sub>) 3.58 (2H, s), 3.79 (3H, s), 6.85-7.25 (4H, m), <sup>13</sup>C NMR (300 MHz, CDCl<sub>3</sub>) 40.55, 55.67, 114.46, 125.68, 130.84, 159.23 and 179. GC-MS-m/z: [M] 152.

### 3.3.3. Oligo AC (OAC) Synthesis

A 50 ml reaction vessel was equipped with a magnetic stirrer, reflux condenser, gas inlet and a rubber septum. It was charged with 145 mg of OMPA dissolved in 20 ml of anhydrous ethanol. To this mixture was added drop-wise, with stirring, 2 ml of a solution of sodium hydroxide (2M). The mixture was refluxed and stirred under Argon atmosphere for 24 h. The OAC was precipitated in diethyl ether. The yield was about 65 %. The obtained oligomer exhibits a good solubility in commonly used solvents (CHCl<sub>3</sub>, CH<sub>2</sub>Cl<sub>2</sub>, THF...)

## 4. Conclusions

In this study we showed that the acidic hydrolysis of a functionalized oligophenylene (OMPA) can be used for controlling the optical properties of the resulting material. The OMPA was obtained by the electrochemical oxidation of (4-methoxy phenyl) acetonitrile. The chemical modification, performed on its oligomer, led to a highly modified oligophenylene processing a carboxylic moiety as a pendant chain. The obtained material was characterized by various spectroscopic techniques: photoluminescence, NMR, FTIR, and UV. The optical study revealed that, in solution, the modified oligomer exhibited two emissions at 380 and 485 nm, taking place 90 nm lower than the non-modified material and that the optical gap changed from 3.1 eV to 2.75 eV.

## Acknowledgments

This research was supported by the Ministry of Higher Education and Scientific Research, Tunisia.

## References

- [1] T. A. Skotheim, J. Reynolds, *Conjugated Polymers: Theory, Synthesis, Properties, and Characterization*, third edition. CRC Press, Taylor & Francis Group CRC Press. Boca Raton London, New York (2007).
- [2] Wallace, G.G., Sprinks, G.M., Kane-Maguire, L.A.P., Teasdale, P.R. *Conductive Electroactive Polymers: Intelligent Materials Systems*, second edition. CRC Press, Taylor & Francis Group CRC Press. Boca Raton, London, New York (2009).
- [3] Gunes, S., Neugebauer, H., Sariciftci, N.S. *Chem. Rev.* **107** (2007), 1324.
- [4] J. Roncali, *Chem. Rev.* **92** (1992) 711.
- [5] S. J. Higgins, *Chem. Soc. Rev.* **26** (1997) 247.
- [6] M. Leclerc and K. Faid, *Adv. Mater.* **9** (1997) 1087.
- [7] T. M. Swager., *Acc. Chem. Res.*, **31** (1998) 201.
- [8] A. Cravino, G. Zerza, M. Maggini, S. Bucell, M. Svensson, M.R. Andersson, H. Neugebauer, N. S. Sariciftci. *Chem. Commun.*, **24** (2000) 2487.
- [9] Cihaner, A. Önal. A.M. *Synth. Met.* **150** (2005) 39.
- [10] J. Roncali, *Chem. Rev.* **97** (1997) 173.
- [11] Wang, H-J., Chan, L-H., Chen, C-P., Lin, S-L., Lee R-H., Jeng, R-J. *Polymer* **52** (2011) 326.
- [12] Chen, J-C., Liu, Y-C., Ju, J-J., Chiang, C-J., Chern, Y-T. *Polymer* **52** (2011) 954.
- [13] Karsten, B. P., Bijleveld, J. C., Viani, L., Cornil, J., Gierschner, J., Janssen, R.A. J. *J. Mater. Chem.* **19** (2009) 5343.
- [14] Paul-Roth, C., Rault-Berthelot, J., Simonneaux, G., Poriel, C., Abdalilah, M., Letessier, J. *J. Electroanal. Chem.* **597** (2006) 19.
- [15] Rault-Berthelot, J., Paul-Roth, C., Poriel, C., Juillard, S., Ballut, S., Drouet, S., Simonneaux, G. *J. Electroanal. Chem* **623** (2008) 204.
- [16] Killian, J. G., Gofer, Y., Sarker, H., Poehler, T.O., Searson, P.C. *Chem. Mater.* **11** (1999) 1075.
- [17] Lu, Y., Chena, H., Houa, X., Hub, X., Ng, S-C. *Synth. Met.* **160** (2010) 1438.
- [18] Koyuncua, F.B., Koyuncub, S., Ozdemir, E.A. *Electrochim. Acta.* **55** (2010) 4935.
- [19] Pan, X.Y., Liu, S.P., Chan, H.S.O., Ng, S.C. *Macromolecules* **38** (2005) 7629.
- [20] Ben Amor, S., Haj Said, A., Chemek, M., Ayachi S., Massuyeau F., Wéry, J., Alimi, K., Roudesli, S. *J. Mol. Struct.* **1031** (2013) 186
- [21] Massuyeau, F., Faulques, E., Lefrant, S., Majdoub, M., Ghedira, M., Alimi, K., Wéry, J. *Journal of Luminescence* **131** (2011) 1541.
- [22] Janietz, S., Bradley, D.D.C., Grell, M., Gieberler, C., Inbasekaran, M. E.P. Woo *Appl. Phys. Lett.*, **73** (1998) 2453.
- [23] Bredas, J. L., Silbey, R., Boudreaux, D. S., Chance, R. R. *J. Am. Chem. Soc.*, **105** (1983) 6555.

# A comparative study of the structural, magnetic and magnetocaloric properties in $\text{Pr}_{0.6}\text{La}_{0.1}\text{M}_{0.3}\text{MnO}_3$ manganites ( $\text{M} = \text{Ca}, \text{Ba}$ and $\text{Mg}$ )

S. Zouari<sup>1</sup>, E. K. Hlil<sup>2</sup>, M. L. Kahn<sup>3</sup>, M. Ellouze<sup>1</sup> and F. Elhalouani<sup>4</sup>

<sup>1</sup> LMF, University of Sfax, Faculty of Sciences of Sfax, B. P. 1171 - 3000, Tunisia

<sup>2</sup> Institut Néel, CNRS et Université Joseph Fourier, BP 166, F -38042 Grenoble Cedex 9, France

<sup>3</sup> Laboratory of Chemical of Coordination (LCC) of CNRS, University Paul Sabatier, BP 44099, F -31077, Toulouse, Cedex 4, France

<sup>4</sup> National Engineering School of Sfax, B. P. W - 3038, Tunisia

\*Corresponding author: Sana Zouari email: Zouari\_sana85@yahoo.fr

Received date: April 09, 2016; revised date: November 02, 2016; accepted date: December 04, 2016

## Abstract

The Comparison of the structural, magnetic and magnetocaloric properties of  $\text{Pr}_{0.6}\text{La}_{0.1}\text{M}_{0.3}\text{MnO}_3$  ( $\text{M} = \text{Ca}, \text{Ba}$  and  $\text{Mg}$ ) compounds have been studied using X-ray diffraction (XRD) and magnetic measurements. Our compounds have been prepared using the Sol-Gel method reaction at room temperature. Rietveld refinements of the X-ray diffraction patterns reveal that our compounds are single phase and crystallize in the orthorhombic system with  $Pnma$  space group. Magnetization measurements versus temperature in a magnetic applied field of  $0.05\text{T}$  indicate that samples display a ferromagnetic (FM) - paramagnetic (PM) transition with increasing temperature. The Curie temperature  $T_c$  is found to be  $94\text{ K}$ ,  $39\text{ K}$  and  $64\text{ K}$  for  $\text{M} = \text{Ca}, \text{Ba}$  and  $\text{Mg}$ , respectively. From the magnetization data as a function of magnetic applied field, we have determined the associated magnetic entropy change, the maximum of the magnetic entropy  $|\Delta S_M^{\text{Max}}|$  and the relative cooling power (RCP) for  $\text{Pr}_{0.6}\text{La}_{0.1}\text{M}_{0.3}\text{MnO}_3$  ( $\text{M} = \text{Ca}, \text{Ba}$  and  $\text{Mg}$ ) compounds. In the vicinity of  $T_c$  and in a magnetic applied field of  $2\text{ T}$ ,  $|\Delta S_M^{\text{Max}}|$  reached, the values of  $0.87\text{ J/kg K}$ ,  $1.43\text{ J/kg K}$  and  $0.79\text{ J/kg K}$  for  $\text{M} = \text{Ca}, \text{Ba}$  and  $\text{Mg}$ , respectively.

**Key words:** sol-gel, X-ray diffraction, Magnetic properties, Magnetocaloric effect.

## Introduction

Mixed valence manganese oxides  $\text{Ln}_{1-x}\text{A}_x\text{MnO}_3$  ( $\text{Ln} = \text{rare-earth}, \text{A} = \text{alkali metal or alkaline-earth}$ ) with perovskite structure are the topic of continuing interest for various decades. This interest appears from their fascinating magnetic performance and transport properties, as well as practical applications [1, 2]. In these compounds, double exchange interactions and the limited lattice distortions, starting from Jahn-Teller effect, have been implored to clarify the magneto-transport properties [3, 4]. Now, magnetic refrigeration is enhancing hopeful technology to modify the conventional gas-compression expansion technique [5]. The magnetocaloric effect (MCE) is a subject property of a magnetic material appears due to the coupling of

magnetic sub-lattice with the magnetic field. With the aim of achieving large magnetic entropy changes induced costs, by the low tunable magnetic field changes at low temperature, many researchers have revealed that Curie temperature as well as magnetic entropy change can be tuned by controlling relative ratio  $\text{Mn}^{3+}/\text{Mn}^{4+}$  [6], the average size of the  $\langle r_A \rangle$  cation site [7]. Our present study has been carried out to study the effect of Ca, Ba and Mg substitution on the magnetic and magnetocaloric properties of  $\text{Pr}_{0.6}\text{La}_{0.1}\text{M}_{0.3}\text{MnO}_3$  ( $\text{M} = \text{Ca}, \text{Ba}$  and  $\text{Mg}$ ) compounds. These samples, with fixed  $\text{Mn}^{3+}/\text{Mn}^{4+}$  ratio, and various  $\langle r_A \rangle$  values, provide a good system to detect the individual magnetic nature of rare earth ion in perovskite manganites.

## 2. Experimental techniques

$\text{Pr}_{0.6}\text{La}_{0.1}\text{M}_{0.3}\text{MnO}_3$  ( $\text{M} = \text{Ca}, \text{Ba}$  and  $\text{Mg}$ ) compounds have been prepared using the Sol-Gel method at room temperature. Stoichiometric amounts of  $\text{Pr}_2\text{O}_3$ ,  $\text{La}_2\text{O}_3$ ,  $\text{BaO}$ ,  $\text{CaO}$ ,  $\text{MgO}$  and  $\text{Mn}_2\text{O}_3$  were dissolved in nitric acid,  $\text{HNO}_3$ . Suitable amounts of

citric acid and ethylene glycol as coordinate agent were added with respect to the compounds formation and a complete homogenous transparent solution was obtained. Finally, the resulted precursor was annealed in air at  $1000^\circ\text{C}$  for 3 hours.

Phase purity, homogeneity and cell dimensions were checked by powder X-ray diffraction at room temperature. Structural analysis was carried out using the standard Rietveld technique using the FULLPROF program [8, 9]. Magnetization measurements versus

temperature in the range 0–200 K were carried out using a SQUID magnetometer. MCE was deduced from the magnetization measurements versus magnetic applied from 0 to 5T at several temperatures around the Curie temperature ( $T_c$ ).

### 3. Results and discussion

#### 3.1. Structural properties

The  $\text{Pr}_{0.6}\text{La}_{0.1}\text{M}_{0.3}\text{MnO}_3$  ( $M = \text{Ca}, \text{Ba}$  and  $\text{Mg}$ ) compounds were characterized by the X-ray powder diffraction (XRD) patterns at room temperature [10–12]. All reflection lines were successfully indexed according to the orthorhombic perovskite structure with  $Pnma$

space group. The unit cell volume and the lattice parameters obtained by whole patterns refinements are given in Table 1.

**Table. 1** Lattice parameters, unit cell volume, magnetic properties and grain size (D) of  $\text{Pr}_{0.6}\text{La}_{0.1}\text{M}_{0.3}\text{MnO}_3$  ( $M = \text{Ca}, \text{Ba}$  and  $\text{Mg}$ ) compounds.

$\text{Pr}_{0.6}\text{La}_{0.1}\text{M}_{0.3}\text{MnO}_3$	a (Å)	b (Å)	c (Å)	V (Å <sup>3</sup> )	D	$T_c$ (K)
M = Ca	5.4549 <sub>1</sub>	7.6861 <sub>2</sub>	5.4415 <sub>3</sub>	228.14 <sub>8</sub>	37.05	94
M = Ba	5.4315 <sub>6</sub>	7.6476 <sub>1</sub>	5.4173 <sub>7</sub>	225.03	28	39
M = Mg	5.4856	7.7348	5.4760	232.35 <sub>1</sub>	29.28	64

The unit cell volume decreases with  $\langle r_c \rangle$  increasing (Table. 2). This behavior is due to the difference ionic radius of Ca, Ba and Mg. The tolerance factors ( $t_c$ ) were estimated [13]. The calculated tolerance factors ( $t_c$ ) ranges between 0.89 and 0.96 in agreement with an orthorhombic structure (Table 2). The ionic radii were taken according to Shannon [14, 15].

**Table. 2** Variation of  $\langle r_A \rangle$ ,  $\langle r_M \rangle$ ,  $\langle r_B \rangle$  and  $t_G$  for  $\text{Pr}_{0.6}\text{La}_{0.1}\text{M}_{0.3}\text{MnO}_3$  ( $M = \text{Ca}, \text{Ba}$  and  $\text{Mg}$ ) compounds.

Compounds	$\text{Pr}_{0.6}\text{La}_{0.1}\text{M}_{0.3}\text{MnO}_3$		
	M = Mg	M = Ca	M = Ba
$r_M$ (Å)	0.72	1.18	1.57
$r_A$ (Å)	1.045	1.183	1.3
$r_B$ (Å)	0.61	0.61	0.61
V (Å <sup>3</sup> )	232.35	228.1	225.03
$T_c$	0.862	0.914	0.952

The average grain size (D) was estimated from the X-ray diffraction peaks using the Scherrer formula [16]:  $D = \frac{K\lambda}{\beta \cos\theta}$ .  $\lambda$  is the X-ray wavelength employed,  $\theta$  is the diffraction angle for the most intense peak [17] and  $\beta$  is defined as  $\beta^2 = \beta_m^2 - \beta_s^2$ . Here,  $\beta_m$  is the experimental full width at half maximum (FWHM) and  $\beta_s$  is the FWHM of a standard silicon sample the experimental full width at half-maximum (FWHM) of the same peak. The values of the effective particle size (D) are summarized in Table 1. We conclude that the  $\text{Pr}_{0.6}\text{La}_{0.1}\text{Ba}_{0.3}\text{MnO}_3$  compound has the smaller Grain size (D = 28nm).

#### 3.2. Magnetic properties

Magnetization measurements as a function of temperature in a magnetic applied field of 0.05T prove that our synthesized compounds display a ferromagnetic to paramagnetic transition with increasing temperature (Fig. 1). The Curie temperatures ( $T_c$ ) values, defined in terms of the inflection point of M (T) curve obtained using the derivative  $dM/dT$  as function of temperature are listed in Table 1. It should be observed that the magnetization decreasing at low temperature observed in  $\text{Pr}_{0.6}\text{La}_{0.1}\text{Ba}_{0.3}\text{MnO}_3$  and  $\text{Pr}_{0.6}\text{La}_{0.1}\text{Mg}_{0.3}\text{MnO}_3$  compounds arise from the polarization of the magnetic rare earth

ion sub-lattice influenced by the molecular field of Mn ions [18].

In order to conclude the type of magnetic phase transition in  $\text{Pr}_{0.6}\text{La}_{0.1}\text{M}_{0.3}\text{MnO}_3$  (M = Ca, Ba and Mg) compounds, we have analyzed H/M versus  $M^2$  curves extracted from the isothermal M vs. H data (Fig. 2) using Banerjee criterion [19]. According to this criterion, the magnetic transition is the first order (second order) if the slope the plot H/M is negative (positive). For our compounds, a second order phase transition has been proved from the positive slope of H/M versus  $M^2$  curves.

### 3.3. Magnetocaloric effect

The total magnetic entropy  $|\Delta S_M|$  as a function of temperature and magnetic applied field for our synthesized compounds were valued from magnetization isotherms. According to the thermodynamic theory based on Maxwell relations, the entropy change  $|\Delta S_M|$  can be given through the formula:

$$\left(\frac{\delta M(H,T)}{\delta T}\right)_H = \left(\frac{\delta S_M(H,T)}{\delta H}\right)_T$$

which directly implies that:  $\Delta S_M(T, H) = \int_0^H \left(\frac{\delta M}{\delta T}\right)_H \delta H$

The  $|\Delta S_M|$  values of  $\text{Pr}_{0.6}\text{La}_{0.1}\text{M}_{0.3}\text{MnO}_3$  (M = Ca, Ba and Mg) compounds for different external magnetic applied field are listed in Table.3.

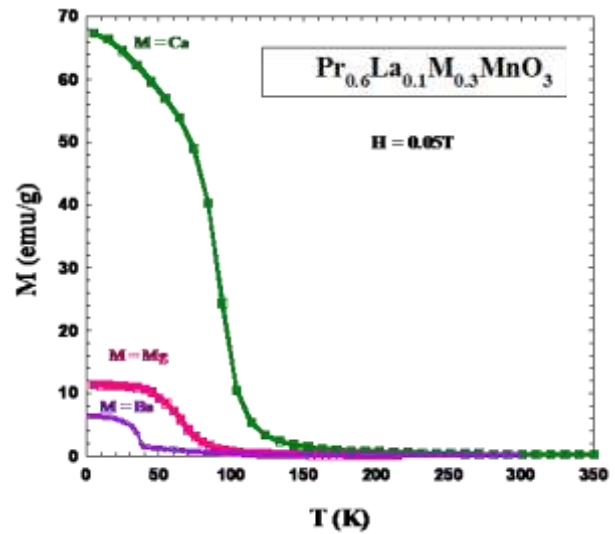


**Figure 1.** Temperature dependence of the magnetization at  $\Delta H = 0.05\text{T}$  for  $\text{Pr}_{0.6}\text{La}_{0.1}\text{M}_{0.3}\text{MnO}_3$  (M = Ca, Ba and Mg) compounds.

**Table. 3** The maximum of the magnetic entropy  $|\Delta S_M^{\text{Max}}|$  of  $\text{Pr}_{0.6}\text{La}_{0.1}\text{M}_{0.3}\text{MnO}_3$  (M = Ca, Ba and Mg) compounds.

Magnetic fields	$\text{Pr}_{0.6}\text{La}_{0.1}\text{M}_{0.3}\text{MnO}_3$		
	M = Ca	M = Ba	M = Mg
	$ \Delta S_M^{\text{Max}} $ (J/Kg.K)	$ \Delta S_M^{\text{Max}} $ (J/Kg.K)	$ \Delta S_M^{\text{Max}} $ (J/Kg.K)
1 T	0.54	0.56	0.40
2 T	0.87	1.43	0.79
3 T	1.72	2.48	1.10
4 T	2.23	2.83	1.42
5 T	2.7	2.92	1.74

All our compounds reveal large MCE effect close to the Curie temperature due to the large drop in magnetization. The maximum of the magnetic entropy achieves the highest value of 1.43 J/kg K at 39 K upon a magnetic field change of 2 T for  $\text{Pr}_{0.6}\text{La}_{0.1}\text{Ba}_{0.3}\text{MnO}_3$  compound. The value of  $|\Delta S_M^{\text{Max}}|$  of  $\text{Pr}_{0.6}\text{La}_{0.1}\text{Ba}_{0.3}\text{MnO}_3$  compound at 5T (Table3), is found to be higher than that reported recently by Kh. Sbissi et al. in  $\text{Pr}_{0.8}\text{Bi}_{0.2}\text{MnO}_3$  compound ( $|\Delta S_M^{\text{Max}}| = 2.77$  J/kg K for H = 5T at 114 K) [20].

The relative cooling power (RCP) is estimated as  $\text{RCP} = -\Delta S_M^{\text{max}} \times \delta T_{\text{FWHM}}$ , where  $\delta T_{\text{FWHM}}$  is the full width of half maximum of  $|\Delta S_M^{\text{max}}|$  versus temperature [21]. The RCP values achieved upon a magnetic applied change of 2T are respectively, 68.87 J/kg, 45.49 J/kg and 38.74 J/kg at 2 T for M = Ca, Ba and Mg. In Table 3, we list the MCE values of the present compounds in comparison with those reported in the literature having similar Tc.

Compared with other materials considered as suitable for applications in magnetic refrigerators and having similar  $T_c$ , our results are interesting enough to

cover the way for investigations of materials useful as a possible refrigerant for low temperature magnetic refrigeration (Table. 4).

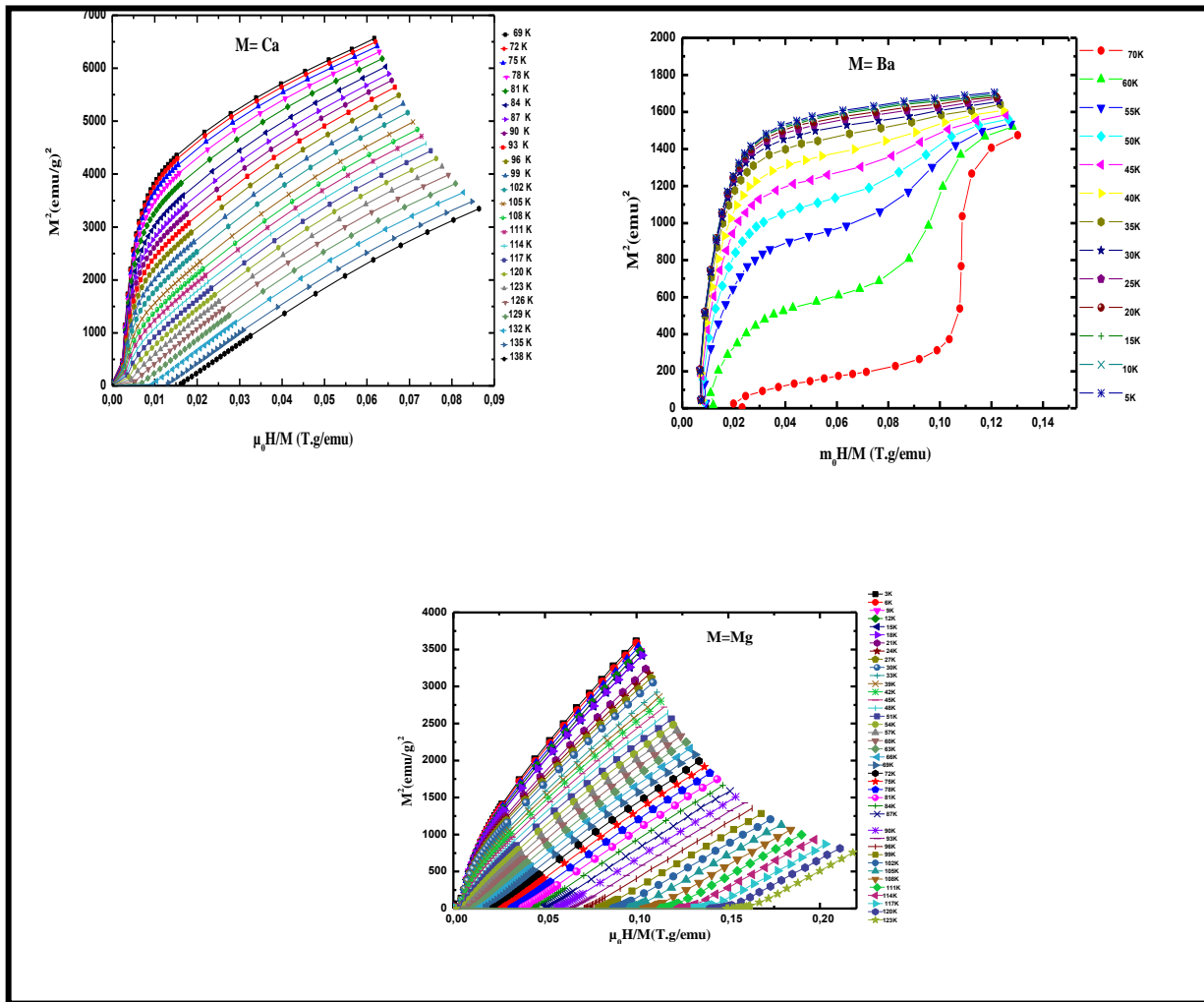


Figure 2. Arrot curves  $M^2$  versus  $\mu_0 H/M$  for  $Pr_{0.6}La_{0.1}M_{0.3}MnO_3$  (M = Ca, Ba and Mg) compounds.

Table. 3 The maximum of the magnetic entropy  $|\Delta S_M^{Max}|$  of  $Pr_{0.6}La_{0.1}M_{0.3}MnO_3$  (M = Ca, Ba and Mg) compounds.

	$T_c$ (K)	$\Delta H(T)$	$ \Delta S_M^{Max} $ (J/Kg.K)	RCP (J.K <sup>-1</sup> )	Ref
$Pr_{0.6}La_{0.1}Ca_{0.3}MnO_3$	94	2	0.87	68.87	This work
$Pr_{0.6}La_{0.1}Mg_{0.3}MnO_3$	65	2	1.43	38.74	This work
$Pr_{0.6}La_{0.1}Ba_{0.3}MnO_3$	39	2	0.79	45.49	This work
$La_{0.5}Ca_{0.5}MnO_3$	220	2	1.13	67.8	[22]
$La_{0.4}Gd_{0.1}Ca_{0.5}MnO_3$	100	2	0.78	67.84	[22]
$Pr_{0.8}Pb_{0.2}MnO_3$	175	1.35	2.64	55	[23]
$La_{0.62}Bi_{0.05}Ca_{0.33}MnO_3$	248	2	5.3	125	[24]
Gd	294	5	5	196	[25]

#### 4. Conclusion

The  $\text{Pr}_{0.6}\text{La}_{0.1}\text{M}_{0.3}\text{MnO}_3$  ( $M = \text{Ca}, \text{Ba}$  and  $\text{Mg}$ ) compounds were studied using X-ray and magnetic measurements. The structural study proves that all our synthesized compounds crystallize in the orthorhombic structure with  $\text{Pnma}$  space group. All our compounds display a FM - PM transition with temperature increasing. Large MCE has been achieved in all compounds at the Curie temperature  $T_c$  and the maximum of the magnetic entropy  $|\Delta S_M^{\text{Max}}|$  acquire the

highest value of 1.43 J/kg K for the  $\text{Pr}_{0.6}\text{La}_{0.1}\text{Ba}_{0.3}\text{MnO}_3$  compound upon a magnetic applied field change of 2 T. The study of the magnetocaloric effect proves that the  $\text{Pr}_{0.6}\text{La}_{0.1}\text{Ca}_{0.3}\text{MnO}_3$  compound is the most important candidate for potential applications in the field of magnetic refrigeration at low temperatures. The attained RCP values of our compounds are similar with other reported values for materials used as magnetic refrigerants at low temperature.

#### Acknowledgment

This study has been supported by the Tunisian Ministry of Scientific Research and Technology, the Neel Institute and the laboratory of chemical coordination (LCC) of Toulouse.

#### References

- [1] T. Venkatesan, M. Rajeswari, Z.-W. Dong, S.B. Ogale, R. Ramesh, Philos. Trans. R. Soc. Lond, Ser. A 356, (1998), 1661.
- [2] M. Khelifi, E. Dhahri, E.K. Hlil, J. Alloy. Comp. 587, (2014), 771-777
- [3] C. Zener, Phys. Rev. 82 (1951) 403.
- [4] S. Othmani, M. Bejar, E. Dhahri, E.K. Hlil, J. Alloy. Comp. 475(1-2), (2009), 46-50.
- [5] R.D. Shull, R.D. McMichael, J.J. Ritter, Nanostruct. Mater. 2 (1993) 205.
- [6] A.M. Aliev, A.G. Gamzatov, A.B. Batdalov, A.S. Mankevich, I.E. Korsakov, Physica B, 406, (2011), 885.
- [7] V.S. Kolat, T. Izgi, A.O. Kaya, N. Bayri, H. Gencer, S. Atalay, J. Magn. Magn. Mater. 322, (2010), 427.
- [8] R. Madar, P. Chaudouet, E. Dhahri, J.P. Senateur, R. Fruchart, B. Lambert, J Solid Stat. Chem. 56(3, 1) (1985) 335-342.
- [9] J. Rodriguez. Carvajal: Fullprof98. Laboratoire Leon Briouillon (CEACNRS) (1998)
- [10] S. Zouari, A. Nasri M. Ellouze, · E.K. Hlil, ·F. Elhalouani, J Supercond Nov Magn, s10948, 2435.
- [11] S. Zouari, M. Ellouze, E.K. Hlil, F. Elhalouani, M. Sajieddine, Solid State Communication, 180, (2014), 16.
- [12] S. Zouari, · M. L. Kahn, M. Ellouze, ·F. Elhalouani, J Supercond Nov Magn, European Physical Journal Plus, · 2, (2015), 15177.
- [13] P. K. Siwach, P. Srivastava, H.K. Singh, A. Asthana, Y. Matsui, T. Shripathi, O.N. Srivastava, *J. Magn. Magn. Mater*, 321, (2009), 1820.
- [14] R. D. Shannon, Prewitt, T.Ch: Structural crystallography and crystal chemistry. Acta Crystallogr, Sect. B, *Struct. Crystallogr. Cryst. Chem.* 25, 925-946 (1969).
- [15] R. D.Shannon: Crystal physics, diffraction, theoretical and general crystallography. *Acta Crystallogr, A Cryst. Phys. Diffr. Theor. Gen. Crystallogr.* 32, (1976), 767.
- [16] A. Guinier, in: X. Dunod (Ed.), *Theorie et Technique de la Radiocristallographie*, (1964), 482.
- [17] S. H. Mahmood, J. Dawood, A. F. Lehlooh, A. W. Cheikhrouhou, A. Ammar, 196, (2010), 385
- [18] N. Rama, V. Sankaranarayanan, M. Opel, R. Gross, M.S. Ramachandra Rao, *J.Alloys Compd*, 443, (2007), 7.
- [19] S. k. Banerjee, *Phys. Lett*, (1964), 16.
- [20] Kh. Sbissi· M. L. Kahn M. Ellouze F. Elhalouani, *J Supercond Nov Magn*, 28, (2015), 2899.
- [21] J. S. Amaral, M. S. Reis, V. S. Amaral, T. M. Mandonca, J. P. Araujo, M. A. Sa, P. B. Tavares, J. M. Vieira, *J. Magn. Magn. Mater*, 290, (2005), 686.
- [22] A. Krichene, W. Boujelben, A. Cheikhrouhou, *J. Alloys. Compd*, 550, (2013), 75.
- [23] Gschneidner, K. A, Pecharsky, V. K.: *AnnuRev, Mater, Sci*, 30, 387, (2000).
- [24] H. Gencer, S. Atalay, H.I. Adiguzel, V.S. Kolat, *Physica B* 357 (2005) 326.
- [25] V. K. Pecharsky, K.A. Gschneidner, *J. Phys. Rev. Lett*, 78, (1997), 4494.

# Effects of substitution of some rare earth on the structural and magnetic properties in the site (A) of $\text{Ca}_{2-x}\text{Ln}_x\text{MnO}_4$ , where Ln=Nd and Sm compound.

F. S. Shokr<sup>a</sup>, M. Hussein<sup>a</sup> and E. Dhahri<sup>b</sup>

<sup>a</sup>Physics Department, Rabigh College of Science and Arts, P.O. Box 344, Rabigh, 21911, King Abdulaziz University, Jeddah, Saudi Arabia

<sup>b</sup>Laboratoire de Physique Appliquée, Faculté des Sciences, B.P. 1171, 3000 Sfax, Université de Sfax, Tunisie.

Corresponding author: email: drf.shokr@outlook.com

Received date: April 09, 2016; revised date: November 02, 2016; accepted date: December 01, 2016

## Abstract

The present study reports the effect of rare earth doping on the structural and magnetic properties in the  $\text{Ca}_{2-x}\text{Ln}_x\text{MnO}_4$ , where Ln=Nd and Sm Ruddlesden Popper-type. The studied specimens were synthesized as powder samples by solid state reaction at high temperature. The analysis by powder X-ray diffraction using Rietveld refinement showed the crystallization in the tetragonal system for all compounds. The magnetic measurements were studied as a function of temperature ( $T = 2-300$  K). When the temperature decreases, each compound has shown first a ferromagnetic-paramagnetic (FM-PM) transition and then an antiferromagnetic-ferromagnetic (AFM-FM) one. The transition temperatures are found to be rare earth doping dependent. For all compounds, a spin-glass phenomenon is evidenced by FC/ZFC magnetization curves.

**Keywords:** Ruddlesden-Popper, structural, magnetic and spin-glass phenomenon;

## 1. Introduction

Besides the perovskite family, the Ruddlesden-Popper manganites, which consist of a regular intergrowth of single rock-salt with multiple perovskite layers, were studied most extensively. The crystal chemistry of these oxides shows numerous studies, which are complex and subject to controversy [1]. The  $\text{Ca}_2\text{LnMnO}_4$  compounds (Ln=Pr, Sm, Gd, Ho...) are good examples of Ruddlesden-Popper manganites. These compounds display diverse magnetic and electronic phases such as antiferromagnetic (AFM) insulating, ferromagnetic (FM) conductor, paramagnetic (PM) insulating [2], spin-glass [3-5] and charge-ordering [6]. In the other hand, these Ruddlesden-Popper manganites display interest magnetic properties depending on materials-doping, multiple phase transitions, saturation and no-saturation magnetization. The Ln-doped manganites of  $\text{Ca}_2\text{MnO}_4$  compound induces a mixed valence state ( $\text{Mn}^{3+}/\text{Mn}^{4+}$ ) and enhances magnetic behavior transition; which can be explained by the double exchange interaction between  $\text{Mn}^{3+}$  and  $\text{Mn}^{4+}$  ions [7]. It has been shown that  $\text{Ca}_2\text{LnMnO}_4$  (Ln=Pr, Sm, Gd, Ho...) compounds, which despite their pure bidimensional character submit a spin-glass transition at low temperatures. For the praseodymium phases  $\text{Ca}_2\text{PrMnO}_4$ , all compounds exhibit semiconductor behavior. In this paper, we report the effect of Nd and Sm doping on structure and magnetic properties of  $\text{Ca}_{2-x}\text{Ln}_x\text{MnO}_4$  compounds.

## 2. Experimental section

Specimens of  $\text{Ca}_{2-x}\text{Ln}_x\text{MnO}_4$  (Ln=Nd, Sm) were prepared by solid state reaction method [8]. The  $\text{CaO}$ ,  $\text{Ln}_2\text{O}_3$  and  $\text{MnO}_2$  precursors (all of 99.9% purity) were mixed in appropriate ratios. The obtained powders were pressed under 4 tones into pellets about 1 mm thickness and 8 mm diameter and sintered at 1373 K for 4 days in air with several intermediate regrinding and repressing into pellets. Finally, the mixtures were calcined in air at 1523 K for 24 h on Pt boat. The microstructure was observed by scanning electron microscope (SEM). The pictures were taken at room temperature on a Philips XL 30 equipped with a field emission gun at 19.7 kV. The structure was characterized at room temperature by X-ray powder diffractometer (Siemens D5000) with Cu-K $\alpha$  radiations ( $\lambda = 1.54056$  Å). The phase analysis was checked using FULLPROF program based on the Rietveld method. The magnetization measurements were carried out using a vibrating sample magnetometer in the temperature range 2-300K under an applied field up to 0.07 T.

## 3. Results and discussion

### 3.1. Structural properties:

In order to make sure that all samples are single phase and all chemical elements (Ca, Ln, Mn, and O) are present in  $\text{Ca}_{2-x}\text{Ln}_x\text{MnO}_4$  compounds, XRD and EDAX analysis have been realized. Using Fullprof

program, the diffraction peaks corresponding to  $x=0.000$  (Fig. 1) can be indexed in the tetragonal system with

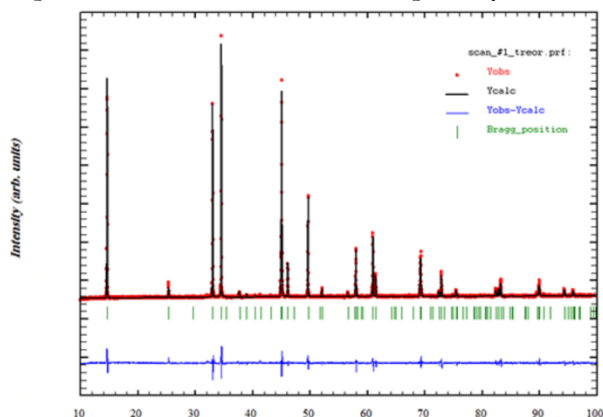


Figure 1. Observed (dots) and calculated Rietveld refinement plots of the XRD parent compound  $\text{Ca}_2\text{MnO}_4$ . The difference between observed and calculated is shown at the bottom. Vertical tick marks represent Bragg positions.

Table 1: Space group and Rietveld refinement parameters results of  $\text{Ca}_{2-x}\text{Ln}_x\text{MnO}_4$  compounds.

	Space group	a (Å)	b (Å)	c (Å)
$\text{Ca}_2\text{MnO}_4$	I 41/acd	5.183	5.183	24.117
$\text{Ca}_{1.8}\text{Sm}_{0.2}\text{MnO}_4$	I 4/mmm	3.728	3.728	11.93
$\text{Ca}_{1.8}\text{Nd}_{0.2}\text{MnO}_4$	I 4/mmm	3.729	3.729	11.93

### 3.2. Magnetic properties:

A systematic investigation of magnetization with temperature has been undertaken at an applied magnetic field of 0.07 T for all samples (Fig. 3). When increasing temperature, all specimens show a ferromagnetic-paramagnetic transition (FM-PM) one, at Curie temperature ( $T_c$ ). The substitution of Ca by Sm leads to the appearance of a second transition at a temperature known as the Neel temperature noted TN. However, this transition does not appear in the case of doping with Nd and the undoped case. This is explained by the fact that the samarium is an element antiferromagnetic (Fig. 4). These two transitions occur at the Curie temperature ( $T_c$ ) and the Neel temperature ( $T_N$ ) determined from the pick of  $(-dM/dT)$  vs. T curves (Fig. 4). For all compounds, the Curie temperature  $T_c$  was found to be constant (around 105 K) and independent to the applied field.

In the other hand, the substitution provides the  $\text{Mn}^{3+}$  ions and induces a mixed  $\text{Mn}^{3+}/\text{Mn}^{4+}$  valence, enhancing the

$I41/acd$  space group. This result is in agreement with those found by Takahashi et al. [9] and Fawcett et al. [10].

The substitution of Ca by Nd or Sm generates spectral modifications a little different to Fig. 1, and the diffraction peaks can be indexed in the same tetragonal system with  $I4/mmm$  space group [11]. The lattice constants of  $\text{Ca}_{2-x}\text{Ln}_x\text{MnO}_4$  at room temperature are given in Table 1.

Fig. 2 shows an example of EDAX analysis spectral realized at room temperature for  $\text{Ca}_2\text{MnO}_4$ ,  $\text{Ca}_{1.8}\text{Sm}_{0.2}\text{MnO}_4$  and  $\text{Ca}_{1.8}\text{Nd}_{0.2}\text{MnO}_4$  compounds ( $x=0.200$ ). This analysis reveals that all elements are present and any element has been volatilized in the course of the heating for all  $x$  compositions.

conduction by  $e_s$  electrons hopping through  $\text{Mn}^{3+}\text{-O-Mn}^{4+}$  system [12, 13]. Such physical phenomenon, called double exchange (DE), is proved by Zener [14] and used by several authors to explain the electrical transport and the magnetic properties undoped manganites. This DE, characterized by a FM state, explains the increase of magnetization with the doped rare earths. These values of magnetization are given in Fig. 5. So, the Sm-doping leads to a competition between two states, AFM and FM, during the doping. This behavior, related to the presence of ferromagnetic nano-domains coupled together by complex interactions (FM and AFM), promotes the formation of a spin glass [15]. To verify the existence of such system, measurements of magnetization in ZFC and FC mode was performed (Fig. 6). It should be noticed that, for all samples, the ZFC curve does not coincide with FC curve below a given temperature  $T_{sg}$ , which is a characteristic of a spin-glass order [11]. These values are given in Table 2.

Table 2: values of Weiss temperature, experimental effective paramagnetic moments and spin-glass temperature of  $\text{Ca}_{2-x}\text{Ln}_x\text{MnO}_4$  compounds.

Echantillons	$\theta_p$ (K)	$\mu_{eff}^{exp}$ ( $\mu_B$ )	$T_{SG}$ (K)
$\text{Ca}_2\text{MnO}_4$	100	3.887	101
$\text{Ca}_{1.8}\text{Sm}_{0.2}\text{MnO}_4$	104	3.62	101
$\text{Ca}_{1.8}\text{Nd}_{0.2}\text{MnO}_4$	99.88	3.91	53

From this table, we can deduce that the temperature spin glass for  $\text{Ca}_{1.8}\text{Nd}_{0.2}\text{MnO}_4$  made is very low comparing to  $\text{Ca}_{1.8}\text{Sm}_{0.2}\text{MnO}_4$ . This difference is mainly due to an AFM behavior of Sm. **Fig. 7** shows the temperature dependence of inverse magnetic susceptibility  $\chi^{-1}$  at different magnetic field. As is well known for FM system, the relation between  $\chi$  and the temperature T should follow the Curie-Weiss law in the PM region:

$$\chi = \frac{C}{T - \theta_p}$$

where C and  $\theta_p$  are the Curie constant and the Weiss temperature, respectively. C and  $\theta_p$  were obtained by fitting the linear paramagnetic region of  $\chi(T)$  curve. The experimental effective paramagnetic moments were calculated from the following formula:

$$C = \frac{N_A \mu_B^2}{3k_B} \mu_{\text{eff}}^2$$

where  $N_A = 6.023 \times 10^{23} \text{ mol}^{-1}$  is the number of Avogadro,  $\mu_B = 9.274 \times 10^{-21} \text{ emu}$  is the Bohr magneton and  $k_B = 1.38016 \times 10^{-23} \text{ J.K}^{-1}$  is the Boltzmann constant.  $\theta_p$  and  $\mu_{\text{eff}}$  are listed in **Table 2**, where it can be seen that the substitution of Ca ion by Sm and Nd one leads to the lightweight decrease of the Weiss temperature. The positive  $\theta_p$  values indicate a FM interaction between spins. Moreover, the decrease of effective magnetic moment from the  $\text{Ca}_{1.8}\text{Sm}_{0.2}\text{MnO}_4$  is related to the AFM behavior, due of Sm element inserted. In addition, the FM to behavior is related to the substitution of Ca ion by Nd ones, which increases the effective magnetic moment of the  $\text{Ca}_{1.8}\text{Nd}_{0.2}\text{MnO}_4$ .

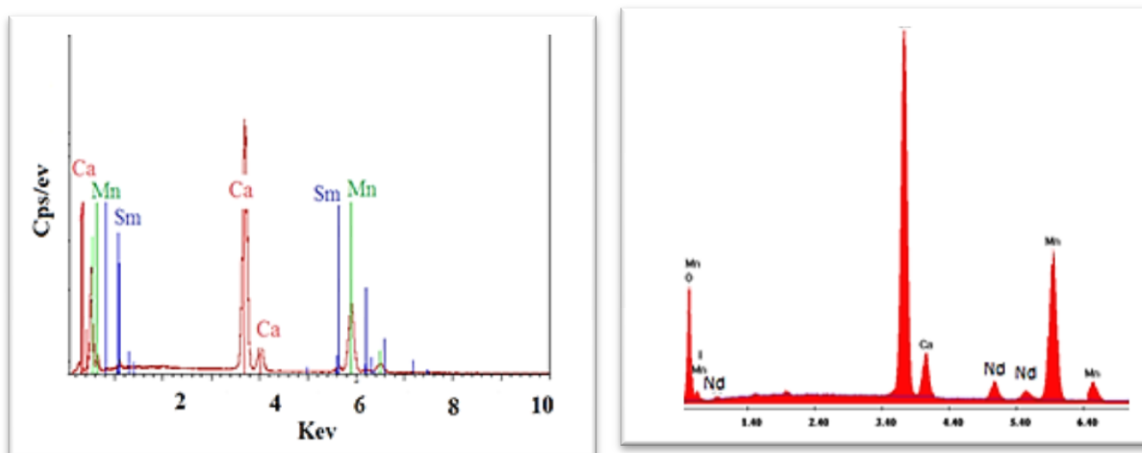


Figure 2. EDAX analysis of  $\text{Ca}_{1.8}\text{Sm}_{0.2}\text{MnO}_4$  and  $\text{Ca}_{1.8}\text{Nd}_{0.2}\text{MnO}_4$  compounds

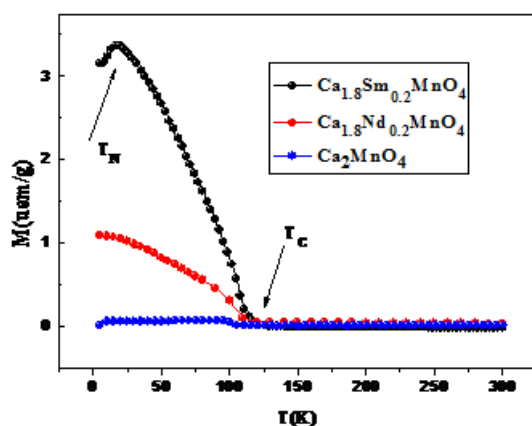


Figure 3. Temperature dependence of magnetization measured at 0.07 T for  $\text{Ca}_2\text{MnO}_4$ ,  $\text{Ca}_{1.8}\text{Sm}_{0.2}\text{MnO}_4$  and  $\text{Ca}_{1.8}\text{Nd}_{0.2}\text{MnO}_4$  compounds

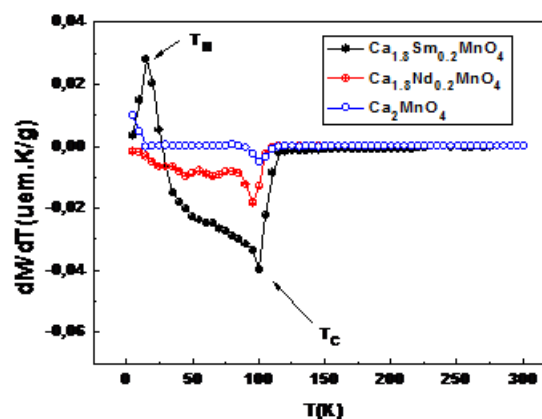


Figure 4. Variation of  $(dM/dT)$  as function of temperature T for all compounds at an applied magnetic field of 0.07 T.

#### 4. Conclusion

In this work, we have investigated the structure and magnetic properties of Ruddlesden Popper family  $\text{Ca}_2\text{MnO}_4$ ,  $\text{Ca}_{1.8}\text{Nd}_{0.2}\text{MnO}_4$  and  $\text{Ca}_{1.8}\text{Sm}_{0.2}\text{MnO}_4$  compounds. There is no structural transition due to substitution of  $\text{Ca}^{2+}$  by  $\text{Ln}^{3+}$ . All the samples crystallize in a tetragonal structure: with space group  $I41/acd$  for  $x = 0$  and  $I4/mmm$  for  $\text{Ca}_{1.8}\text{Ln}_{0.2}\text{MnO}_4$ . The Curie temperature

TC is found to be around 105 K for all samples. At low temperature, the Nd, Sm-doping leads to a competition between the AFM and FM states, and promotes the formation of a spin-glass state. This state is confirmed by a magnetization study in ZFC and FC mode. This last phenomena is absent for Nd dopage, and as for the undoped compound.

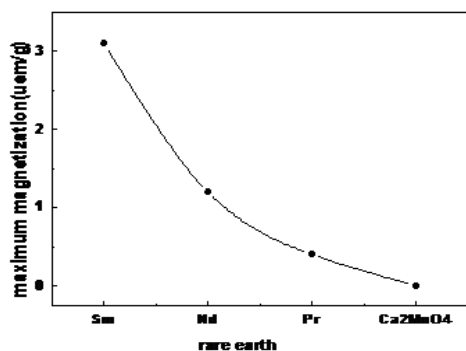


Figure 5. variation of the magnetization as a function of substituted rare earth.

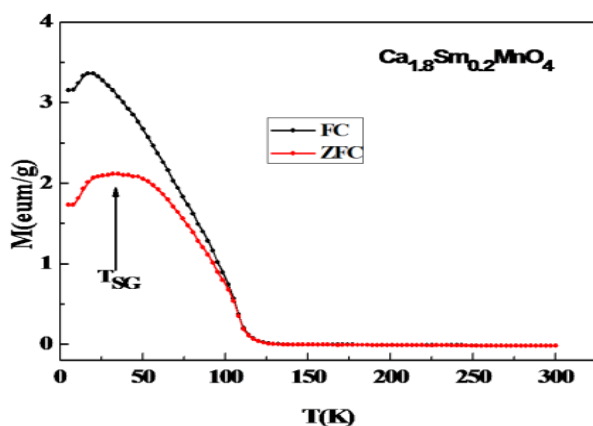
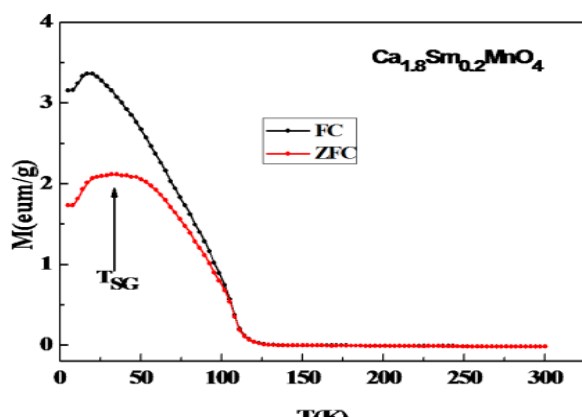
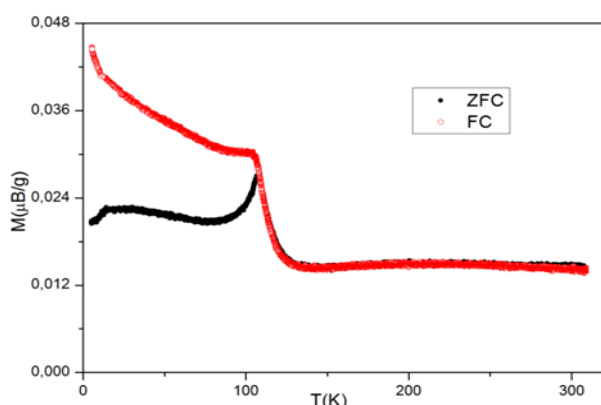


Figure 6. Magnetization (M) as a function of temperature (T) for all compounds measured at 0.07 T under the field-cooled (FC) and zero-field-cooled (ZFC) modes

### Acknowledgement

This Project was funded by the Deanship of Scientific Research (DSR) at King Abdulaziz University, Jeddah, under grant no. G-374-665-37. The authors, therefore, acknowledge with thanks the DSR for technical and financial support.

### References:

- [1] D.K. Han, S.H. Kim, K.P. Hong, Y.U. Kwon, S. Kim and J.S. Lee: Journal of Solid State Chemistry 177 (2004) 1078–1086.
- [2] A. Maignan, C. Martin, G. Van Tendeloo, M. Hervieu, B. Raveau: J. Mater. Chem. 8 (1998) 2411.
- [3] W. Bao, C.H. Chen, S.A. Carter, S.-W. Cheong: Solid State Commun. 98 (1996) 55;
- [4] B.J. Sternlieb, J.P. Hill, U.C. Wildgruber, G.M. Luke, B. Nachumi, Y. Moritomo, Y. Tokura: Phys. Rev. Lett. 76 (1996) 2169.
- [5] C.S. Hong, W.S. Kim, E.O. Chi, N.H. Hur, T.N. Choi: Chem. Mater. 14 (2002) 1832.
- [6] C. Autret, R. Retoux, M. Hervieu, and B. Raveau: Chem. Mater. 2001, 13, 4745-4752
- [7] C. Zener: Phys. Rev. 82 (3) (1951) 403-405.
- [8] M. T. Tlili, M. Bejar, E. Dhahri, M. Sajieddine, M. A. Valente, E. K. Hlil, Mater. Charact., 62; (2011) 243.
- [9] J. Takahashi, T. Kikuchi, H. Satoh, N. Kamegashira, J. Alloys Compd., 192, (1993) 96.
- [10] J. Takahashi, H. Nakada, H. Satoh, N. Kamegashira, J. Alloys Compd., 598, (2006) 408–412.
- [11] J. Takahashi, N. Kamegashira, Mater. Research Bull., 28, (1993) 451-460.
- [12] A.M. Haghiri-Gosnet, J.P. Renard, J. Phys. D, Appl. Phys., 36, (2003) 127.
- [13] M. Bejar, R. Dhahri, E. Dhahri, M. Bali, E. K. Hlil, J. Alloys Compd., 442, (2007) 136-138.
- [14] C. Zener, Phys. Rev., 82, (1951) 403.
- [15] C. Autret, R. Retoux, M. Hervieu, B. Raveau, Chem. Mater., 13, (2001) 45-47.

## Detection of electrical faults with infrared thermography

Abderrahmane Dib and Ali Djermane

Laboratory of electrical engineering and Automatics,

University of Larbi Ben M'Hidi, B.P. 358, Oum El Bouaghi 04000, Algeria

e-mail: dib\_abderrahmane@yahoo.com

Received date: July 26, 2016; revised date: October 13, 2016; accepted date: December 06, 2016

### Abstract

One of the problems that concern most often the electricians is how to determine the conditions or the state of operation of electrical systems quickly, without physical contact with the components and without disconnecting the network system. In other words, how to identify and locate latent defects that would cause unpredictable catastrophic failures, such as poor contact caused by corrosion and oxidation, loosening or bad crimp lugs, overloading of cables and transformers, imbalance phase loads, etc. Most electrical faults are characterized by loss of energy and overheating of the components and eventually by the emission of a quantity of infrared energy which varies with the temperature of the components, according to Plank's law. The detection of this radiation by the infrared thermography technique it is possible to inspect hundreds of points and identify the presence or absence of electrical faults.

IR thermography is a technique that converts the IR radiation into a visual image of the temperature difference shown by the surface of the components. The image obtained is a color map more or less clear showing "hot" zones and "cold" zones filmed surfaces. The inspection and comparison of the image obtained with the IR image of the reference corresponding normal operating state permit to locate the faults undetectable by the human eye. For example, a hot electrical interconnection may indicate poor contact requiring repair.

The tool used in the IR thermography is a portable camera with a pyrometric sensor capable of measuring temperatures of  $-40\text{ }^{\circ}\text{C}$  to  $1500\text{ }^{\circ}\text{C}$ , with a resolution of about  $0.1\text{ }^{\circ}\text{C}$ . In this article, we present infrared thermography and its application for inspection and predictive / preventive maintenance of electrotechnical and electrical systems.

**Keywords:** Infrared, Thermography, preventive maintenance, fault diagnosis;

### 1. Introduction

In the electricity industry, the temperature is often considered an excellent indicator of the status or condition of operating systems because it is a very influential constraint on the reliability of the electrical components. Indeed, the life of an electrical component is significantly reduced when it is subjected to high temperature variations. To prevent failures it is often advisable to perform frequent inspections of the operating temperature of the hot spots of the electrical system, including contacts, connections and junction points. However, frequently check the temperature of dozens of points in an electrical system using temperature sensors such as thermocouples, is a difficult task, costly and can be hazardous. Now, there is the IR infrared thermography which allows the presentation in a visual form the radiant heat energy very many points on the surface of an electrical system. This technique measures the temperature of a large number of points simultaneously without physical contact and without danger. IR thermography consists in taking an infrared image of distribution of heat from the surface of a body.

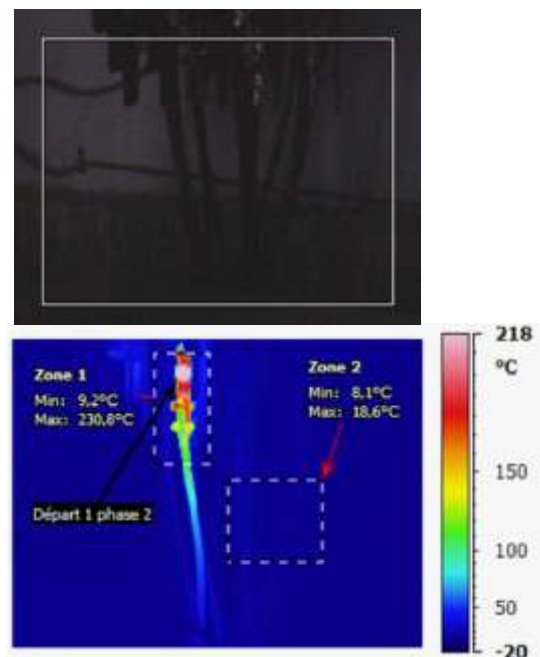


Figure 1. Thermography of depart distribution board

The points where there is a too low or too high heat emission as compared to normal conditions are source of defects in the system. However, taking an image, computer processing and interpretation of infrared images are delicate tasks as they require a good knowledge in IR material and its sources of uncertainty.

Industrial applications of infrared thermography are unlimited, in particular in electrical and mechanical domains. For example, it is effective for the inspection of transmission lines, transformers, thyristors, contactors, fuses, control equipment, motors and electric control switchboards.

In the following sections, infrared thermography technique will be described and its use as a preventive maintenance tool electrical systems.

## 2. Infrared radiation [1]

Electromagnetic radiation is the energy transfer process in the form of electromagnetic waves. These waves do not require hardware support and propagate into space. Planck, German physicist, announced that radiant energy can be emitted or absorbed in the form of quanta. The energy  $E$  contained in radiation quanta is proportional to the frequency  $\gamma$  of the radiation:  $E = h\gamma$  where  $h =$  Planck constant. Electromagnetic radiation are also characterized by their wavelengths  $\lambda = c/\gamma$  into space,  $c = 3.10^8 m/s$ . Electromagnetic radiation is generated by the movements of electric charges or by energy transitions between various quantum states of molecules or nucleus. On the spectrum of electromagnetic radiation, visible light can be distinguished, which covers the range of 0.4 to 0,7 $\mu m$ , and infrared, which is invisible to the human eye [2], extends from 0.7 to 1000 $\mu m$ . Infrared and its thermal properties have been evidenced by Sir William Herschel in 1800 using a thermometer placed in the solar radiation dispersed by a prism [3].

In general, all heated bodies radiate electromagnetic energy by the laws of Planck, Wien and Stefan-Boltzmann. The radiation luminance of a body is so much greater that its temperature is higher.

The field of the IR ( $> 0.7 \mu m$ ) is arbitrarily divided by the IR detectors manufacturers in: NIR (0.7 to 1  $\mu m$ ), short-wave infrared (1 to 3  $\mu m$ ); mid-wave infrared (3 to 5  $\mu m$ ) and long-wave infrared (7 to 14  $\mu m$ ) and very long-wave infrared (14 to 30  $\mu m$ ) [4]. The transmission of infrared radiation is affected by absorption in the atmosphere. This absorption is related to the concentration of gases and particles which constitute the atmosphere; IR transmission depends on many factors, particularly the absorption of each gas, temperature and altitude and weather conditions. The Figure.2 [5] illustrates the rate of transmission of infrared radiation by the atmosphere clear.

The interesting IR spectral range is between 7 and 14  $\mu m$ . Moreover, this broadband has encouraged the

development of IR detectors based on thermal receivers as thermopile, bolometer and the pneumatic detector.

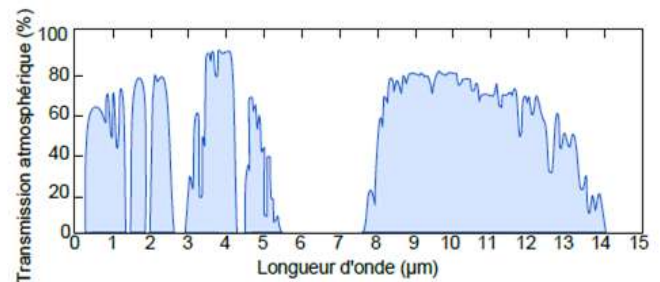


Figure 2. Transmission of IR radiation by the atmosphere

The receptors of these detectors are not selective. There are, however other types of IR detectors called quantum detectors which rely on the photo-emissive effect photoconductive or photovoltaic.

## 3. Thermography IR and electrical maintenance [6]

Infrared applications for the diagnosis of electrical systems, based on the detection of thermal radiation generated by its components to determine the operating conditions of the overall system, that they are normal or abnormal. Also, through to thermography it is possible to make the system images without the need to enlighten.

The military value of thermography is obvious: it allows to observe the enemy at night without sending it to radiation, easy to detect and that betray the observer. Its usefulness in industrial maintenance is even more important.

IR thermography devices employ punctual detectors or mosaic detectors which, associated with a mechanical scanning usually, provide a temperature map as a scanner as an image with a sensitivity of the order of 0.1 °C. The map points who find excessive amounts of heat are the origin of a latent defect in the system.

The employment benefits of thermography in electrical diagnosis are many, namely more efficiency, more safety, more reliability in the results, low cost and operation time.

### 3.1. Thermal variances in an electrical system

Thermal energy generated by an electrical component is directly proportional to the time  $t$  and the square of the current flowing through the component multiplied by the resistance ( $W = RI^2t$ ). Gradually, as the component conditions deteriorate, the resistance tends to increase and generate more heat. More the component temperature increases, resistance also augment according to the equation  $R = R_0(1 + \alpha T)$ ; where  $R_0$  is the resistance at 0°C, and  $\alpha$  a coefficient to the metal; it is of the order of  $4.10^{-3}$  if the temperature  $T$  is given in degrees Celsius. This amplification process continues until the lowest melting point of the component is reached.

A component that heater is not always linked to an intrinsic event, but it can be linked to an overcurrent caused by other system components; in the case of an overload condition or unbalance in three-phase systems. All thermal radiation emitted by a surface are not due only to the temperature of the surface. It is therefore important to take this into consideration in the analysis and the interpretation of the IR images because the apparent radiation can be misleading and lead to erroneous conclusions about the existence or otherwise of a defect. The thermal variations of a surface can result:

- Variations in the real temperature: the temperature distribution caused by the IR energy following the surface of the component itself.
- variations in the apparent temperature: these radiations are produced by sources other than the temperature of the inspected object;

### 3.1.1. The real temperature

In electrical systems, the causes of temperature variations at the surface of the components and represents good indications of a fault are mainly: the increase in resistance, the load, harmonics and thermal induction. There are other causes but provide little information about the operating conditions of the system, namely mass transport (wind), thermal capacitance (solar gain) and the phase change (rain, snow ...).

### 3.1.2. The apparent temperature

The main causes of the apparent temperatures are: emittance, reflection, transmittance and geometric variations of the surface.

The apparent temperature is a major source of uncertainty in the results of the diagnosis by thermography. Indeed, the relationship between the real temperature and the apparent temperature is an important factor to be considered in interpreting the IR images. The problem is that this ratio varies from one point to another in random sequence. Therefore, the temperature variances indicated by the IR image is not only caused by the electrical components themselves, but also by external influences creating false defects that mask real problems.

## 3.2. Causes of electrical faults

### 3.2.1. Contact resistance

Overheating of an electrical component can be linked to several factors; the most important are the defects of contact. A contact appears when you realize a connection with low pressure parts in contact, with a malformed welding, or with materials in contact oxidized or worn, e.g. decrease the spring tension, thread wear or tightening excessive of screws of electrical appliances.

Also, the insulation degradation of the conductors in the motors raises an increase of the absorbed current. Gradually, as the component continues to deteriorate, the temperature will

continue to increase until the material melting point is reached; this is the fault.

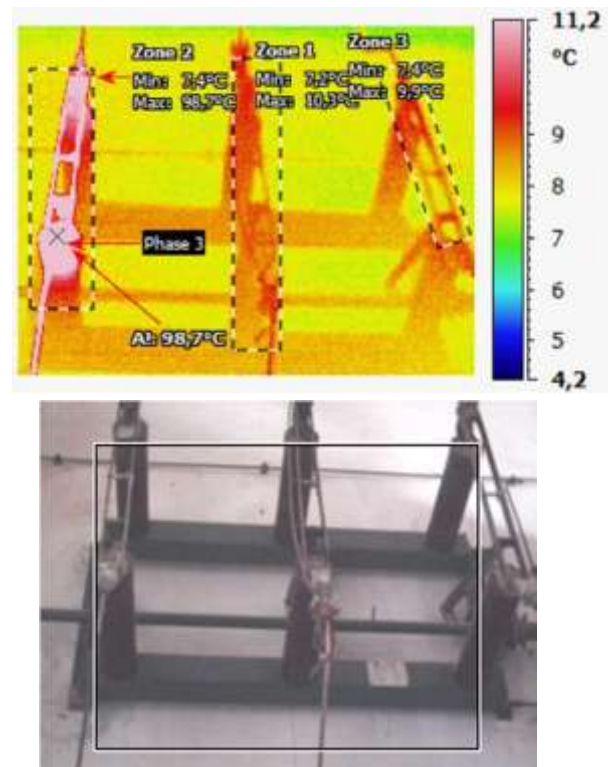


Figure 3. Thermography of disconnect switch

This type of fault can be identified because he will appear as the hottest spot in the IR image. This means that the heat generated is the largest at the point where the fault is located with a portion of thermal energy that propagates away from the defect by conduction or convection.

### 3.2.2. The load

Overloading also causes an increase in thermal energy. Thermographic viewpoint, a load is often considered a different type of problem with a specific thermal signature. When the load applied to an electrical component increases, the current consumption also increases which in turn causes an increase temperature of the component.

A balanced load of a three phase system should result in a uniform temperature distribution on the three phases. And an anomaly is identified as the temperature of an entire component or conductor is too high or too low. A balance condition is identified by the phases that do not observe even temperatures.

An unbalanced or overloaded component may generally be identified because the temperature remains relatively constant along the conductor or component as the size and mass of the object are fixed.

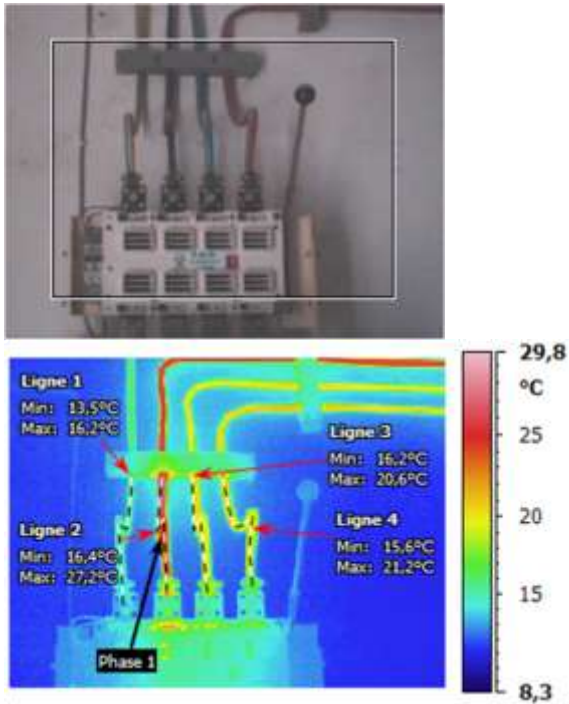


Figure 4. Thermography of an imbalance of the load

3.2.3. Harmonic

Harmonics are currents and voltages whose frequency is a multiple of fundamental frequency 50 Hz of the electric network. Presumably the risk harmonics are odd harmonics. These odd harmonics are superimposed on the fundamental harmonic and generate overvoltage, overcurrent and possible overheating.

Thus, the odd harmonics can cause significant heating and even cause melting of the conductors, connections, contact surfaces, and power outlets. Other equipments affected by the harmonics are transformers, motors, telecommunications equipment, electrical panels, breakers, disconnectors and busbars

3.2.4. The heat-induced

The induced heat is the heat generation in a material or a surface by the induced currents or by the inductive magnetic field created by an external source. This phenomenon occurs in the media located in a strong electromagnetic field, as is the case of HV equipment, Transmitters, and thermal induction equipment. The magnetic induction and also relates ferrous ferromagnetic material placed in a changing magnetic field.

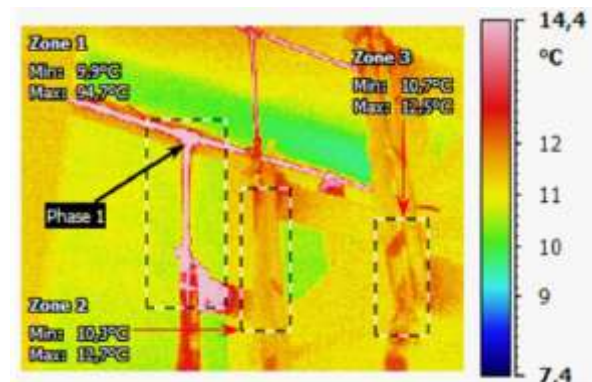


Figure 5. Thermography of a defect busbars

The induced currents or fault currents summed of losses due to the hysteresis cycle causes heating of the magnetic material.

Table1. Electrical faults and their potential effects:

Equipment:	Faults:	Potential effects:
Distribution post of electrical energy, capacitors, spark gaps; conductors or wires junction; Disconnecter	Contact weak / poor / worn; Badly made connection or junction; Bad switch connection; spark gaps defective; Overheating, Overload; Broken strands wires	Overheated; Arc striking; Fire; Burning device; Cable break; Fall of airline line, capacitor inoperative losing the protection against transient overvoltage; Losses of electrical energy (cost) Replacement Parts (cost); Security problems.
Various electrical equipments; Switches.: loads Station; motors control post of	Worn or weak connection; Bad contact; Unbalanced load; Overload. Overheated.	Arc striking; Short Circuit; burning, fire. Repair or replacement of the control post (high cost) Loss of energy (cost) Security problem.
Transformers;	Weak or deteriorated connection; through transformer overheating; Low contact (tap changer); Overload; Unbalanced three-phase load; Clogged or restricted cooling tube. Fluid level.	Arc striking; Short Circuit; burning, fire. Rewind (expensive) replacement (more expensive) Loss of energy (cost)
Motors and Generators;	Overheat bearings; unbalanced load; open-circuit or shorted turns; heating brushes; rings and switches: overload / overheating; ventilation or cooling blocked.	Defective bearings causing damage to the steel core or windings; Brooms defective → damage rings or switches → damage to the windings. Damage to the driven load. Rewinding motor (cost) Replacement Parts (cost) Security problems.

This process creates a true change in temperature on the surface. When warming concerns Steel or aluminum busbar bolts, it is often difficult to know a priori that it is a default component or a variation of emissivity.

### 3.3. Effects of electrical faults [6]

The following table presents some electrical devices that can be inspected using the IR thermography technique. Table 1 also indicates in columns 2 and 3, the most common electrical faults and their potential effects.

The application of thermography is also useful for the precise localization of drawing of electric cables heat and of any defects, monitoring power installations "sensitive" to which an operation stop for verification is not feasible, and even the detection Fluid leaks in underground pipes or exposed, and the detection of insulation defects, etc.

## 4. Instruments IR thermography

IR cameras the most common and most precise are two types: mechanical scanning cameras on a single receiver and pyroelectric vidicon camera [7].

### 4.1. mechanical scanning cameras

This type of camera is constituted by a movable flat mirror associated with another fixed parabolic mirror, allows, by an appropriate two-dimensional scanning to combine all the points of a landscape with a single receiver.

These cameras are the most popular to date; they may scan 200 lines of 200 points in 30 seconds, with a thermal resolution of 0.1 °K to about 300 °K temperature objects.

### 4.2. Pyroelectric vidicons cameras (pyricons)

The pyricons are newer IR cameras that compete with mechanical scanning cameras. Their principle is to project a thermal image on a pyroelectric target. There is obtained a relief of related electrical charges that can be read with a beam of electrons as in an ordinary vidicon. After digital video signal processing, we come to a resolution in temperature of 0.5 °K on an object at 300 ° K. The frequency reached 15 images per second. Thus, images are obtained whose quality of 250 lines approaches the visible television commercial.

In trade, many IR camera models are offered by manufacturers FLIR SYSTEMS and AGEMA. Two models are cited as an example: the IR camera around 2 to 5 µm, make AGEMA Thermovision 470, and IR camera using 7.5 to 13 µm, make FLIR SYSTEMS THERMACAM PM 595

With these cameras IR thermal scenes from -40 °C to 1500 °C can be thermography with a temperature resolution of up to tenths of a degree and a spatial resolution of less than 2 cm to 10 meters.

## 5. CONCLUSION

IR thermography is an effective tool for predictive and preventive maintenance of electrical failures. It measures, without physical contact and safe, component temperature from thermal radiation emitted. The result is a visual image which shows the "hot" areas and "cold" zones characterizing the importance of thermal stress and the presence or absence of latent faults in power systems. Factors causing warming components are mainly the contact resistance, the load, harmonics and thermal induction.

However, the use of thermography requires special precautions and rigorous knowledge to avoid IR image interpretation errors that may be distorted by the effects of emissivity, reflection, transmittance and geometrical variations in the surface.

The benefits of IR thermography are many, including:

- Fault location quickly without interruption of service or production
- Reduction of unplanned outages and costs caused by the unavailability of equipment
- Extension the lifetime of the of the equipment by the identification of defects before the occurrence of catastrophic failure
- Equipment check for problems before the warranty expires
- Confirmation that appropriate repairs are made correctly
- Acquisition of Spare Parts can be done before the failure, and downtime is kept to a minimum
- Security inspection of systems at risk,
- Locating areas of energy loss in generation systems, transmission and distribution of electrical energy.

## Bibliographie

- 1- A. Hadani, *Infrared*, Collection What do I know?, PUF, Paris 1975
- 2- J. Martínez R. Lagioia, *Experience performing infrared thermography in the maintenance of a distribution utility*, 19th International Conference on Electricity Distribution, Vienna, 21-24 May 2007
- 3- C. Meola, G. M Carlomagno, *Recent Advances in the Use of Infrared thermography*, Measurement Science And Technology 15 (2004) R27-R58
- 4- Z. Yuan Wang, *Near-Infrared Organic Materials and Emerging Applications*, CRC press 2013
- 5- G. Gaussorgues, *the Infrared Thermography Technique and Documentation*, Paris, 1980.
- 6- R. Newport, *Improving Electrical System Reliability with Infrared Thermograph*, The Electricity Forum, 1999.
- 7- P. Barchwitz, *Infrarouge et ses Applications*, Encyclopedia Universalis, 1999.

# Effective Process Optimization Of Indigo Rope Dyeing: A Case Study

Shumaila Meraj<sup>1</sup>, Amtul Qayoom<sup>1</sup> and Saeeda N. Al<sup>1</sup>

<sup>1</sup>Department of Chemistry, NED University of Engineering and Technology, Karachi-75270, Pakistan.

Corresponding author: email: amtulq@gmail.com

Received date: June 23, 2016; revised date: December 03, 2016; accepted date: December 11, 2016

## Abstract

Despite of limited availability and high cost of utilities, Pakistan is now declared as the second largest denim exporter country. With the advent of denim garment, it has been crucially important to face the upcoming challenges of the process optimization, cost effectiveness and utilities consumption from pre-treatment of raw yarn to quality finished denim. The focus of this study was to understand industrial scale optimization of sodium dithionite and water consumption for indigo rope dyeing process. Consumption of sodium dithionite was reduced from 16.99 gm/meter to 10.62 gm/meter from the month of July-15 till February-16 which resulted in steady utilization of indigo. Reduced utilization of chemicals decreased water requirement for post washing dyed yarn. These factors lead to comparatively cleaner, cost effective indigo dyed yarn production with required shade consistency.

**Keywords:** denim; indigo; optimization; utilities consumption; raw yarn; dyeing

## 1. Introduction

The denim industry has been playing an important role in the textile sector with approximately 636,000 tons per annum production [1],[2]. Pakistan is the second largest exporter of denim fabric with 40 major production units producing around 50 million square meters of finished denim fabrics per month [3]. Traditionally denim fabric is produced by dyeing cotton yarn with naturally occurring indigo dye but nowadays due to enormous consumption of denim fabrics and articles, a larger percentage of synthetic indigo dyes are also used for dyeing[4],[5]. There are number of techniques used for indigo dyeing but rope dyeing is one of the most suitable indigo dyeing processes in terms of uniformity of dyeing yarns [6]. Indigo is water insoluble vat dye and cannot mobilize itself towards cotton fiber until it is converted into water soluble form known as "leuco" through the process of reduction. Sodium dithionite ( $\text{Na}_2\text{S}_2\text{O}_4$ ) aka sodium hydrosulphite or hydro is one of the most commonly used reducing agent in indigo dyeing process. Approximately 150 liters water per kg fabric is utilized in a typical indigo dyeing process. Consumption of large quantity of chemicals and fresh water ends up in increased product cost and larger volume of chemically loaded effluents; particularly excess sodium dithionite, unfixed indigo dye and their byproducts. Optimization of various dyeing parameters can reduce consumption of chemicals and water requirement for typical denim dyeing processes. For an optimum rope indigo dyeing process, it is recommended to regulate some of the dyeing parameters e.g. concentration of sodium dithionite ( $\text{Na}_2\text{S}_2\text{O}_4$ ), pH value of caustic soda ( $\text{NaOH}$ ), dipping time and airing time etc.

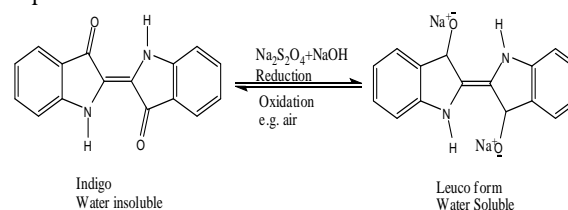
This case study presents the statistical comparison of eight months data based on optimization of amount of sodium hydrosulphite ( $\text{Na}_2\text{S}_2\text{O}_4$ ), and water consumption control for rope dyeing process in a denim industry which will ultimately result in the reduction of unit cost per meter in dyeing yarn.

## 2. Reduction Mechanism Of Indigo

The indigo bath consists of indigo dye, caustic soda ( $\text{NaOH}$ ) and sodium dithionite ( $\text{Na}_2\text{S}_2\text{O}_4$ ) as reducing agent. During reduction process  $\text{Na}_2\text{S}_2\text{O}_4$  react with  $\text{NaOH}$  and break it into  $\text{NaO}$  and nascent hydrogen; both of which adhere to indigo dye molecule. Nascent hydrogen opens the indigo vat dye molecule by letting it join with water and the water carry the vat dye to the cotton fibre. This reduction process is termed as vatting[7].

During dyeing process the concentration of leuco is maintained in the dye bath by the addition of sodium dithionite. Once indigo is applied on fabric, it oxidizes back to its original insoluble form in order to make it stay within the fibre by skying process [8].

Reduction oxidation mechanism is shown in following equation.



### 3. Indigo Dyeing Process

Indigo dyeing process involves number of stages shown in Figure 1. Rope of 300 to 400 individual threads are continuously dyed in the following steps:

- Pre-treatment
- Prewashing
- Indigo dip
- Post washing

On top of each dip squeeze rollers are arranged to oxidize dye with air.

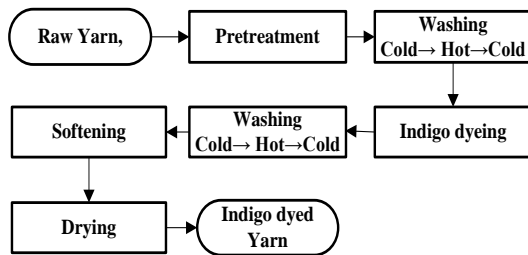


Figure 1 Steps involved in typing indigo rope dyeing process

#### 3.1. Pre-treatment of raw yarn

In the pre-treatment process, ropes are fed into scouring baths where warp yarn is treated with wetting agent, detergent and caustic soda at 70-80°C. The purpose of this step is to remove trapped air from cotton yarn and guarantee uniform wetting and dyeing. Then, ropes are fed into one or more water rinsing baths.

#### 3.2. Prewashing

Pretreated raw yarn is thoroughly washed with hot water to remove remains of caustic which might change the pH of the dye bath. After hot wash, yarn is cold washed to lower down the yarn temperature as indigo dyeing is carried out at room temperature [9].

#### 3.3. Recipe for dyeing liquor and vat dye stock [8].

The dyeing tanks contain about 2000 liters of bath comprising:

- Caustic soda (27% by weight), 5 ml/l
- Sodium dithionite, 1.5g/l
- Stock vat, 62.5 ml/l

The bath (about 16 000 liters) is constantly re-circulated and automatically reinforced by mother solution on the basis of the weight of the yarn being dyed.

The dyeing stock is prepared as follows

- 85 g/l Indigo Pure
- 76 g/l Hydro

- 57 g/l Caustic Flakes or 74 ml/l caustic 50°Be
- 1 ml/l Dispersing Agent
- 1 gm/l wetting agent

Mostly the vat stock is prepared by adding indigo dye with 0.8-0.9 time's sodium dithionite and 0.7-0.8 time's caustic soda. The quantity of caustic soda and sodium dithionite must be monitored regularly according to required amount.

#### 3.4. Indigo Dyeing

After prewashing the yarn ropes are fed into dyeing equipment which consists of series of dye baths where multiple lower and upper rolls are provided to twist and squeeze yarn ropes between the dye baths. Above the middle set of multiple dye baths, there are skying rolls. After wetting out of the first dye bath, they pass at about 20 to 30 m/min to the skying rolls and dipped for 20 -30 seconds in leuco indigo dye liquor and then skied for 2 minutes after leaving the dye box[9]. The skying floor should be high enough for complete oxidation of the dye. This step is repeated for each dye liquor box followed by skying for oxidation. In the successive dye box more leuco indigo is consumed followed by oxidation and the fibre surface is gradually dyed with indigo pigment. There are more than six dye boxes used for finer layers of indigo on yarn surface [10].

#### 3.5. Post washing and softening

After dyeing the unfixed dye and residual of caustic from the yarn surface are removed by washing the ropes with the water at about 60°C. Washed ropes are lubricated so that individual threads can be easily separated during re-beaming process. For lubrication the bath contain water, softener, acetic acid and this application occurs at room temperature.

#### 3.6. Drying

In the last, the ropes are dried at about 120°C with the residual of 8% humidity. Dried yarn ropes are stored in a can in such a way that threads will not be twisted.

## 4. Process Control Parameters Of Rope Dyeing For Denim

#### 4.1. Concentration of dye in dye bath

Mostly the concentration of indigo dye depends on the need of the depth of the shade and the number of dips used. It is usually in between 2 to 6 g/l [11]. If the dye concentration is high, it will show a poor rubbing fastness with more reddish duller shade of indigo dyeing. When yellow leuco indigo oxidizes, it transforms into greenish and then gradually turns into blue oxidized form. Small quantity of sodium dithionite must be added to dye bath for maintaining clear yellow leuco and to prevent premature oxidation of dye into greenish form.

#### 4.2. Dipping time

Longer dipping time results in high penetration of dye in the yarn which reduces the ring dyeing effect. On the other hand for short dipping time, there must be a negative effect on dye penetration depth. The dipping time should be in the range of 20-30 seconds for each dye bath. On exceeding more than 60 seconds, darker shades are obtained due to high take up of dyestuff [11].

#### 4.3. Concentration of Sodium dithionite ( $\text{Na}_2\text{S}_2\text{O}_4$ )

Concentration of sodium dithionite plays very vital role in indigo dyeing process. Higher concentration of sodium dithionite results in lighter bluer shade and ultimately consumption of indigo will be much higher if darker shade is required. At relatively low concentration of sodium dithionite, darker shades can easily be produced. A further decrease in sodium dithionite concentration results in unreduced indigo which will bleed in the next bath and post washing.

#### 4.4. Redox potential

The redox potential depends on the final desired shade. Typically it should be in the range of -760 to -860 millivolts. In order to keep the leuco indigo stable, the level of redox potential should be low. The potential of insoluble indigo in dye bath remains same until all the leuco indigo molecules are oxidized to raise the potential in the positive direction. Reduction capacity is monitored by millivolt meters to ensure optimum redox potential mentioned above.

#### 4.5. Caustic soda or pH value

pH of indigo dye bath greatly affect dye penetration and its affinity to fabric. Being weakly acidic, indigo dye exists as mono-phenolate ions at pH 10.5-11.5 which is most substantive form for ring dyeing as compared to its other ionic forms [10]. Therefore alkaline pH (10.5 to 11.5) is maintained by adding caustic soda to dye bath in order to achieve a high strike rate of the dye to the yarn and for good wash down activities[12].

#### 4.6. Airing time

Airing time for the fixation of dye should not be more than 60 to 75 seconds because longer time results in high tension on the yarn and subsequent process becomes difficult.

#### 4.7. Optimization of sodium dithionite concentration

The indigo and sodium dithionite concentration must be efficiently managed through continuous feeding of both ingredients otherwise shade will be altered after vatting[13]. Although sodium dithionite enables very short fixing times in various dyeing methods and produces levelness in

continuous dyeing [7], it is unstable and can be easily oxidized by atmospheric oxygen. Higher temperature further reduces stability of its alkaline solutions and it gets oxidized even in the absence of oxygen. Therefore, excess quantity of sodium dithionite and caustic soda are needed over the stoichiometric requirements of the reduction process. Concentration of sodium dithionite should be enough to completely reduce insoluble indigo dye into its soluble leuco form. Sodium dithionite is also required to prevent possibility of unwanted oxidation of soluble leuco dye back into insoluble indigo. At lower concentration of sodium dithionite, oxidized dyestuff present in dye bath with adheres on the fibrous material and results in duller red shades. On the other hand, high concentration of free dithionite in the dye bath will cause insufficient oxidation in skying and will bleed the colour in the next successive bath resulting in low colour yield. In this case, more indigo dosing is required to get the desired shade which will disturb equilibrium of dye bath.

This case study refers to an unstable process control resulting in higher concentration of sodium dithionite in the dye bath which caused huge shade fluctuation. For an ensured optimized dyeing process, sodium dithionite concentration was regularly monitored and controlled which ultimately resulted in stabilized indigo consumption.

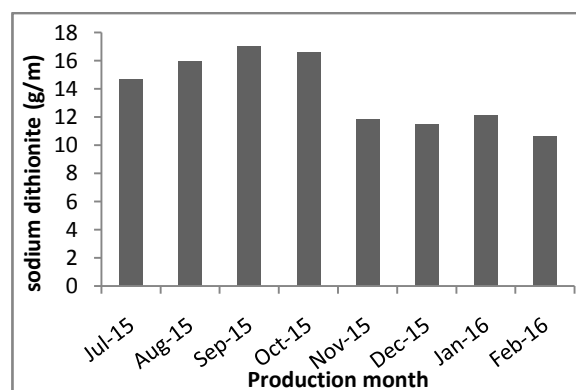


Figure 2 Month wise consumption of sodium dithionite (g/m)

Figure 2 shows the gradual reduced consumption of dithionite per meter of dyed yarn from the month of October-15 to February-16. But from July-15 to September-15 it was not effectively optimized which caused high consumption of dithionite. Sodium dithionite consumption was monitored and control was achieved from October-15 to February-16 keeping in view that there must not be any shade alteration. The statistics shows that the consumption of dithionite gm/m reduced from 16.99 gm/m to 10.62 gm/m from the month of July-15 till February-16. This optimization of sodium dithionite not only lead to the steady consumption of indigo and washing water but also reduced the cost of dyed yarn as mentioned in further discussion.

4.8. Steady Consumption of indigo

Figure 3 shows the steady utilization of indigo from November-15 to February-16. While before November-15 there was abrupt consumption of indigo because of an un-optimized dithionite concentration which resulted in higher consumption of indigo for dyeing yarn.

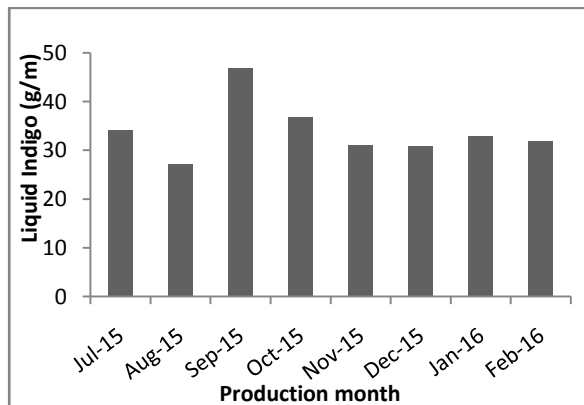


Figure 3. Production (m) versus liquid indigo consumption (grams per m)

4.9. Reduced water consumption

This study also includes optimized water consumption during pre and post washings of cotton yarn. The fix dosing of inlet fresh water for prewashing in order to remove caustic from fiber was controlled by installing digital flow meter while in post washing the water consumption became steady from October-15 to February-15 just by optimizing the concentration of Na<sub>2</sub>S<sub>2</sub>O<sub>4</sub>. Month wise water consumption is shown in Figure 4.

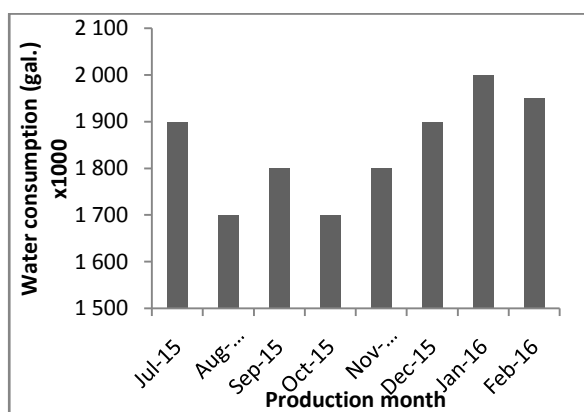


Figure 4. Month wise consumption of water (gallons) for rope indigo dyeing process

As the high concentration of sodium dithionite in the indigo baths ultimately resulted in insufficient oxidation during aeration this caused bleeding of unfixed dye in post washing chambers. The more unfixed dye stuff on the surface of the yarn, the more water required to wipe it off. In this manner an effective reduction in water

consumption has been seen by optimization of sodium dithionite concentration.

4.10. Effective cost reduction per meter

Due to stable circulation and concentration of sodium dithionite, the cost required for chemicals has been effectively reduced as shown in Figure 5. The cost reduction is about 2.88 Rs./m of dyed yarn which is specifically good for consistent and reproducible dyeing.

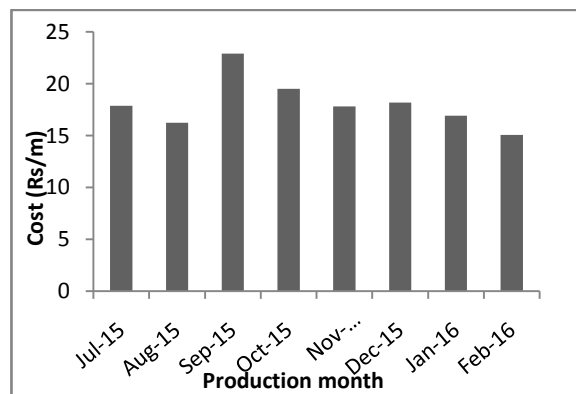


Figure 5. Month wise production cost (Rs/m)

5. Introduction About Industry

The textile unit under study was established in 1949. Operating on an area of 165,922 square meters and employing 7,650 people, it has the ability to cater to specific client needs with package deals such as product development at source, design support, shorter lead times, on-time deliveries and warehousing facilities. Their latest undertaking is the new state of the art denim mill which will take their production capacity to 36 million meters per annum.

6. Aims of Case study

There are number of factors affecting optimal indigo dyeing process. This case study was particularly focused on the optimization of indigo dyeing process by reducing consumption of overall sodium dithionite and rinsing water which ultimately reduced the dyeing cost per meter of dyed yarn. This was done by continuous monitoring and controlling of various factors for eight months without hurting the shade consistency with reduced consumption of sodium dithionite in gm/m of dyed yarn.

7. Process Optimization

Table 1 represents eight month's data for optimization of indigo rope dyeing process in the industrial unit under study.

**Table 1. Month wise production data collected from industrial unit under study for indigo rope dyeing.**

Month	Product (m)	Na <sub>2</sub> S <sub>2</sub> O <sub>4</sub> (g/m)	Liquid Indigo (g/m)	Water (gal.)	Cost Rs/m
Jul-15	1,399,470	14.64	34.28	3,700	17.88
Aug-15	1,326,400	15.94	27.28	3,850	16.25
Sep-15	1,423,500	16.99	46.89	2,800	22.89
Oct-15	1,348,720	16.55	36.88	2,300	19.5
Nov-15	1,464,150	11.85	31.17	2,100	17.81
Dec-15	1,600,320	11.46	30.9	1,990	18.18
Jan-16	1,532,660	12.13	33	2,300	16.91
Feb-16	1,210,079	10.62	31.92	2,500	15.05

### 8. conclusion

This case study was focused on controlling the concentration of sodium dithionite in the dye bath for an effective optimized indigo dyeing process with the required shade consistency. Optimization of Na<sub>2</sub>S<sub>2</sub>O<sub>4</sub> concentration reduced the water consumption during pre and post wash and also stabilized the indigo consumption in grams per meter. Reduction in water and chemical consumption ultimately resulted in reduced cost per meter of dyed yarn. It was also expected that process optimization would maintain lesser discharge of effluent containing harmful byproducts of indigo dyeing process hence producing comparatively cleaner, cost effective and consisted dyed products.

### References

- [1] M. Sala and M. C. Gutiérrez-Bouzán, "Electrochemical Techniques in Textile Processes and Wastewater Treatment," *Int. J. Photoenergy*, vol. 2012, pp. 1-12, 2012.
- [2] A. Roessler, D. Crettenand, O. Dossenbach, W. Marte, and P. Rys, "Direct electrochemical reduction of indigo," *Electrochim. Acta*, vol. 47, no. 12, pp. 1989-1995, 2002.
- [3] N. A. Memon, "Denim: Pakistan second largest exporter of denim fabrics," *Pakistan Text. J.*, vol. 64, no. 6, p. 36, 2015.
- [4] A. Gürses, M. Açıkyıldız, K. Güneş, and M. S. Gürses, "Dyes and Pigments: Their Structure and Properties BT - Dyes and Pigments," A. Gürses, M. Açıkyıldız, K. Güneş, and S. M. Gürses, Eds. Cham: Springer International Publishing, 2016, pp. 13-29.
- [5] A. Rutkin, "Tint without taint," *New Sci.*, vol. 229, no. 3055, p. 18 -, 2016.
- [6] S.M. Imtiazuddin and M. S. Tiki, "Indigo and sulphur rope dyeing in Denim," *Pakistan Text. J.*, vol. March, p. 22, 2010.
- [7] M. Božič and V. Kokol, "Ecological alternatives to the reduction and oxidation processes in dyeing with vat and sulphur dyes," *Dye. Pigment.*, vol. 76, no. 2, pp. 299-309, 2008.
- [8] N. Meksi, M. Ben Ticha, M. Kechida, and M. F. Mhenni, "Using of ecofriendly  $\alpha$ -hydroxycarbonyls as reducing agents to replace sodium dithionite in indigo dyeing processes," *J. Clean. Prod.*, vol. 24, pp. 149-158, 2012.
- [9] A. Gürses, M. Açıkyıldız, K. Güneş, and M. S. Gürses, "Dyeing and Dyeing Technology BT - Dyes and Pigments," A. Gürses, M. Açıkyıldız, K. Güneş, and S. M. Gürses, Eds. Cham: Springer International Publishing, 2016, pp. 47-67.
- [10] M. G. Uddin, "Indigo Ring Dyeing of Cotton Warp Yarns for Denim Fabric," *Chem. Mater. Eng.*, vol. 2, no. 7, pp. 149 - 154, 2014.
- [11] J. H. Xin, C. L. Chong, and T. Tu, "Colour variation in the dyeing of denim yarn with indigo," *Color. Technol.*, vol. 116, no. 9, pp. 260-265, 2000.
- [12] R. S. Blackburn, T. Bechtold, and P. John, "The development of indigo reduction methods and pre-reduced indigo products," *Color. Technol.*, vol. 125, no. 4, pp. 193-207, 2009.
- [13] Dogan Dogan and H. Turkdemir, "Electrochemical Treatment of Actual Textile Indigo Dye Effluent," *Polish J. Environ. Stud.*, vol. 21, no. 5, pp. 1185-1190, 2012.

# Improving the performance of vibratory treatment based on polymeric composite binder

Youcef Rouabhi<sup>a,b</sup>, Azzeddine Lounis<sup>b</sup> and A. P. Babichev<sup>c</sup>

<sup>a</sup>Department of mechanical and industrial engineering, Faculty of Technology, Mohamed BOUDIAF University, BP 166 M'sila, Algeria

<sup>b</sup>Department of materials Science, Faculty of mechanical and Processes engineering, LSGM, University USTHB, BP 32 ELAlia, Algiers, Algeria

<sup>c</sup>Department of mechanical and industrial engineering, Faculty of Technology, University DSTU, Rostov on Don, Russia

Corresponding author: email: rouabhiyoucef@yahoo.fr

Received date: February 05, 2016; revised date: December 03, 2016; accepted date: December 11, 2016

---

## Abstract

*The advanced technology still requires a good surface finish at a low cost. This scenario asks the industries and the scientific community to develop new finishing processes. Currently, there are many techniques and the most promising of them is the abrasive vibratory treatment (AVT). The performance of the AVT depends on the operating mode (Amplitude, oscillation frequency of the work chamber, thermal and energy parameters), devices design features and other factors, among which the central place is occupied by the functional properties of the granules, generally, based on the composites, predetermining the important role and the main task of the vibratory treatment. However, the analysis of the works in this domain shows that AVT gives good results with the right selection of granules that is the shape, the size and the composition of them, which are determined by the configuration and material of the treated parts thus shows that the functional properties of granules are not completely used. Therefore, the purpose and task of the relevant work is the intensification of the AVT process by improving functional properties and performance of abrasive granules based on a polymeric binder (PB).*

*Keywords: vibratory treatment, abrasive granules, functional properties, polymeric binder, performance;*

---

## 1. Introduction

The development prospects of modern industry are largely due to the introduction of new materials and technologies. Some of these materials are polymeric composite materials (PCM). The PCM uses extensively in the automotive industry, aerospace, naval construction, oil and gas industries. We examine in our work a new field application of polymers: their use in the AVT, which is based on the capacity of the polymers, which mechanically activate the surface deformation and the dispersion of the solid bodies.

At the current stage of development of metal processing technology, the questions of improving environmental performance are increasingly relevant. The modern mechanical production represents a complex set of processes using different types relating to the energy influence, a wide range of basic and auxiliary materials in solid, liquid or gaseous, solutions, granules and electrolytes of various compositions and concentrations. To achieve the quality and the required performance is often used toxic materials and granules. In this regard, the significant interest is presented by the development of new granules of treatment, excluding the application of such materials and substances, the introduction of ecologically rational

and appropriate technologies so the exploitation of the waste of diverse productions [1]. The industrial production of various abrasive granules (AG) allows extended using the methods of AVT [2]. The important significance to guarantee the cutting properties of these granules belongs to the binder of AG. The binder must solidly retain the abrasive grains and constantly be triturated for the denudation of new cutting edges. It represents an important component, influencing considerably on the performance of granule [3]. The AG is generally manufactured containing a polymeric, metallic and ceramic binder. However, the most widespread is polymeric [4].

Currently the volume of the production of diamond tools with a polymeric binder (PB) represents approximately 70 % of all abrasive production [5, 6]. That is expressed by the positive influence of PB on the treatment processes. PB promotes the reception performance of the treated surface; ensure a low coefficient of friction, consequently, a low temperature, and a capacity of auto-sharpening, which increases granules cutting performance and intensification of AVT production [7, 8]. Generally, AG with elastic and rigid PB are largely used in the industry, as elastic PB is uses compositions, inserting rubber, polyvinyl chloride and phenol-formaldehyde novolac resin [9]. However, it is

advisable to note that the major part of the AG is industrialized with the rigid PB [10]. The basis of these agglomerating is composites filled with polymer. The international market, offers a very wide nomenclature granule of different characteristics and particularly containing polyamide and poly benzene resins. But more and more PB based on resins of epoxy, polyurethane and fluoride found an increasing use [4,10].

The analysis of the granules applied in processes of the vibratory treatment, makes it possible to classify them according to various characteristics, in particular, nature of origin, structure, type and shape of granules. Depending on the nature of origin, all granules are divided into two principal groups [11]: inorganic (natural, synthetic) and organic granules according to Figure 1.

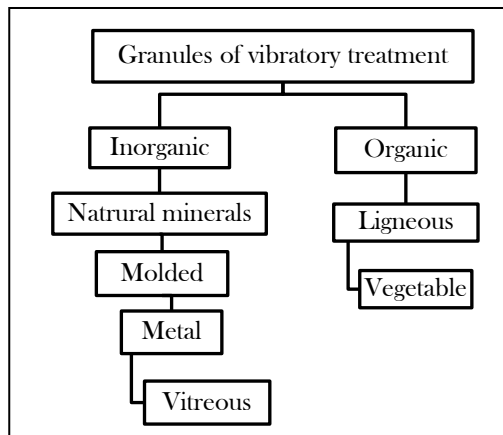


Figure 1. Classification of vibratory treatment granules based on its nature

In recent years, many companies have considerably activated the research of production and sale of AG with defined geometric shape. These works are completed, particularly, in Germany (by Rösler and Walther Trowal companies) according to Figure 2, in the Russian Federation by abrasive factory of Moscow, in USA by Finishing Systems and others companies.



Figure 2. Some granules produced by RÖSLER

The primary reason for such extensive use of AG based on PB is higher cutting capacity, which is due to the

release of a large number of macro radicals during the attrition of this binder [12].

The longevity of free radicals under normal conditions is very short, because as reactivity, they can interact with compounds, atoms and molecules that act as locators of unpaired electrons (acceptor). Since generated radicals interact with atoms or molecules of the compounds, their recombination in these conditions is impossible (at least limited). Thus, polymeric granules and compounds used in conjunction during AVT, allow producing even more reactionary radicals, which must more intensify the treatment.

Currently, abrasive fillers are based on traditional materials such as black and green silicon carbide, white and normal electro-corundum and other materials [13]. Natural corundum is a rare material, artificial is expensive. In this context, it is interesting to use non-conventional abrasive materials, including wastes from various industries. In particular, it is known in the field of metallurgical production that slag possesses high abrasive properties and is not deficient and costly. The manufacturing process of abrasive tools is well-known [14], in which the abrasive is mixed with polymer and hardener then the mixture is placed in an appropriate mold, the mold is heated to a temperature of 70° [4].

## 2. Experimental study

The objective of our study is the production of the AG and the lowering of their cost prices, by replacing one or more expensive components for others less expensive, while preserving the physical and mechanical properties in order to improve the ecological security of this production, thus to solve the task of improving the wear resistance [15], the absence of the clogging and good wettability of AG surfaces. The result which can be achieved in the implementation of this method consists in using:

- 1) As the abrasive - normal electro-corundum (NE) with a particle size at 06 to 10  $\mu\text{m}$ , granulated slag of blast furnace, slag crushed for the road works and sand.
- 2) As a polymer - Poly methyl methacrylate (PMMA).
- 3) As the monomer - methyl methacrylate (MMA) in liquid.
- 4) As the hardener - dimethyl aniline

### 2.1. Technological equipment

Experimental studies of the process are conducted with vibratory equipment 4×10 according to Figure 3. The machine has a base 9, welded iron of U-shape, on the basis is assembled metallic square structure 8 for the fixing of the electric motor 5, and the intermediate support 7 with shaft 6 transmitting the rotation of the electric motor by

two elastic couplings 4 to vibrator shaft 3, fixed under the vibrating table 1. The vibrating table is installed on four screws springs, relying on the base. On which at the same time fixed the work chambers 2 volumes of 1 up to 10 dm<sup>3</sup>. The presentation of the liquid system consists of a pump, pipes and tank 10. The technical characteristics of this equipment are given in Table 1. The advantage of the equipment is the simplicity of conception, easiness of use, and the universality that is reflected by the use of this machine in the laboratories of research as well as in industrial enterprises.

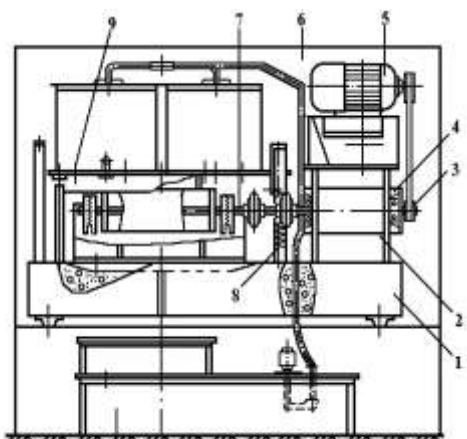


Figure 3vibratory equipment 4×10

The experiments were accomplished with free loading of parts in the work chamber. The consumable loading volume (granules, solutions) and parts, it's about 80 % of the work chamber volume, the entire experience was conducted with continuous solutions.

Table 1. Technical characteristics of vibratory equipment 4×10

Designation	Measuring units	Equipment 4×10
Volume of work chamber	dm <sup>3</sup>	10
Number of work chamber	unit	4
Driving device	-	Eccentric weight
Disposition of vibrator	-	Horizontal
Engine power	Kw	1.1
Vibration amplitude	mm	0.5-2.5
Oscillation frequency	Hz	16, 26, 33, 40
Dimensions	m	1.3×0.95×1.37
Weight	Kg	820
Volume of settler	dm <sup>3</sup>	200

2.2. Studied granules

To study the influence of granule characteristics of AVT performance and in treating surface finish, as well as the determination of granules functional characteristics, we used:

- Abrasive granules in triangle prisms shape with dimensions of 20×20 mm (TP 20×20).
- Granules epoxy 520, cone-shaped with dimensions of 20 mm and granulometry M40 from 28 to 40 µm.
- Newabrasive materials cone-shaped with dimension of 25 mm, based on polymeric binder + PMMA + MMA + hardener + abrasive grains granulometry M40 and dimension from 28 to 40 µm.
- Normal electro-corundum (NE-10) of 10 µm with an abrasive concentration from 45 to 70%, and the introduction of non-standard agent of load instead of the abrasive, particularly the metallurgical production waste.
- Also, slags of fusion in grains and crushed roadwork granulometryM50 from 40 to 50 µm and M10 from 7 to 10 µm, and sand M6 from 3 to 6 µm.

Noting that before preceding to the experimental studies all the granules must past a prior treatment for 30 minutes.

2.3. Solution and treated materials

In order to study the AVT process when using AG based on a polymer composite, we use an aqueous solution 5% of Na<sub>2</sub>CO<sub>3</sub>. Studies are conducted on parts of different materials and the most used in the industry: steel 45, copper Cu-B, aluminum 2024A and CuZn40Y40. Exploiting the vibratory equipment 4×10, the operating mode of treatment is the following: amplitude varying from 2 to 2.5 mm, oscillation frequency from 16.7 to 26.7 Hz.

2.4. Technological characteristics (functional)

To perform comparative tests of technological characteristics of new granules compositions, we use the method [4], which takes into account the functional properties and the main parameters of abrasive granules exploitation and which is calculated as follows:

- Concentration of abrasive grains:

$$C_g = \frac{v_a}{v_c} \cdot 100 \% \quad (1)$$

Where  $v_a$ - Volume of abrasive grains, %;  $v_c$ - binder layer volume containing abrasive grains.

- Cutting capacity of abrasive grains:

$$R_{CC} = \frac{Q}{t * S_p} ; \frac{g}{h * cm^2} \quad (2)$$

$$R_{CC} = (r_0 + k_a \cdot V_a) \cdot 10^{-4}$$

Where Q - metal removal of the part surface; t - processing time; S<sub>p</sub>- surface area of the part; r<sub>0</sub>, k<sub>a</sub> - empirical coefficients.

- Consumption of the abrasive granules in mass:

$$P_m = \frac{I_m}{t} ; \frac{g}{h} \quad (3)$$

- Consumption of the abrasive granules in volume:

$$P_v = \frac{I_v}{t} ; \frac{dm^3}{h} \quad (4)$$

Where I<sub>m</sub>, I<sub>v</sub>- Mass and volume of consumed granules layer.

- Treatment coefficient (specific metal removal):

$$k_0 = \frac{Q}{I_m S_p} ; \frac{1}{cm^2} \quad (5)$$

$$K_0 = (b_a - c_a \cdot V_a + q_a \cdot V_a^2) \times 10^{-5}$$

Where b<sub>a</sub>, c<sub>a</sub>, q<sub>a</sub> - empirical coefficients.

- Wear resistance of abrasive granules:

$$U = \frac{I_m}{M} ; \frac{\%}{h} \quad (6)$$

$$U = u_0 + k_a \cdot V_a$$

Where M- one hour of the total initial weight of abrasive granules; u<sub>0</sub>, k<sub>a</sub> - empirical coefficients.

- established roughness under normal processing conditions (minimum value R<sub>a</sub> of treated parts is achieved at the fixed operating mode of treatment).

### 3. Results and discussions

The comparative tests of MMA+ PMMA and epoxy resin according table 2 are showed that:

- The cutting capacity in Graph 1 and the wear resistance of the granules in Graph 2 are high compared to granules based on epoxy resin.
- The treatment coefficient in Graph 3 is almost three times higher than for the granules containing epoxy resins.
- The established roughness in Graph 4 is higher than for epoxy resins.

By comparing the experimental results on parts of different materials when using granules with a new polymeric composite binder (PMMA + MMA), epoxy resin (Epoxy 520) and ceramic (TP 20×20), we can say that, the use of new granules gives good results for

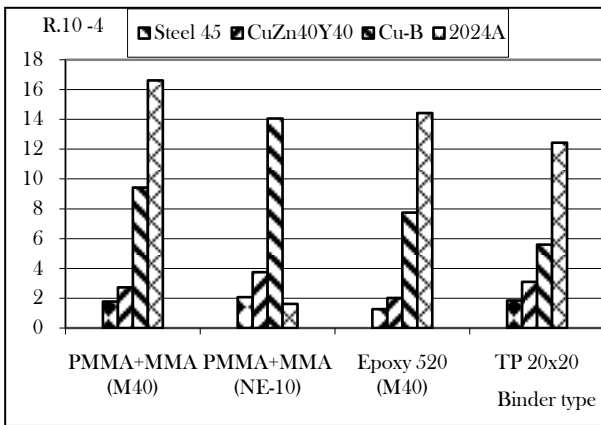
improvement and intensification of AVT, with a less expensive cost, ensuring high properties of granules without any influence on the environment. It's good to note that, the abrasive granules based on polymer binder increase productivity; ensuring a stable surface quality, an economy of abrasive granules which reflect their wear resistance.

Table 2. Comparative tests of MMA + PMMA and the epoxy resin 520

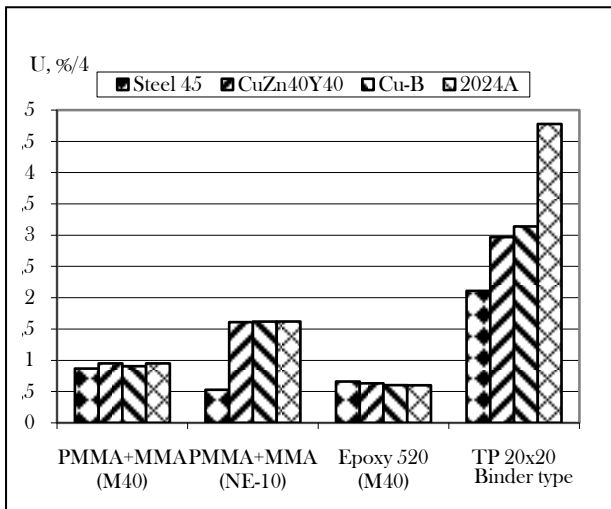
№	Type of binder	Type of processed material (AFNOR)	Cutting capacity R×10 <sup>4</sup> g/h×cm <sup>2</sup>
1	PMMA+MMA (M40)	Steel 45	1.78
2	PMMA+MMA (NE-10)	Steel 45	2.073
3	PMMA+MMA (M40)	CuZn40Y40	2.73
4	PMMA+MMA (NE-10)	CuZn40Y40	3.75
5	PMMA+MMA (M40)	Cu-B	9.43
6	PMMA+MMA (NE-10)	Cu-B	14.063
7	PMMA+MMA (M40)	2024A	16.62
8	PMMA+MMA (NE-10)	2024A	32.67
9	EPOXY-520 (M40)	Steel 45	1.27
10	EPOXY-520 (M40)	CuZn40Y40	2.02
11	EPOXY-520 (M40)	Cu-B	7.75
12	EPOXY-520 (M40)	2024A	14.43
13	TP 20×20	Steel 45	1.85
14	TP 20×20	CuZn40Y40	3.1
15	TP 20×20	Cu-B	5.6
16	TP 20×20	2024A	2.44

Following Table 2

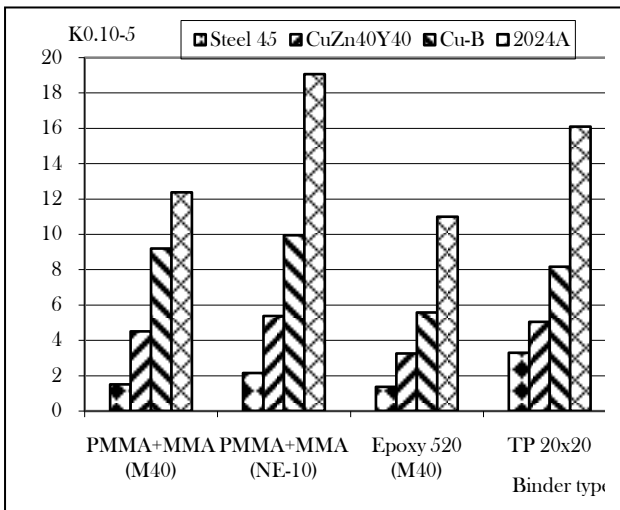
№	Wear resistance U, %/4	Treatment coefficient K <sub>0</sub> ×10 <sup>5</sup> 1/cm <sup>2</sup>	Established roughness R <sub>a</sub> , um
1	0.867	1.5	0.77
2	0.528	2.144	1.16
3	0.95	4.5	0.642
4	1.61	5.37	0.718
5	0.905	9.19	0.924
6	1.619	9.94	1.248
7	0.95	12.37	1.172
8	1.62	19.06	2.006
9	0.66	1.36	0.8
10	0.631	3.25	0.71
11	0.602	5.57	1.01
12	0.6	10.99	1.97
13	2.11	3.29	1.84
14	2.97	5.04	1.212
15	3.141	8.16	1.17
16	4.78	16.09	2.99



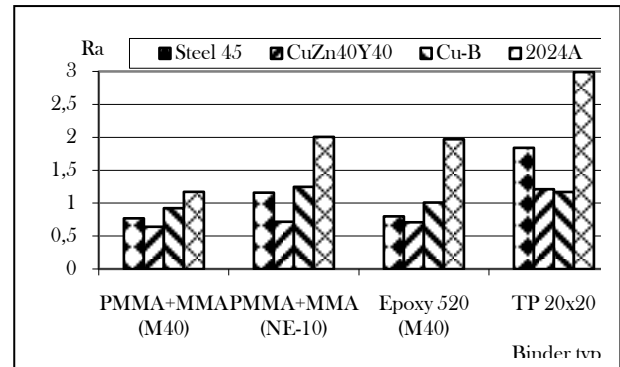
Graph 1 Change of cutting capacity



Graph 2 Change of wear resistance



Graph 3 Change of treatment coefficient



Graph 4 Change of established roughness

**Conclusion**

The surface treatment and particularly AVT is a very complex process, requesting attention because many factors are involved both during treatment, so far that it's known as Mass Finishing. In this work we try to:

- Reveal a mysterious phenomenon, a cutting tool which is present by abrasive granules, which are composed of the rest of abrasive discs and ceramic with a particle size of 8 to 40 μm.
- Accomplish a set of theoretical and experimental studies, to improve the quality of abrasive granules and increase the efficiency of AVT.
- Develop a system of operating parameters of abrasive granules, allowing conducting comparative studies of several granules compositions.
- Thus, this work presents the classification of abrasive granules containing a polymeric binder, taking into consideration the operating parameters (functional) of abrasive granules according to their nature and their designation.

The right chooses of the granules component is the key to improving the performance of vibratory treatment.

**References**

- [1] S.Chagnard, *GalvanoOrgano*. 783(2009) 35-37.
- [2] LaRoux K. Gillespie, *Mass Finishing Handbook*, SME, USA, 2006.
- [3] Y. Rouabhi, *Proceedings of the International Symposium on Scientific Research and High Tech Technology*, October 01-04 DSTU, Rostov on Don, Russia, 2013, pp. 312-318.
- [4] A. P. Babichev, I. A. Babichev, *Basics of vibration technology*, DSTU, Rostov on Don, Russia, 2008.
- [5] S. M.Harlal, Jai Kishan, *Proceedings of the 5st International Symposium*, December 12-14, 2014 AIMTDR, Guwahati, Assam, India, pp. 820-823.
- [6] C. Sandeep, M. Sushil, *Int. J. Res. Aeronaut. Mech. Eng.* 2 (2014) 77-83.
- [7] T. Kenton, *Metal Finishing* 107 (2009) 22-24.

- [8] L. M. Lubenskaya, *Oriente-European Adv. Tech. 4* (2007) 18-25.
- [9] A.C.Wang, S.H. Weng, *J. Mater. Process Tech.192-193* (2007) 486-489.
- [10] T. A.Shumakova, E.Melnikova, I. A.Chesnokov, *Vib. Eng. Tech.2* (2010) 219-233.
- [11] M. A. Kalmikov, *Vib. Eng. Tech.3* (2009) 69-72.
- [12] S. Rajesha, G.Venkatesh, A. K. Sharma, P. Kumar, *Indian J. Eng. Mater. S.117* (2010) 407-413.
- [13] G.Venkatesh, K. S. Apurbba; S. Nitish, *Simulat. Pract. Theory 51* (2015) 1-13.
- [14] j. Cherian, M. I. Jeeju, *Int.J. Emerging Tech. Adv. Eng.3* (2013) 554-557
- [15] M. R. Thakare, J. A. Wharton, R. J. K. Wood, C. Menger, *Wear 276-277* (2012) 16-28.

# Numerical Analysis Of Turbulent Forced-Convection Flow In A Channel With Staggered L-Shaped Baffles

Y. Menni, A. Azzi , C. Zidani and B. Benyoucef

*Unit of Research on Materials and Renewable Energies - URMER -*

*Department of Physics, Faculty of Sciences, Abou Bekr Belkaid University,*

*BP 119-13000-Tlemcen, Republic of Algeria,*

Corresponding author: email: czidani10@yahoo.fr

Received date: April 05, 2016; revised date: December 03, 2016; accepted date: December 11, 2016

---

## **Abstract**

*Characteristics of fluid flow and heat transfer are analyzed for a constant property fluid flowing turbulently through a two-dimensional horizontal rectangular cross section channel with staggered, transverse L-shaped baffles (STLBs) and a constant temperature along both walls. The Commercial CFD software FLUENT 6.3 is used to simulate the fluid flow and heat transfer fields. As a part of the same package, a preprocessor Gambit is used to generate the required mesh for the solver. The governing equations, based on the Shear Stress Transport (SST)  $k-\omega$  model used to describe the turbulence phenomena, are discretized using the Finite Volume Method (FVM) with Semi Implicit Method for Pressure-Linked Equations (SIMPLE) algorithm for pressure-velocity coupling. Air is the working fluid with the flow rate in terms of Reynolds numbers ranging from 12,000 to 30,000. The effects of the baffle L-shape as well as Reynolds numbers are examined. A detailed description of turbulent heat transfer flow behaviors around the STLBs was presented. In particular, contour plots of velocity and pressure fields, axial velocity profiles, local and average heat transfer coefficients, and friction loss evaluations were obtained at constant wall temperature condition along the top and bottom channel walls. The numerical results are validated with available rectangular-baffle measured data and found to agree well with measurement. The results reveal essentially, that the flow pattern of using STLBs is characterized by strong deformations and large recirculation regions. The highest values in the velocity and pressure fields are found near the top channel wall with an acceleration process that starts just after the second STLB. Also, an increase in the Reynolds number causes a substantial increase in the Nusselt number but the pressure loss is also very significant.*

*Keywords: CFD ; Finite volume method ; Forced-convection ; L-shaped baffle ; Rectangular channel ; Turbulent flow.*

---

## **1. Introduction**

The use of baffles and fins in channels is commonly used for passive heat transfer enhancement strategy in single phase internal flow. Considering the rapid increase in energy demand, effective heat transfer enhancement techniques have become important task worldwide. Some of the applications of passive heat transfer enhancement strategies are in process industries, thermal regenerator, Shell-and-tube type heat exchanger, Internal cooling system of gas turbine blades, radiators for space vehicles and automobiles, etc. In literature, numerous studies on baffled channel heat transfer are reported, but only the relevant articles are cited here. Yuan [1] reported a numerical study for the characteristics of the periodically fully developed turbulent flow and heat transfer in a channel with transverse opposite-positioned fins. The influence of the thermal boundary condition of the fin to the heat transfer was verified. Yuan and others also studied experimentally the duct with periodic rectangular fins along the main flow direction [2] and the duct with winglet fins [3]. They can both increase heat transfer largely

comparing with smooth duct. An experimental investigation was done by Habib et al. [4] to study the characteristics of the turbulent flow and heat transfer inside the periodic cell formed between segmented baffles staggered in a rectangular duct. The parameters of the experimental work were the Reynolds number and the baffle height. The results indicated that the pressure loss increases as the baffle height does, for a given flow rate. Also, the local and average heat transfer parameters increase with increasing Reynolds number and baffle height. Demartini et al. [5] presented the numeric and experimental analysis of the turbulent flow of air inside a channel of rectangular section, containing two rectangular baffle plates. Hot wire anemometry and the Finite Volume Method, by means of commercial program FLUENT 5.2 were applied in that research work. Tsay et al. [6] numerically investigated the heat transfer enhancement due to a vertical baffle in a backward-facing step flow channel. The effect of the baffle height, thickness and the distance between the baffle and the backward facing step on the flow structure was studied in detail for a range of Reynolds number varying from 100 to 500. They found that an introduction of a baffle into the flow could increase

the average Nusselt number by 190%. They also observed that the flow conditions and heat transfer characteristics are strong function of the baffle position. The heat transfer enhancement in a heat exchanger tube by installing a baffle was reported by Nasiruddin and Kamran Siddiqui [7]. In that study, the effect of baffle size and orientation on the heat transfer enhancement was studied in detail. The results showed that a significant heat transfer enhancement in a heat exchanger tube can be achieved by introducing a baffle inclined towards the downstream side, with the minimum pressure loss. Numerical studies for both solid and porous baffles in a two dimensional channel for the turbulent flow [8] and for the laminar flow regimes [9,10] were conducted and similar thermal performance results for both the solid and porous cases were reported. Ko and Anand [11] carried out an experiment for turbulent channel flow with porous baffles and found that the porous baffles present a flow behavior as good as the one with solid baffles. Dutta and Dutta [12] first reported the enhancement of heat transfer with inclined solid and perforated baffles. In that study, the effects of baffle size, position, and orientation were studied for internal cooling heat transfer augmentation. Dutta and Hossain [13] experimentally investigated the local heat transfer characteristics and the associated frictional head loss in a rectangular channel with inclined solid and perforated baffles. A combination of two baffles of same overall size was used in their experiment. The upstream baffle is attached to the top heated surface, while the position, orientation, and the shape of the other baffle are varied to identify the optimum configuration for enhanced heat transfer. A constant surface heat flux was applied from the top surface, but the bottom and the side surfaces were maintained at an adiabatic condition. The experimental results showed that the local Nusselt number distribution is strongly depended on the position, orientation, and geometry of the second baffle plate. The friction factor ratio goes up with an increase in the Reynolds number, but its value depends on the arrangement of baffles. Karwa and Maheshwari [14] presented results of an experimental study of heat transfer and friction in a rectangular section duct with fully perforated baffles (open area ratio of 46.8%) or half perforated baffles (open area ratio of 26%) at relative roughness pitch of 7.2-28.8 affixed to one of the broader walls. The authors showed an enhancement of 79-169% in Nusselt number over the smooth duct for the fully perforated baffles and 133-274% for the half perforated baffles while the friction factor for the fully perforated baffles is 2.98-8.02 times of that for the smooth duct and is 4.42-17.5 times for the half perforated baffles. Later on, a number of research groups have utilized the perforated baffle concept for internal cooling augmentation both experimentally [15] and numerically [16-18]. In those studies, different aspect ratio channels

and different porosity baffles were used. Other authors studied in detail the effect of the shape of baffles and orientations on the heat transfer enhancement in the heat exchanger channels. Laminar periodic flow and heat transfer in a two dimensional horizontal channel with isothermal walls and with staggered diamond-shaped baffles was investigated numerically by Sripattanapipat and Promvong [19]. Wang et al. [20] summarized computational and experimental results for research on the flow and heat transfer process of a rectangular channel embedded with staggered pin fins of various shapes (i.e., circular, elliptical, and drop-shaped) in a staggered arrangement. Guerroudj and Kahalerras [21] reported a numerical simulation of laminar mixed convective in a two-dimensional parallel plate channel provided with porous blocks of various shapes (i.e., rectangular, trapezoidal, and triangular-shaped). Benzenine et al. [22] presented a computational analysis of the turbulent flow of air in a pipe of rectangular section provided with two waved fins sequentially arranged in the top and the bottom of the channel wall. The influence of baffle turbulators on heat transfer augmentation in a rectangular channel with Z-shaped baffles was investigated experimentally and numerically by Sriromreun et al. [23]. Numerical and experimental predictions of the flow and heat transfer in shell-and-tube heat exchangers helical baffles were investigated by Lei et al. [24], Dong et al. [25], and Wen et al. [26]. Other similar works can be found in literature as Promvong [27,28], Promvong and Kwankaomeng [29], Tamma et al. [30], and Jedsadaratanachai et al. [31] studied the heat transfer and flow over V-shaped baffles submitted to laminar and turbulent flows using numerical and experimental techniques. All these shapes increase the thermal transfer rate but created catastrophic pressure losses. The principal objective of the present study is to show the influence of STLBs on the fluid flow and heat transfer characteristics when the Reynolds number effects are simultaneously present. This was decided after literature search has revealed that no work has been reported on the computation of the flow in L-baffled rectangular channels. This has motivated the present numerical simulation which is a contribution to the previous studies on improvement techniques of heat transfer. Throughout the study, a constant temperature is assumed from the entire wall of the computational domain. The simulation results of an L-shaped obstacle pair are also compared with conventional CFD simulations and the experimental data of previous researchers.

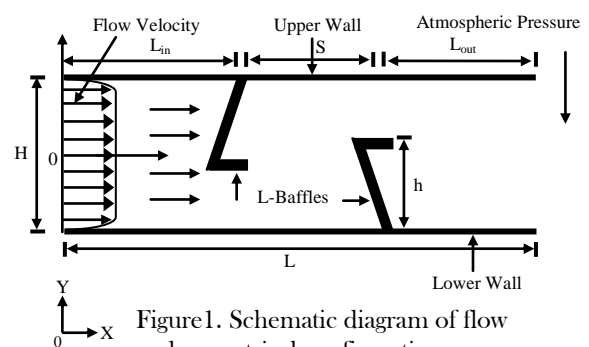


Figure 1. Schematic diagram of flow and geometrical configuration

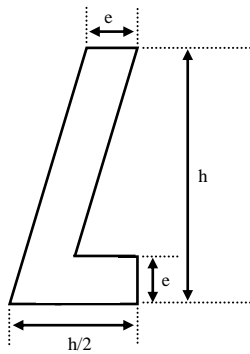


Figure 2. Cross-sectional geometry of the L-shaped baffle

**2. Physical model**

The system of interest is a two-dimensional isothermal wall rectangular cross section channel with a staggered transverse L-shaped baffle pair placed on both the upper and lower walls in staggered arrangement and pointing towards the upstream end as shown in Figure 1. A schematic view of the baffle shape is shown in Figure 2. The flow is two-dimensional, turbulent, incompressible and in steady state with no internal heat generation and neglecting viscous dissipation. The Prandtl number is taken equal to 0.71. All physical properties of the fluid and solid are considered to be constant.

The geometric dimensions of our problem have been based on the experimental work of Demartini et al. [5]. In their study, the experiment was conducted in a two-dimensional domain, which represents a rectangular duct of  $L = 0.554$  m long and  $H = 0.146$  m high, provided by two baffle plates, through which a steady flow of turbulent air. The first plate is attached to the top wall at a distance of  $L_{in} = 0.218$  m and the second inserted to the bottom wall at  $L_{out} = 0.37$  m from the entrance. The distance between the upper edge of the baffle and the wall was kept constant at  $h = 0.08$ m. This corresponds to the area reduction of 54.794 % at the baffle edge. The thickness of the two baffles is a  $e = 0.01$  m.

**3. Mathematical modeling**

Based on the above assumptions, the channel flow is governed by continuity, Navier-Stokes and energy equations, respectively

$$\nabla \cdot \vec{V} = 0 \tag{1}$$

$$\rho(\vec{V} \cdot \nabla \vec{V}) = -\nabla P + \mu_f \nabla^2 \vec{V} \tag{2}$$

$$\rho C_p (\vec{V} \cdot \nabla T) = K_f \nabla^2 T \tag{3}$$

where:  $\vec{V}$  is the velocity vector.  $P$  represents the pressure.  $\rho$ ,  $\mu$ ,  $K$  and  $C_p$  are the density, the dynamics viscosity, the thermal conductivity and specific heat of fluid, respectively.

To ensure realistic accurate turbulent modeling, the performance of four different turbulent models, namely Spalart-Allamaras model, Standard  $k-\epsilon$  model, Shear Stress Transport (SST)  $k-\omega$  model, and Reynolds Stress model were evaluated by Nasiruddin and Kamran Siddiqui [7], solving Navier-Stokes equations. The comparison of the simulated results obtained from these turbulent models with the experimental data made the selection easy. In that study, the SST  $k-\omega$  model was found to be the one that most accurately predicts the flow and modification due to the baffle. The selected turbulent model is capable of calculating the rapidly evolving two-dimensional flow and also in predicting, interactions with the wall. Another advantage of the selected turbulent model is that the model equations behave appropriately in both the near-wall and far-field regions. The SST  $k-\omega$  model is defined by two transport equations, one for the turbulent kinetic energy,  $k$  and the other for the specific dissipation rate  $\omega$ , as given below [32]

$$\frac{\partial}{\partial x_i} (\rho k u_i) = \frac{\partial}{\partial x_j} \left( \Gamma_k \frac{\partial k}{\partial x_j} \right) + G_k - Y_k + S_k \tag{4}$$

$$\frac{\partial}{\partial x_i} (\rho \omega u_i) = \frac{\partial}{\partial x_j} \left( \Gamma_\omega \frac{\partial \omega}{\partial x_j} \right) + G_\omega - Y_\omega + D_\omega + S_\omega \tag{5}$$

Where

$$G_k = -\rho u_i u_j \frac{\partial u_j}{\partial x_i} \tag{6}$$

$$G_\omega = \alpha \frac{\omega}{k} G_k \tag{7}$$

$$\Gamma_k = \mu + \frac{\mu_t}{\sigma_k} \tag{8}$$

and

$$\Gamma_\omega = \mu + \frac{\mu_t}{\sigma_\omega} \tag{9}$$

In these equations,  $x$  and  $x$  are the spatial coordinates.  $G_k$  represents the generation of turbulence kinetic energy due to mean velocity gradients.  $G_\omega$  represents the generation of  $\omega$ .  $\Gamma_k$  and  $\Gamma_\omega$  represent the effective diffusivity of  $k$  and  $\omega$ , respectively.  $Y_k$  and  $Y_\omega$  represent the dissipation of  $k$  and  $\omega$  due to turbulence, respectively.  $D_\omega$  represents the cross-diffusion term.  $S$  and  $S_\omega$  are user-defined source terms.

The commercial CFD software FLUENT6.3 [33] is used to calculate the heat and fluid flow characteristics in the computational domain with STLBs. The governing equations were discretized by the QUICK-scheme [34],

decoupling with the SIMPLE-algorithm [34] and solved using the Finite Volume Method [34]. For closure of the equations, the SST  $k-\omega$  model [32] was used in the present study. The mesh was generated by the pre-processor software Gambit 2.3. Structured meshes, with type-Quadrilateral elements were built and tested with the Fluent 6.3 [33]. To ensure the independence of the mesh with the numerical results, a serial of test was performed. To control the update of the computed variables for all iterations, under relaxation was varied between 0.3 and 1.0. The solutions were converged when the normalized residual values were less than  $10^{-7}$  for all variables but less than  $10^{-9}$  only for the energy equation.

**3.1 Boundary conditions**

The hydrodynamic boundary conditions are chosen according to the experimental work of Demartini et al. [5] while the thermal boundary conditions are set according to the numerical work of Nasiruddin and Kamran Siddiqui [7]. Air was used as the working fluid for all simulation runs. The boundary conditions were given as, (i) the air entered the channel at ambient temperature with a uniform one-dimensional velocity ( $u = U_m, v = 0, T_m = 300$  K); (ii) the pressure at the inlet of the computational domain was set equal to the zero (gauge); (iii) the turbulence intensity was kept at  $I = 2\%$  at the inlet; (iv) A constant temperature of  $102^\circ\text{C}$  ( $T_w = 375$  K) was applied on the entire wall of the computational domain as the thermal boundary condition. (v) impermeable boundary and no-slip wall conditions are imposed at the walls; and (vi) in the channel outlet it is prescribed the atmospheric pressure ( $P = P_{atm}$ ). The Reynolds number of the experiments [5] is  $Re = 8.73 \times 10^4$ , defined as

$$Re = \frac{\rho \bar{U} D_h}{\mu} \tag{10}$$

where  $\bar{U}$  is the entrance (reference) velocity, 7.8 m/s, and  $D_h$  is the hydraulic diameter of the channel, equal to 0.167 m. The total length of the channel is equivalent to  $3.307 \times D_h$ , which is not sufficient for the flow development. Therefore, no influence will result from the side walls, so that the flow can be considered as being two-dimensional.

The skin friction coefficient,  $Cf$ , is given by

$$Cf = \frac{\tau_w}{\frac{1}{2} \rho \bar{U}^2} \tag{12}$$

The numerical friction factor was computed from the pressure drop,  $\Delta P$ , across the length of computational flow domain,  $L$ , having the hydraulic diameter, using Darcy Weisbach formula. That is,

$$f = \frac{(\Delta P/L) D_h}{\frac{1}{2} \rho \bar{U}^2} \tag{13}$$

The local Nusselt number,  $Nu_x$  is evaluated as follows

$$Nu_x = \frac{h_x D_h}{\lambda_f} \tag{14}$$

The average Nusselt number,  $Nu_{av}$  can be obtained by

$$Nu_{av} = \frac{1}{L} \int Nu_x \partial x \tag{15}$$

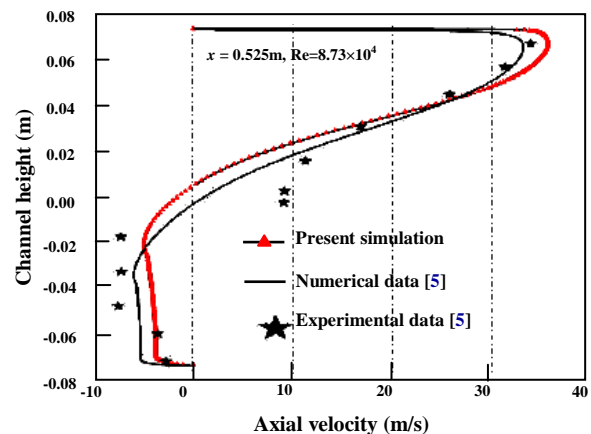
where  $h$  represents the local convective heat transfer coefficient

**3.2 Grid sensitivity**

The mesh was generated by the Pre-processor software Gambit 2.3. The mesh was refined at all solid boundaries, with volumes growing in geometrical progression with the increasing distance from the wall, as given by the expression

$$a_n = a_1 (q^{n-1}) \tag{16}$$

where  $a_n$  is the length of the last volume from the wall,  $a_1$  is the length of the first volume adjacent to the wall,  $q$  is the growth ratio and  $n$  is the number of volumes. This expression is valid for the regions near the walls. For the regions more distant from the walls, the mesh is uniform, as reported by Demartini et al. [5]. A fine non-uniform mesh with the minimum cell number of  $(220 \times 95)$  and the maximum cell number of  $(420 \times 235)$  were provided through the walls. It is found that the variation in  $Nu_{av}$  and  $f$  values for the staggered L-shaped baffles at  $Pi = 0.142$  and  $Re = 8.73 \times 10^4$  is marginal when increasing the number of cells from  $(220 \times 95)$  to  $(420 \times 235)$ . Hence, there is no such advantage in increasing the number of cells beyond this value. Considering both convergent time and solution precision, the grid system of  $(220 \times 95)$  cells (in  $X$  and  $Y$  directions, respectively) was adopted for the current computation. The grid density was kept higher in the vicinity of the heated wall and the STLBs to capture the variations in the flow and temperature fields within the hydraulic and thermal boundary layers.



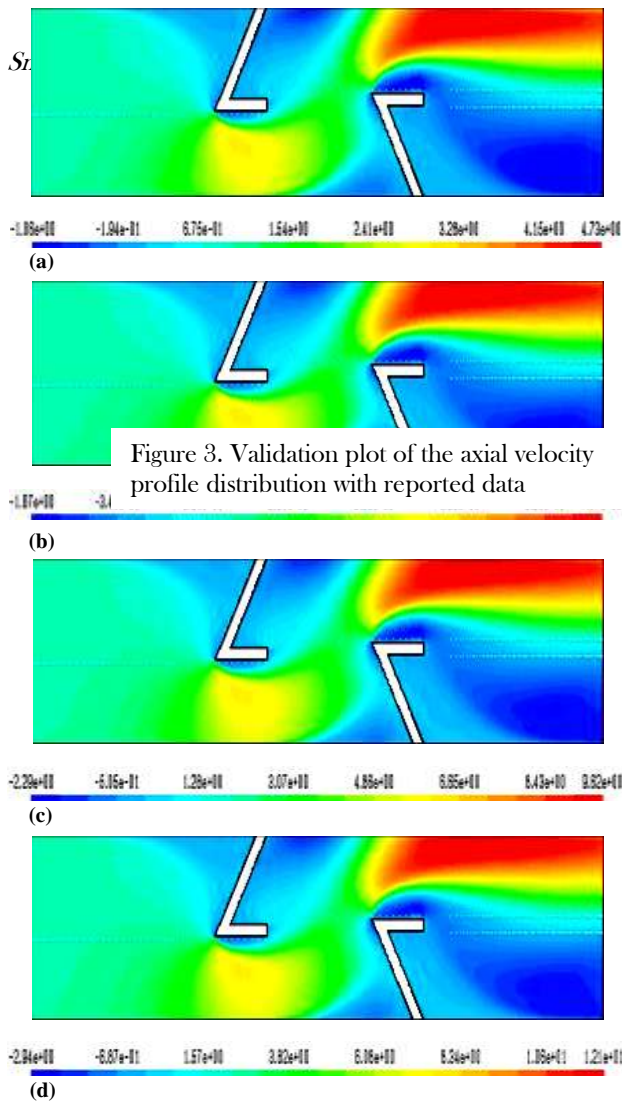


Figure 3. Validation plot of the axial velocity profile distribution with reported data

Figure 4. Two-dimensional axial velocity field in the L-baffled channel at different flow Reynolds numbers: (a)  $Re = 12,000$ , (b)  $Re = 18,000$ , (c)  $Re = 24,000$ , and (d)  $Re = 30,000$ . Airflow is from left to right. Velocity values in m/s.

**4. Results and discussion**

To verify our numerical simulation, a comparizon was made with the numerical and experimental data obtained by Demartini et al. [5] in the case of a rectangular channel, where two baffle plates were placed in opposite walls. The geometry of the problem is a simplification of the geometry of baffle plates found in shell-and-tube heat exchangers.

A quantitative comparison between both the experimental and numerical velocity profiles after the lower wall baffle, near the channel outlet is shown in Figure 3. For the case of axial velocity profiles at a position  $x = 0.525$  m,

measured downstream of the entrance, there is a good agreement between the present study and previous work [5]. These results give confidence that the numerical scheme used was accurate.

The two-dimensional horizontal constant temperature-surfaced rectangular cross section channel flow structure in the presence of STLBs could be easily discerned by considering the velocity contour plots in Figure 4(a-d). The figures present axial velocity fields of turbulent channel flow through STLBs using the SST  $k-\omega$  model for  $Re = 12,000, 18,000, 24,000,$  and  $30,000$ , respectively. The largest variations in the velocity fields occur in the regions near to the staggered STLBs, as expected. The peak velocity values are seen near the heated top channel wall with an acceleration process that starts just after the lower wall STLB, while the velocity is observed to be very low at the locations corresponding to the zones of counter rotating flow in the regions downstream of both STLBs as seen in the figure. In the regions between the tip of both STLBs and the channel walls, the velocity is increased. The effect of the flow rate on the fluid velocity is also depicted in the figure which shows that the velocity value increases with the increase of Reynolds number.

The structure of the near wall flow in the channel with two solid STLBs which are arranged on the top and bottom channel walls in a periodically staggered way can be displayed by considering the axial velocity profile plots in transverse stations for four different Reynolds number values ( $Re = 12,000, 18,000, 24,000,$  and  $30,000$ ) as depicted in Figure 5(a-g) at various axial positions,  $x = 0.159, 0.189, 0.255, 0.285, 0.315, 0.345,$  and  $0.525$  m, respectively. At Reynolds numbers of  $12,000$  to  $30,000$ , the air flows under, between and above the STLBs by taking their exact shape with presence of recirculation zones downstream from each STLB whose size increases by increasing the Reynolds number from  $12,000$  to  $30,000$ . When the inertia effects become important, the great quantity of the fluid, at a higher velocity, flows over the STLBs which will certainly causes a higher heat transfer than that of the lower Reynolds number. Between and downstream the STLBs there is appearance of larger vortices whose size changes with the value of the Reynolds number. The comparison of axial velocity profiles at different axial stations shows that the influence of the deformation of the flow field increases as the air approaches the upper wall STLB, increasing the velocity of the flow approaching the passage under the baffle (see  $x = 0.159$  m and  $x = 0.189$  m in the figure). The plots also show that as the flow is accelerated and redirected near the first STLB, a very small recirculation zone is formed in the vicinity of the upper left corner (see Fig. 5a and b). Downstream of the first STLB, as a result of sudden expansion in the cross-section, the airflow separates, a larger clockwise vortex is formed behind the upper wall STLBs in the upper part of the channel and flow reattachment is then established (see Fig. 5c and d).

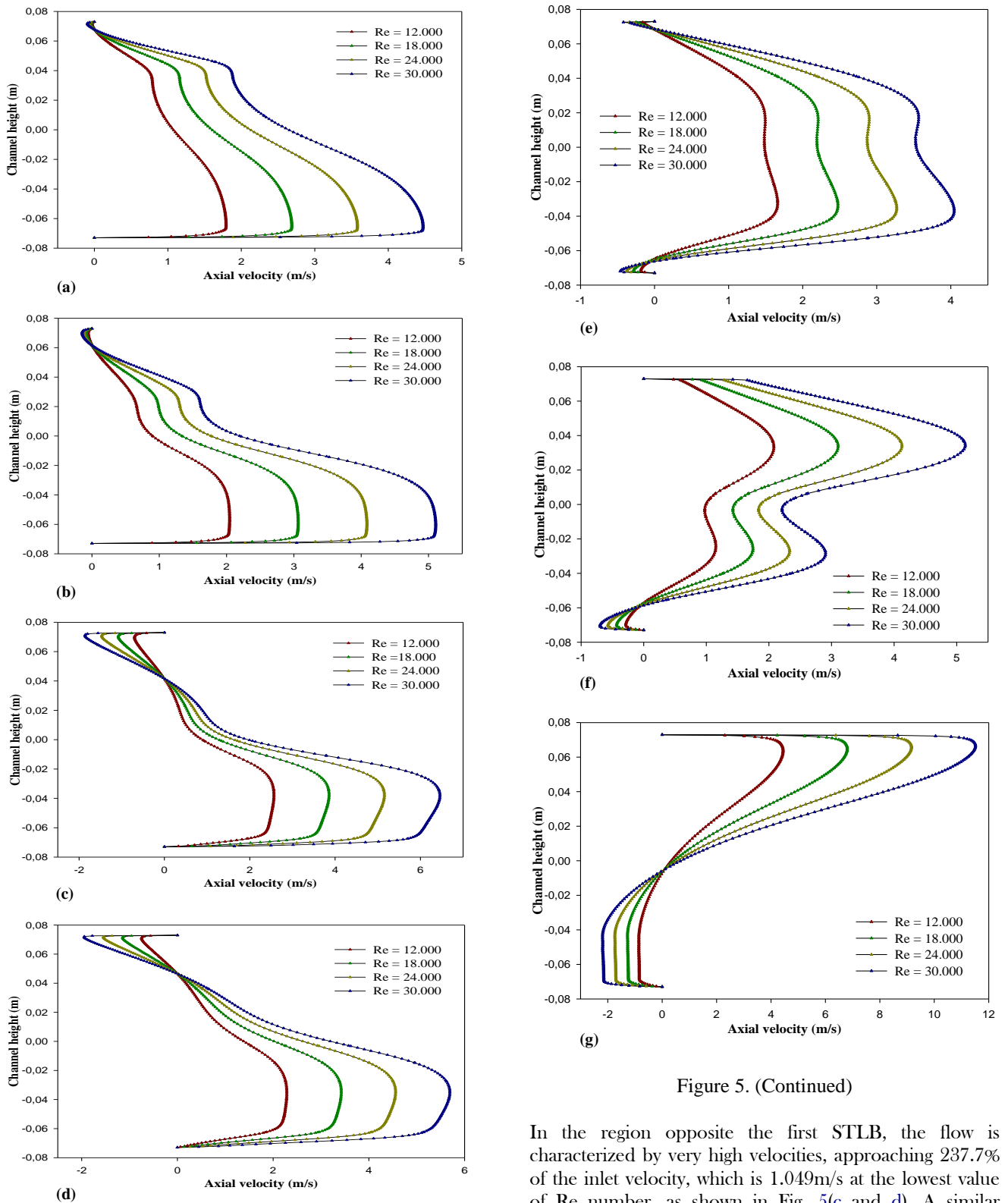


Figure 5. (Continued)

Figure 5. Plots of axial velocity profiles at axial stations given by (a)  $x=0.159$  m, (b)  $x=0.189$  m, (c)  $x=0.255$  m, (d)  $x=0.285$  m, (e)  $x=0.315$  m, (f)  $x=0.345$  m, and (g)  $x=0.525$  m, measured downstream of the entrance

In the region opposite the first STL B, the flow is characterized by very high velocities, approaching 237.7% of the inlet velocity, which is 1.049m/s at the lowest value of Re number, as shown in Fig. 5(c and d). A similar behavior is observed near the STL B mounted on the lower wall with counterclockwise vortices at the upstream (see Fig. 5e and f) and downstream STL B (see Fig. 5g). The plots of Figure 5(e and f) shows that as the airflow

approaches the second STLB, its velocity is reduced in the lower part of the channel, while in the upper part is increased. In these locations ( $x = 0.315$  m and  $x = 0.345$  m) the negative velocities indicate the presence of a small recirculation zone at the lower left corner behind the lower wall STLB. The axial velocity profile distribution obtained for different values of Reynolds number after the lower wall STLB, near the channel outlet is also shown in Figure 5. At a position  $x = 0.525$  m, 0.145 m after the second STLB and 0.029 m before channel outlet, the value of the velocity reaches 4.443m/s, 4.233 times higher than the entrance velocity at the lowest value of Re number, as shown in Figure 5g. In the lower part of the channel, a strong counterclockwise vortex is observed downstream of the considered baffle, which was induced due to the flow separation. The vortex is located close to the solid wall and its height was approximately equal to the extent of the flow blockage by the STLB, which is equal to 0.08m (see Fig. 5g).

30,000. Airflow is from left to right. Dynamic pressure values in Pa.

The presence of the STLBs influences not only the velocity field but also the pressure distribution in the whole domain examined. The contour plots of dynamic pressure are shown in Figure 6 (a-d) for different Re values. The plots in Figure 6 show very low dynamic pressure values adjacent to the STLBs. In the regions downstream of both STLBs, recirculation cells with very low dynamic pressure values are observed. This fact is associated to the negative velocities at the upstream and downstream both STLBs shown in Figure 5. In the regions between the tip of the STLBs and the channel walls, the dynamic pressure is increased.

It indicates that the highest dynamic pressure value can be observed at the area of high velocities especially at the area near the upper channel wall with an acceleration process that starts just after the second STLB.

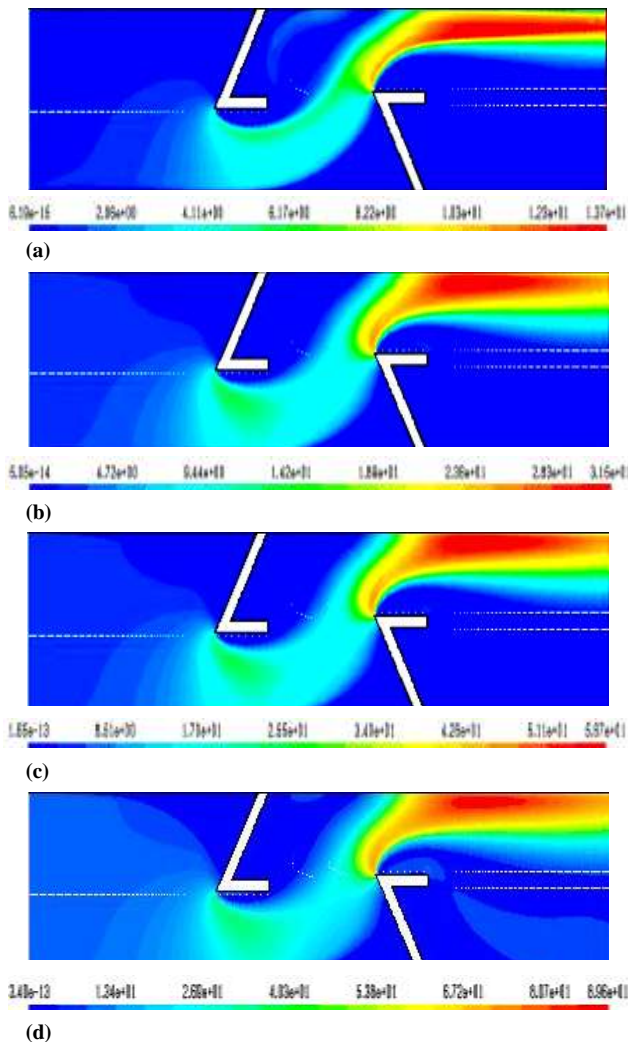


Figure 6. Two-dimensional dynamic pressure field in the L-baffled channel at different Reynolds numbers: (a) Re = 12,000, (b) Re = 18,000, (c) Re = 24,000, and (d) Re =

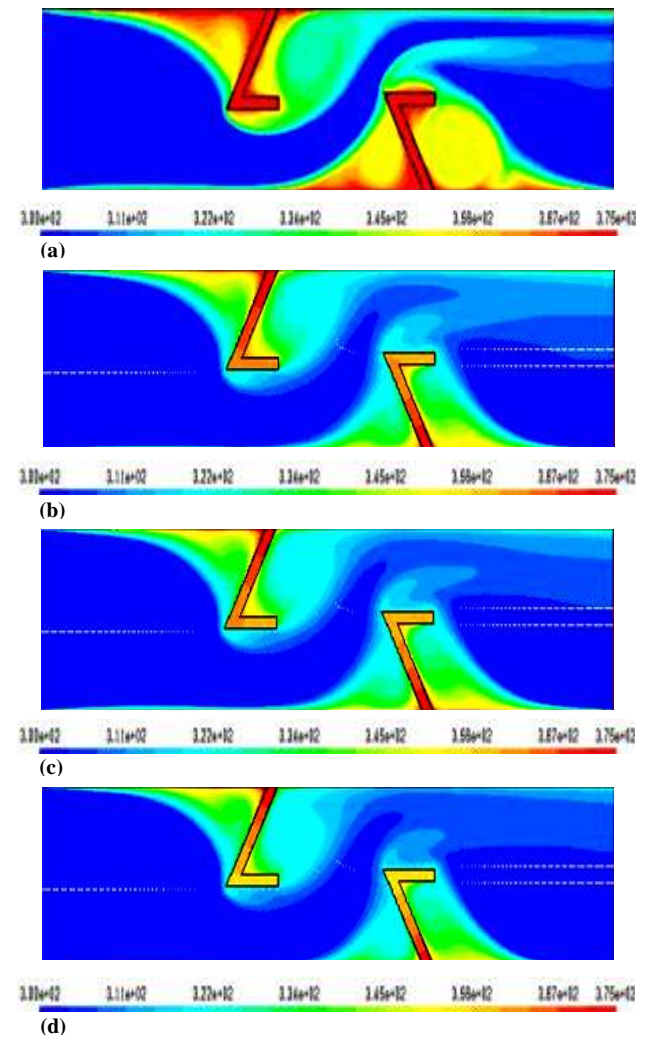


Figure 7. Two-dimensional temperature field in the L-baffled channel at different Reynolds numbers: (a) Re = 12,000, (b) Re = 18,000, (c) Re = 24,000, and (d) Re =

30,000. Airflow is from left to right. Fluid temperature values in K.

The temperature field is an important indicator to reflect the performance of a baffled channel. The contour plots of temperature field distributions in the given channel with the guidance of two-STLBs and a constant wall temperature condition along the top and bottom walls for the tested Reynolds number range of 12,000-30,000 are shown in Figure 7(a-d), respectively. In the figure, the lowest temperature value can be observed where the flow impinges the channel wall, especially in the region opposite the STLB tip where the velocity in this region is somewhat high while the highest one is found at the STLB corner area where the corner recirculation zone occurs, especially area behind the STLBs. The figure shows that the fluid temperature in the recirculation region is significantly high as compared to that in the same region of no STLB. It is also shown that in the recirculation regions, the fluid temperature is increased by approximately 75% due to the insertion of STLBs. The most intense in the temperature field is that occurring downstream of the lower-wall STLB, responsible for the high flow velocities observed at the outlet of the channel, creating a negative velocity profile which introduces mass inside the test channel through the outlet (see Fig. 5g).

The temperature field is also affected by the Reynolds number. Figure 7(a-d) also depicts the temperature field contour plots as a function of the Reynolds number. In the figure, it is worth noting that the fluid temperature value tends to decrease with the rise of Reynolds number for all locations due to the augmentation of the inertia forces further to the augmentation of the flow rate while the flow velocity shows an opposite trend (see Fig. 4 and 5). By increasing the Reynolds number from 12,000 to 30,000, large recirculation regions and velocity gradients are observed behind the STLBs. The generation of these vortex flows from using the STLBs as well as the role of better fluid mixing and the impingement is the main reason for the augmentation in the temperature gradient over the heating wall.

The axial distribution plots of local Nusselt number profiles as a function of Reynolds number at the surface of the lower and upper walls of the channel are shown in Figure 8(a and b), respectively. It is seen in the figure that the largest variations on both the upper and lower walls of the given channel are found near the tip of the STLBs, due to the strong velocity gradients in that region. In the regions downstream of both STLBs, the local heat transfer is significantly enhanced for all Re values investigated. This enhancement is due to the intense mixing by the vortices. Due to the changes in the flow direction produced by the STLBs, the highest  $Nu$  values appear in the region opposite the lower wall STLB with an acceleration process that starts just after the second STLB. Concerning the effect of the flow rate on the local heat transfer characteristics, it can be seen from this figure and for this range of Reynolds number ( $12,000 \leq Re \leq 30,000$ ) that the  $Nu$  value tends to increase with the rise of Re values for all locations. This could be due to the reason that an increase in the Re value cause an increase in the length and strength of the vortices, which enhance mixing and mixing length. The average heat transfer results are done on the heated top and bottom surfaces and presented in terms of a non-dimensional Nusselt number ratio,  $Nu_w/Nu_0$ , along the tested channel walls.  $Nu_0$  is the Nusselt number for fully developed flow in a smooth channel at the same Reynolds number, and is given by

$$Nu_0 = 0.023 Re^{0.8} Pr^{0.4} \tag{17}$$

The  $Nu_0$  is used as a reference to minimize the Reynolds number effect in the presented results. The Nusselt number ratio essentially indicates the amount of enhancement in heat transfer obtained by the flow guidance turbulators over the smooth rectangular channel.

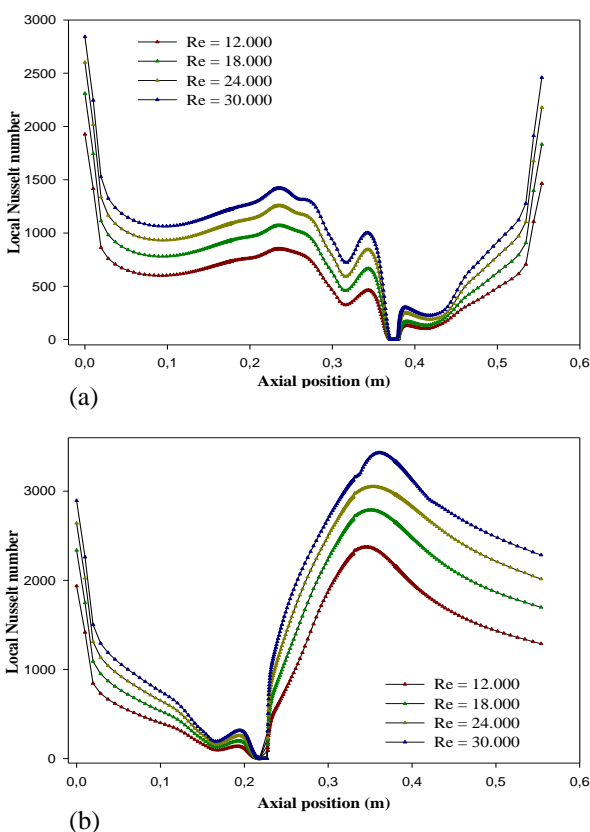


Figure 8. Axial variation of local Nusselt number with Reynolds number at the surface of (a) top and (b) bottom walls of the L-shaped baffled channel

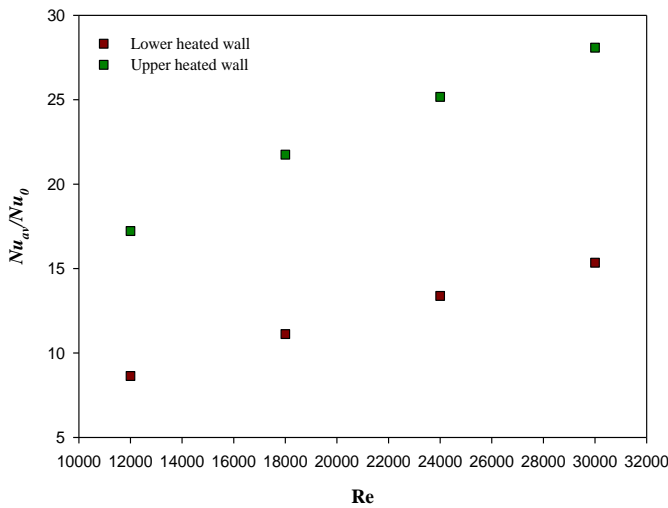
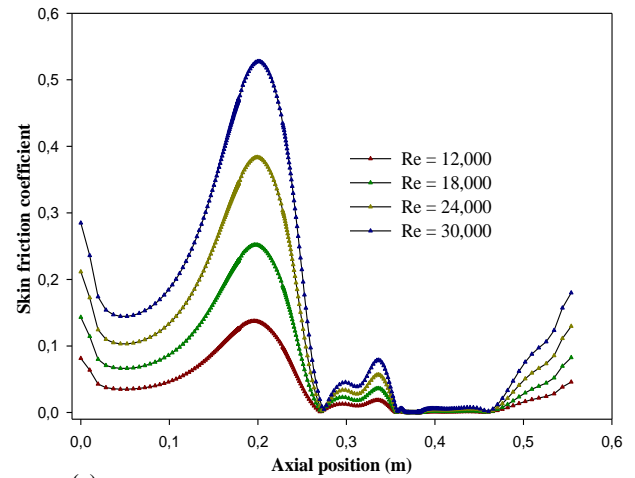


Figure 9. Variation plots of Normalized Nusselt number as a function of Reynolds number at the surface of the top and bottom channel walls

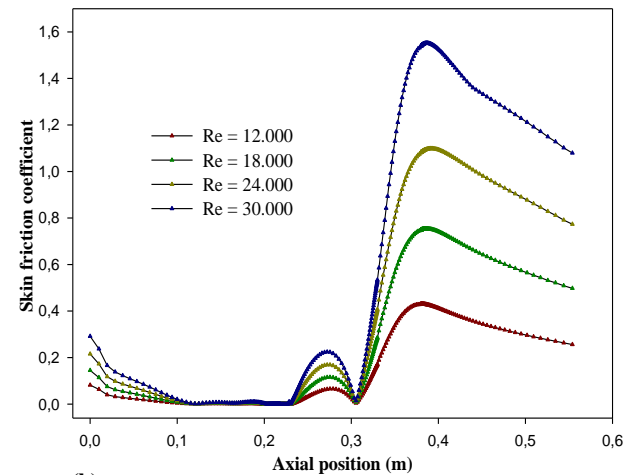
Figure 9 shows the normalized average Nusselt number versus the Reynolds number (based on the hydraulic diameter) for the channel with upper and lower wall-mounted STLBs. The figure shows as expected, that the heat transfer rate increased with the Reynolds number. Both channel walls show similar trend but with different values. The largest variations are found at the heated top surface of the channel, due to the strong velocity gradients in that region. It is also noted that the use of the STLBs lead to extremely considerable increase in the convective average Nusselt number rate in comparison with the plain channel with no baffle. The heat transfer rate value for the STLBs is found to be higher by about 8.637-28.081 times over the plain channel with no baffle, depending on the wall surface and the Reynolds number values.

Figure 10(a and b) shows the axial distribution plots of local skin friction coefficient profiles along the lower and upper channel walls in the range of Reynolds number investigated, respectively. We will start analyzing the effect of the STLB presence before discussing the influence of flow Reynolds number. Similarly to the results in Figure 8, the largest  $CF$  value is found in the region opposite the upper and lower wall STLBs, due to the strong velocity gradients in that region while the smallest  $CF$  value is found, firstly, upstream of the top wall STLB in the upper part of the channel and, secondly, downstream of the bottom wall STLB in the lower part of the channel, due to the orientation of the airflow by these deflectors. However, the skin friction coefficient is increased again at the locations corresponding to the zones of recirculation as seen in the figure. It indicates that the highest skin friction coefficient can be observed at the top heated surface of the channel in the area of high velocity especially at the top face of the STLB mounted on the lower wall of the

channel. The variation of isothermal skin friction coefficient value with Reynolds number for the STLBs is also shown in Figure 10. It is clear from this figure that the  $CF$  tends to increase with raising the Reynolds number value, as expected.



(a)



(b)

Figure 10. Axial variation of skin friction coefficient with Reynolds number at the surface of (a) top and (b) bottom walls of the L-shaped baffled channel

Figure 11 shows the variation of the dimensionless pressure drop given by the friction factor ratio,  $f/f_0$ , with Reynolds number ( $12,000 \leq Re \leq 30,000$ ). Here  $f_0$  is the friction factor in a fully developed smooth channel at the same Reynolds number, and it can be presented as

$$f_0 = \frac{1}{(0.79 \ln Re - 1.64)^2} \tag{18}$$

As expected, obviously it can be observed that values of  $f/f_0$  become higher with increasing values in Reynolds number.

In the figure, the L-shaped baffled channel flows give higher values of friction factor than that for smooth channel flow due to the induction of high recirculation or vortex flow and thin boundary layer in the baffled channel, leading to higher temperature gradients, heat transfer and pressure drop.

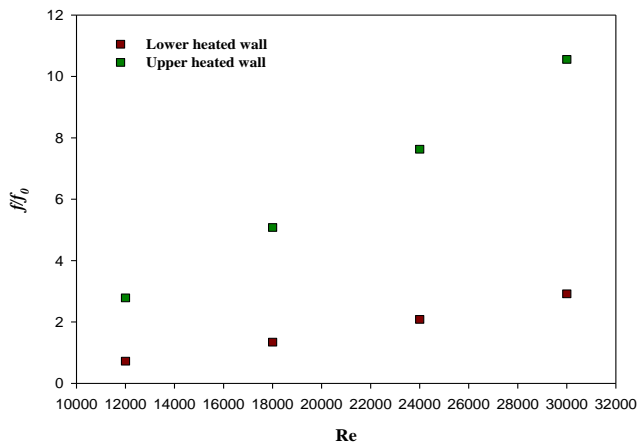


Figure 11. Normalized friction factor versus the Reynolds number at the surface of the top and bottom channel walls

The maximum  $f/f_0$  values for both upper and lower channel walls are found to be about 0.722-2.918 and 2.784-10.554 times above those for the smooth duct with no baffle, respectively, depending on the  $Re$  values. Thus the flow blockage due to the existence of baffle as well as the role of turbulence degree in the core region is a key factor to cause an extreme pressure drop.

#### 4. Conclusion

A numerical study has been conducted to examine the fluid flow and heat transfer characteristics in a two-dimensional horizontal constant temperature-surfaced rectangular cross section channel with lower and upper wall-mounted L-shaped baffles in the turbulent regime from  $Re = 12,000$  to  $30,000$ . The aim at using the STLBS is to create vortex flows having a significant influence on the flow pattern leading to higher heat transfer enhancement in the given channel. The computations are based on the Finite Volume Method, and the SIMPLE-algorithm has been implemented. The effects of the baffle L-shape geometry as well as Reynolds numbers are examined. The obtained results are compared with available experimental data from the literature and good agreement is obtained. The velocity profiles, and pressure and temperature fields over the baffled channel are the most notable characteristics of the effects of the STLBS on the mainstream flow. These effects are: mainstream flow separation, recirculation, and secondary flow. The comparison of axial velocity profiles at different Reynolds numbers shows that as the airflow is accelerated and

redirected near the STLBS, a very small recirculation zone is formed in the vicinity of the upper left corner. Downstream, as a result of sudden expansion in the cross-section, the flow separates, a larger clockwise recirculation zone is formed behind the upper wall STLBS and flow reattachment is then established. A similar phenomenon is found near the STLBS mounted on the lower wall with counterclockwise recirculation zones at the upstream and downstream STLBS. The length of these recirculation zones strongly depend on the flow Reynolds number value. The appearance of these recirculation flows can help to increase higher the heat transfer in the channel with two- STLBS because of transporting the fluid from the core to the near wall regimes, and in general, an increase in the flow Reynolds number causes a substantial increase in the flow velocity, leading to a high temperature gradient along the heating channel walls but the pressure loss is also very significant.

The above results suggest that a significant heat transfer enhancement in a heated channel can be achieved by introducing STLBS into the flow. The study can be extended for different number, sizes, positions, arrangements, orientations, and inclination angles, of the L-shaped baffles at different boundary conditions for temperature and velocity.

#### AUTHOR'S CONTRIBUTIONS

Each author of this manuscript made considerable contributions in developing the mathematical modeling, data-analysis and contributed to the writing of this manuscript.

#### NOMENCLATURE

$a_n$	Length of the last volume from the wall, m
$a_1$	Length of the first volume adjacent to the wall
$C_p$	Specific heat at constant pressure, J/kg K
$CF$	Skin friction coefficient
$D_h$	Hydraulic diameter of rectangular channel, m
$e$	L-shaped baffle thickness, m
$f$	Friction factor
$f_0$	Friction factor in smooth channel at the same Reynolds number
$G_s$	Turbulent kinetic energy generation due to mean velocity gradient
$G_w$	Kinetic energy generation due to buoyancy
$H$	Channel height, m
$h$	L-shaped baffle height, m
$h_c$	Local convective heat transfer coefficient, W/m <sup>2</sup> K
$k$	Turbulent kinetic energy, m <sup>2</sup> /s <sup>2</sup>
$L$	Length of rectangular channel in x-direction, m
$L_{in}$	Distance upstream of the first L-shaped baffle, m
$L_{out}$	Distance downstream of the second L-shaped baffle, m
$n$	Number of volumes.

$Nu_w$	Average Nusselt number
$Nu_s$	Local Nusselt number
$Nu_b$	Nusselt number for fully developed pipe flow at the same Reynolds number
$P$	Pressure, Pa
$P_{atm}$	Atmospheric pressure, Pa
$Pr$	Prandtl number
$q$	Growth ratio
$Re$	Reynolds number based on the channel hydraulic diameter
$S$	L-shaped baffle distance or spacing, m
$S_k, S_\omega$	Source term of $k$ and $\omega$
$T$	Temperature, °C
$T_w$	Inlet fluid temperature, °C
$T_w$	Wall temperature, °C
$\bar{U}$	Mean axial velocity of the section, m/s
$U_w$	Inlet velocity, m/s
$u, v$	Velocity component in x- and y- direction, m/s
$u$	Velocity component in x-direction, m/s
$\vec{V}$	Velocity vector, m/s
$x, y$	Cartesian coordinates, m
$Y_k, Y_\omega$	Dissipation of $k$ and $\omega$

### Greek symbols

$\omega$	Specific dissipation rate, m <sup>2</sup> /s
$\Gamma_k, \Gamma_\omega$	Effective diffusivity of $k$ and $\omega$
$\rho$	Fluid density, kg/m <sup>3</sup>
$\mu$	Dynamic viscosity, Kg/m s
$\mu_t$	Fluid dynamic viscosity, Kg/m s
$\mu_t$	Turbulent viscosity, Kg/m s
$\tau_w$	Wall shear stress, Kg/s <sup>2</sup> m
$\lambda$	Fluid thermal conductivity, W/m °C
$\Delta P$	Pressure drop, Pa

### Subscript

$atm$	Atmospheric
$f$	Fluid
$i, j$	Refers coordinate direction vectors
$in, out$	Inlet, outlet of the computational domain
$t$	turbulent
$w$	Wall
$x$	Local

## 6. REFERENCES

- [1] Z. X. Yuan, Numerical Study of Periodically Turbulent Flow and Heat Transfer in a Channel with Transverse Fin Arrays, *Int. J. Numerical Methods for Heat & Fluid Flow*, vol. 10, N°8, pp. 842-861, (2000).
- [2] Z. X. Yuan, Q. W. Wang and W. Q. Tao, Experimental Study of Enhanced Heat Transfer in Ducts with Periodic Rectangular Fins Along the Main Flow Direction, *Pro. 11th IHTC*, 23-28 August, Kyongju, Korea, vol. 5, pp. 327-32, (1998).
- [3] Z. X. Yuan, W. Q. Tao and Q. W. Wang, Experimental Investigation of Heat Transfer Enhancement in Ducts with Winglet Fins, *Pro. First Int. Conference of Engineering Thermophysics*, 21-23 August, Beijing, China, pp. 457-63, (1999).
- [4] M. A. Habib, A. M. Mobarak, M. A. Sallak, E. A. Abdel Hadi and R. I. Alfify, Experimental Investigation of Heat Transfer and Flow over Baffles of Different Heights, *Trans. ASME, J. Heat Transfer*, vol. 116, pp. 363-368, (1994).
- [5] L. C. Demartini, H. A. Vielmo and S. V. Möller, Numeric and Experimental Analysis of the Turbulent Flow through a Channel with Baffle Plates, *J. the Braz. Soc. of Mech. Sci. & Eng.*, vol. 26, N° 2, pp. 153-159, (2004).
- [6] Y. -L. Tsay, T. S. Chang and J. C. Cheng, Heat Transfer Enhancement of Backward-facing Step Flow in a Channel by Using Baffle Installation on the Channel Wall, *Acta Mech.*, vol. 174, N° 1-2, pp. 63-76, (2005).
- [7] Nasiruddin and M. H. Kamran Siddiqui, Heat Transfer Augmentation in a Heat Exchanger Tube Using a Baffle, *Int. J. Heat and Fluid Flow*, vol. 28, pp. 318-328, (2006).
- [8] Y. T. Yang, C. Z. Hwang, Calculation of Turbulent Flow and Heat Transfer in a Porous Baffled Channel, *Int. J. Heat Mass Transfer*, vol. 46, pp. 771-780, (2003).
- [9] B. M. Da Silva Miranda and N. K. Anand, Convective Heat Transfer in a Channel with Porous Baffles, *Numer. Heat Transf., A Appl.*, vol. 46, N° 5, pp. 425-452, (2004).
- [10] N. B. Santos and M. J. S. De Lemos, Flow and Heat Transfer in a Parallel-plate Channel with Porous and Solid Baffles, *Numer. Heat Transf., A Appl.*, vol. 49, N° 5, pp. 471-494, (2006).
- [11] K. H. Ko and N. K. Anand, Use of Porous Baffles to Enhance Heat Transfer in a Rectangular Channel, *Int. J. Heat Mass Transfer*, vol. 46, pp. 4191-4199, (2003).
- [12] P. Dutta and S. Dutta, Effect of Baffle Size, Perforation and Orientation on Internal Heat Transfer Enhancement, *Int. J. Heat Mass Transfer*, vol. 41, N° 19, pp. 3005-3013, (1998).
- [13] P. Dutta and A. Hossain, Internal Cooling Augmentation in Rectangular Channel Using two Inclined Baffles, *Int. J. Heat and Fluid Flow*, vol. 26, pp.223-232, (2005).
- [14] R. Karwa and B. K. Maheshwari, Heat Transfer and Friction in an Asymmetrically Heated Rectangular Duct with Half and Fully Perforated Baffles at Different Pitches, *Int. Comm. in Heat and Mass Transfer*, vol. 36, pp. 264-268, (2009).
- [15] I. Ziolkowska, M. Dolata, D. Ziolkowski, Heat and Momentum Transfer in Fluids Heated in Tubes with Turbulence Generators at Moderate Prandtl and Reynolds Numbers. *Int. J. Heat Mass Transfer*, vol. 42, N° 4, pp. 613-627, (1999).
- [16] Y. L. Tsay, J.C. Cheng and T. S. Chang, Enhancement of Heat Transfer from Surface-mounted Block Heat Sources in a Duct with Baffles, *Numerical Heat Transfer; Part A*, vol. 43, N° 8, pp. 827-841, (2003).
- [17] Y. T. Yang, C. Z. Hwang, Calculation of Turbulent Flow and Heat Transfer in a Porous-baffled Channel. *Int. J. Heat Mass Transfer*, vol. 46, N° 5, pp. 771-780, (2003).

- [18] M. Yilmaz, The effect of Inlet Flow Baffles on Heat Transfer, *Int. Comm. Heat Mass Transfer*, vol. 30, N° 8, pp. 1169-1178, (2003).
- [19] S. Sripattanapipat and P. Promvonge, Numerical Analysis of Laminar Heat Transfer in a Channel with Diamond-Shaped Baffles, *Int. Comm. Heat Mass Transfer*, vol. 36, pp. 32-38, (2009).
- [20] F. Wang, J. Zhang and S. Wang, Investigation on Flow and Heat Transfer Characteristics in Rectangular Channel with Drop-Shaped Pin Fins, *Propulsion and Power Research*, vol. 1, N° 1, pp. 64-70, (2012).
- [21] N. Guerroudj and H. Kahalerras, Mixed Convection in a Channel Provided with Heated Porous Blocks of Various Shapes, *Energy Conversion Management*, vol. 51, pp. 505-517, (2010).
- [22] H. Benzenine, R. Saim, S. Abboudi and O. Imine, Numerical Analysis of a Turbulent Flow in a Channel Provided with Transversal Waved Baffles, *Thermal Science*, vol. 17, N° 3, pp. 801-812, (2013).
- [23] P. Srirromreun, C. Thianpong and P. Promvonge, Experimental and Numerical Study on Heat Transfer Enhancement in a Channel with Z-Shaped Baffles, *Int. Comm. Heat Mass Transfer*, vol. 39, pp. 945-952, (2012).
- [24] Y. G. Lei, Y. L. He, R. Li and Y. F. Gao, Effects of Baffle Inclination Angle on Flow and Heat Transfer of a Heat Exchanger with Helical Baffles, *Chemical Engineering and Processing: Process Intensification*, vol. 47, pp. 2336-2345, (2008).
- [25] C. Dong, Y. -P. Chen and J. -F. Wu, Flow and Heat Transfer Performances of Helical Baffle Heat Exchangers with Different Baffle Configurations, *Applied Thermal Engineering*, vol. 80, pp. 328-338, (2015).
- [26] J. Wen, H. Yang, S. Wang, Y. Xue and X. Tong, Experimental Investigation on Performance Comparison for Shell-and-Tube Heat Exchangers with Different Baffles, *Int. J. Heat Mass Transfer*, vol. 84, pp. 990-997, (2015).
- [27] P. Promvonge, Heat Transfer and Pressure Drop in a Channel with Multiple 60° V-baffles, *Int. Commun. Heat Mass Transfer*, vol. 37, pp. 835-840, (2010).
- [28] P. Promvonge, Numerical Analysis of Laminar Flow Heat Transfer in Square Duct with V-shaped Baffles, *Chiangmai University Int. Conference 2011*, vol. 1, N° 1 pp. 83-92, (2010).
- [29] P. Promvonge and S. Kwankaomeng, Periodic Laminar Flow and Heat Transfer in a Channel with 45° Staggered V-baffles, *Int. Comm. Heat Mass Transfer*, vol. 37, pp. 841-849, (2010).
- [30] S. Tamma, S. Skullong, C. Thianpong and P. Promvonge, Heat Transfer Behaviors in a Solar Air Heater Channel with Multiple V-baffle Vortex Generators, *Solar Energy*, vol. 110, pp. 720-735, (2014).
- [31] W. [Jedsadaratanachai](#), S. [Suwannapan](#) and P. [Promvonge](#), Numerical Study of Laminar Heat Transfer in Baffled Square Channel with Various Pitches, *Energy Procedia*, vol. 9, pp. 630-642, (2011).
- [32] F. R. Menter, Two-equation Eddy-viscosity Turbulence Models for Engineering Applications, *J. AIAA.*, vol. 32, pp. 8, (1994).
- [33] Fluent Inc., User's Guide 6.3, Centerra Park Lebanon, NH, USA, 2006.
- [34] S. V. Patankar, *Numerical heat transfer and fluid flow*, Hemisphere Publishing Corporation, New York, 1980.

# The effect of excess energy in the simulation of dendritic growth using the phase field model coupled with a CALPHAD database.

A. Kerboub\*, E. Belbacha, A. B. Bouzida, A. Hidoussi, and Y. Djaballah

*Physico-chemical studies of materials laboratory, Department of Physics, University of Batna1, (05000) Batna, Algeria*

Corresponding author: email: [kerboubhako@gmail.com](mailto:kerboubhako@gmail.com)

Received date: May 25, 2016; accepted date: December 29, 2016

---

## Abstract

*In this work, we aim to use the Warren-Boettinger model for isothermal solidification to predict the dendritic growth in binary alloys; using the phase field method coupled with a CALPHAD database (CALCulation of PHase Diagram). The main benefit of this work is to study the effect of the excess energy in the phenomena of dendritic growth for the real solution. We took in consideration, the contribution of the regular solution interaction parameter associated with the excess energy of mixing solid and liquid in the phase field equation  $\varphi(x, t)$  and the concentration equation  $c(x, t)$ . The model we proposed is able to simulate the microstructural evolution of the real solution Ni-Cu by linking directly the phase field model to the CALPHAD thermodynamic database. The comparison of the numerical calculations for the Ni-Cu real solution and the Ni-Cu ideal solution shows that the addition of the excess energy has an important effect on the dendrite form.*

*Keywords: Dendritic growth; Phase field model; CALPHAD; Excess energy.*

---

## 1. Introduction

The phase field models have become an important tool in material science simulation [1], i.e : the formation of microstructure and growth of dendrites [2] and the process of solidification of binary alloys [3-7]. They have been the subject of numerous studies and different simulation [8]. The phase field method is a powerful kinetic tool for simulating microstructure evolution at the meso-scale [9-12], whereas phase equilibrium information such as equilibrium phases and their compositions can be obtained from the CALPHAD method [13-17]. Therefore, the coupling of these two methods is useful for effectively predicting kinetic microstructure evolution in alloy systems. The phase field simulation coupled with the CALPHAD method have also been reported for solidification such as temporal evolution of interfacial composition profiles during solidification, dendrite growth, and solidification microstructure formation [18- 24].

The numerical simulation adopted and performed in this work for the dendritic growth in the case of binary alloy was much discussed previously, for example we mention in this context the work of Warner and Boettinger [6], who created the first model to predict the dendritic growth in binary alloys, Steinbach [25,26], Provatas and Elder [27], Chen [28], and in particularly the work of Mathis Plapp [29], they studied the digital side by changing the methods of solving and mesh pattern. All these works treated the Ni-Cu alloys as an ideal solution where the mixing energy is neglected. For example the

model of Warner and Boettinger [6] imposes an ideal Ni-Cu solution, but indeed, considering the Ni-Cu solution as ideal is not entirely justified, since in reality it may not be close to the ideal, despite the similarity of the physical properties of Ni and Cu elements and the nature of the Ni-Cu phase diagram [27].

In a real solution AB, it is necessary that the energy of the mixture called also the excess energy is less than the energy of pure elements A and B (for more details see ref [31]). Our contribution falls within this context; it involves the development of the Warner and Boettinger model [6], where we consider the Ni-Cu alloy as a real solution by introducing the term of excess energy. To get this contribution, we must take into account the interaction parameter associated with the excess energy of mixing solid and liquid phases [6, 30, 31]. The thermodynamic modeling of the Ni-Cu phase diagram with CALPHAD methods gives us directly the excess energy parameters of solid and liquid phases. This setting was previously assumed to be zero in the model of Warner and Boettinger [6] also the same in [7, 9, 27]. The introduction of the interaction parameter in the phase field and the concentration equations in the model of Warner and Boettinger lead us finally to a model reflecting dendritic growth for real solutions.

Our contribution is to study the dendritic growth of a real solution, the growth evolution is presented and a comparative study is made between our results and the others results found in the literatures.

## 2. Mathematical Model

The Warren-Boettinger model [6] describes the progress of solidification of binary alloy in time  $t$ , by two partial differential equations system, the phase field and the concentration equations with two independent variables:  $\varphi$  and concentration,  $c$ .

### 2.1. The phase field equation

$$\frac{1}{M_\varphi} \frac{D\varphi(x,t)}{Dt} = \bar{\epsilon}^2 \nabla \cdot (\eta^2 \nabla \varphi) - (1-c)H_A(\varphi, T) - cH_B(\varphi, T) - \bar{\epsilon}^2 \frac{\partial}{\partial x} \left( \eta \eta' \frac{\partial \varphi}{\partial y} \right) + \bar{\epsilon}^2 \frac{\partial}{\partial y} \left( \eta \eta' \frac{\partial \varphi}{\partial x} \right) \quad (1)$$

Where:

$M_\varphi > 0$  : is the interfacial mobility

$$M_\varphi = cM_B - (1-c)M_A \quad (2)$$

$$M_X = \frac{(T_m^X)^2 \beta_X}{\sqrt{2} L_X \delta_X} \quad (3)$$

$\beta_X$  The linear kinetic coefficient of component  $X$ ,

$T_m^X$  The melting temperature of component  $X$ ,

$\delta_X$  The interface thickness of component  $X$ ,

$L_X$  The latent heat of component  $X$

$$\bar{\epsilon}^2 = \frac{6\sqrt{2}\delta_X\sigma_X}{T_m^X} \quad (4)$$

$\sigma_X$  The surface energy of component  $X$

$H_X$  The free energy of element  $X$

$$H_X(\varphi, T) = W_X g'(\varphi) + 30g(\varphi)L_A \left(1 - \frac{T}{T_m^X}\right) \quad (5)$$

$T$  The absolute temperature

$$g(\varphi) = \varphi^2(1-\varphi)^2 \quad (6)$$

$$g'(\varphi) = \frac{\partial g(\varphi)}{\partial \varphi} \quad (7)$$

$$W_X = \frac{3\sigma_X}{\sqrt{2}T_m^X\delta_X} \quad (8)$$

In order to include the effects of anisotropy  $\eta$  in the model, Warner and Boettinger [6] follow the ideas put forth by [2, 4] and [24]:

$$\epsilon_\theta = \bar{\epsilon}\eta = \bar{\epsilon}(1 + \gamma \cos k\theta) \quad (9)$$

Where  $\theta$  is given by equation:

$$\tan\theta = \frac{\varphi_y}{\varphi_x} \quad (10)$$

$\varphi_x, \varphi_y$  : are the partial derivatives of  $\varphi$ .

$$\eta' = \frac{\partial \eta}{\partial \varphi} \quad (11)$$

$\gamma$ : The anisotropy

$k$ : The mode number

### 2.2. The concentration equation

$$\frac{Dc}{Dt} = \text{div} \left( D(\varphi) \left( \nabla c + \frac{V_m c(1-c)}{R} (H_B(\varphi, T) - H_A(\varphi, T)) \nabla \varphi \right) \right) \quad (12)$$

$D(\varphi)$  The inter diffusion coefficient

$$D(\varphi) = D_s + p(\varphi)(D_L - D_s) \quad (13)$$

$D_L, D_s$  The diffusivities in liquid and solid respectively

$$p(\varphi) = \varphi^3(10 - 15\varphi + 6\varphi^2) \quad (14)$$

$V_m$ : The specific volume

$R$ : The gas constant

### 2.3. The addition of excess energy term in the model

In the warren-Boettinger model [6], the Ni-Cu is an ideal solution, so the interaction parameter  $\lambda(\varphi) = 0$ , but in our prediction  $\lambda(\varphi)$  is associated with the excess energy of mixing solid and liquid [30, 31] and equal to:

$$\lambda(\varphi) = \lambda_s + p(\varphi)(\lambda_L - \lambda_s) \quad (15)$$

$\lambda_s, \lambda_L$  : The excess energy of mixing solid and liquid respectively.

$$\text{And, } \frac{\partial \lambda(\varphi)}{\partial \varphi} = p(\varphi)'(\lambda_L - \lambda_s) \quad (16)$$

$\lambda_S, \lambda_L$ : They are presented by the Redlich-Kister polynomial [30] in the thermodynamic assessment of the binary systems by CALPHAD methods. These energies are given by: [30, 31]

$$\lambda_S = \sum_{i=0}^n (a_i^S - b_i^S T)(1 - 2c)^i \quad (17)$$

$$\lambda_L = \sum_{i=0}^n (a_i^L - b_i^L T)(1 - 2c)^i \quad (18)$$

Where:  $(a_i^S, b_i^S), (a_i^L, b_i^L)$  are the interactions parameters between the atoms in solid and liquid respectively. These parameters can be taken directly from the development of the phase diagram using the CALPHAD method. If  $i = 0$  the solution is regular else the solution is real.

After replacing  $\lambda(\varphi)$  in the phase field development, we find the new free energies:

$$H_A^E(\varphi, T) = W_A g'(\varphi) + L_A p'(\varphi) \left(1 - \frac{T}{T_m}\right) + \frac{c^2}{T} \left[30g(\varphi)[(a_i^L - b_i^L T)(1 - 2c)^i - (a_i^S - b_i^S T)(1 - 2c)^i]\right] \quad (19)$$

$$H_B^E(\varphi, T) = W_B g'(\varphi) + L_B p'(\varphi) \left(1 - \frac{T}{T_m}\right) + \frac{(1-c)^2}{T} \left[30g(\varphi)[(a_i^L - b_i^L T)(1 - 2c)^i - (a_i^S - b_i^S T)(1 - 2c)^i]\right] \quad (20)$$

Finally the phase field and concentration equations for the real solution with the excess energy addition are:

$$\frac{1}{M_\varphi} \frac{D\varphi(x, t)}{Dt} = \bar{\epsilon}^2 \nabla \cdot (\eta^2 \nabla \varphi) - (1 - c) H_A^E(\varphi, T) - c H_B^E(\varphi, T) - \bar{\epsilon}^2 \frac{\partial}{\partial x} \left( \eta \eta' \frac{\partial \varphi}{\partial y} \right) + \bar{\epsilon}^2 \frac{\partial}{\partial y} \left( \eta \eta' \frac{\partial \varphi}{\partial x} \right) \quad (21)$$

$$\frac{Dc}{Dt} = \text{div} \left( D(\varphi) \left( \nabla c + \frac{V_m c (1 - c)}{R} (H_B^E(\varphi, T) - H_A^E(\varphi, T)) \nabla \varphi \right) \right) \quad (22)$$

### 3. Computer Program : Numerical simulation

We present physical simulation of the dendrite growth during the solidification of Ni-Cu alloy. To perform this

simulation, we consider the two dimensional isothermal anisotropic model of Warren and Boettinger [6] with the introduction of the excess energy in the model. As we know, in the phase field models, the interface thickness between the solid and liquid interfaces must be very small, this restriction requires a very dense mesh in the simulations of dendrite growth such that the mesh size should be sufficiently less than the interface thickness, otherwise the simulation of dendritic growth cannot be realized [7]. The model was solved with boundary conditions applied only at the edges of a computational box. Zero Neumann boundary conditions for  $c$  and  $\varphi$  were imposed at the boundaries. The phase field and concentration equations are solved on two dimensional uniform grids with the grid spacing  $\Delta x, \Delta y$  using finite difference approximations to the derivatives, the second order for space discretization and the first order centered difference formula for time discretization. The choice of the numerical method to solve the equation  $\varphi$  and  $c$  influences only over the time of resolution, not the results

For convenience, the governing equations (21) and (22) are transformed into dimensionless form. Length and time have been scaled with a reference length  $l = 0.94 \delta$  and the diffusion time  $\frac{l^2}{dl}$  respectively [6,7]. The dimensionless form of discretization is:

$$\frac{\varphi^{t+1} - \varphi^t}{\Delta t} = \epsilon_2 \left[ \eta^2 \overline{\Delta \varphi^t} - (1 - c^t) \frac{l^2 H_A^E}{\epsilon^2} - c^t \frac{l^2 H_B^E}{\epsilon^2} \right] + \epsilon_2 \eta \eta' \left[ \sin(2\theta) (\overline{\varphi_{yy}^t} - \overline{\varphi_{xx}^t}) + \overline{\varphi_{xy}^t} 2 \cos(2\theta) \right] - \frac{\epsilon_2}{2} (\eta'^2 + \eta \eta'') \left[ 2 \sin(2\theta) \overline{\varphi_{xy}^t} - \overline{\Delta \varphi^t} - \cos(2\theta) (\overline{\varphi_{yy}^t} - \overline{\varphi_{xx}^t}) \right] \quad (23)$$

$$\frac{c^{t+1} - c^t}{\Delta t} = \bar{d} \overline{\Delta c^t} + \bar{d} c^t (1 - c^t) \left( \frac{V_m}{R} H_b^E - \frac{V_m}{R} H_a^E \right) \overline{\Delta \varphi^t} + \left[ \bar{d} p + \bar{d} (1 - 2c^t) \left( \frac{V_m}{R} H_b^E - \frac{V_m}{R} H_a^E \right) \right] \overline{\Delta \varphi^t \Delta c^t} + c^t (1 - c^t) \left[ \bar{d} p \left( \frac{V_m}{R} H_b^E - \frac{V_m}{R} H_a^E \right) + \bar{d} \left( \frac{V_m}{R} H_b^E p - \frac{V_m}{R} H_a^E p \right) \right] \overline{\Delta \varphi^t \Delta \varphi^t} \quad (24)$$

$$dl = D_l [m^2/s] \quad (25)$$

$$\epsilon_2 = \frac{M_\varphi \bar{\epsilon}^2}{dl} \quad (26)$$

$$l = 0.94 \delta [m] \quad (27)$$

$$\overline{\Delta x} = \frac{\Delta x}{l} \quad (28)$$

$$\overline{\Delta t} = \frac{\Delta t dl}{l^2} \quad (29)$$

$$\bar{d} = \frac{d}{dl} \quad (30)$$

$$\frac{dp}{d\varphi} = \frac{dl}{d\varphi} \quad (31)$$

$$dp = \frac{\partial p}{\partial \varphi} \quad (32)$$

$$H_b^E p = \frac{dH_b^E p}{d\varphi} \quad (33)$$

$$H_a^E p = \frac{dH_a^E p}{d\varphi} \quad (34)$$

#### 4. Results and Discussion

We have developed a computer program to simulate the progress of dendritic growth using the finite difference method for solving the governing differential equations system (phase field and concentration). The simulation conditions of dendrite solidification process have a significant effect on the simulated microstructure. In this simulation, the calculation of the solidification progress is carried out using a square box size of  $35 \mu\text{m}$  with grid point numbers  $750 \times 750$ . The initial condition was a small square area of solid  $\varphi = 0$  in the center of a liquid  $\varphi = 1$  with the concentration everywhere equals  $c_0$ . We have used the physical data of Ni-Cu real solution (see table1) where the alloy containing  $c_0 = 0.408$  atomic fraction of Cu in Ni and  $T=1574 \text{ K}$ . For this temperature, the equilibrium concentration is in the liquid  $c_l = 0.4668$  and in the solid  $c_s = 0.3994$ . Therefore, the initial super-saturation of liquid was  $\Delta = 0.86$ . For the interaction parameters, they are calculated by Miettinen [31], where the excess enthalpies of solid and liquid phases are developed to the first order ( $a_0^S = 8366, b_0^S = 2.802, a_0^L = 11760, b_0^L = 1.084, a_1^S = -4360, b_1^S = 1.812, a_1^L = -1670, b_1^L = 0$ ) in the thermodynamic assessment of (Ni-Cu-Sn) system by CALPHAD method and Redlich-Kister model.

**Table1.** Physical data of Cu and Ni elements [10].

Propriety	Unit	Nickel	Cooper
Melting temperature ( $T_m$ )	$K$	1728	1358
Latent heat ( $L$ )	$J/m^3$	$2350.10^6$	$1758.10^6$
Diff. coef. liquid ( $D_l$ )	$m^2/s$	$10^{-9}$	$10^{-9}$
Diff. coef. solid ( $D_s$ )	$m^2/s$	$10^{-13}$	$10^{-13}$
Linear kinetic coefficient ( $\beta$ )	$m/K/s$	$3.3 \cdot 10^{-3}$	$3.9 \cdot 10^{-3}$
Interface thickness ( $\delta$ )	$m$	$8.48 \cdot 10^{-8}$	$6.01 \cdot 10^{-8}$
Surface energy ( $\sigma$ )	$J/m^2$	0.37	0.29
Molar volume ( $V_m$ )	$m^3$	$7.46 \cdot 10^{-6}$	$7.46 \cdot 10^{-6}$
Mode Number ( $k$ )		4	4
Anisotropy ( $\gamma$ )		0.04	0.04

#### 5. Results

The figures (1.a, 1.b, 1.c and 1.d) show the microstructure development for the case of Ni-Cu real solution where the excess energy is well-considered. The figure (1.a) presents the initial solid seed where ( $\varphi = 0$ ). The figures (1.b, 1.c, and 1.d) show that the value of the phase field parameter  $\varphi$  decreases from 1 to 0; this means a variation in the solid concentration, therefore, the initial seed grows. On the other hand, we see the appearance of primary branches of the dendrite and also the creation of second branches between the primary ones. In the figure (1.d) we remark an overlap of the primary and second branches. Figure (1.e) presents the variation of  $\varphi$  in function of time ( $t$ ), as can be seen, the variation of the order parameter  $\varphi$  is almost linear, where it decreases rapidly until zero, which represents the time of dendritic formation and,  $\Delta t = 1.11$  represent the time of formation.

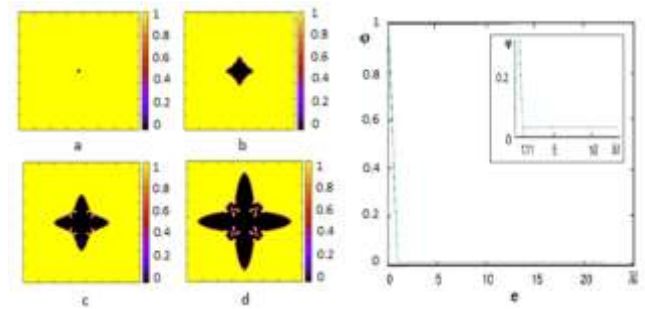


**Fig.1** Dendritic growth with excess energy at different time t (a, b, c, and d:  $\varphi$  distribution, e:  $\varphi$  variation).

The figures (2.a, 2.b, 2.c and 2.d) show the concentration distribution at different time ( $t$ ). The figure (2.a) presents the initial solution containing  $c_0 = 0.408$  atomic fraction of Cu in Cu-Ni alloy. The figure (2.e) shows that the value of the concentration of Cu element in the area of the dendrite changes in the range  $[0.39, 0.47]$ , the concentration of Cu increases from 0.408 to 0.425 almost linearly, then it decreases from 0.425 to 0.408 with a slope shape. The increases phase corresponds to the formation of the dendrite shape, and the decreases phase presents the rejecting of Cu element. In the previous pictures, we remark the creation of a thin film rich in Ni around the shape of the dendrite, due to the absorption of Cu element by the dendrite from the interface liquid-solid. According to figures (2.e), the variation of  $c$  proves also the

complete formation of the dendrite at  $\bar{\Delta}t = 1.11$  as can be seen in figure (1.c).

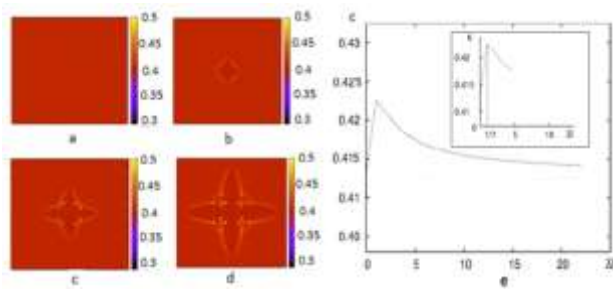


**Fig. 2** Dendritic growth with excess energy at different time t (a, b, c, and d: concentration distribution, e: concentration variation).

Figure 3 shows the phase field distribution of the dendritic growth simulation, using the Warren-Boettinger model [6] by Adrian et al. Ref [9], where they have treated the effect of the noise term in figure 3.a and 3.b. Also, figure 3.c shows the phase field distribution where we have added the effect of excess energy.

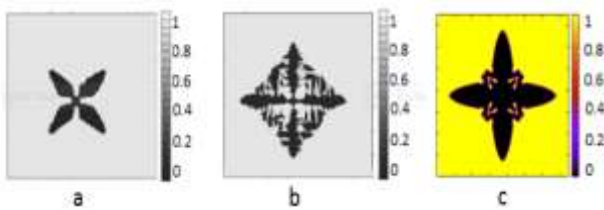


**Fig. 3** The results of simulation of dendritic growth of  $\phi$  distribution (a: without noise term [9], b: with noise term [9], c: our work without noise).

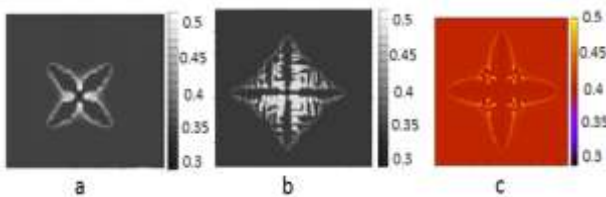


**Fig.4** The results of simulation of dendritic growth of c distribution (a: without noise term [9], b: with noise term [9], c: our work without noise).

The calculation of dendrite growth with neglecting the noise term and the effect of excess energy gives the dendrite a shape of a four simple clover leaves (see figure 3.a). The introduction of the excess energy factor to the phase field and concentration equations changes the dendrite form. Numerical calculations show that the introduction of the excess energy in the model of Warren

and Boettinger [6] produce the second branch without the addition of the noise term and also a secondary branches grow between the axis of principals branches (see figure 3.c).

The comparison between our results and the results of Adrian et al. Ref. [9] shows clearly a difference between the Ni-Cu ideal solution and Ni-Cu real solution growth behavior. This latter drives us to conclude that the effect of the introduction of the excess energy gives to the dendrite a second branches between the principal ones, even if there is no noise term.

In the modeling of Ni-Cu ideal solution, the dendrite shape does not change after the formation of the principal branches. But in the modeling of dendritic growth of Ni-Cu real solution, we see the formation of the second branches between the principal ones, then an overlap of the primary and second branches.

### 6. Conclusions

- The model of Warner and Boettinger is limited to modeling the ideal solution, but the changes we have made to this model has improved it to model the dendritic growth whatever the nature of its solution.
- the development of Warner and Boettinger model by adding the excess energy, gives us an attempt to find out the effect of this energy in dendritic growth
- We have not studied the noise effect with the excess energy effect at the same time, because the two effects produce side branches so we can't distinguish the difference between them.
- The simulation of the simple case of dendritic growth (neglecting excess energy and the noise term) presents a simple leaves has four branches but:
  - The addition of excess energy produces inter-branches which grow between the principal branches with an angle of  $45^\circ$ .
  - The addition of the noise produces branches perpendicular to the principal branches.

So the difference between the two previous additions can be a subject of discussion to future research.

**References**

- [1] Steinbach, *Modeling and Simulation in Materials Science and Engineering*, B17 (2009) 073001.
- [2] R. Kobayashi, *Physica D*, B63(1993)410-423.
- [3] Z.Bi, R.F.Sekarka, *Physica A*, B26(1998) 95-106.
- [4] G.B. McFadden, A.A.Wheeler, R.J. Braun, S.R. Coriell, and R.F.Sekerka, *Phys. Rev.* B48 (1993)20-16.
- [5] S.-L Wang, *Physica D*, B69(1993) 189.
- [6] J.A. Warren, and W.J. Boettinger. *Acta metall. Mater.*, B43 (1995) 689-703.
- [7] I.Longinova,G.Amberg, J.Agren, *ActaMetallurgica et Materialia*, B49 (2001) 573-581.
- [8] W.J.Boettinger, J.A.Warren,C. Beckermann, C.A.Karma, *Annu. Rev. Mater. Res.*, B 32 (2002)163-94
- [9] H. Adrian, and K. Spiradek-Hahn, *Archives of Materials Science and Engineering*, B40 (2009) 89-93.
- [10] A. Rasheed, *Solidification dendritique de mélanges binaires de métaux sous l'action de champs magnétiques: modélisation, analyse mathématique et numérique*. Institut de Recherche Mathématique de Rennes. (2010).
- [11] N.Moelans, B.Blanpain, *Computer Coupling of Phase Diagrams and Thermochemistry*, B32 (2008)268-294.
- [12] H.L. Lukas, S.G. Fries,B. Sundman, *Computational Thermodynamics, the Calphad Method*, Cambridge University Press.(2007).
- [13] B.Kaouil, M.Noureddine, R.Nassif, Y.Boughaleb, M. J. *Condensed Matter*, B6(2005) 109-112.
- [14] J.C. Ramizer; C.Beckermann, A .Kerma, H.J. Diepers, *Physical Review E*, B 69 (2004)(051607-1)-(051607-16).
- [15] J.C.Ramizer, C.Beckermann, *ActaMaterialia*, B 53 (2005)1721-1736.
- [16] J.C.Ramizer, C.Beckermann, A.Kerma, H.J.Diepers, *Physical Review E*, B69(2004) 1-16.
- [17] J.C. Ramizer, and C. Beckermann, *ActaMaterialia*, B53(2005)1721-1736.
- [18] U.Grafe, B.Bottger, J.Tiaden. *Scripta Mater.* B42 (2000)11-79.
- [19] U.Grafe, B.Bottger, J.Tiaden. *Modell. Simul. Mater. Sci. Engng.* B8(2000)71.
- [20] H.Kobayashi, M.Ode, S.G.Kim. *Scripta Mater*, B48 (2003)689.
- [21] U.Hecht, L.Granasy, T.Pustzai. *Mater. Sci. Engng.* B46(2004) 1.
- [22] A. Jacot, M. Rappaz. *Acta Mater*, B50(2002) 1909.
- [23] R.S.Qin, E.R.Wallach, R.C.Thomson. *J.Cryst. Growth*, B27 (2005)163.
- [24] A.A.Wheeler, B.T.Murray, R.J.Schaefer. *Physica D*, B66 (1993) 243.
- [25] B.Bottger, J.Eiken, I.Steinbach. *Acta Mater*, B54 (2006) 26-97.
- [26] I. Steinbach, B.Bottger, J.Eiken. *J. Phase Equilibrium Diffusion*, B 28 (2007)101.
- [27] N. Provatas, K. Edler, *Phase field methods in material science and engineering*, Wiley-VCH Verlag GmbH & Co. KGaA, (2010)
- [28] Long-Qing Chen, *Annual Review of Materials Research*, B 32(2002) 113-140.
- [29] M. Plapp, A. Karma, *Phys. Rev. E.* B 63, (2001)031504
- [30] O.Redlich, A.T.Kister. *Indust.Eng. Chem.* B40 (1945) 345.
- [31] J.Miettinen. *Computer coupling diagrams and thermochemistry*, B27 (2003) 309-318.

## Recovery of nickel and copper from metal finishing hydroxide sludge by kinetic acid leaching

R. Salhi<sup>\*1</sup>; M. Boudjouada<sup>1</sup>; S. Messikh<sup>1</sup> and N. Gherraf<sup>2</sup>

*Department of Chemistry, Faculty of Exact Sciences, University of Constantine 1, ALGERIA*

*<sup>2</sup>Laboratoire des Ressources Naturelles et Aménagement des milieux sensibles, Larbi ben M'hidi university, Oum Elbouaghi, 04000, Algeria*

*Corresponding author: email: salhiram@yahoo.fr*

Received date: June 06, 2016; revised date: December 03, 2016; accepted date: December 11, 2016

---

### **Abstract:**

*The aim of the present work was the recovery of nickel and copper from metal finishing hydroxide sludge by kinetic acid leaching. The study was divided into two main parts: First, a kinetic model of precipitate leaching with the presence of acid was developed and subjected to theoretical approach so as to determine optimal leaching conditions (pH and time). Next, the study was conducted experimentally on pure metals hydroxides and then on electroplating sludges. The leaching operation was performed at atmospheric pressure with constant stirring. pH and solubility versus time at different temperature values and different amounts of sludge were carried out. The resulting filtrate was found to contain more than 99% of nickel and copper.*

**Keywords:** Acid leaching, Copper, Nickel, Electroplating sludge, Metal recovery

---

### **Introduction**

The electroplating waste waters are generally detoxified (oxidation of cyanide and reduction of chromium) and then neutralized to precipitate metal hydroxides [1-3]. In the present work, the electroplating sludges are subjected to precipitation so as to get rid of hazardous metals. Many studies reported that the sludges may present a great danger to the environment. The economic considerations are also worth considering because of the appreciable loss of metals. Since the eighties, the environment protection, the waste minimization and the metals recovery became a social and political issue in the U.S.A.[4-7] where the volume of sludges is so important owing to the large electroplating industries. To combat this problem some solutions can be convenient to be implemented such as:

➤ The clean technologies (membranes processes): The rinsing wastewaters are directly treated by electrodialysis, ultrafiltration, and solvent extraction. The metals are concentrated and reused in the electrodeposition bath. The water is also recycled. [8-20]. However some economic, technical and psychological considerations hindered a rapid progress of this approach.

➤ The metal recovery from electroplating sludges: This solution is extremely necessary to treat, at least, the existing sludges. The American government through the EPA encouraged this solution and research projects were supported.

The economical recovery of metals with a sufficient purity is quite intricate and needs a big effort and hard research based on two main aspects:

- First, it is necessary to develop simple and economical analysis methods to define the sludges composition. The simultaneous precipitation of many metals is always accompanied by secondary processes such as: co-precipitation, occlusion adsorption etc. The precipitate aging is also a problem.

- Secondly it is required to choose of a qualitative method of selective dissolution (acidic, ammoniacal, etc) depending on the sludge composition and the leaching agent (recyclable or not) . This step needs a deep knowledge of chemical equilibrium, the mutual influences (E-pH), solubility complex, etc). [21-39]

## Theory

### Kinetic and Thermodynamic Theory of Acid -

#### Basic Leaching

#### Kinetic Aspect

The leaching of industrial waste is generally nonreactive. The reactions are most often carried out at high temperature or pressure and administered by heterogeneous kinetic characteristics. In most cases, the rate of the overall reaction is characterized by diffusion of reactant and is therefore proportional to its concentration. Furthermore the overall rate increases with stirring owing to the slow diffusion in the electrolyte. In some cases, the overall dissolution rate may be affected by the transfer of the charged particles making up the initial crystal through a solid-electrolyte interface [40].

The most extensive study performed up to date on the leaching behavior of metal hydroxides and metal sulfide sludge may be the study reported by Hohman who developed a kinetic model of precipitate leaching [41]. The leaching process was based upon an area-dependent mass transfer controlled process. The driving force for the leaching process was assumed to be proportional to the difference between the concentration of metal in solution (C) and the saturation concentration (C<sub>s</sub>) predicted from precipitate equilibria consideration. The basic differential equation describing the leaching process is as follows [48, 49]:

$$\frac{dc}{dt} = K.A(C_s - C) \quad (1)$$

Where:

C<sub>s</sub>: saturation concentration of metal (moles/L)

C: metal concentration in solution at time t (moles/L)

A: area available for mass transfer, (cm<sup>2</sup>)

K: mass transfer coefficient (cm<sup>2</sup>.min<sup>-1</sup>)

t: leaching time (min).

and the fraction leached (α) of dissolved sludge depends on:

r: initial radius of precipitate particle (cm).

K<sub>sp</sub>: metal hydroxide solubility product (moles<sup>n</sup>/L<sup>n</sup>).

WT: total weight of precipitate (g).

ρ: molar density of the precipitate particles (moles/cm<sup>3</sup>).

ρ<sub>s</sub>: mass density of the precipitate (g/cm<sup>3</sup>).

V<sub>s</sub>: volume of solution (L).

For large particles (1mm < r < 1cm) the change in particle size influences the leaching behavior. The slow concentration rise indicates that the surface area

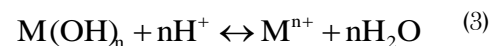
decreases quickly, causing a rapid dropping in effective mass transfer coefficient. For small particles (1μm < r < 10μm), the driving force dominates, causing a rapid rise in the heavy metal concentration until saturation. Intermediate radius values show a balance of both effects.

In the case of small molecules, it is considered that the specific surface area is constant, so the integrated equation (1) becomes:

$$\int_{C_0}^C \frac{dc}{C_s - C} = KA \int_0^t dt \Rightarrow \frac{C_s - C_0}{C_s - C} = e^{KA t} \quad (2)$$

C<sub>0</sub>: the initial consumable concentration of metal. (C<sub>0</sub>=0)

and the leaching reaction is:



So leaching concentration (mole/L) of M<sup>n+</sup> requires (nC mole/L) of H<sup>+</sup>:

The consumable concentration of H<sup>+</sup> is:

$$[H^+]_c = n(C - C_0) \quad (4)$$

The remaining amount of H<sup>+</sup> in the solution at the time t is:

$$[H^+]_c = [H^+]_0 - n(C - C_0) \quad (5)$$

If C<sub>0</sub>=0

$$C = \frac{[H^+]_0 - [H^+]}{n} \quad (6)$$

and

$$C = C_s(1 - e^{-KA t}) \quad (7)$$

This relationship is represented in Fig. 1. a.

where we note that when:

$$t \rightarrow \infty$$

$$C = C_s$$

to find the variation of pH with respect to time we replaced C of the equation (6) in the equation (7) we get:

$$[H^+]_c = [H^+]_0 - nC_s(1 - e^{-KA t}) \quad (8)$$

The concentration of the saturated solution is:

$$K_{sp} = [M^{n+}][OH^-] \Rightarrow C_s = [M^{n+}] = \frac{K_{sp}}{K_w^n} [H^+]^n \quad (9)$$

We replaced C<sub>s</sub> of the equation (9) in the Equation (8)

we got:

$$[H^+] = [H^+]_0 - n \frac{K_{sp}}{K_w^n} [H^+]^n (1 - e^{-kAt}) \quad (10)$$

$$pH = -\log\left([H^+]_0 - n \frac{K_{sp}}{K_w^n} [H^+]^n (1 - e^{-kAt})\right) \quad (11)$$

This relationship is shown in Fig. 1. b.

Where we note that when:

$$t \rightarrow \infty$$

$$pH \rightarrow pH_s = -\log\left([H^+]_0 - n \frac{K_{sp}}{K_w^n} [H^+]_s^n\right) \quad (12)$$

Where:

pH<sub>s</sub>, [H]<sub>s</sub>: pH and [H] concentration of saturation concentration of metal (moles/L)

we replaced n=2 in equation (10) we get:

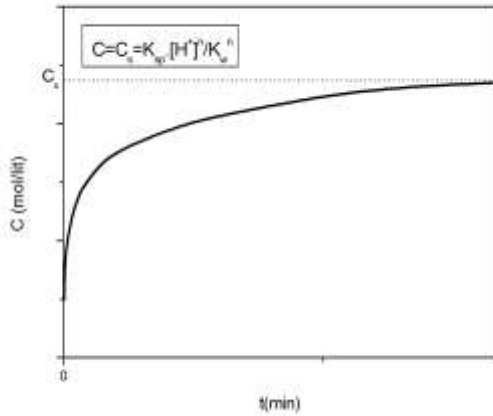
$$2 \frac{K_{sp}}{K_w^2} [H^+]_s^2 + [H^+]_s - [H^+]_0 = 0 \quad (13)$$

$$[H^+]_s = \frac{1 + \sqrt{1 + 8 \frac{K_{sp}}{K_w^2} [H^+]_0}}{4 \frac{K_{sp}}{K_w^2}} \quad (14)$$

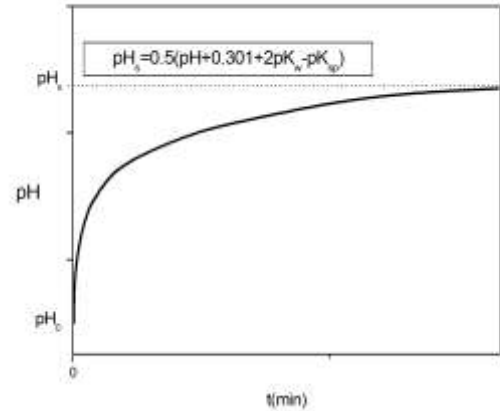
$$pH_s = -\log\left(\frac{1 + \sqrt{1 + 8 \frac{K_{sp}}{K_w^2} [H^+]_0}}{4 \frac{K_{sp}}{K_w^2}}\right) \quad (15)$$

$$pH_s \approx -\frac{1}{2} \log\left(\frac{[H^+]_0}{4 \frac{K_{sp}}{K_w^2}}\right) \quad (16)$$

$$pH_s \approx \frac{1}{2} (0.301 + pH_0 + 2pK_w - pK_{sp}) \quad (17)$$



a- The variation of the concentration of dissolved ion



b- pH variation

Fig. 1: Qualitative hydroxides leaching curves

If the specific surface area A is known, the constant K can be determined by the following relationship:

$$\ln(C_s - C) = \ln(C_s - C_0) - KA t \quad (18)$$

If we plot the curve  $\ln(C_s - C) = f(t)$ , we can determine the constant KA from the tangent to the curve.

From this theoretical approach, we conclude that to dissolve 1 mg of hydroxide containing N mole of hydroxyle [OH], we need N mole of [H] ions. If using 1 liter of acid solution with a concentration ([H]<sub>0</sub>) we obtain a saturated solution with a concentration: Cs = N/n (mol/L), and with a pH equal to:

$$pH_s \approx \frac{1}{2} (0.301 + pH_0 + 2pK_w - pK_{sp}) \quad (17)$$

The speed of leaching increases with the increase of the amount of [H].

**Thermodynamic Aspect**

Most dissolution reactions occur in strong acid medium such as (HCl, HNO<sub>3</sub>, H<sub>2</sub>SO<sub>4</sub>) depending on the type and composition of the material to be dissolved. These reactions are applied to metals oxides, mining and industrial wastes. In Lewis acids and bases the ion in the mineral compound is displaced by the proton in the acidic medium and fixes the O<sup>2-</sup> or OH<sup>-</sup> to give dissolved

**Experimental**

The solubility of nickel and copper was experimentally studied using:

- 1- Analytical Ni(OH)<sub>2</sub> , Cu(OH)<sub>2</sub> , (CuO) were purchased from Aldrich
- 2- Sludges (mixture of Ni(OH)<sub>2</sub> , Cu(OH)<sub>2</sub> , Fe(OH)<sub>3</sub> and Cr(OH)<sub>3</sub>) were prepared by precipitation from respective solutions of NiSO<sub>4</sub>, CuSO<sub>4</sub> with NaOH before being washed with distilled water and dried at 40C. The electroplating sludges were originated from the industrial area of 'El alma', in ALGERIA, where a galvanization plant had previously operated. These sludges are classified as F006 by the EPA [7].

**Kinetic Aspect**

**Solubility Experiments for Pure Hydroxides and Electroplating Sludges**

**Kinetic Leaching Behavior of Metal Hydroxides:**

A mass m (in g) of Ni(OH)<sub>2</sub> , Cu(OH)<sub>2</sub> and electroplating sludges respectively, was put into a 50 mL using a screw-

complex in the basic medium, as shown in the solubility curves represented in Fig. 2.

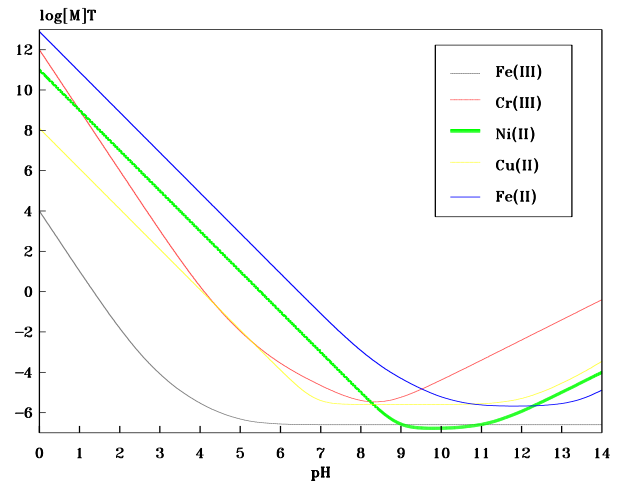


Fig. 2: The variation of the hydroxides solubility with pH

**Table 1 : Compositions of four electroplating sludges, g kg<sup>-1</sup>**

Metal	Sludge number			
	1	2	3	4
Ni	139.8	134.3	124.2	85.9
Fe	67.4	98.4	55.6	50.3
Cu	39.9	11.25	32.6	14
Cr	0.72	0.083	0.39	0.028

The compositions of four hydroxide sludges are shown in Table 1 and purities of the dried hydroxides were higher than 99%. The sludges and hydroxides were dissolved in sulfuric acid and after filtration. The metal concentrations in the filtrate were determined by atomic absorption spectroscopy.

cap glass bottle with known initial conditions (temperature, pH, specific conductivity), The bottle was shaken continuously, and the pH and specific conductivity were measured as function of time. At different times, small volumes (1 mL) of solution were taken and filtered

immediately. The metal concentrations in the filtrate were measured by atomic absorption spectroscopy.

**Thermodynamic Aspect**

different amounts of Ni(OH)<sub>2</sub>, Cu(OH)<sub>2</sub> and electroplating sludges were put into a 50 mL screw cap glass bottle to which 25 mL of a solution ranging from 1 to 0.01 mol/L of acidic solution was subsequently added. The pH of the bottled solutions was adjusted by adding a

predetermined amount of NaOH, H<sub>2</sub>SO<sub>4</sub> and H<sub>2</sub>O, in such a way that the volume in the bottle was not substantially changed. The bottles were shaken for 8 h at 25°C, after which the pH was measured and the solution was filtered immediately. The metal concentrations in the filtrate were measured by atomic absorption spectroscopy.

**Dissolution Kinetics**

**A- Effect of Temperature on the Dissolution Rates:**

Figure 3 illustrates the difference between the leaching process when the initial pH is 0.5, 1 and 1.5, Figs. 4, 5.

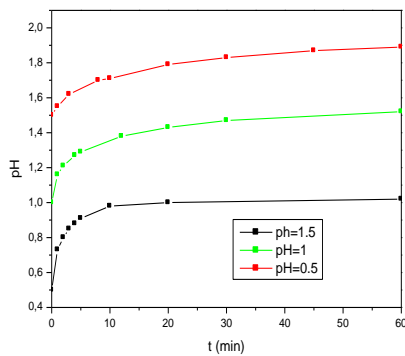


Fig. 3: The difference between the leaching of hydroxidesludge when the initial pH is 0.5, 1 and 1.5.

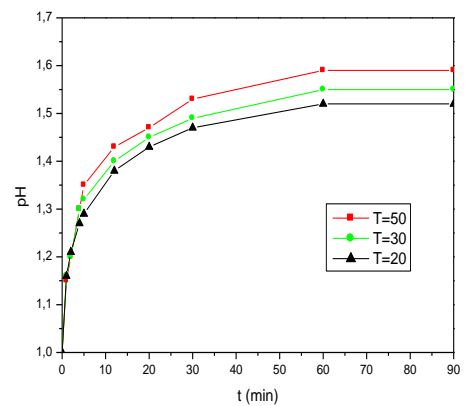


Fig. 5: The temperature effect on leaching of hydroxide sludge when the initial pH is 1

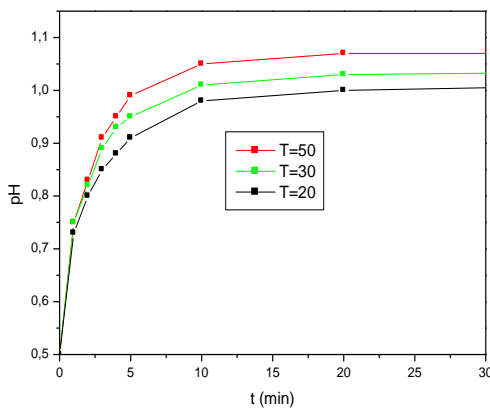


Fig. 4: The temperature effect on leaching of hydroxide sludge when the initial pH is 0.5

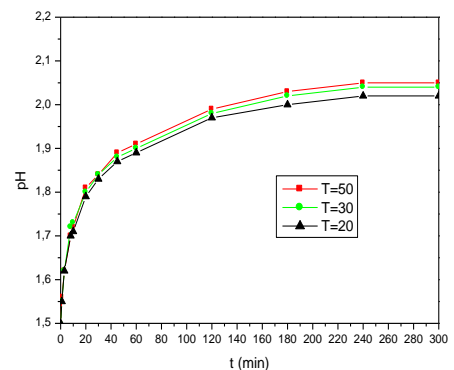


Fig. 6: The temperature effect on leaching of Hydroxide sludge when the initial pH is 1.5

**B- Effect of the Mass of Sludge on the Dissolution Rates**

Under the same conditions of initial leaching, pH, temperature and volume are kept constant; only the mass of sludge is varied. The impact of the increase in the sludge mass is highlighted by the increase of the

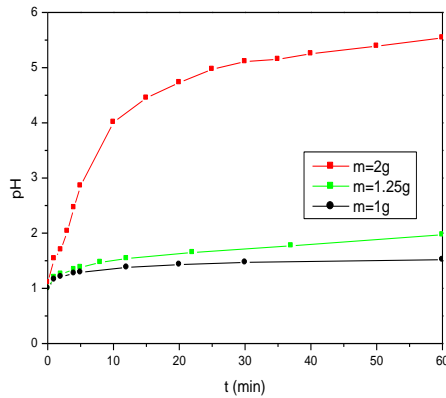


Fig. 7: The mass of hydroxide sludge effect on leaching of hydroxide sludge when the initial pH is 1

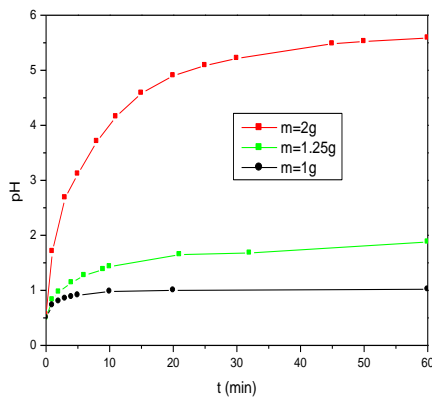


Fig. 8: The mass of hydroxide sludge effect on leaching of hydroxide sludge when the initial pH is 0.5

**Results and Discussion**

According to the dissolution kinetic curves of the hydroxides, the dissolution starts when the pH is less than the values specified in theory and in particular for the trivalent hydroxides such as  $(Cr(OH)_3, Fe(OH)_3)$ .

consumption of the acid, and then leading to an increase in pH value which in role leads to a precipitate of trivalent cations such as iron and chromium. Then the pH leveled up at about 6 for the remaining time. Figs. 7. 8. show the mass of hydroxide sludge effect to the starting pH value.

These two hydroxides begin to dissolve in theory at pH of 3.35 and 7.3 respectively. However in practice their dissolution is very slow and does not even begin at pH = 0.5 as shown in tables 2 and 3. For other hydroxides, such as  $(CuO, Ni(OH)_2)$ , the dissolution starts quickly, even at pH of 1.5.

**Table 2 : the dissolution kinetics of Iron (III) hydroxide at t=0; (v=70ml, [HCl]=20mmol,  $pH_0=0.5$ ) + 0.25g  $Fe(OH)_3$**

Time (min)	0	4	21	30	40	2 days
pH	0.50	0.49	0.50	0.51	0.52	0.50
Conductivity $\cdot 10^3 (\Omega^{-1} cm^{-1})$	69.8	69.5	69.96	69.7	69.6	69.95

**Table 3: the dissolution kinetics of chromium (III) hydroxide At t=0;**

$(v=70ml, [HCl]=20mmol, pH_0=0.5) + 0.25g Cr(OH)_3$

Time (min)	0	14	15	18	43	2 days
pH	0.50	0.49	0.5	0.51	0.52	0.51
Conductivity $\cdot 10^3 (\Omega^{-1} cm^{-1})$	69.98	69.55	69.96	69.7	69.9	50.70

The copper oxide dissolution rate is greater than that of nickel hydroxide although  $CuO$  is more soluble than  $Ni(OH)_2$  : as shown in Fig. 9 and 10, ( $pK_{S_{Ni(OH)_2}} = 17$ ,  $pK_{S_{CuO}} = 19.9$ ) and the basicity of  $CuO$  is low compared to that of nickel ( $pK_{a_{(Ni^{2+}/Ni(OH)_2)}} = 8.9$ ;  $pK_{a_{(Cu^{2+}/CuO)}} = 6.85$ ). This difference relies on the structures of these hydroxides. In fact the structure of the nickel hydroxide is crystalline whereas that of copper is colloidal. The same behavior was observed in the leaching of the

mixture of two hydroxides ( $\text{CuO}$ ,  $\text{Ni(OH)}_2$ ) and three hydroxides ( $\text{Fe(OH)}_3$ ,  $\text{CuO}$ ,  $\text{Ni(OH)}_2$ ) as shown in fig. 11 and 12, as well as the hydroxide sludge as shown in fig 13,14,15, 16 and 17, where a higher leaching copper rate was recorded compared to that of nickel even if the amount of nickel in these samples ranged from 4 to 6 times the amount of copper.

On the contrary the iron hydroxide (III) does not begin to dissolve even at  $\text{pH} = 0.5$ . The lixiviation solutions of industrial sludge at  $\text{pH}=1.5$  contain iron ions, which confirm that the sludge contains iron other than  $\text{Fe(OH)}_3$ .

At  $\text{pH} = 0.0$  the leaching of all metal components of hydroxide sludge is complete. Copper and Nickel can be separated from iron and chromium starting from initial  $\text{pH}$  of 1 over a period of 90 minutes and leveling up at  $\text{pH}$  of 1.6 where almost 100% of copper and more than 70% of Nickel were dissolved, whereas the iron dissolution does not exceed 30% over that period. The separation may take place from initial  $\text{pH}$  of 0.5 over a period of 25 minutes and leveling up at 1 where 70-80% of copper and 60-70% of nickel were dissolved, however iron is dissolved only within 20-50%.

The separation may also occur by leaching from initial  $\text{pH}$  of 1.5, but over a longer period of about 240 minutes where  $\text{pH}$  levels up at 2. Under these conditions 100% of copper and 95% of nickel were dissolved while iron does not exceed 19%.

Based on the previous results we suggest the following procedure for copper and nickel dissolution from hydroxide sludge as seen in figure 18.

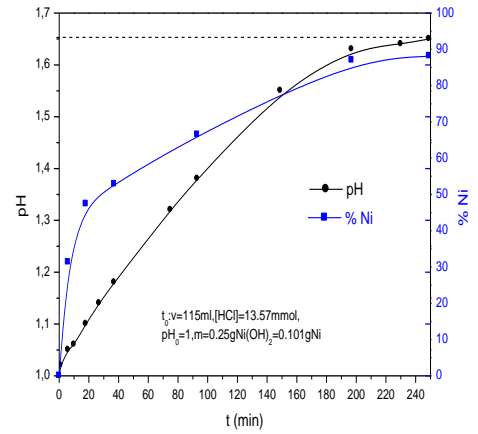


Fig 9: The variation of pH and the concentration of dissolved nickel ion from nickel hydroxide ( $\text{Ni(OH)}_2$ )

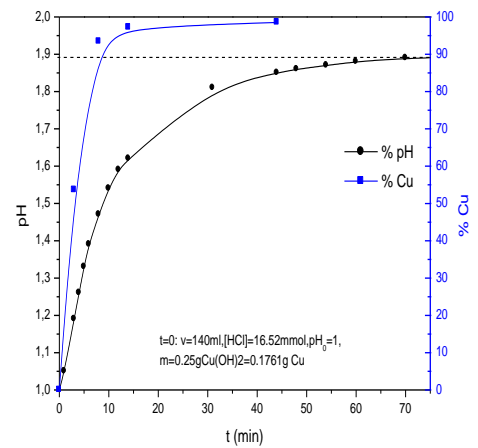


Fig 10: The variation of pH and the concentration of dissolved copper ion from copper hydroxide ( $\text{Cu(OH)}_2$ )

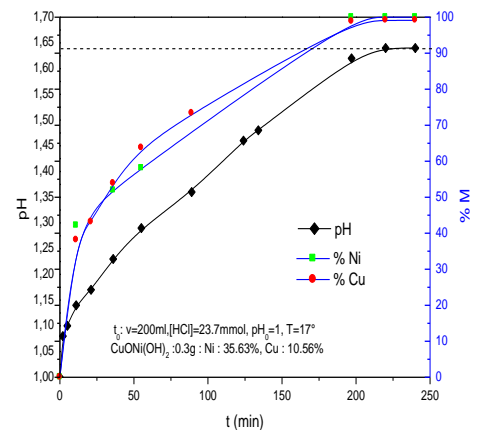


Fig 11: The variation of pH and the concentration of dissolved copper and nickel ion from mixture of hydroxides ( $\text{CuONi(OH)}_2$ )

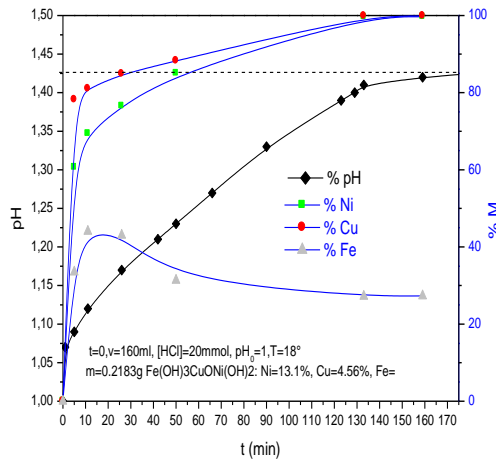


Fig 12: The variation of pH and the concentration of dissolved copper, iron and nickel ion from mixture of hydroxides  $Fe(OH)_3CuONi(OH)_2$

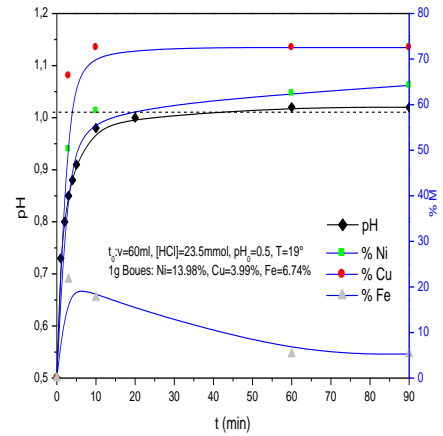


Fig 15: The variation of pH and the concentration of dissolved copper, iron and nickel ion from hydroxide sludge at pH0.5 (m=1g, v=60ml)

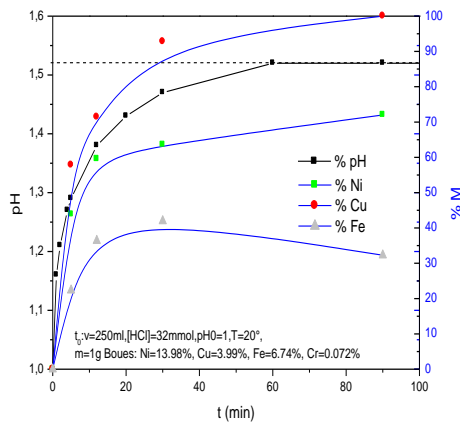


Fig 13: The variation of pH and the concentration of dissolved copper, iron and nickel ion from hydroxide sludge at pH1 (m=1g, v=250ml)

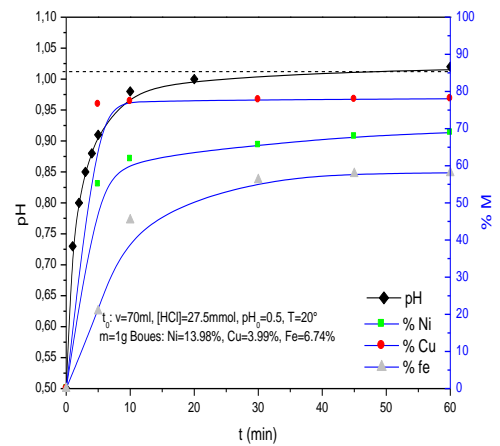


Fig 16: The variation of pH and the concentration of dissolved copper, iron and nickel ion from hydroxide sludge at pH0.5 (m=1g, v=70ml)

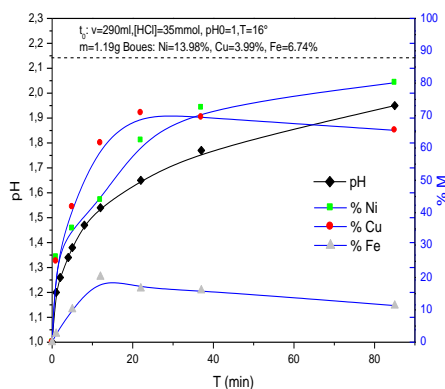


Fig 14: The variation of pH and the concentration of dissolved copper, iron and nickel ion from hydroxide sludge at pH1 (m=1.19g, v=290ml)

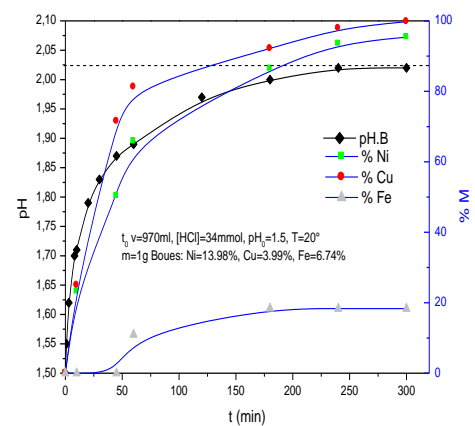


Fig 17: The variation of pH and the concentration of dissolved copper, iron and nickel ion from hydroxide sludge at pH =1.5 (m=1g, v=250ml)

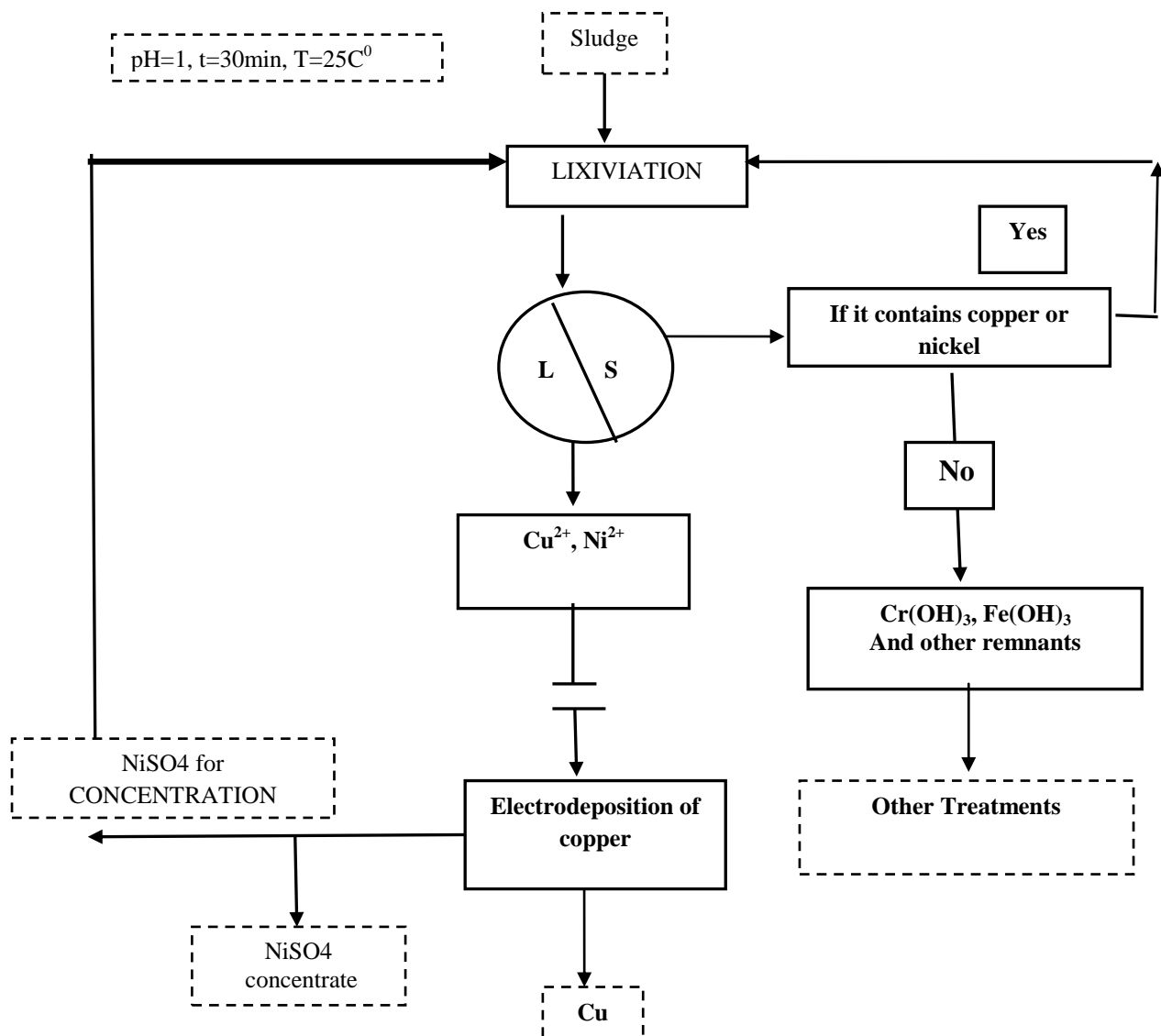


Fig 18: the various stages of the process of separation of Cu and Ni

## REFERENCES

- [1] W. Canning, "The Canning Handbook: Surface Finishing Technology, 23rd Ed., Hardcover - CBS Publishers & Distributors New Delhi (India), (2005)
- [2] Ng, W.J., Industrial wastewater treatment, London. Imperial College Press. (2006).
- [3] F. R. Spellman, Handbook of Water and Wastewater Treatment Plant Operations, Third Edition, CRC Press, Boca Raton (2014)
- [4] L.Wang, D.C.W.Tsang, C.S. Poon, *Chemosphere*, 122 (2015) 257-264
- [5] I. Mantis, D. Voutsas, C. Samara, *Ecotoxicology and Environmental Safety*, 62(3) (2005) 397-407
- [6] Z. He, T. Liao, Y. Liu, Y. Xiao, T. Li, H. Wang, *Journal of Central South University*, 19(12) (2012) 3540-3545
- [7] M. Kharub, A. Rajor, S.K. Mittal. *Journal of Biotechnology*, 11(40) (2012) 9612-9618
- [8] J. Hu, G. Chen, M.C. Irene, *Water Research*, 39(18) (2005) 4528-4536

- [9] M. Al-Shannag, Z. Al-Qodah, K. Bani-Melhem, M. R. Qtaishat, M. Alkasrawi, *Chemical Engineering Journal*, 260 (2015)749-756
- [10] M. Revathi, M. Saravanan, C.A. Basha, M. Velan *CLEAN - Soil, Air, Water*, 40(1) (2012) 66-79
- [11] C. Gábor K. Tamás, I.T. Tamás, *Hydrometallurgy*, 77(1-2) (2005) 19-28
- [12] W. Shijie, *JOM*, 60(10) (2008) 41-45
- [13] F. Fenglian, W. Qi, a Review, *Journal of Environmental Management*, 92(3) (2011) 407-418
- [14] C.A.M. Ruan, A.B. Daniel, A. F. Carlos and D. R. A. Franco, *International Journal of Chemical Engineering*, 2012(1-2), <http://dx.doi.org/10.1155/2012/179312>
- [15] M. Hunsom, K. Pruksathorn, S. Damronglerd, H. Vergnes, P. Duverneuil, *Water Research*, 39(4) (2005) 610-616
- [16] I. Giannopoulou, D. Panias, *Minerals Engineering*, 20(8) (2007) 753-760
- [17] I.A. Khattab, M.F. Shaffei, N.A. Shaaban, H.S. Hussein, S.S. Abd El-Rehim, *Egyptian Journal of Petroleum*, 23(1) (2014) 87-91
- [18] B. Dan, C. Mike, B. Dana, *Plating And Surface Finishing*, (1988) 26-31
- [19] J. Luo, J. LL, Z. Yang, X. Liu, 23(2) (2013) 524-529
- [20] A. Dąbrowski, Z. Hubicki, P. Podkościelny, E. Robens, *Chemosphere* 56(2) (2004) 91-106
- [21] R. Salhi. *Mineral Processing and Extractive Metallurgy*, 119(3) (2010) 147-152
- [22] R. Salhi, *Iran. Chem. Chem. Eng.(IJCCE)*, 24(3) (2005) 29-39
- [23] R. Salhi, K.E. Bouhidel, *Asian Journal of Chemistry*, 17(1) (2005) 245-258
- [24] K. E. Bouhidel, R. Salhi, "Energy and Electrochemical Processing for a Cleaner Environment", 97, 28, pp. 323-329, Walton, CW, Ed. Pennington: Electro-chemical society Inc (Series: Electrochemical Society Series, Vol. 97 (1998).
- [25] J.E. Silva, D. Soares, A.P. Paiva, J.A. Labrincha, F. Castro, *Journal of Hazardous Materials*, 121(1-3) (2005) 195-202
- [26] G. Rossini, A.M. Bernardes, *Journal of Hazardous Materials*, 131(1-3) (2006) 210-216
- [27] K. Świerk, A. Bielicka, I Bojanowska., Z. Maćkiewicz., *Polish.J. of Environ. Stud.*, 16(3) (2007) 447-451
- [28] D.H. Rubisov, V.G. Papangelakis, *Hydrometallurgy*, 58(1) (2000) 13-26
- [29] N.M. Al-Mansi., N.M. Abdel Monem, *Waste Management*, 22(1) (2002) 85-90
- [30] E.A. Abdel-Aal, M.M. Rashad, , *Hydrometallurgy*, 74(3-4) (2004) 189-194
- [31] A.S. Marinos, K. Demetra, H. Katherine-Joanne, J.I. Vassilis, G.M. Konstantinos, D.L. Maria, *Desalination*, 215(1-3) (2007) 73-81
- [32] A. Bielicka, I. Bojanowska, A. Wiśniewski, Pol. J. Environ. Stud, 14(2) (2005) 145-148
- [33] I. Bojanowska, *Polish Journal of Environmental Studies*, 11(2) (2002) 117-121
- [34] J. Jitka, S. Tat'ana, Ni. Romana, *Hydrometallurgy*, 57(1) (2007). 77-84
- [35] T. Fukuta, H. Matsuda, F. Seto, K. Yagishita, *Global NEST Journal*, 8(2) (2006) 131-136
- [36] D. Kuchar, T. Fukuta, M. Kubota, H. Matsuda, *International Journal of Civil and Environmental Engineering*, 2(2) 62-66 (2010)
- [37] H. Kondo, T. Fujita, D. Kuchar, T. Fukuta, H. Matsuda, K. Yagishita, *Hyomen gjjutsu*, 57(12) (2006) 901-906
- [38] Garole, V.J. Garole, D.S. Dalal, *Research Journal of Chemical Sciences*, 2(3) (2012) 61-63
- [39] P. P. Li, C. S. Peng, F. M. Li, S. X. Song, A. O. Juan, *Int. J. Environ. Res.*, 5(3) (2011)797-804.
- [40] G. Tian, J. Li, Y. Hua, *Trans. Nonferrous Met. Soc. China*, 20 (2010) 513-520
- [41] W. Robert, Reters, F. Jeff, *Hazardous Waste And Hazardous Materials*, 4(4) (1987) 325-3

# Modification of the Thermally Exfoliated Vermiculite by Sonication and Grafting Methods

S. Terchi<sup>\*a</sup>, H. Bougherara<sup>a</sup>, S. Hamrit<sup>c</sup>, B. Boudine<sup>b</sup> and B. Kebabi<sup>a</sup>

<sup>a</sup> Laboratoire Pollution et Traitement des Eaux, Département de Chimie, Faculté des Sciences Exactes, Université Mentouri Constantine, 25000, Constantine, Algérie

<sup>b</sup> Laboratoire de Cristallographie, Département de Physique, Université des frères Mentouri, 25000, Constantine, Algérie.  
<sup>c</sup> Faculté de Technologie, Université Mohamed Boudiaf-M'sila, B.P 166 Ichbilâ, M'sila, 28000 Algérie.

\*Corresponding author: [terchismail@gmail.com](mailto:terchismail@gmail.com)

Received date: November 11, 2016; accepted date: December 20, 2016

## Abstract

In the present study, the thermally exfoliated vermiculite has been sonicated in order to grafting with the butyl-imidazolium. A suspension of vermiculite-water with 1% of concentration was sonicated at 20 KHz. This led to the decrease in the size of grains to 16  $\mu\text{m}$  after 2 h of treatment. Increasing of sonication time, presence of  $\text{H}_2\text{O}_2$ , and the increase of the vermiculite concentration have caused an accentuation of sonication effect, this resulted the decreasing of the size to 10  $\mu\text{m}$ . Moreover, a 2% fraction of submicron-sized particles was appeared. The pH of the vermiculite suspensions was increased. The number of the -OH sites was determined by acid-base titration using Gran method. The infrared spectra of the raw and sonicated vermiculites in  $\text{H}_2\text{O}$  or containing  $\text{H}_2\text{O}_2$  were very similar. In the presence of  $\text{H}_2\text{O}_2$ , two bands were observed at 1380 and 1460  $\text{cm}^{-1}$ . These are due to the presence of carbonates anions formed during sonication in  $\text{H}_2\text{O}_2$ . XRD spectra showed that the sonication did not affect the vermiculite structure. The grafting was carried out on sonicated samples during 5 h in  $\text{H}_2\text{O}$ . This was realized in two steps. In the first step, we grafted 3-chloropropyltrimethoxysilane instead of the -OH sites. In the second step, we conducted a nucleophilic substitution of chlorine with methyl-imidazole. We proved by infrared spectroscopy and Gran method that grafting was real and XRD that this was not an intercalation.

**Keywords:** clay, vermiculite, sonication, grafting, ionic liquids;

## 1. Introduction

Vermiculite is a layered phyllosilicate (type 2:1 or TOT), its sheet is an octahedral layer (type of Mg, Al, and Fe) sandwiched between two tetrahedral layers (type of Si and Al). Isomorphous substitution of  $\text{Si}^{4+}$  by  $\text{Al}^{3+}$  leads to the appearance of a negative charge at the sheet that will be compensated by hydrated exchangeable cations ( $\text{Ca}^{2+}$ ,  $\text{Mg}^{2+}$ ,  $\text{Cu}^{2+}$ ,  $\text{Na}^+$ ,  $\text{K}^+$ ,  $\text{H}^+$ ...) [1]. The adjacent sheets are attached by electrostatic forces and combinations of Van der Waals forces. Water molecules can be adsorbed in the interlayer space forming layers with interlayer cations, leading to swelling of the vermiculite. This adsorption depends on the hydrated cations state, which can be dehydrated, monohydrated or bihydrated, corresponding to the intercalation of 0, 1, or 2 plans of water molecules [2, 3].

The interaction of certain organic molecules with vermiculite may occur by adsorption, consequence of its large surface area or by intercalation consequence of swelling power of its interlayer space [4-6].

Vermiculite is also used for the adsorption of heavy metals [7-9]. These properties in addition to its environmental inertia make it a good candidate to be used in the water treatment field. Several scientific studies have been realised for the modification of vermiculite.

The most studied modification is the thermal exfoliation [10-18, 4]. Exfoliation improves certain properties of the vermiculite without diminishing its environmental inertia. This modification of the vermiculite causes a reduction of the apparent density and its thermal conductivity and an increase in its surface area and its melting point. Increasing the surface area of the vermiculite improves its adsorption capacity.

This improvement will be enhanced by decreasing the grains size by simple milling [6] or by sonication [19-26]. Mechanical milling is the simplest technique to reduce the grains size; it can be reduced to 40  $\mu\text{m}$  [19]. However, aggressive milling can damage the vermiculite structure. The use of ultrasound seems to give better results [20].

They allow to obtain lower grains size without destroying the molecular structure of the clay.

Sonication in the presence of hydrogen peroxide for 10 hours can reduce the grains size of vermiculite to 15.5  $\mu\text{m}$ . A size of 0.7  $\mu\text{m}$  was obtained after 80 hours of sonication [24]. A size of 1.7  $\mu\text{m}$  was obtained after 25 minutes of sonication [27]. However, the increase of the sonication time can result aggregation of vermiculite [21, 23]. A finer grains size and higher surface area were obtained by "vibration milling, unfortunately this technique can lead to the destruction of the vermiculite structure [28].

The sonication is the most appropriate method for obtaining nanoparticles without denaturation of physical or chemical properties of the material. The scattering of acoustic waves in the suspension of vermiculite-liquid (distilled water, hydrogen peroxide, alcohol ... ..) until the imploding of formed bubbles generates Physical effects leading to fragmentation of the particles and producing smaller particles [29]. Generally, treatment with low-frequency ultrasound (20-100 kHz) has a physical effect on the adsorbents without changes in chemical structures. On the contrary high frequencies (>100 kHz) lead only to chemical effects.

Grafting vermiculite by specific chemical groups was also used to improve its water decontamination capabilities. The vermiculite has been grafted by manganese oxide [30]. Fernández et al grafted vermiculite by silane group [31]. This technique gives the best results when the limit to the modification by milling or sonication is achieved. Because generally, the grafting of clays was carried out on the -OH groups located at the edges of the sheets. To increase the yield of grafting, it is essential to reduce the size grains of vermiculite and increase the number of -OH groups at the edges of the sheets.

In this study, we have investigated the effect of various parameters of sonication on the decrease of the thermally exfoliated vermiculite particles size. Knowing that ionic liquids have a special affinity with metals [32-37]. We grafted the smaller particles of vermiculite with butyl imidazolium to so as increase their capacity for adsorption of heavy metals.

## 2. Materials and methods

### 2.1. Clay

The studied vermiculite was provided by the CMMP (French company), originating from Yuli-China, (millimetric plates). Thermal exfoliation was achieved after a thermal shock in an oven at 600°C for 5 min. It was washed with deionized water several times. The insoluble impurities such as sand were precipitated and the exfoliated vermiculite floats on the water surface. After washing, the vermiculite is dried in an oven at 105°C for 12 h and was then milled to obtain a powder (denoted as: raw vermiculite). Its empirical formula is found to be:  $(\text{Si}_{3.2}\text{Al}_1)(\text{Mg}_{2.02}\text{Fe}_{0.32}\text{Ti}_{1.06})\text{O}_{10}(\text{OH})_2\text{K}_{0.15}\text{Ca}_{0.08}$  [38-39]. It has a cation exchange capacity of 148.6 meq/100 g.

### 2.2. Characterisations

#### 2.2.1. Infrared spectrophotometry

The samples were conditioned in a pellet form by compressing under 7 tons. 1.5 mg of sample was dispersed in 300 mg of potassium bromide. The infrared spectra were carried out between 400 and 4000  $\text{cm}^{-1}$  with a resolution of 2  $\text{cm}^{-1}$  with 64 scans by a spectrophotometer Thermo Electron Corporation-Nicolet 380 FTIR spectrometer, brand.

#### 2.2.2. Laser granulometry

Laser granulometry allows us to calculate the average size of the particles and determine the speciation percentage of each size. It is based on the diffraction of light according to the Fraunhofer theory. The used sail is MALVERN -INSTRUMENT brand, Mastersize type, S 32734-60 model. It allows the characterization of particles with diameters ranging from 0.02 to 2000  $\mu\text{m}$ . The concentration of particles suspension must exceed 1  $\text{g.L}^{-1}$  so that the obscuration ratio will be satisfactory (about 9-10%). Before measurement the sample must be homogeneous in distilled water to ensure good dispersion. If the particles are agglomerated it is imperative to use an ultrasonic container for deagglomerated.

#### 2.2.3. Acid-base titration

The acid-base titration allows us to quantify the -OH groups of clay, which will subsequently be used for grafting of butyl imidazolium. We have used the Gran method [41]. The experiment was carried out under argon atmosphere at 18°C. Clay-water suspension (1 g in 100 ml water UHQ) was firstly acidified at  $\text{pH} \approx 3$  with hydrochloric acid (0.01 M). Then the basic titration was carried out with (NaOH 0.01 M) until the  $\text{pH} \approx 10$  [42, 43]. The concentration of electrolyte (NaCl) was adjusted to 1  $\text{mol.L}^{-1}$  to remove the exchange effects that can occur between the  $\text{H}^+$  ions and the interlayer cations of the vermiculite. The representation of the function :

$$(V_0 + V_{\text{at}} + V_{\text{b}}) \cdot 10^{-\text{pH}} = f(V_{\text{b}})$$

$$(V_0 + V_{\text{at}} + V_{\text{b}}) \cdot 10^{+\text{pH}} = f(V_{\text{b}})$$

for acid side and for the basic side, ( $V_0$  is the volume of clay suspension,  $V_a$  is the volume of added acid to achieve a pH around 3 and  $V_b$  is the volume of added base) allowed us to determine the equivalent points  $V_{\text{eb1}}$  and  $V_{\text{eb2}}$  ( $V_{\text{eb1}}$  is equivalent to OH ions that neutralize the excess of  $\text{H}^+$  ions in the suspension and  $V_{\text{eb2}} - V_{\text{eb1}}$  is equivalent to OH ions which react with acceptor sites of clay) using extrapolations on the two branches of the curve Gran. The concentration of surface sites (CSSA) was calculated by the following formula:

$$\text{CSSA}(\text{mmol.L}^{-1}) = \frac{[(V_{\text{eb2}} - V_{\text{eb1}})_{\text{sample}} - (V_{\text{eb2}} - V_{\text{eb1}})_{\text{blank}}] \times C_{\text{b}}}{V_0}$$

The number of active sites (NSA) was deducted from the above formula by divided the number of moles of active sites surface ( $V_0 \times \text{CSSA}$ ) to the mass of the clay (1g) in the suspension. Sites active number was given by following equation:

$$\text{NSA}(\text{mmol.g}^{-1}) = [(V_{\text{eb2}} - V_{\text{eb1}})_{\text{sample}} - (V_{\text{eb2}} - V_{\text{eb1}})_{\text{blank}}] \times C_{\text{b}}$$

The representations of Gran (below) are plotted as function of  $V_b$ . Therefore, the second branch of acid-base titration which was used (passage of acid pH to basic pH). We have performed the acid-base titration for the blank (100 ml of 1M NaCl solution), where:  $V_{\text{eb1 blank}} = 2.3$  ml and  $V_{\text{eb2 blank}} = 5.7$  ml (Figure 3.(a))

#### 2.2.4. X-ray diffraction (XRD)

The XRD analyses were performed in a Bragg-Brentano geometry using a Brukers D8 Advance

diffractometer (acceleration voltage of 40 kV and an electron current of 30 mA) equipped with a Ge monochromator and using the Cu  $k_{\alpha}$  incident radiation ( $\lambda=1,5406$  nm).

### 2.2.5. pH of vermiculite-solvent suspensions

The pH of clay-solvent ( $H_2O$  or  $H_2O_2$ ) was measured using a pH meter (NF ISO 10390, 2005) before and after the sonication. The pH measurement was performed after the preparation of clay suspension in water or hydrogen peroxide at a ratio of 1/5 (v/v).

### 2.3. Ultrasonic treatment

The raw vermiculite was sonicated in aqueous solution either in presence or absence of hydrogen peroxide (concentration of 35%). The used reactor for the sonication is a glass reactor 60 ml of volume. It is a cylinder at double-walled which allowed us to maintain the suspension at 25°C during sonication. Ultrasound is generated by a generator Sonics and Materials 500W Ultrasonic Processor-VC505. The used titanium probe has a diameter of 13 mm and was immersed to a 1.5 cm in the suspension. The frequency of sonication was 20 KHz and the power was set at 70% of 500 W that can produced by the generator. The concentration of the vermiculite in aqueous solution either in presence or absence of hydrogen peroxide was set at 1 and 7%. The time of sonication was set at 2 and 5 h. After treatment, the obtained samples were dried at 80°C for 48 h.

The calorimetric method was applied to determinate the acoustic power of our system. A thermocouple was immersed in distilled water to control the increase in temperature during the sonication (for a few minutes (3 min) without cooling) in the cylindrical reactor. The values of (t, T) were: (0, 295.5), (30, 303.95), (60, 312.05), (90, 320.35), (120, 326.65), (150, 333.15), (180, 339.05), where: t is the sonication time (s) and T is the temperature of our system (K). The acoustic power was calculated using the following equation [40]:

$$U_p = m \cdot C_p \cdot \frac{dT}{dt}$$

Where  $C_p$  is the heat capacity of solvent at a constant pressure ( $J \cdot kg^{-1} \cdot K^{-1}$ ), m is the solvent mass (kg) and  $\frac{dT}{dt}$  ( $K \cdot s^{-1}$ ) is the rate of temperature increase. A 56 W acoustic power was found for our system.

### 2.4. Grafting procedure

The grafting was carried out on sonicated vermiculite sample in  $H_2O$  at 7% of concentration for 5 h (denoted as V:  $H_2O$ , 5 h). Before grafting, the sample was dried with nitrogen liquid for 3 h and introduced overnight in a desiccator. The used reagents (methyl-imidazole, acetonitrile, toluene, and 3-chloropropyltrimethoxysilane 3-CPTMS) for grafting have a purity of 99% and originating from Sigma Aldrich. The grafting was carried out in two steps. At the first step, we grafted the 3-

chloropropyltrimethoxysilane (3-CPTMS) on the edge surface of the vermiculite sheets (Figure .1).

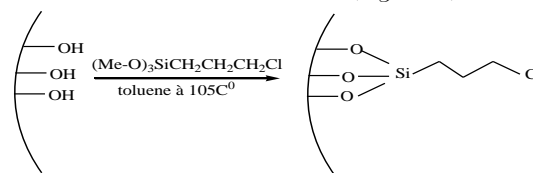


Figure 1: Schematic illustration of the procedure of the first grafting step.

During the second step, we have carried out a nucleophilic substitution of chlorine with methyl-imidazole (Figure .2).

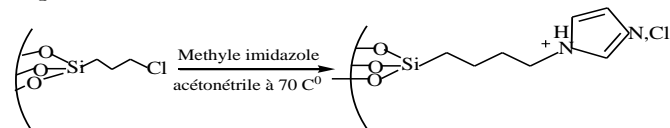


Figure 2: Schematic illustration of the procedure of the second grafting step.

During the first step, an amount of 10 g of sample was introduced into 50 ml of dry toluene with an excess of 3-CPTMS in a three-necked flask. The system was kept under reflux system at 105°C under argon atmosphere for 6 h. The obtained product (denoted as V-CPTMS) was filtered under vacuum, washed six times with a water-acetonitrile mixture and dried with liquid nitrogen and placed in a desiccator. This step allowed making the substitution of -OH of vermiculite edges by 3-CPTMS. For the second step of grafting, we introduced the product of the previous reaction (V-CPTMS) with 40 ml of dry acetonitrile and excess of methyl-imidazole (4 ml) in a three-necked flask. The system was stirring under reflux system at 70°C for 48 h. The obtained product was filtered, washed 6 times with distilled water and dried at 80°C for 48 h (denoted as V-CPTMS-Me.Im). This step has achieved the nucleophilic substitution of chlorine with methyl-imidazole.

## 3. Results and discussion

### 3.1. Modification by ultrasonic irradiation

#### 3.1.1. Measurements of pH

The pH measurements of vermiculite suspensions in water either in presence or absence of hydrogen peroxide were performed before and after sonication. The obtained results are summarized in the table 1. The effect of ultrasound on the pH of vermiculite suspension depends on the sonication time and is depreciated with time. The sonication of the vermiculite in water either in presence or absence of hydrogen peroxide leads to the dissolution of the interlayer cations ( $Ca^{2+}$  and  $K^+$ ) in the solution. The water molecules located on the clay surface dissociate into  $OH^-$  and  $H^+$  ions.  $OH^-$  ions were released into the solution to keep the electrical equilibrium while  $H^+$  ions were captured by -OH groups of clay surface or intercalated in the interlayer space. The excess of  $OH^-$  ions in solution has led to the increase of pH [44]. Muromtsev et al [45] noted the expulsion of interfoliares exchangeable ions ( $Mg^{2+}$  and  $Ca^{2+}$ ) in aqueous solution by exfoliated

vermiculite, in addition, the appearance of OH ions to keep electrical equilibrium. These ions react with carbon dioxide dissolved in solution during sonication to form carbonate anions  $\text{CO}_3^{2-}$ . This reaction is evidenced by infrared characterization of the sonicated vermiculite (Figure 4). The pH of vermiculite-water suspensions either in presence or absence of hydrogen peroxide was increased with respect time, but this increase was greater in the presence of hydrogen peroxide. This is explained by the decomposition of hydrogen peroxide, which increases the concentration of OH anions during sonication (in addition to those released by the clay). Increasing the concentration of vermiculite from 1% to 7% decreases the effect of ultrasound on the pH. In fact, this increase has led to an increase in the viscosity of the suspension which has interfered cavitation effects.

**Table 1:** pH of the solvent-vermiculite suspensions before and after the ultrasonic irradiation.

Concentration of clay	1%			7%		
	0	2	5	0	2	5
Time of sonication (h)	0	2	5	0	2	5
pH of H <sub>2</sub> O-clay suspensions	9	9.5	9.6	9.4	9.7	9.84
pH of H <sub>2</sub> O <sub>2</sub> -clay suspensions	3.4	5.36	---	5.7	6.27	6.34

3.1.2. Acid-base titration

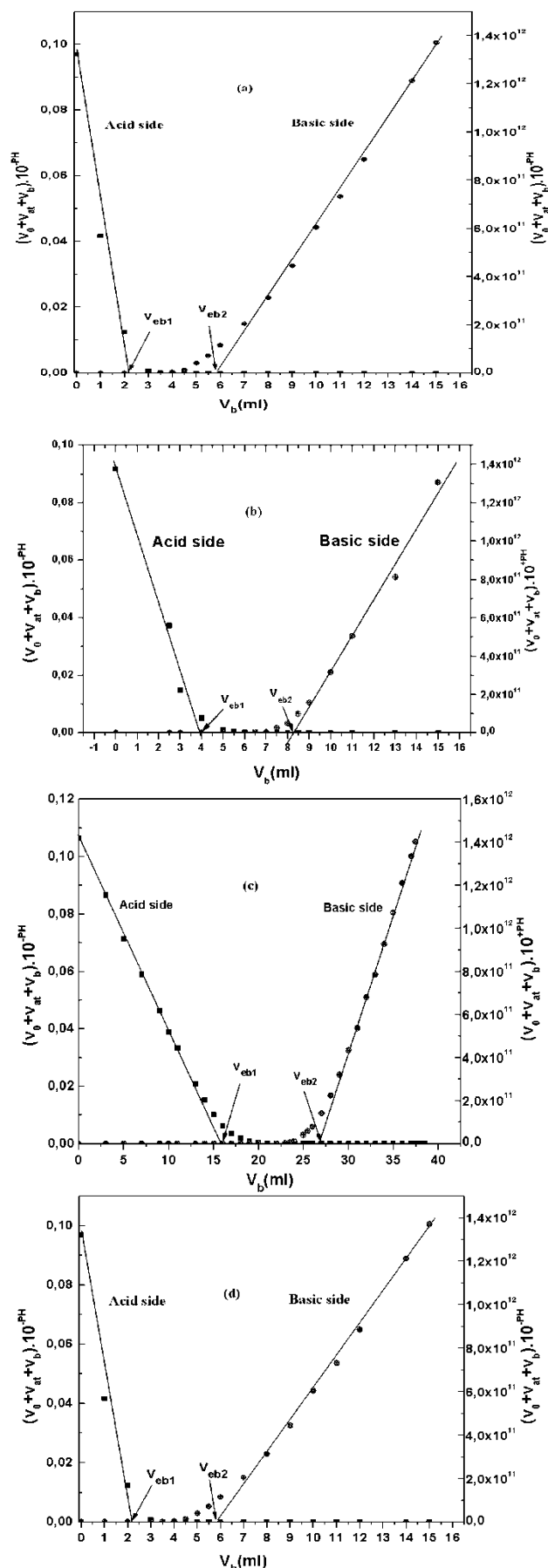
The number of -OH sites located on the edges of the vermiculite sheets were determined by acid-base titration using the Gran method. Based on the acid-base determination method that was mentioned above, we can plot the Gran curves, which allow determining the number of -OH sites. After linearization, we found that  $V_{eb1}=3.9$  ml and  $V_{eb2}=8.3$  ml for the raw vermiculite (Figure 3.(b)). Using the following relation:

$$NSA = [(V_{eb2} - V_{eb1})_{sample} - (V_{eb2} - V_{eb1})_{blank}] \times C_b = 0.010 \text{ mmol.g}^{-1}$$

Where  $V_{eb2}$  and  $V_{eb1}$  of blank were measured previously (Figure 3.(a)). For sonicated sample during 5h in the presence of peroxide hydrogen (Figure 3.(c)), we found that  $V_{eb1}=16$  ml, and  $V_{eb2}=27$  ml.  $NSA=0.076$  mmol.g<sup>-1</sup> (Table 2). The number of active sites (-OH) of the raw vermiculite was 0.010 mmol.g<sup>-1</sup>. After ultrasonic irradiation, the value of NSA was clearly increased. After 5 h of sonication in H<sub>2</sub>O<sub>2</sub> media, it was reached at 0.076 mmol.g<sup>-1</sup>, which that represents 7.6 times of the raw clay. This increase was a consequence of the perpendicular rupture of the clay layers, resulting -OH groups on the edges of the new smaller particles.

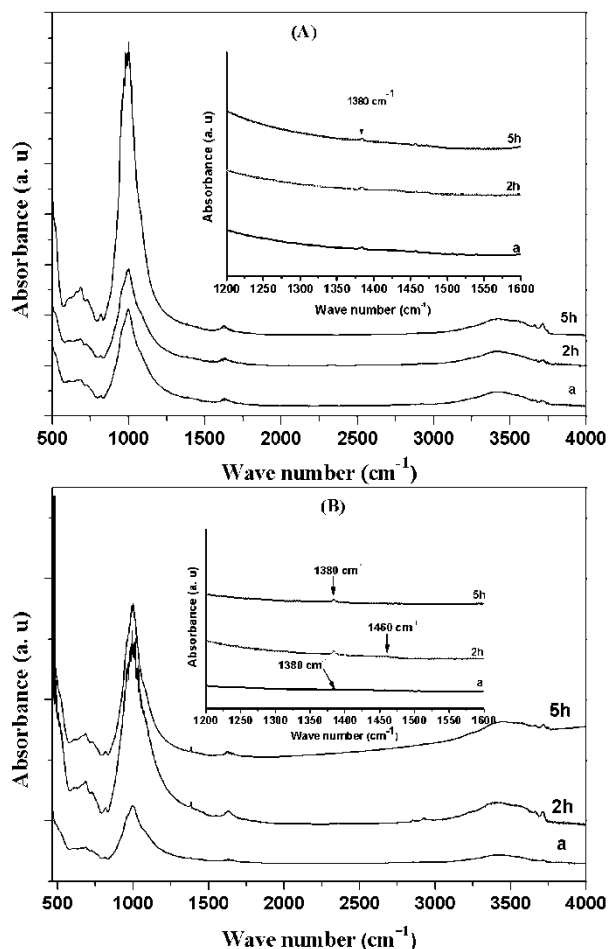
**Table 2:** The values of  $V_{eb1}$ ,  $V_{eb2}$ , CSSA and NSA for raw vermiculite, V: H<sub>2</sub>O<sub>2</sub>, 5 h and V-CPTMS samples.

Clay	Raw vermiculite	V: H <sub>2</sub> O <sub>2</sub> , 5h	V-CPTMS
$V_{eb1}$ (ml)	3.9	16	2.1
$V_{eb2}$ (ml)	8.3	27	5.8
NSA (mmol.g <sup>-1</sup> )	0.01	0.076	0
CSSA (mmol.L <sup>-1</sup> )	0.1	0.76	0



**Figure 3:** Curve Gran of: (a) blank (0.1 M NaCl), (b) raw vermiculite, (c) V: H<sub>2</sub>O<sub>2</sub>, 5 h and (d) V-CPTMS .

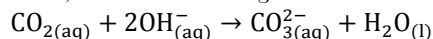
### 3.1.3. Infrared spectra



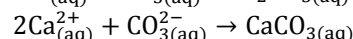
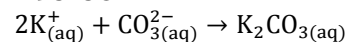
**Figure 4:** Infrared spectra of the clays: (A) raw vermiculite -a- and its sonicated samples in water after 2 h and 5 h, (B) raw vermiculite -a- and its sonicated samples in hydrogen peroxide after 2 h, and 5 h.

Figure 4. show the infrared spectra of the raw and sonicated vermiculites samples in water (a) and in water containing hydrogen peroxide at 7% of concentration (b), it can be seen that the results were very similar. This indicates that no structural change of the sheets during the irradiation. The broad band at  $1000\text{ cm}^{-1}$  was attributed to the stretching vibration of the group (Si-O). The two broad bands at  $450\text{ cm}^{-1}$  and  $686\text{ cm}^{-1}$  were attributed to the stretching vibration of the group (Al-O) [46]. The broad vibrational band of water at  $3430\text{ cm}^{-1}$  was assigned to the asymmetric and symmetric stretching vibrations of the group -OH. The two bands at  $3660\text{ cm}^{-1}$  and  $3720\text{ cm}^{-1}$  were assigned to the stretching vibration of the -OH groups of the sheets. The frequency at  $3660\text{ cm}^{-1}$  was assigned to the stretching vibrations of -OH groups in  $\text{Mg}(\text{OH})_2$  tetrahedron of the vermiculite [46, 47]. For sonicated vermiculites in water containing hydrogen peroxide, two bands were observed, the first was intense and narrow at about  $1380\text{ cm}^{-1}$  while the second was broad at about  $1460\text{ cm}^{-1}$  (Figure 4.(B)). They were assigned to the presence of carbonates ions formed by the dissolution of carbon dioxide of the air with the hydroxide ions (OH) released by the clay [48] and those generated by the decomposition of hydrogen peroxide. We also noted that there was a small amount of carbonates in the raw vermiculite (Figure 4.(B)), (The peak was less intense compared to the

sonicated samples for 2 and 5 h). This amount was increased after sonication. The carbonates ions  $\text{CO}_3^{2-}$  were formed during the sonication, which were generated by the reaction of carbon dioxide of the air with the hydroxide ions (OH). The ultrasounds also induce to the decomposition of the hydrogen peroxide leading to an increase of the amount of OH ions in the solution. The OH ions in the solution were the result of the decomposition of hydrogen peroxide and the (OH) ions released by the vermiculite. These two sources of OH lead to the increase in amount of dissolved carbon dioxide in the suspension, and this according to the reaction:



The formed carbonates react with the interlayer ions to form  $\text{K}_2\text{CO}_3$  and  $\text{CaCO}_3$  salts.



For the sonication in water, there is a single source, OH ions released by the clay leading to the reduction in the quantity of dissolved  $\text{CO}_2$  gas during the sonication, that is why the intensity of the peak around  $1380\text{ cm}^{-1}$  is lower than that observed with hydrogen peroxide (Figure 4.(B)).

### 3.1.4. Granulometric curves

Before sonication, the granulometric curve of the raw vermiculite showed a single peak (Figure 5.), the average particles size was  $80\text{ }\mu\text{m}$  (the maximum of peak position), the full width at half maximum (FWHM) of the peak was  $220\text{ }\mu\text{m}$ , the percentage volume was 9% and all the particles located in the range of  $2\text{-}800\text{ }\mu\text{m}$ . Firstly, we have sonicated a 1% vermiculite solution. After 2 h of sonication, a peak at  $16\text{ }\mu\text{m}$  was appeared with a FWHM of  $35\text{ }\mu\text{m}$  and a volume percentage of 11.3%, the particles size was in the range of  $1\text{-}110\text{ }\mu\text{m}$ . There is also a small peak located in the range of  $0.5\text{-}1\text{ }\mu\text{m}$  was appeared, which is related to submicron-sized particles and which has a percentage of 0.8%. After 5 hours of sonication, a peak at  $12.2\text{ }\mu\text{m}$ , with a FWHM of  $20\text{ }\mu\text{m}$  and a volume percentage of 11.6%, was appeared, the particles were in the range of  $1\text{-}44\text{ }\mu\text{m}$  and the percentage of the submicron-sized particles was increased to 1.6%. The sonication effect is interpreted by the effectiveness of the physical effects of ultrasound caused by acoustic cavitation leading to the fragmentation of vermiculite particles. In the presence of hydrogen peroxide, after two hours of sonication, a peak at  $15\text{ }\mu\text{m}$  was appeared with a FWHM of  $25\text{ }\mu\text{m}$  and 12% of volume percentage, the particles was in the range of  $1\text{-}80\text{ }\mu\text{m}$  and the percentage of the submicron-sized particles was 1%. The sonication leads to a reduction of the grains size.

This decrease is accentuated by the presence of hydrogen peroxide in solution during treatment. This is the result of the decomposition of hydrogen peroxide which generates oxygen gaz that produces a pressure between the sheets and thus break the vermiculite particles. This phenomenon was very clearly at low concentration of clay. Secondly, we have increased the vermiculite concentration to 7% in order to increase the yield of low particles size. In this case, after 2 hours of ultrasonic treatment in the absence of hydrogen peroxide, the average grains size has

decreased, and the maximum of the peak correspond the particles size distribution is located at 16  $\mu\text{m}$ , the particles were in the range 1-60  $\mu\text{m}$ , the percentage volume was 13% and the percentage volume of submicron-sized particles was 0.8%. After 5 hours of treatment, the maximum of the peak of the grains size distribution curve is decreased to 10  $\mu\text{m}$ , the particles were in the range 1-40  $\mu\text{m}$  with 11% of percentage volume and the percentage volume of submicron-sized particles was 2%. The presence of hydrogen peroxide does not improve the efficiency of the sonication at this concentration. Indeed, the maximum of the peak of the size distribution curve was 16  $\mu\text{m}$  after 2 hours of treatment and it was 12  $\mu\text{m}$  after 5 hours of treatment. The particles were in the range of 1-63  $\mu\text{m}$  for 2 hours and in the range of 1-40  $\mu\text{m}$  for 5 hours of treatment. The submicron-sized particles were in the range 0.5-1  $\mu\text{m}$  and the volume percentage of these particles was 0.8% and 2% for 2 hours and 5 hours of treatment, respectively. Increasing the vermiculite concentration reinforces ultrasonic effects on particles size. This is due to the increase of collision probability between the vermiculite particles. This result was observed by Michael [49], for the ultrasonic treatment of the alumina in aqueous solution. Granulometric curves showed that the ultrasound efficiency is important at the beginning of treatment and this in either the presence or absence of hydrogen peroxide. The treatment time is important for the obtained amount of submicron-sized particles.

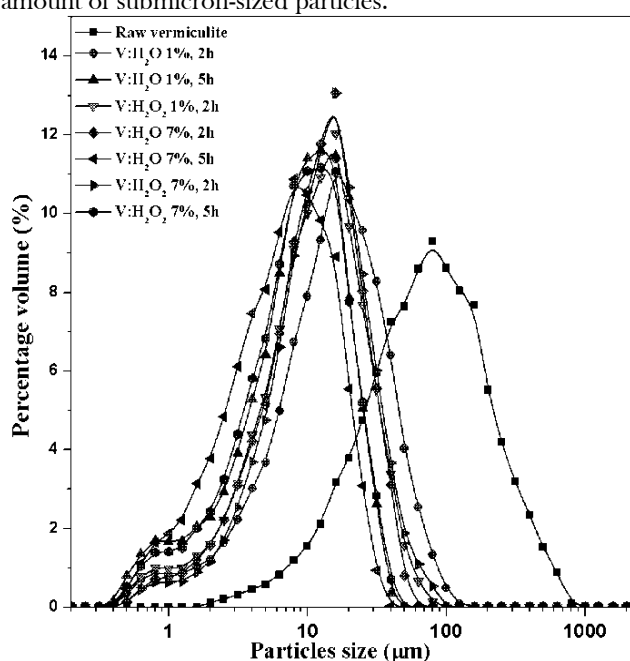


Figure 5: Granulometric curves of the raw and sonicated vermiculites.

### 3.1.5. X-ray diffraction (XRD)

We performed the XRD spectra of the raw vermiculite and sonicated samples at 7% of concentration either in presence and absence of hydrogen peroxide (Figure 6). This was in order to determine the sonication effect on the grains structure. The basal spacing is modified by the presence of hydration water molecules. This results in the change of the peaks position in the XRD spectra. Studied Vermiculite contains two cations in its interlayer space:

potassium  $\text{K}^+$  and calcium  $\text{Ca}^{2+}$ . Potassium being dehydrated while calcium is intercalated with a monolayer water [2, 3]. The narrow and more intense peak in spectra (identified as (002a)) which is located at  $2\theta=6.04^\circ$  corresponds to a basal spacing  $d=14.60 \text{ \AA}$  (interfoliare space) [12, 18, 50]. Another narrow and intense peak (identified as (002e)) located at  $2\theta=8.84^\circ$  corresponds to a basal spacing  $d=10.0 \text{ \AA}$ , this spacing contains the dehydrated  $\text{K}^+$  ions. This peak is the only one which stayed on the XRD spectra when vermiculite was exchanged by  $\text{K}^+$  ions (Figure 6). The peak identified as (002b) located at  $2\theta=7.02^\circ$  corresponds to a basal spacing  $d=12.57 \text{ \AA}$ , where is containing the monohydrated  $\text{Ca}^{2+}$  ions. The other peaks (identified as (002c) and (002d)) located at  $2\theta=7.40^\circ$  and  $2\theta=8^\circ$  correspond respectively to basal spacing  $d=11.93 \text{ \AA}$  and  $d=11.04 \text{ \AA}$  were the result of interbedded layers containing  $\text{K}^+$  and  $\text{Ca}^{2+}$  ions. The sonication of the vermiculite in water led to decrease in the intensity and broadening of the peak (002a). This effect was more pronounced with time. After sonication of the vermiculite in water during 2 hours, the peak intensity related to (002a) reflection was greatly decreased which results in enlargement of the FWHM of the peak that was  $\omega=0.0021$  rad and becomes 0.0031 rad. After 5 hours of sonication, the peak intensity was more decreased and FWHM was more increased and becomes 0.0054 rad. The other peaks associated to (002b), (002c) and (002d) reflections were also decreased after two hours of sonication. After 5 hours of sonication, the intensity of these peaks was more reduced. The intensity of the peak related (002e) reflexion was also more reduced with time. Generally no destruction of the crystal structure has been noted. But the average of crystallites size was decreased after the sonication. We can calculate the average crystallites size according to -c- axis using the Debye-Scherrer's equation:

$$a = \frac{0.9\lambda}{\omega \cdot \cos\theta}$$

((002a) reflexion at  $2\theta=6.04^\circ$ ). Where: a is the average crystallites size (nm),  $\lambda$  is the X-ray wavelength (0.15406 nm for  $\text{Cu K}\alpha$ ),  $\omega$  is the FWHM of the peak (radians) and  $\theta$  is the angle diffraction (deg.). Therefore, the size of the raw vermiculite was about of 67 nm; it became 45 nm after 2 hours and reached to 31 nm after 5 hours of sonication. This reduction can be explained by the fragmentation of grains and desorption of interfoliares cations in the solution. Concerning the sonicated samples in the presence of hydrogen peroxide, the same remarks were observed, but the crystallites size were more reduced; therefore, after 2 hours of sonication became 36 nm and reached to 27 nm after 5 hours of sonication (Table 3). So, the ultrasound at 20 KHz has a breaking effect of vermiculite particles in water suspension either in presence or absence of hydrogen peroxide due to acoustic cavitation. We can say that the ultrasound at this frequency has only a mechanical effect.

Table 3. The values of the crystallites sizes of the raw and sonicated vermiculite.

Solvent	H <sub>2</sub> O			H <sub>2</sub> O <sub>2</sub>		
	0	2	5	0	2	5
Average crystallites size according to -c- axis (nm)	67.5	45	31.5	67.5	36	27

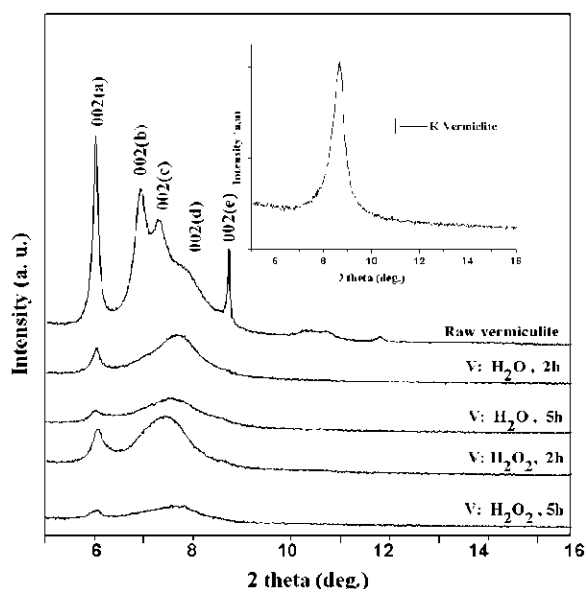


Figure 6. XRD spectra of the raw vermiculite and sonicated samples in aqueous solution in absence and presence of hydrogen peroxide.

### 3.2. The grafting modification

The sonication of vermiculite allowed us to reduce its grains size and thus increase the number of -OH sites which will be grafted. The mixture of the vermiculite with 3-CPTMS under inert atmosphere has allowed to grafting -OH groups with later. The obtained sample (V-CPTMS) was washed to eliminate the rest of the 3-CPTMS which can be intercalated or adsorbed. After that, the obtained sample was reacted with an excess of methyl-imidazole to have a substitution of the latter instead of chlorine. Then, we washed the grafted sample (V-CPTMS-Me.Im) to get rid of any intercalated or adsorbed methyl-imidazole. The infrared spectra of the initial and grafted samples were shown in Figure 7.

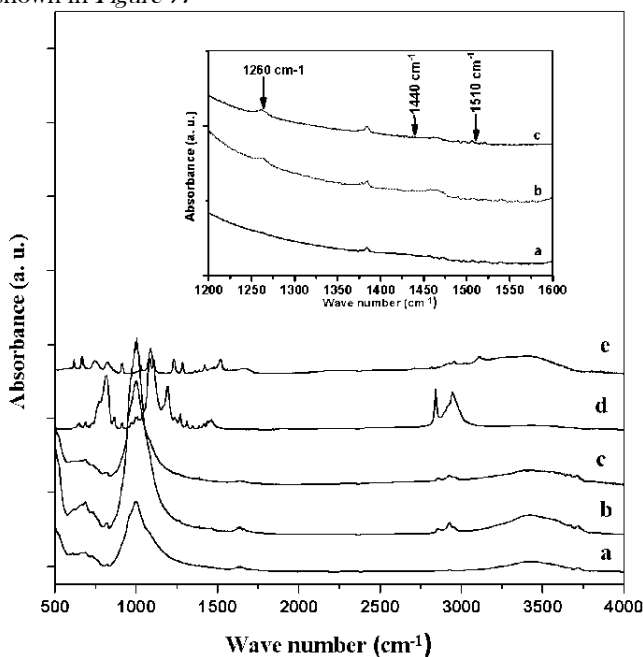


Figure 7. FTIR spectra of the sonicated vermiculite in H<sub>2</sub>O for 5 h and grafted vermiculite: V: H<sub>2</sub>O<sub>2</sub>, 5 h (a), V-CPTMS (b), V-CPTMS-Me.Im (c), 3-CPTMS (d) and methyl imidazole (e).

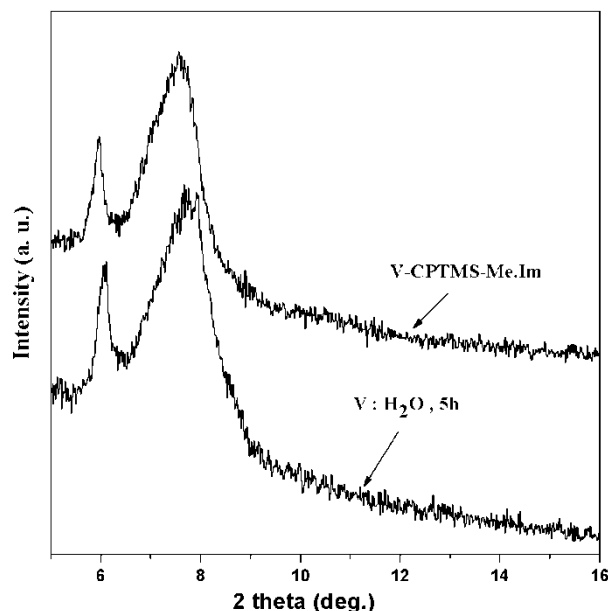


Figure 8. XRD spectra of the grafted and sonicated vermiculite in H<sub>2</sub>O for 5 h.

The similar bands on the spectra of the samples a,b and c were: The broad band between 3200 cm<sup>-1</sup> and 3600 cm<sup>-1</sup> was assigned to the asymmetric and symmetric stretching vibrations of the group -OH of water ( $\nu_{OH}$ ). The band around of 1600 cm<sup>-1</sup> was a binding of the physisorbed water on clay ( $\delta_{OH}$ ). The broad band at 1000 cm<sup>-1</sup> was assigned to the Si-O group ( $\nu_{Si-O}$ ). The two broad bands at 450 cm<sup>-1</sup> and 686 cm<sup>-1</sup> were attributed to Al-O group ( $\nu_{Al-O}$ ). The narrow band around 1380 cm<sup>-1</sup> was attributed to a quantity of carbonate ions formed by dissolving carbon dioxide gas during sonication. New peaks were appeared on the spectra (b). The first three were about 2860 cm<sup>-1</sup>, 2930 cm<sup>-1</sup>, 2960 cm<sup>-1</sup>. These peaks were assigned to stretching vibration symmetric and asymmetric of (C-H) group due to the presence of propyl group of CPTMS [Cl-CH<sub>2</sub>-CH<sub>2</sub>-CH<sub>2</sub>-Si(O-CH<sub>3</sub>)<sub>3</sub>] and at 1410 cm<sup>-1</sup> for -CH<sub>2</sub>-bending [51]. Another peak due to stretching vibration of Si-O-Si group was appeared at around 1260 cm<sup>-1</sup>. This proved that CPTMS was grafted onto vermiculite. On the spectra (c), low peak at 3250 cm<sup>-1</sup> was observed, it was assigned to the stretching vibration of N-H group of imidazole ( $\nu_{N-H}$ ). Other bands of imidazole were very weak. We performed a zoom on the part of spectra ranging between 1200 and 1600 cm<sup>-1</sup> to be able to see the Figure 7. Two peaks were appeared at around 1510 cm<sup>-1</sup> and 1440 cm<sup>-1</sup>. They were assigned to the stretching vibrations of C=C and C=N groups, respectively. This proved that the methyl imidazole was grafted onto vermiculite. We vigorously washed the grafted sample to eliminate intercalated or adsorbed methyl imidazole onto vermiculite, and we proved by XRD spectra that no intercalated molecule during grafting was observed. The XRD spectra of the vermiculite before and after grafting were represented in the Figure 8. There was an attenuation of the peak intensity and no shift of its position was observed. This removed any risk of new intercalation during grafting. The decrease of the peak intensity after grafting is a frequently observed phenomenon [31, 52]. We also plotted the Gran curve of the V-CPTMS sample

(Figure 3.(d)). After linearization, we found that  $V_{\text{chl}}=2.1$  ml and  $V_{\text{chl}}=5.8$  ml, so  $NSA \approx 0 \text{ mmol. g}^{-1}$  (Table 2), we proved that all -OH sites of initial vermiculite were replaced by CPTMS.

#### 4. Conclusion

In this work, we have studied the effect of ultrasound on the thermally exfoliated vermiculite in order to grafting with butyl imidazolium. The raw and modified vermiculites were characterized by laser granulometry, X-ray diffraction, infrared spectrophotometry, measurements of pH of suspensions and acid-base titration. The sonication was performed in aqueous solution with a clay concentration of 1% and 7%. Then, we have studied the effect of the presence of hydrogen peroxide in aqueous solution on the ultrasound efficiency. The clay concentration has been increased from 1 to 7% in order to increase the sonication efficiency. Our study has shown that the effect of ultrasound on the size of the vermiculite particles was important in beginning of sonication, it was decreased with time. The average grains size of vermiculite was achieved to 10  $\mu\text{m}$  after five hours of sonication with appearance a small fraction of submicron-sized particles. The fragmentation of the clay particles led to increasing of clay suspensions pH and the number of -OH groups located on the edges of the clay sheets. This fragmentation was accentuated with increasing of the sonication time, increasing of clay concentration and the presence of hydrogen peroxide. The infrared and XRD spectra showed that no structural change of the vermiculite after sonication. Infrared spectra of the raw and sonicated vermiculite were very similar, the exception of the appearance of a peak at around 1380  $\text{cm}^{-1}$  which showed the formation of carbonates ions ( $\text{CO}_3^{2-}$ ) during sonication of vermiculite in the presence of hydrogen peroxide. XRD spectra showed the decrease of the vermiculite crystallites size. The grafting of butyl imidazolium was performed on Vermiculite sample having the smallest grains size; it was carried out in two steps. Firstly, we grafted 3-chloropropyltrimethoxysilane (CPTMS-3) on the edge surface of the vermiculite sheets. Then, we carried out a nucleophilic substitution with methyl imidazole. We have proved by infrared spectroscopy and Gran method that the grafting is real and XRD that this is not an intercalation.

#### References

- [1] F. Bergaya and G. Lagaly. General Introduction, Handbook of Clay Science, 2<sup>nd</sup> edition. Elsevier, Oxford, 2013, 1-17.
- [2] E. Ferrage, B. Lanson, L.J. Michot, J.L. Robert, J. Phys. Chem. C. 114 (2010), 4515-4526.
- [3] E. Ferrage, B.A. Sakharov, L.J. Michot, A. Delville, A. Bauer, S. Grangeon, G. Frapper, M. Jimenez-Ruiz, G.J. Cuello, J. Phys. Chem. C. 115 (2011) 1867-1881.
- [4] M. Valašková, G. S. Martynkova,; InTech, 2012, 209-238.
- [5] L. Wang, Z. Chen, X. Wang, S. Yan, J. Wang, Y. Fan, Appl. Clay Sci. 51 (2011) 151-157.
- [6] D.G.H. Ballard, G.R. Rideal, J. Mat. Sci. 18 (1983) 545-561.
- [7] N.C. Das, M. Bandyopadhyay, Water Environment Research. 64 (1992) 852-857.
- [8] O. Abollino, A. Giacomino, M. Malandrino, E. Mentasti, Appl. Clay Sci. 38 (2008) 227-236.
- [9] S. Malamis, E. Katsou, J. Hazard. Mater. 252- 253 (2013) 428- 461.
- [10] W. Baumeister, M. Hahn, Micron. 7 (1976) 247-251.
- [11] A. Obut, I. Girgin, Miner. Eng. 15 (2002) 683-687.
- [12] L.A. Pérez-Maqueda, V. Balek, , J. Poyato, J.L. Pérez-Rodriguez, J. Šubr, I.M. Bountsewa, I.N. Beckman, Z. Málek, J. Thermal Anal. Cal. 71 (2003) 715-726.
- [13] J.R. Hindman, Society for Mining Metallurgy and Exploration Inc., Littleton, Colorado , 1994, 1103-1111.
- [14] G.F. Walker, Mineralogical Society, London, 1961, 297-342.
- [15] T. Wada,; US. Patent 3753923, 1973a.
- [16] T. Wada,; US. Patent 3758415, 1973b.
- [17] D. Friedman, R.W. McKinney, C. Ou, R. M. Spotnitz, S. Wu,; US. Patent 5340558, 1994.
- [18] F.H. Muiambo, W.W. Focke, M. Atanasova, I.V.D. Westhuizen, L.R. Tiedt, Appl. Clay Sci. 50 (2010) 51-57 .
- [19] L.A. Pérez-Maqueda, M.C.J. De Haro, J. Poyato, J.L. Pérez-Rodriguez, J. Mat. Sci. 39 (2004) 5347-5351.
- [20] L.A. Pérez-Maqueda, O.B. Caneo, J. Poyato, J.L. Pérez-Rodriguez, Phys. Chem. Miner. 28 (2001) 61-66.
- [21] A. Wiewiora, J.L. Perez-Rodriguez, J.L. Perez-Maqueda, J. Drapala, Appl. Clay Sci. 24 (2003) 51-58.
- [22] M.C. Jimenez de Haro, J.M. Martinez Blanes, J. Poyato, L.A. Pérez-Maqueda, A. Lorf, J.L. Pérez-Rodriguez, J. Phys. Chem. Solid. 65 (2004) 435-439.
- [23] J. Poyato, J.L. Perez-Rodriguez, V. Ramirez-Valle, A.Lorf, F.E. Wagner, Ultrason. Sonochem. 16 (2009) 570-576.
- [24] J.L. Perez-Rodriguez, F. Carrera, J. Poyato, L.A. Perez-Maqueda, Nanotech. 13 (2002) 382-387.
- [25] L.A. Pérez-Maqueda, A. Duran, J.L. Pérez-Rodriguez, Appl. Clay Sci. 28 (2005) 245-255.
- [26] M.X. Reinholdt, F. Hubert, M. Faurel, E. Tertre, A. Razafitianamaharavo, G. Francius, D. Prêt, S. Petit, E. Béré, M. Pelletier, E. Ferrage, Appl. Clay Sci. 77-78 (2013) 18-32.
- [27] I.C. Hinds, P.J. Ridler, B.R. Jennings, Clay. Miner. 31 (1996) 549-556.
- [28] T. Hongo, S. Yoshino, A. Yamazaki, A. Yamasaki, S. Satokawa, Appl. Clay Sci. 70 (2012) 74-78.
- [29] S.J. Doktycz, K.S. Suslick, Science. 247 (1990) 1067-1069.
- [30] A. Sari, M. Tuzen, Micropor. Mesopor. Mat. 170 (2013) 155-163.

- [31] M.J. Fernández, M. Dolores Fernández, I. Aranburu, *Eur. Polym. J.* 49 (2013) 1257-1267.
- [32] Z. Li, Q. Wei, R. Yuan, X. Zhou, H. Liu, H. Shan, Q. Song, *Talanta*. 71 (2007) 68-72.
- [33] V.A. Cocalia, J.D. Holbrey, K.E. Gutoswky, N.J. Bridjes, R.D. Rodgers, *Tsinghua .Sci. Technol.* 11 (2006) 188-193.
- [34] R. Germani, M.V. Mancini, G. Savelli, N. Spreti, *Tetrahedron. Lett.* 48 (2007) 1767-1769.
- [35] M.V. Mancini, N. Spretia, P.D. Profiob, R. Germanic, *Sep .Purif .Technol.* 116 (2013) 294-299.
- [36] J. Castilloa, M.T. Collb, A. Fortuny, P.N. Donosoa, R. Sepúlvedac, A.M. Sastreb, *Hydrometallurgy*. 141 (2014) 89-96.
- [37] M. Cegłowski, G. Schroeder, *Chem. Eng. J.* 259 (2015) 885-893.
- [38] X. Huo, L. Wang, L. Liao, *Journal of the Chinese Ceram. Soc.* 39 (2011) 1517-1522.
- [39] X. Huo, L. Wu, L. Liao, Z. Xia, L. Wang, *Powder. Technol.* 224 (2012) 241-246.
- [40] F.R. Contamine, A.M. Willhelm, J. Berlan, H. Delmas, *Ultrason. Sonochem.* 2 (1995), S43-S47;
- [41] G. Gran, *Analyst*. 77 (1952) 661-671.
- [42] W. Liu, *Wat. Res.* 35 (2001) 4111-4125.
- [43] Q. Du, Z. Sun, W. Forsling, H. Tang, *J. Colloid. Interf. Sci.* 187 (1997) 221-231.
- [44] E. Üçgül, İ. Girgin, *Turk. J. Chem.* 26 (2002) 431-440.
- [45] V.A. Muromtsev, N.M. Zolotukhina, A.K. Mamina, *Inorg. Mater+*. 26 (1990) 868-871.
- [46] V.C. Farmer, *Mineralogical Society, London*, 1974.
- [47] M. Fernandez, J.M. Serratos, W.D. Johns *Proc, Reunion Hispano Belga de Minerales de la Arcilla, Consejo Superior de Investigaciones Cientificas, Madrid*, 1970, 163.
- [48] P. Jeevanandam, Yu. Koltypin, A. Gedanken, *Mater. Sci. Eng. B.* 90 (2002), 125-132;
- [49] M.D. Kass, *Mater. Lett.* 42 (2000) 246-250.
- [50] A.M. Mathieson, *Am. Mineral.* 43 (1958) 216-227.
- [51] D. Lin-Vien, N.B. Colthup, W.G. Fateley, J.G. Grasselli, *Academic Press, San Diego, California*, 1991.
- [52] J. Li, T. Qi, L. Wang, C. Liu, Y. Zhang, *Mater. Lett.* 61 (2007) 3197-3200.

# Numerical Modelling of boron diffusion for micro-pyramidal textured N-type silicon

Hanane Lachachi<sup>a\*</sup>, Abdellatif Zerga<sup>a</sup> and Batoul Benabadji<sup>a</sup>

<sup>a</sup> *Third-generation Solar Cells, Research Unit of Materials and Renewable Energies (URMER),  
Abou Bakr Belkaid University, B.P. 119, Tlemcen, Algeria*

Corresponding author: email: [lachachihanane@yahoo.fr](mailto:lachachihanane@yahoo.fr)

Received date: June 06, 2016; revised date: December 03, 2016; accepted date: December 11, 2016

---

## **Abstract**

*The formation of the emitter is considered as a crucial technological sequence during the manufacture of solar cells the thermal diffusion from a solid source in acylindrical quartz tube constitutes the most widely know and used technique for the formation of the emitter. Indeed, doping of n-type silicon with boron diffusion allows the formation of the p<sup>+</sup> emitter. This distribution is often difficult in terms of homogeneity to control and requires adequate detailed understanding of physical phenomena in order to optimize the best profile of dopant diffusion. However, this work is dedicated to the optimization of boron diffusion profile by investigating the effects of temperature and time diffusion on the planar and textured. A comparison with the experimental profile measured by SIMS (Spectroscopy Secondary Ion Mass) was performed. The differences between planar and textured surface are discussed.*

*Keywords: Crystalline silicon solar cells; Boron emitter; Doping profile; N-type silicon; Texturing.*

---

## **1. Introduction**

In the photovoltaic industry, the most widely used material is crystalline silicon. However, the price thereof occurs approximately 40% of the cost of manufacturing modules. The recovery silicon n-type can reduce the cost and solve the problem of shortage of silicon in the solar cell industry. The c-Si materials market is further diversify, as shown in Figure 1, according to the study carried out by International Technology Roadmap for Photovoltaic (ITRPV) in March 2016[1]. It confirms also the predicted shift from p-type to n-type mono-Silicon and this material will dominate the market share after 2020.

The n-type silicon solar cells are promising alternatives with respect to their p-type counterparts because of higher energy potential conversion efficiencies and a large availability of the raw material [2]. Furthermore, the n-type silicon is known to have

several advantages over p-type. First, unlike the p-type substrates, n-type one are less sensitive to most metal impurities present in the substrates of solar grade, and that could be introduced in industrial processes to low-cost mass production [2]. Second instead, Czochralski (Cz) n-type substrates do not suffer degradation of SRH lifetime light-induced because of B-O type defects that are commonly found in industrial Cz p-type silicon [3]. As a result, minority carriers lifetime in n-type substrates are generally higher compared to their p-type counterparts [4].

Increasing the efficiency of solar cells requires a multitude of improvements in the different stage of manufacturing. The emitter is the most important element of n-type solar cell. A more promising technology is the direct thermal diffusion of boron

from a boron trichloride (BCl<sub>3</sub>) or boron tribromide (BBr<sub>3</sub>) source.

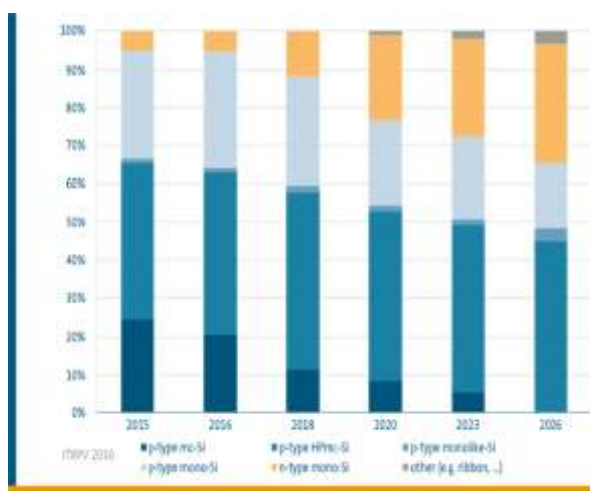


Fig1. Development of different C-Si materials in solar cell fabrication (ITRPV) [1].

Boron doping is a solution extensively investigated today by the scientific community [5, 6]. Boron is also evaluated as a solution to achieve the BSF (Back Surface Field) on the p-type cells [7, 8], but is rarely used commercially because of its long and costly development for this type of application. In literature, boron diffuses mainly through interstitial mechanisms instead of vacancy mechanisms [9]. Theoretical and experimental studies of Bracht [10] and De Salvador [11] proved that the responsible interstitials are  $I^0$  and doubly-positive interstitials ( $I^{++}$ ). Since the diffusing species is  $BI^0$ , they interact with negatively charged substitutional boron (B<sub>s</sub>) and become  $BI^+$  by capturing or losing a hole [12].

Process simulation provides an accurate prediction of the resulting doping profiles and provides precious advice in process optimization. In this work, the main motivation is to optimize the emitter, according to the various parameters involved in the diffusion (temperature, time, pressure ...). Using our

modeling of boron diffusion, we show that profiles boron can be numerically simulated for planar and textured silicon substrate. The profile measured by the mass of secondary ions Spectroscopy (SIMS) is compared with ones simulated using the Athena Silvaco® Simulator in which several diffusion parameters were modified and used to calibrate boron diffusion simulation. After calibration, the boron profiles on textured samples were obtained by process simulation.

## 2. EXPERIMENT

The Boron diffusion is briefly discussed here. The process of diffusion of boron was performed in an industrial furnace quartz tube and subjected to low pressure about 200-600 mbar. The gases are introduced by means of two different injectors positioned at the rear of the tube. N<sub>2</sub> is considered the carrier gas from the dopant source through a bubbler. Oxygen gas O<sub>2</sub> is introduced into the diffusion tube to ensure the oxidation of silicon at high temperatures. The diffusion process is achieved in two steps: a pre-deposition step which forms a borosilicate glass (BSG) and a layer in situ drive-in in which boron atoms diffuse deeper in the silicon substrate at highest temperature. In the pre-deposition step, Boron reacts with oxygen and forms a layer of B<sub>2</sub>O<sub>3</sub> which is located inside the borosilicate Glass (BSG for Boron Silicate Glass). Subsequently B<sub>2</sub>O<sub>3</sub> reacts with Si and forms SiO<sub>2</sub> and boron. The reaction can be written as



This reaction can be limited by Si oxidation:



The deposition of BSG has similar temperature dependence as the growth of phosphosilicate glass (PSG) [13]. At the involved temperatures, boron

diffuses into silicon matrix forming the p-n junction with the n-type base initially doped at  $5e^{15} \text{ cm}^{-3}$  with a bulk resistivity of  $1\Omega\cdot\text{cm}$ . All the wafers have a thickness of  $200\mu\text{m}$ .

### 3. SIMULATION APPROACH

Process simulations were carried out to reproduce the 1D boron depth profiles measured on planar sample using TCAD simulator software (SILVACO, the Athena module) [14]. As boron diffuses entirely via the interstitial mechanisms, the vacancy diffusion mechanisms were turned off in the simulations. Both neutral state interstitial  $I^0$  and doubly positively charged interstitial  $I^{++}$  were considered to contribute to the boron diffusion process similar as the approach taken by De Salvador and al [11]. The boron diffusion profile has a strong impact on the recombination activity in the emitter region via Auger and surface recombination. It is recommended to optimize the boron diffusion profile in order to minimize Auger and surface recombination while maintaining a reasonably low contact resistance. Boron profile optimization is typically achieved by tuning diffusion process. The Figure2 shows the experimental profile of boron doping ( $\text{BCl}_3$ ) during the emitter formation in n-type mc-Si obtained by Secondary Ion Mass Spectroscopy SIMS analysis. By considering a tolerable error range, good agreement with the experimental doping profile confirms the validity of the simulation model and the parameters that have been adopted. As expected, the profile presents a relatively high surface concentration for a depth of  $0.3\mu\text{m}$ .

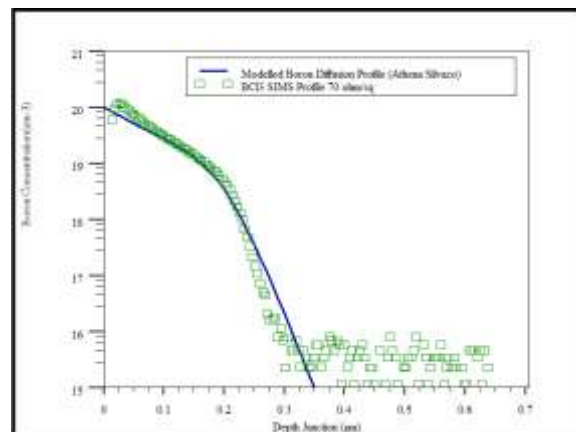


Fig.2. Modelling of the SIMS experimental boron diffusion profile.

## 4. RESULTS

### 4.1. Process simulation on planar samples

#### 4.1.1 Effect of diffusion temperature

The temperature variation is the simplest way to obtain different sheet resistance emitters. In figure 2, the variation of boron profile versus temperature is showed for a diffusion constant time. The sheet resistance has been measured by using a four probe method. As the temperature increases, the formed junctions are deeper and the sheet resistance decrease. These results were then compared with experimental data in order to be validated [15]. An increase of deposition temperature shows a strong influence on the boron dopant profile. This behaviour is explained by variation of the diffusion coefficient with temperature. For this reason, the process temperature to achieve the required junction depth has proven to be rather delicate. The advantage of this model is to determine the amount of boron be injected during the process for emitter concentration and desired depth.

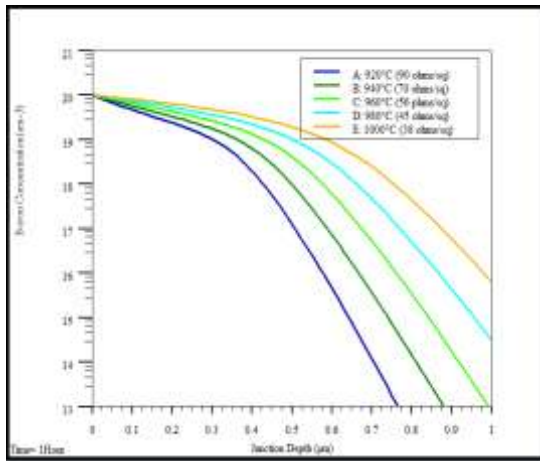


Fig.3. Boron diffusion profiles in silicon obtained with various diffusion temperatures for 1 hour diffusion time

4.1.2 Effect of diffusion time

Time is a very important parameter in the boron diffusion. Penetration of the boron atoms in the silicon controls also the desired junction depth. The time of the drive-in step, permit to give the monitoring of the junction depth. Indeed, BSG introduced in the pre-deposition step, acts as a constant dopant source in a time period at constant temperature. All these results confirm that the diffusion of boron in silicon is strongly affected by tube furnace conditions.

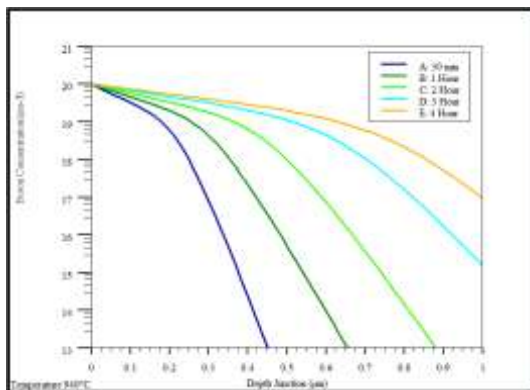


Fig.4. Boron diffusion profiles in silicon obtained with various diffusion times at 940°C.

4.2. Process simulation for pyramidal textured samples

1D boron profile has been successfully reproduced in the numerical simulation of the process. After optimizing the diffusion parameters on a planar surface, we proceeded to simulate 2D boron profiles. Characterization of boron distribution under textured surfaces is a challenging task. For textured surfaces we use the same thermal parameters profiles B and C (Figure.3), both the pre-deposition and

drive-in steps contribute to these profiles. The width of the simulated inverted micro-pyramids is 3.5(µm). Figure 5 shows the effect of the temperature diffusion on emitter junction depth. For profile C the junction depth is deeper compared to the one of profile B, the junction depth is 0.4µm and 0.3µm, respectively. The results of simulated 2D boron profile also show that the emitter junction depths differ considerably for the temperature diffusion.

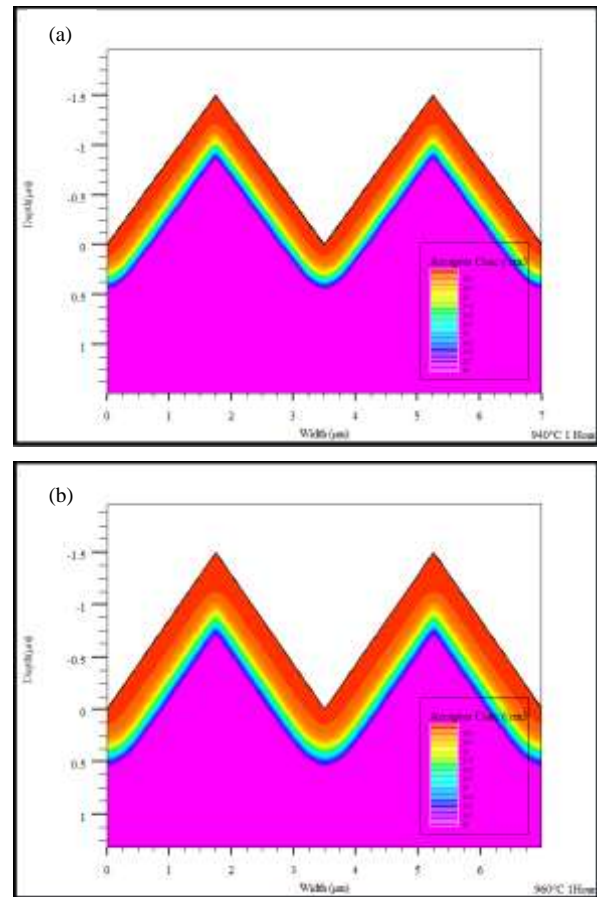


Fig.5. Simulated 2D boron profiles for two profiles: profile B (a) and profile C (b) on pyramidal textured surface.

Boron diffusivity is dependent on temperature, but also on the concentration of silicon self-interstitials [16]. Figure 6 shows the junction depth formed in top and bottom region to pyramid. For both profiles B and C, the junction depth is deeper at the top region of the pyramid than in the bottom region and sidewalls. Because of the pyramids geometry, concentration of silicon self-interstitials is dense in the top regions and is less dense in the bottom. This is a result of the geometry of the pyramids on the textured surface, which causes the unevenness of the emitter region.

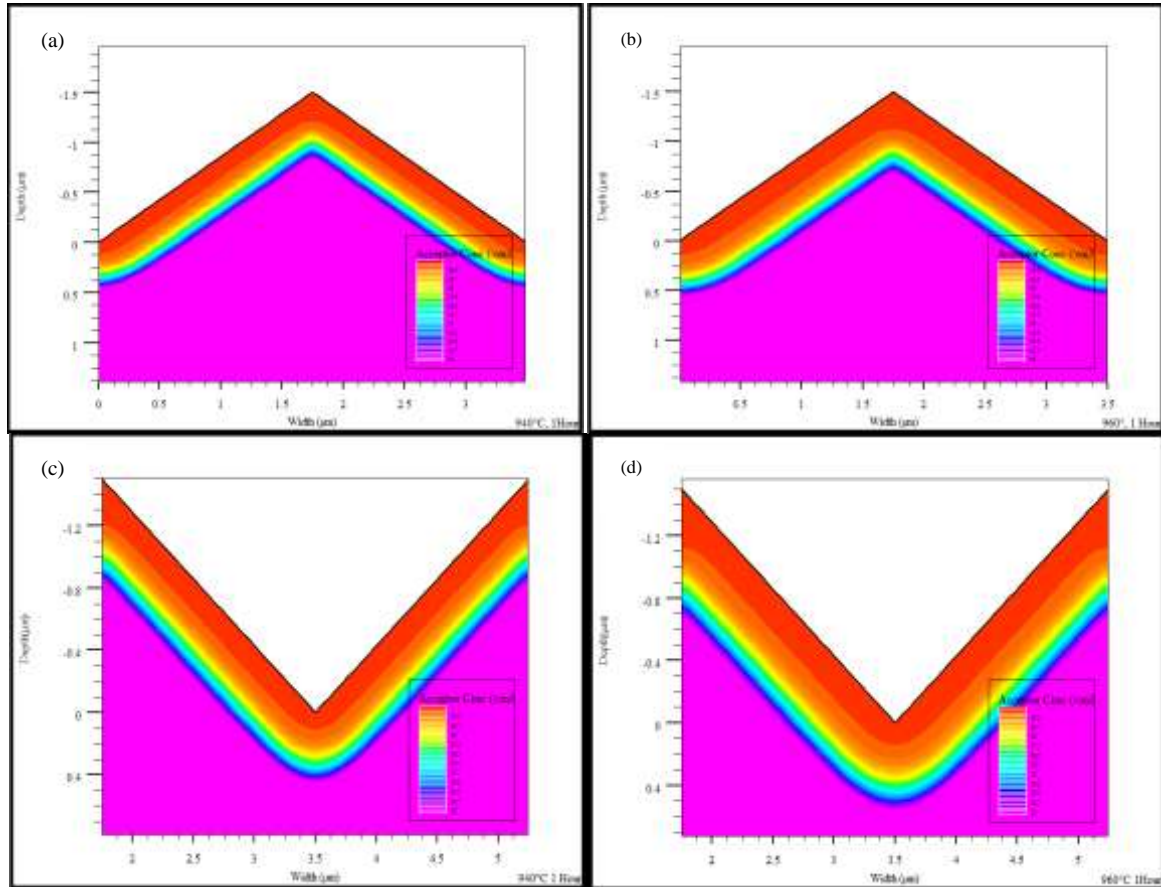


Fig.6. Cross-sectional image of emitter junction from SILVACO, Athena module. Profile B in (a) top pyramid, (c) bottom pyramid. Profile C in (b) top pyramid, (d) bottom pyramid.

## 5. CONCLUSION

For the N-type solar cell with the potential to improve its efficiency and reliability, the boron diffusion mechanism underlying the formation of p<sup>+</sup> layers has been studied for planar and textured surfaces. A suitable 2D numerical simulation of the boron diffusion profile for pyramidal textured samples is presented in this work. Simulated 1D depth profiles agree very well with measured profile. We have seen that the temperature and time of diffusion can control the junction depth and quality emitter formed to planar and textured. Our simulation results showed that deeper and shallower junctions were formed near the top and bottom regions in the textured Si surface, respectively. We propose that the nonuniform distribution of Si self-interstitials caused by the geometry of the pyramid texture leads to the enhancement or retardation of B diffusion, which is responsible for the formation of unevenness junction profiles in the p<sup>+</sup> emitter of textured Si solar cells

## 6. ACKNOWLEDGEMENTS

The authors thank the Ministry of Higher Education and Scientific Research and Technological Development of Algeria for funding the national research project PNR

## 7. REFERENCES

- [1] International Technology Roadmap for Photovoltaic (ITRPV), 2015 results, Seventh Edition, March 2016.
- [2] J. E. Cotter, J. H. Guo, P. J. Cousins, M. D. Abbott, F. W. Chen, and K. C. Fisher, "P-Type Versus n-Type Silicon Wafers: Prospects for High-Efficiency Commercial Silicon Solar Cells," *Electron Devices, IEEE Transactions on*, vol. 53, pp. 1893-190, 2006.
- [3] J. Schmidt, and A. Cuevas, *J. Appl. Phys.* 86, 3175, 1999.
- [4] D. Macdonald and L. J. Geerligs, *Appl. Phys. Lett.* 85, 4061, 2004.
- [5] J. Benick, B. Hoex, G. Dingemans, W. M. M. Kessels, A. Richter, M. Hermle, and S. W. Glunz, "High efficiency n-type silicon solar

- cells with front side boron emitter," presented at the 24th EUPVSEC, Hamburg, Germany, 2009.
- [6] V- D. Mihailetschi, G. Coletti, Y. Komatsu, L. J Geerligs, R. Kvande, L. Arnberg, K. Wambach, C. Knopf, R. Kopecek, and A.W Weeber, "Large area and screen printed n-type silicon solar cells with efficiency exceeding 18%," presented at the 23rd EUPVSEC, Valencia, Spain, 2008.
- [7] R. Cabal, N. Auriac, B. Grange, Y. Veschetti, and D. Heslinga, "Process Integration of Boron BSF by CVD Technique on Large Surface in P-Type Bifacial Solar Cell Process Flow," presented at the 25th EUPVSEC, Valencia, Spain, 2010.
- [8] S. Riegel, S. Gloger, B. Raabe, and G. Hahn, "Comparison of the passivation quality of boron and aluminium BSF for wafers of varying thickness," presented at the 24th EUPVSEC, Hamburg, Germany, 2009.
- [9] N-E-B. Cowern, K-T-F. Janssen, G-F.-A. Van de Walle and D-J. Gravesteijn, *Phys. Rev. Lett.* 65, 2434, 1990.
- [10] H. Bracht, H-H. Silvestri, I-D. Sharp, and E-E. Haller, *Phys. Rev. B* 75, 03521, 1 2007.
- [11] D. De Salvador, E. Napolitani, G. Bisognin, M. Pesce, A. Carnera, E. Bruno, G. Impellizzeri and S. Mirabella, *Phys. Rev. B* 81, 2010.
- [12] S. Mirabella, D. De Salvador, E. Napolitani, E. Bruno, and F. Priolo, *J. Appl. Phys.* 113, 031101, 2013.
- [13] P. Negrini, D. Nobili and S. Solmi, *J. Electrochem. Soc.* 122, 1254, 1975.
- [14] ATHENA User's Manual, Silvaco Int., Santa Clara, CA, 2010.
- [15] J. Armand, C. Oliver, F. Martinez, B. Semmache, M. Gauthier, A. Foucaran, Y. Cuminal, "Modeling of the Boron Emitter Formation Process from BCl<sub>3</sub> Diffusion for N-Type Silicon Solar Cells Processing", *Advanced Materials Research*, Vol. 324, pp. 261-264, 2011
- [16] Ning Steven, *Simulation and Process Development for Ion-Implanted N-type Silicon Solar Cells*, Phd thesis, 2013.

# Vegetation effects on urban street microclimate and thermal comfort during overheated period under hot and dry climatic conditions

Samira Louafi Bellara and Saliha Abdou

Laboratory "ABE", University of Constantine3 (25000), Algeria

Corresponding author: email:samira.louafi@univ-constantine3.dz

Received date: October 01, 2016; revised date: December 03, 2016; accepted date: December 11, 2016

---

## Abstract

*Urban Planning has a great impact on local microclimate which in turn affects the comfort and the space quality within a city. This directly influences the absorption and emission of incoming solar and outgoing long wave radiation, which has a significant impact on temperature variations within the street as well as the surrounding environment (Urban Heat Island). Green areas play the most significant role in the city; they provide shade that helps to lower surface temperatures. They also help to reduce air temperatures through the process of evapotranspiration, dissipating ambient heat. The method is experimental, in which empirical measurements are carried out in different stations in a street of the city center of Constantine (Algeria) during overheated period. Moreover series of field simulation are done using a software tool: "TownScope3.2".*

*The results confirm the importance of shade by the vegetation on microclimate and human comfort, and show a positive correlation between the air temperature,  $T_{mrt}$ , and PET in hot seasons. Vegetated urban space influences the quality of perception, the creation of urban ambience and improves pedestrian's thermal comfort. That increases the frequency of use of outdoor spaces for such climate.*

**Keywords:** *Vegetation, Vegetation; Microclimate; Thermal Comfort; Hot and Dry Climate; Urban street*

---

## 1. Introduction

The urban fabric changes the energy balance through its different reflections and heat absorptions due to roughness and absence of green areas, giving rise to the Urban Heat Island phenomena.

The shade is in general the principal outside requirement during overheated period for areas with hot and dry climate. In urban environments, green spaces have proven to act as ameliorating factors of some climatic features related to heat stress, reducing their effects and providing comfortable outdoor settings for people [1]. This shade reduces solar flows considerably, by limiting the heating of surfaces which normally should be sunny, also reduces thermal radiative flows.

It is well known that the presence of vegetation modifies the microclimate (light, heat, wind, and humidity) through shade and evapotranspiration, and also influences the perception of urban spaces by the users [1,2].

On the one hand, the use of plants to improve urban heating is one strategy that has generated significant interest [3,4]. Trees and buildings existing singly or in clusters create strong spatial variability in local heat transfer fluxes that define urban microclimates within the urban canopy layer [5].

Trees planted along the streets and in the parks, around the houses or shops or in the green areas throughout the city improve citizens' quality of life and also the quality of the air and water. On the other hand, the urban green areas offer the possibility of recreation, and make districts more pleasant [6].

The use of vegetation as a strategy to moderate the urban heat island (UHI) and improve the microclimate has been discussed in many researches [7,8]. For the hot and arid climates, the best use of the vegetation should take advantage from its shading aspect to reduce the intense solar radiation in summer as the overheating is mainly due to the heat storage by the sunlit surfaces. Vegetation should be integrated within the built up areas to improve the immediate environment of each construction, because the two main effects of vegetation are the shading impact on solar radiation and the conservation of canopy temperatures close to that of air, between 20°C-35°C, which remain below the temperatures of the surfaces of common urban materials such as asphalt, concrete blocks, etc [9,10].

Researchers like: Grimon, Oke and Cleugh (1993), found that in a hot-dry climate the temperature in a tree-vegetated suburban area in Sacramento, was 5°C to 7°C cooler than in a mineral one. One study indicates that a significant temperature difference of up to 6°C on air temperature 2m above the ground was found in the

summer season between artificial urban materials and vegetated areas in Beirut [11].

Even more [12,13], confirm the importance of tree shading effect on thermal comfort and the influence of reflected and transmitted solar infrared radiation on the energy budget of humans and buildings in their surroundings.

Shading a surface from receiving direct solar radiation is the most important, the first strategy for reducing heat load in a hot and dry climate. Field studies to evaluate the thermal environment have been performed in cities with hot and dry climate; the geometry and orientation has a wide relation to solar exposure of the urban canyon during the day. This one has a considerable effect on solar shading and urban microclimate [14]. Bourbia and Awbi (2004) found that the higher H/W ratio and smaller SVF has a cooler environment and floor-shading fraction in summer increase with increasing (H/W ratio).

Under hot and dry climate at Constantine city by Bourbia and Boucheriba (2010), one study discuss the relationship between canyon geometry (size, orientation) and SVF, how it's impacts on air and ground surface temperatures within the urban street, was done in order to evaluate the impact of geometry on the urban climate. They found that the open stations are exposed to the sun all the day and height albedo of the sol participate in reflecting the solar energy to the outdoor space and participate in increasing the UHI [15].

Further to that a study by Louafi and Abdou (2013) in same city with an open urban space with row trees and a presence of massive vegetation and a mineral one for improving the effect of vegetation on using outdoor space.

Where measurement and observation method was done. Results show that controlling the sky view factor and inclusion of vegetation can reduce temperatures in outdoor spaces [16].

In this present paper a canyon street with different SVF and with the presence or absence of row trees are investigated, microclimate and thermal comfort based on field measurements and questionnaires during the summer, and series of simulation has done, the aim is to assess whether people located under tree shade experience comfort or stress in open spaces during hot-dry season. the study tries to:

- Investigate vegetation' effects in five different spaces on thermal conditions in outdoor spaces with different ratio and SVF.
- Compare the performance of an area shaded by trees to insulated one;
- Discuss whether trees shade affect people's thermal comfort in hot-dry climate, and

- Evaluate outdoor thermal comfort based on comfort indexes "predict equivalent temperature" (PET) and mean radiant temperature (T<sub>mr</sub>); and
- Try to highlight the role of shade on soil temperature and cooling effects of urban planning.

## 2. Site Investigation

The investigation was conducted in Constantine City (Algeria), which is located at 36.17\_ North and 06.37\_East. The altitude is approximately 687m above sea level. This city is characterized by a semi-arid climate that is hot and dry in the summer, with an average maximum temperature of 36°C occurring at 15h00 and an average humidity of 25%. In the winter, the area is cold and humid. In addition, the intensity of solar radiation over this region is high, with clear skies and sunny periods existing during a large portion of the day.

The wind direction comes relatively from the North, with an average speed reaching 2.1 m/s at the meteorological station. All these factors contribute to the climatic harshness of the city. The investigated site is located in the city center.

The city center has a dense traditional urban fabric (up to 80%) deprived from vegetation; and a colonial fabric which was grafted on part of traditional fabric and around this initial core. The presence of the vegetation is not regular there (fig.1).

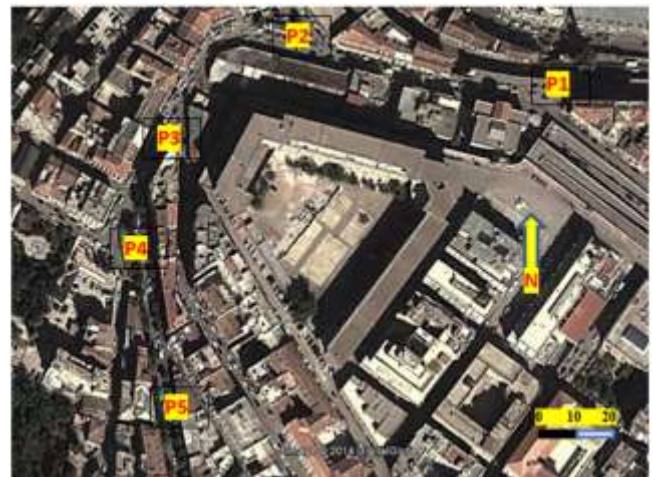


Fig.1. Stations of site measurements. Source: Google Earth 2014

### 3. Methodology

In order to evaluate the effect of vegetation cover on air and ground surface temperatures within the urban street, a series of measurements were collected from five stations that were selected based on variation of the SVF, H/W ratio and presence of trees (fig.1 and Table1).

The measurements were performed in summer during the month of July 2013, representing the hottest period. These were carried out simultaneously over a two weeks period, and one typical daily cycle has been selected to represent each of the detailed monitoring periods. Air temperature data were collected using digital instruments (Multifunction instrument (LM800), Pho-radiometer HD2302.0 with several probes) with an accuracy of ±0.2. The measurements located in the built-up environment at a height of approximately 1.5 m and were recorded every 2 hours at each station from 6:00 to 20:00 each day. Fish-eye photographs were taken at each station at both sensor heights (approximately 1.5 m above ground) with a Nikon 8 mm fish-eye lens (Picture angle of 180°). Consequently, thermal comfort was included in the study, with interviews and questionnaires to assess people’s thermal sensation in different situation coverage street with trees and without trees in the day.

Series of field simulation are used by software tool, TownScope3.2. The objective is to compare the performance of an area shaded by trees to a full insolated area for two kinds of street located in this climate (dry and hot) P1 (SVF=75%, Albedo= 0.28, H/W= 1.35) and P5 (SVF=5%75%, Albedo=0.200, H/W= 1.13)

**Table 1.** Characteristics of Measurement station & Fish-eye photographs.

Point of measurement	Vertical fish-eye	Horizontal fish-eye
<b>P1</b> SVF= 75% Albedo= 0.28 H/W= 1.35		
<b>P2</b> SVF= 1% Albedo= 0.16 H/W= 0.46		
<b>P3</b> SVF= 30% Albedo= 0.29 H/W= 1.34		
<b>P4</b> SVF= 10% Albedo= 0.19 H/W= 1.3		
<b>P5</b> SVF= 5% Albedo= 0.20 H/W= 1.13		

### 4. Result and Discussion

The geometry of urban street plays a decisive role in urban heat island mitigation [15,17]. Moreover, Inclusion of vegetation can reduced and controlling the sky view factor. Shade trees reduce heat gain by directly shading buildings and also by evapotranspiration. Adding vegetation into the environment, planting trees can mitigate UHI, reduce energy use and improve air quality. This study aims to verifie and discuss how vegetation can play an important role on urban microclimate for different types of urban design.

#### 4.1. Impact of the Vegetation on Air Temperature

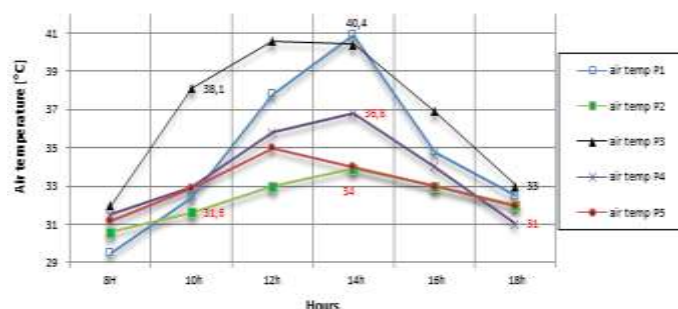


**Fig.2 .** Variation of air temperature in various stations period July.

Figure 2 shows the air temperature evolution during a typical summer day at the five stations of measurement. It shows that open space without trees is warmer from 10h00 to 16h00 than the vegetal areas under trees coverage, which is consistent with previous studies of the literature on this subject [1,2,12,16,18 and 19]). The air temperatures in all stations are higher than 32°C during the day, but the temperatures recorded in Station1and Station3 remain higher than that in the stations Station 2 and station 5 with a variation between -3.6°C and -6.4°C at 14:00 and variation of -3.9°C after mid-day 16:00 this result agrees with the results of many studies[11,20-22].

#### 4.2. Impact of the Vegetation on Air Humidity

The relative humidity depends on the temperature and the quantity on water contained in the air. The values of air humidity at the beginning of the day are very high; on the other hand those of after midday are most significant [23]. The evapotranspiration of a tree can reach up to 400 liters per day, which represents a cooling effect equivalent to 5 units for 20 hours means hot and dry climate [24]

According to the graph in Figure 3, there is a negative correlation between relative humidity and air temperature. It is noted that vegetated or green stations ( P2 and P5) registered higher values of air humidity than station P1. The highest value of relative humidity is recorded at 18:00 (hours) in the station P4 in the street with trees alignment and near a square, note a variation of 23%, compared to station P1 (with no trees and same space configuration).

At the time of the maximum of energy of 12:00 (hours), we observe variation between 3.5% and 10.5% in stations P1, P3 and P4. while the one cumulates solar energy, the

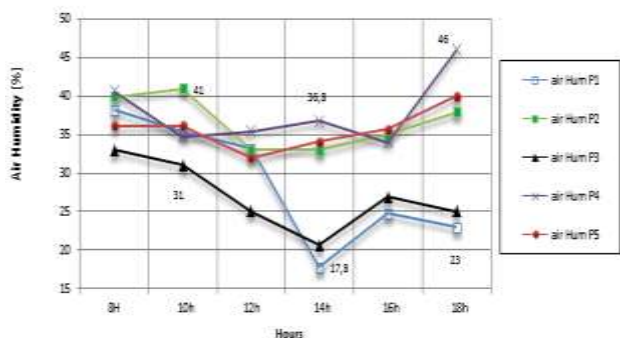


Fig.3.Variation of air humidity in various stations period July.

### 4.3. Impact of the Vegetation on Ground Surface Temperature

According to F Bourbia and F Boucheriba (2010)[15], an open and exposed nature of an urban street can result in an increase in the daytime air temperature within the canyon. He showed that This effect can be reduced by controlling the sky view factor and inclusion of vegetation. For that another purpose of this study was to examine the correlation between shade by trees and ground surface temperature of the streets. The same kind of analysis used for air temperature, was performed for the soil surface temperature inside the designated urban spaces. The foliage of a tree can filter 60 to 90% of solar radiation and crouching vegetation also reduces the solar radiation reflected by the ground [12,26,27]

The soil temperatures of stations P1 and P3 ( highest ratio H/W, lowest SVF and mineral soil surfaces) compared to those of station P4 (tree shaded area with dense foliage coverage about 80%) mentions a difference up to 10°C, and this result is in accordance with those of [14,15], floor-shading fraction in summer increases with presence of trees.

### 4.4. Cooling effect of Vegetation

A comparison between the weather station (open site) and the average temperature measured at the selected site, confirm that the open site field temperatures are lower than the urban areas, with a difference ranging between 3 and 6 °C (Fig. 5).

other one records an increase in the water content, this rise is explained by the effect of the latent heat of the vaporization of the vegetation [25,26].

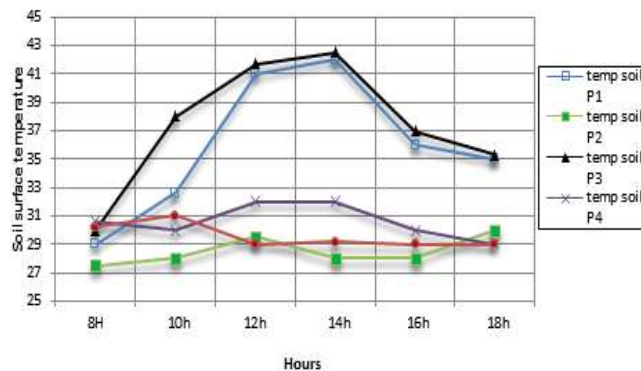


Fig. 4.Variation of soil temperature in different stations period of July

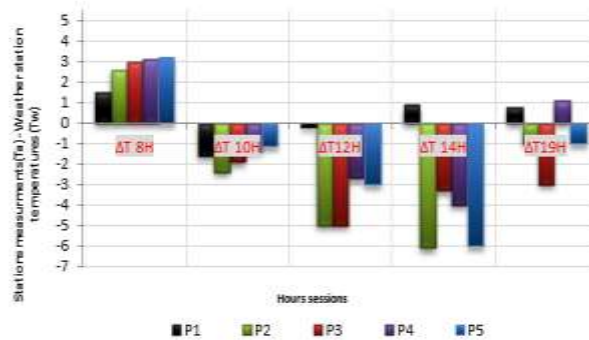


Fig.4.The range of deviation between measured stations and weather.

This difference in temperature is mainly caused by the nature of percentage of reflective surfaces and presence of vegetation. These surfaces tend to have high heat capacities, and are thus efficient at absorbing and reradiating the sun’s energy later on [29].

The difference appears especially during midday session of measurements Those of the afternoon show well the moderating effect of heat in spaces covered with vegetation. The effect of permanent shade of the vegetable is translated by the absorption of the sun rays and the contribution in air humidification.

In contrary area without vegetation presents a heat amplification that is due to mineralization of surfaces, important sky view factor and long day exposure to sun rays.

Furthermore, the relationship between building height and street width is also considered to be the main contributor to the heat island effect in cities. Also, the maximum heat island intensity has been proven to correlate well with the mean sky view factor of the city center for a number of cities around the world [29].

For that vegetation in urban planning create permanent shadows on the ground and the walls, so allowing the habitability of outdoor spaces.

4.5. Thermal Comfort Analysis

The comfort parameters and indices adopted for this study are: air temperature (Ta), mean radiant temperature (Tmrt), and physiologically equivalent temperature (PET).

The mean radiant temperature is an important parameter affecting the human well-being. It expresses the radiative effect of the whole of the environment. Tmrt varies according to the importance of the solar radiations received and reflected by surfaces. Its maximum value reached 63.7°C for station P1.

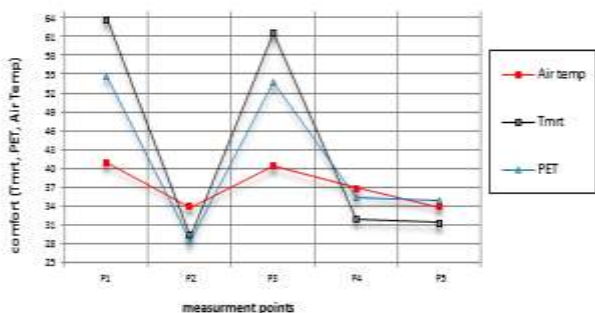


Fig.5. Relation between air temperature, PET and Tmrt in different stations.

Thermal comfort on the level of the two calculated stations is evaluated according to the index of comfort “physiologically equivalent temperature” PET. This index is between 28.5 °C and 35.3°C in the stations where there are shade of the trees (P2, P4 & P5) and about 54.6°C and 53.7°C in the mineral stations (P1 & P3). The value of PET in stations with important shade is lightly hot during all the day. Nevertheless, thermal environment in Station P1 is extremely hot and makes uncomfortable felt in the space (Fig. 6).

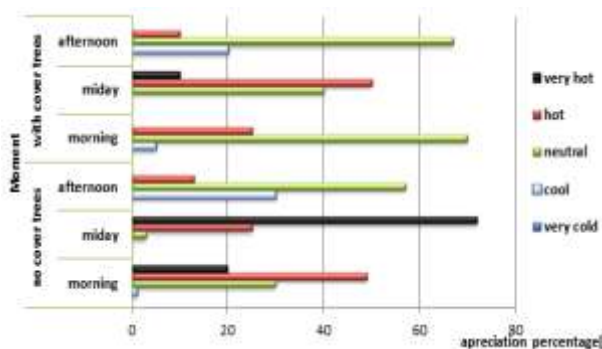


Fig.6. Perception of the urban street in different moment of the day (covre trees and no covre trees)

By questionnaire the number of people and activities outdoors are influenced by the solar radiation (Fig.7). And people from different social backgrounds in hot and dry climates have different approaches to the use of outdoor spaces. The study indicate an appreciation of neutral predominate under spaces with trees coverage witch has a positive condition in comparison to that in streets with no coverage.

The result reveals that there is a great influence of vegetation on human sensation and on PET since when rows of trees are added on the pavement, PET values are lowered due to the shading of the pedestrian pavement. Presence of vegetation optimizes the microclimatic environment for pedestrian’s thermal comfort in urban spaces, under hot and dry climate.

Consequently, in urban environments that have low aspect ratios, the influence of vegetation on outdoor thermal comfort is significant. Similar results found that the direct solar radiation under a tree canopy strongly decreases [30,31].

4.6. Results of Simulation

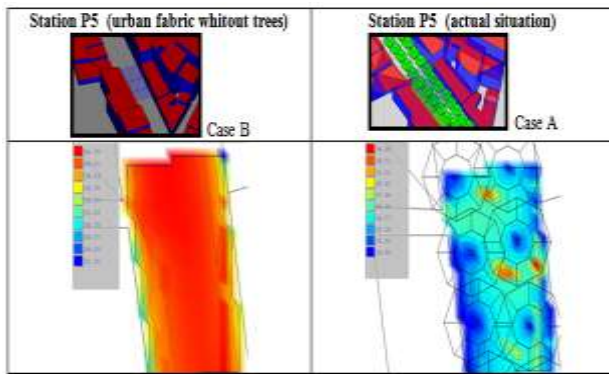
The investigation is based on a three-dimensional model TownScope 3.2 which simulates the microclimate conditions in an urban environment. It is a 3D simulation model developed for numerical modeling of urban microclimate and again the majority of atmospheric processes that affect the microclimate.

The impact of vegetation can be quantified at different levels. Indeed, the consequences of plant presence reflect the microclimatic scale in terms of: quantity of transmitting radiation, air temperature, leaf temperature and comfort.

Table 2.Result of comfort according to the average of the air temperature at 12:00

	Da (m)	Da /W	Air temp (°C)	Air hum (%)	Rad (w/m-²)	Tmrt (°C)	PET (°C)
CaseA (with trees alignment)	10	1.33	24,84	50	130,14	16,2	20,4
CaseB (without trees)	/	0	38,16	20	911,57	69,1	56,9

Table 3. Air temperature of simulated zone [P5] (effect of presence of trees)



In the following tables (table 2 and table 3) the results of the simulation of station P5 show that the presence of trees in actual situation provides shade and minimize global radiation compared to simulated situation without trees with an mean difference of  $890 \text{ w. m}^{-2}$ . This result can improve comfort in these areas. For the P1 were in actual situation trees have an effect on the air temperature, can reduce air and soil temperature about  $13.7^\circ\text{C}$ .

Similarly, the global radiation in the situation (case B) is much higher than that of the actual situation (case A) at 12h: 00 ( $911.57 \text{ W/m}^2$  against  $130 \text{ W/m}^2$ ). The vegetation keeps soil cooler and avoids direct, diffuse and reflected sunlight that may affect the cool buildings [33]. The presence of the vegetation modifies the solar radiations in outside space. According to [34] the improvements due to the effect of the vegetation in the urban outdoor space are sensitive to create sources of freshness. Also, a row of trees decreases the temperature of the surrounding air by  $2^\circ\text{C}$ . The simulation shows that a variation in the air temperature of  $2.5^\circ\text{C}$  to  $3^\circ\text{C}$  in open spaces according to the quantity of the shadow and the sunshine duration.

In the station P1 with no vegetation and open space (actual situation) the areas is exposed in all the day to solar intensity (fig.8). Introducing row of trees global radiation reduce sun duration about half to one hour and procure shade witch make comfort; We can note a variation in the quantity of global radiation under tree canopy in open spaces according to the quantity of the shadow. The  $T_{\text{mrt}}$  index is about  $70.6^\circ\text{C}$  in the station P1 where there is no shade and it is about  $28.8^\circ\text{C}$  under crown trees, in modified landscapes of the space.

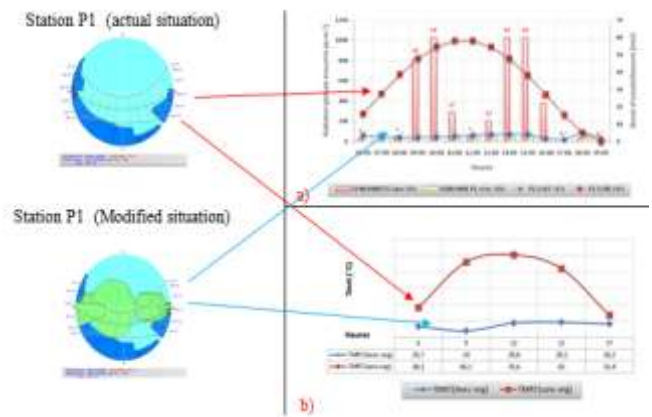


Fig.7 simulation results a) global radiation and sunshine duration in P1 simulated (with and without trees) b)  $T_{\text{mrt}}$  values in P1 of the two situations

## 5. Conclusion

In urban environment vegetated spaces, acting as temperature buffer, have important climatic function such as providing shadow, windbreaks and reducing the heat island effect.

The vegetation makes esthetic improvements to an environment differently dominated by asphalt and concrete. The presence of vegetation modifies the solar radiations in outside space, the temperature and the relative humidity. It has its own cooling system imparted by the process of evapotranspiration; which transforms part of the radiation in latent heat flux. Moreover vegetation can affect the microclimate in many ways, in particular reducing air temperature, soil temperature compared to stations without trees, while getting shades.

In the present consideration, in external environment, the presence of trees has positive effects on space shading, air and soil temperatures and on the microclimatic conditions. The improvement concerns air temperatures and relative humidity as a difference of about 3 degrees and 4,4% are retained respectively.

According to the results of measurements and simulation, we can retain the following projecting points:

- 1) The presence of the vegetation modifies solar radiations effects in external space, air temperature, soil temperature and the air relative humidity;
- 2) Vegetalized space develops lower air temperatures and higher air humidity, thus offers more pleasant comfort and sensation.
- 3) There is a correlation between the air temperature, mean radiant temperature ( $T_{\text{mrt}}$ ), and physiologically

equivalent temperature (PET) in hot seasons, which influences the comfort.

4) Improvement of the urban environment quality by mitigation of the urban heat island.

Very often Trees constitute an important component of the opened external space, which strongly contributes to the environmental quality. For that the valuation of the essential axes is recommended by the deciduous tree implantation for more refined environment.

In addition, the trees increase comfort sensation in external space on period of heat stress in hot and dry Mediterranean climate. where urban planning has a significant impact on the UHI in hot and dry climate and for that we recommend mitigating actions from an urban planning with vegetation cover in open spaces especially and design perspective accordingly.

## References

- [1] M. Nikolopoulou, N.Baker, and K. Steemers, "Thermal comfort in outdoor urban spaces: Understanding the human parameter," *Solar Energy*, vol. 70, no. 3, pp. 227-235, 2001.
- [2] I. Knez . S. Thorsson, Influences of culture and environmental attitude on thermal, emotional and perceptual evaluations of a public square, *Int J Biometeorol* (2006) 50: 258-268
- [3] D. J. Sailor, "Simulations of annual degree-day impacts of urban vegetation augmentation," *Atmospheric Environment*, vol. 32, pp. 43-52, 1998.
- [4] J. E. Simpson, and M. Pherson, "Simulation of tree shade impacts on residential energy use for space conditioning in Sacramento," *Atmospheric Environment*, vol. 32, pp. 69-74, 1998
- [5] T. R. Oke, . "The micrometeorology of the urban forest," *Philosophical Transactions of the Royal Society of London* 1989, vol. 324, pp. 335-349.
- [6] Sreetheran, M., Philip, E., Adnan, M., and Sitizakiah, M; "A historical perspective of urban tree planting in Malaysia," *Unasyva* 223, vol. 57 (2006), pp. 28-3
- [7] M.Taha, S.Douglas, J.Haney, 1997. "Mesoscale meteorological and air quality impacts of increased urban albedo and vegetation". *Energy and Buildings*; 25: 169-77.
- [8] E. Ng, "Policies and technical guidelines for urban planning of high-density cities- air ventilation assessment (AVA) of Hong Kong". *Building and Environment* 2009. 44:1478-88.
- [9] M.Nikolopoulou, and K.Steemers. "Thermal comfort and psychological adaptation as a guide for designing urban spaces," *Energy and Buildings*, vol. 35, no. 1, (2003) pp. 95-101.
- [10] M.Boukhabla, and D.Alkama, 2012. Impact of vegetation on thermal conditions outside, Thermal modeling of urban microclimate, Case study: the street of the republic, Biskra. *Energy Procedia* 18 73 - 84
- [11] N.Kaloustian, and Y.Diab ; 2015. " Effects of urbanization on the urban heat island in Beirut". *Urban Climate* 14 (2015) 154-165
- [12] B. Kotzen,; "An investigation of shade under six different tree species of Negev desert towards their potential use for enhancing microclimatic conditions in landscape," *Architectural development. Journal of Arid Environments*, 2003. vol. 55, pp. 231-274.
- [13] M. F. Shahidan,; M. K. M. Shariff, P., Jones et al; "A comparison of *Mesua ferrea* L. and *Hura crepitans* L. for shade creation and radiation modification in improving thermal comfort," *Landscape and Urban Planning* 2010., vol. 97, pp. 168-181.
- [14] F. Bourbia, and H.B. Awbi, "Building cluster and shading in urban canyon for hot-dry climate". Part 2: shading simulations. *Renewable Energy* 2004.; 29:291-301.
- [15] F. Bourbia, and F. Boucheriba, "Impact of street design on urban microclimate for semi-arid climate (Constantine)". *Renewable Energy* 2010. 35 343-347
- [16] S. Louafi Ep Bellara ; S. Abdou; "Benefits and well-being Perceived by Pedestrian in Vegetated Urban Space in periods of Heat Stress", *IACSIT International Journal of Engineer and Technology*, vol 5 N°1, February 2013 PP. 20-24
- [17] M.Djenane, A.Farhi, M.Benzerzour, and M. Musy. "Microclimatic behaviour of urban forms in hot dry regions, towards a definition of adapted indicators", 25th International Conference on Passive and Low Energy Architecture PLEA2008, Dublin.
- [18] S. Toy and S.Yilmaz,; "Thermal sensation of people performing recreational activities in shadowy environment: case study from Turkey," *Revue/Theatrical and Applied Climatology*, vol. 101, no. 3-4, 2011. pp. 329-343.
- [19] S.Louafi Bellara, and S.Abdou; "«Effect of shading on thermal and visual comfort in external spaces. Case of esplanade of the university Mentouri of Constantine, east of Algeria»; *Revue «Nature and Technology»*, vol. 7, no. 7, June 2012.
- [20] H.Upmanis, "Daytime summer temperature differences between a green area and its build-up surroundings in a high latitude city". In second urban environment symposium and 13th conference on biometeorology and aerobiology, November, 2 - 6. Albuquerque: American Meteorology Society 1998. p 210
- [21] C.Grimmond, T.Oke, and H.Cleugh, 1993 "The role of rural in comparison of observed suburban-rural flux difference," in *Exchange Processes at the Land Surface for a Range of Space and Time Scales*, Proceedings of the Yokohama Symposium, July 1993.
- [22] M.Thitisawat et al, Adaptative outdoor comfort model calibration for a Semitropical region, PLEA 2011, louvain-la-neuve, Belgium (juillet 2011).
- [23] S. Streiling and A.Matzarakis, "Influence of single and small clusters of trees on bioclimatic of city: Case study," *Journal of Arboriculture*, vol. 29, no. 6, (2003) pp. 309-31.
- [24] Y. J. Huang et al. "The potential of vegetation in reducing summer cooling loads in residential buildings". Berkeley; 1987: University of California, 32
- [25] C. Echave, and A.Cuchi. "Habitability Method Analysis in Urban Spaces". "PLEA 2004-21th congrés international, sustainable architecture de passive and

- low energy architecture,” Eindhoven, pp. 19-22, September 2004.
- [26] M. F. Shahidan, and P. Jones; 2008. “Plant canopy design in modifying urban thermal environment: Theory and guidelines,” PLEA -25th Conference on Passive and Low Energy Architecture, Dublin, 22nd to 24th October 2008
- [27] R.D. Brown, T.J. Gillespie, Microclimate Landscape Design: Creating Thermal Comfort and Energy Efficiency. John Wiley & Sons, New York 1995.
- [28] D. Solecki William, C. Rosenzweig, L. Parshall, Gr. Pope, M. Clark, J. Cox; et al. “Mitigation of the heat island effect in urban New Jersey”. Environmental Hazards (2005); 6:39-49.
- [29] TR. Oke; Canyon geometry and the nocturnal urban heat island: comparison of scale model and field observations. Journal of Climatology (1981);1: 237-54.
- [30] F. Ali-Toudert, and H. Mayer “Effects of asymmetry, galleries, overhanging facades and vegetation on thermal comfort in urban street canyons”, Solar Energy 81(2007): 742-754. AlHemaidi, W.K.
- [31] J.M. Ochoa, and R. Serra “Vegetation influences on the human thermal comfort in out-door spaces”, (2009) Retrieved June 10, 2010, from School of Architecture of Barcelona, Dept. Construccions Arquitectòniques I & Dept. Física Aplicada, Website: <http://www.fa.upc.es/personals/jroset/lyonvege.html>
- [32] H. Akbari, M. Pomerantz, Taha, H ; “Cool surfaces and shade trees to reduce energy use and improve air quality in urban areas” Solar energy; Vol. 70, (2001) p. 95-310.
- [33] A. Dimoudi, M. Nikolopoulou; “Vegetation in the urban environment: microclimatic analysis and benefits, Energy and Buildings”, Vol. 35, No. 1, (2003) p. 69-76.

# Preparation, mechanical properties and fracture of the optimal surface modified alumina silicate based ceramic particles reinforced polymer composites

S. Zahi

*Centre de Développement des Technologies Avancées (CDTA), Cité 20 Août 1956 Baba Hassen, Alger, Algeria.  
gsouilah@gmail.com, zsouilah@cda.dz (Souilah Zahi).*

Received date: November 10, 2016; revised date: December 03, 2016; accepted date: December 11, 2016

---

## Abstract

Polyester resin was replete with a high percentage of surface-modified fly ash ceramic particles using a combination of sol-gel and handlay-up techniques. The characterizations of the fly ash powder showed that the ceramic particles were the spherical solid type and composed of both the glass and crystal phases. The composites were subjected to the mechanical and Charpy impact tests as well as the fracture studies. Consequently, the hardness was found to increase linearly. The required results derived from both the mechanical and impact tests indicated that a positive correlation was obtained. The tensile strength of the higher percentage was lowered due to the existence of large size particles and the elongation at break was decreased due to the restriction of the polyester molecular chain flexibility. Finally, the fracture surfaces of the excellent compositions indicated that the particles had strongly bonded with the polyester matrix. This is mostly due to the existence of reasonable (-OH) groups on the particle surfaces.

**Keywords:** *Filler; Polymer; Fracture; Tensile strength; Impact strength*

---

## 1. Introduction

Nowadays filled polymer composites are finding a growing demand in various engineering applications. The improvement of the mechanical, electrical, thermal and optical properties of the polymers, while reducing their costs through the addition of the filler materials and utilizing advanced processing routes, has become an extremely popular research interest [1]. Among the commonly used polymers, include thermoplastic polyesters; usually, they are organic compounds that are chemically based on carbon, hydrogen, and other nonmetallic elements such as O, N, and Si. The polyesters are used in applications such as appliance parts, electric and electrical components, HVAC components, industrial light housings, and automotive. However, because of their excessive brittleness, these thermoset polyesters are being nearly useless if not combined with fillers. On the other hand, fly ash utilization has become a nuisance to governments as much more is produced each day. Fly ash inorganic components are finely divided residues, which are becoming one of the

principal raw materials. A fly ash has several advantages; it contains ceramic materials such as silica and alumina. Silica provides the highest hardness, while alumina is an electrical insulator with a relatively high thermal conductivity.

At present, works are being done to investigate the properties of the fly ash-reinforced polymers. Challenging efforts are being focused on treating the surface of the fly ash with chemical solutions to build a strong interface adhesion between the fly ash particulates and the selected matrix. There are reports made with the addition of unsilanized mica into unsilanized fly ash reinforced polyester, of which an increase of the tensile strength and elongation was reported [1]. The surface-coated fly ash used as filler in biodegradable polyvinyl alcohol (PVA) composite films showed 33% higher strength than those of unmodified fly ash [2]. A surface modified fly ash improved an interface adhesion between fly ash and polyether ether ketone (PEEK) with some improvements in the mechanical and Charpy impact strengths [3]. The study of the surface modification of

the purified fly ash and application in the polymer also showed that a rough surface of the composite fly ash in the  $\text{Ca}(\text{OH})_2\text{-H}_2\text{O-CO}_2$  system improved the interface when blended with polypropylene (PP) [4]. However, there are limited studies done on the fly ash-reinforced polyester resin matrix. There are efforts reported in the study of the polyester resin modified with maleated castor oil while filled with fly ash particles [5]. The polyester resin as an organic binder contained fly ash as a fine aggregate material replaced the normal river sand in polymer concrete systems [6].

In the present paper, the study of the polyester reinforced with different sizes of the fly ash particles of the previous work [7] was extended. The chemical and physical characterizations of the selected fly ash were carried out and applications in the unsaturated polyester were reported. Accordingly, the required properties derived from both the mechanical and Charpy impact tests of different compositions, using the surface-modified precipitated fly ash, were primarily chosen. From the fracture studies, a very distinguished interface for every particle was achieved. This advantage indicates that the methods of the fabrication are effective.

## 2. Materials and Methods

### 2.1 Materials and Sample Preparations

The poly(methyl methacrylate) (PMMA) orthophthalic unsaturated polyester (UP) resin was purchased from a company and the fly ash (FA) powder was collected from a Coal Power Plant located in Malaysia. The surface-modified fly ash was used to study various properties. The preparation of the fly ash by the sol-gel technique was as follows: 30 g of FA particles were mixed with 30 ml of ethanol solution ( $\text{CH}_3\text{CH}_2\text{OH}$ ) and 20 ml of distilled water ( $\text{H}_2\text{O}$ ). The mixture was stirred uniformly by using a hot plate stirrer at 70 °C for almost 30 min. The surface-modified FA was then dried in an oven at 110 °C for 1 h. Next, neat polyester and FA-reinforced polyester samples corresponding to the equation  $UP-\alpha FA$  ( $\alpha = 0-50$  wt.%) were prepared by the hand lay-up technique as follows: the  $\alpha$  wt.% of the FA was mixed homogeneously together with the matrix system consists of polyester and 1% hardener. The mixture was poured into a mold fabricated for three specimens (tensile, Charpy impact and hardness tests). The mold was fabricated on a 20×12.7×1.6 cm aluminum block. The specimens were allowed to cure for about 1 hour at room temperature before removing them from the mold. They were then cured at room temperature for 24 h before post-curing them in an oven at 90 °C for 1 h.

### 2.2 Characterizations and Testings

Particle size distributions of the surface-modified FA particles were analyzed using Mastersizer 2000 particle size analyzer, Malvern Instruments Ltd. Consequently, the powder was pulled from the machine vacuuming system of the analyzer at a pressure of 1 bar and then a computer software was used to calculate the particle sizes. The as-received FA was used to determine the density using the Archimedes's method. The phase identification was performed by XRD analysis using the X'Pert PRO Diffractometer from Panalytical B.V Company. Thus, diffracted X-ray beams were collected and compared to the standard patterns available with expert high score computer software library. The hardness test was done with the Mitutoyo Vickers hardness tester. Accordingly, for each specimen, an average of 20 hardness values was taken at 9.81 N load applied for 12 seconds. The tensile specimens were prepared according to ASTM D-638-I standard, having a gauge length of 50 mm, a gauge width of 13 mm and a thickness of 3.2 mm. The tensile test was done on AG-1 100KN SHIMADZU tensile testing machine, applying an axial tension force gradually to produce an axial elongation rate of 0.2 mm/min. The Charpy impact test was done by using HT-8041A test model having the 7.5-Joule and the pendulum weighs 2.6 Kg. Consequently, each specimen was cast according to ASTM D-6110-10 standard. The samples are 80 mm in length, 10 mm width and 4 mm thickness. The fracture surfaces of the samples subjected to both tensile and impact tests were examined in the ZEISS EVO 50 SEM from Oxford Instruments. The samples were gold coated with an ion sputtering unit beforehand because FA particles contained in the fabricated composite are non-conductive materials. This gold layer serves as a conductor for the electron beam in order to be scanned.

## 3. Results and Discussion

Particle size distribution of the surface-modified FA particles (Fig. 1) lies in the range from 0.02 to about 600  $\mu\text{m}$ . The figure indicates that both narrow size ranges (maximum 15  $\mu\text{m}$ ) and large size ranges (maximum 120  $\mu\text{m}$ ) are used. The mean value of the non-symmetric distribution was almost 60  $\mu\text{m}$ . The density was measured at 1.12  $\text{g/cm}^3$ , which means that the fly ash was the solid type.

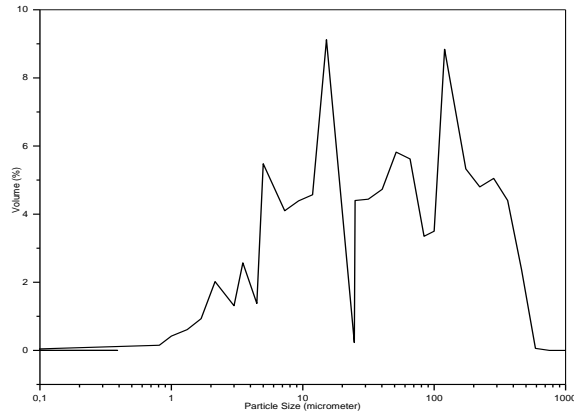
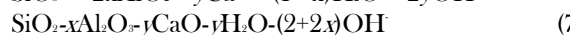
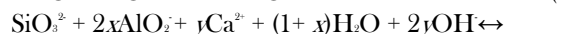


Figure 1. Particle size distribution of the modified fly ash particles

The crystal structure was analyzed by XRD. The XRD pattern of the as-received FA particles (Fig. 2) shows a mild hump ranging from  $15^{\circ}$  to  $25^{\circ}$   $2\theta$  indicating the presence of the amorphous phase. From the percent mass composition of a FA taken from a nearby power plant station, the glass phase consists of  $\text{SiO}_2$ ,  $\text{Al}_2\text{O}_3$ ,  $\text{Fe}_2\text{O}_3$ ,  $\text{CaO}$ ,  $\text{TiO}_2$ ,  $\text{P}_2\text{O}_5$ ,  $\text{MgO}$ ,  $\text{K}_2\text{O}$  and  $\text{MnO}$  [8]. The percentage of the glass in a bulk FA ranges from 45% to 80%, while the remaining percentage is the crystallinity of the FA [9]. As for a chosen FA particle, it had a wide distribution of different carbonaceous materials richer in Si and Al and with minor concentrations of Fe, Ca, Ti, Mg, K, Mn, Na and carbon traces (Table 1). The composition of a particle such as  $\text{Al}_2\text{O}_3$  means the major element is aluminum, but has a minority in any other elements. It is assumed in the hydration reactions that  $\text{SiO}_2$ ,  $\text{Al}_2\text{O}_3$  and  $\text{TiO}_2$  consume hydroxides; while  $\text{Fe}_2\text{O}_3$ , the earth alkalis ( $\text{CaO}/\text{MgO}$ ) and alkalis ( $\text{Na}_2\text{O}/\text{K}_2\text{O}$ ) give them. Thus, the reactions of the glass FA are as given in the equations (1-6). Accordingly, a number of reactions can be produced in different existing conditions, depending on alkali content and temperature of the ambient solution. On account of the chemically activated FA, both the active silica and alumina react with hydrated lime and produce varieties of silicate and aluminate products, which deposit, nucleate and grow on the particle surfaces [04]. Therefore, the equation (7) is the major possible product that occurs thermodynamically.



Where  $x$  and  $y$  are the mole fraction ratio of the glass phases.

In addition, the XRD pattern of the FA particles shows the existence of the peaks of mullite ( $\text{Al}_6\text{Si}_2\text{O}_{13}$ ), quartz ( $\text{SiO}_2$ ), aluminum oxide ( $\text{Al}_2\text{O}_3$ ), calcium aluminum oxide ( $\text{CaAl}_2\text{O}_6$ ) and small amounts of hematite ( $\text{Fe}_2\text{O}_3$ ). Hence, a part of the FA was crystalline (richer in quartz and mullite). This part is nonreactive and contains the crystalline  $\text{SiO}_2$  (in quartz and in mullite) and crystalline  $\text{Al}_2\text{O}_3$  (in mullite and other forms only). Mullite was formed by  $\text{SiO}_2$  reacting with  $\text{Al}_2\text{O}_3$  at the high temperature of  $1200\text{--}1650^{\circ}\text{C}$  in the boiler of the power plant, which had a very stable crystalline form. In the modification, the conditions used were FA/(CH<sub>2</sub>-CH<sub>2</sub>-OH)/H<sub>2</sub>O weight ratio of 1/1/0.5,  $70\text{--}90^{\circ}\text{C}$  slurry temperature, 30 minute heating with constant rpm stirring speed and 1-hour isothermal heating at  $110^{\circ}\text{C}$ . Thus, the coating of the particles was partial to fully achieve. This was proven by XRD of which the intensity of many crystalline products was increased and the significant increase was seen in the peaks of  $\text{Al}_2\text{O}_3$ , which means that crystalline spherical particles richer in Al reacted with the minor elements Ca/Si were formed through the chemical reaction (eq. 7). This is mostly due to the presence of (-OH) groups on the particle surface (eq. 4-7). This thin layer plays a significant role in the reduction of the attractive forces of particle-particle and helps to disperse in the matrix media. The orderly distributed filler in polymer composite attributes higher mechanical strength compared to neat polymer matrix [2].

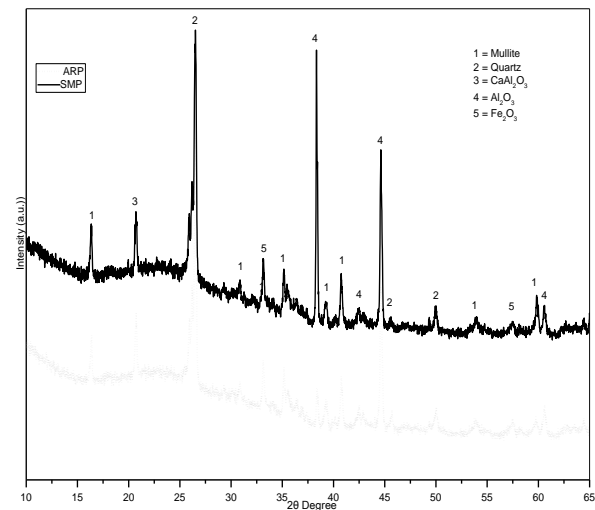


Figure 2. XRD pattern of the as-received (ARP) and surface-modified (SMP) fly ash particles

The microhardness of the samples prepared from the surface-modified FA particles and compared to the surface-original FA particles is given in (Fig.3). For the surface-modified FA, the hardness was increased with the increasing FA particles, which was similar to the hardness obtained in the original FA particles-reinforced polyester matrix.

The almost constant increase of the hardness implied that the particles of the FA were incorporated within the polyester constituents (C-O-H) with a uniform distribution of the particles. The higher hardness of the as-received FA may be due to the numerous existing functional hydroxide (-OH) ions. In general, the hardness depends on the modulus of elasticity.

The higher hardness is, the higher elastic modulus will be. Both hardness and modulus of elasticity ( $E$ ) are related to porosity, and the total porosity is directly related to density ( $\rho$ ). The density of UP ( $1.40 \text{ g/cm}^3$ ) is higher than the solid FA ( $1.12 \text{ g/cm}^3$ ) used in this research, which means a lightweight composite was obtained. It has been mentioned [08.] that at higher volume fractions of spherical particles moving relative to a continuous fluid, the particles interact with each other and reduce the velocity. The model used to describe the velocity is

$$V \propto d^2 (\rho_s - \rho) \quad (8)$$

Where  $d$  is the FA particle diameter ( $60 \mu\text{m}$ ),  $\rho_s$  is the density of the FA spherical particles and  $\rho$  is the density of the polyester. In other words, due to the agglomeration which limited the reaction of the FA particles with the matrix when the amount of FA exceeded a limit, the velocity decreased due to the smaller density of the particles. It was also reported [2] that the decrease in the ultimate mechanical strengths was due to the formation of a cluster or agglomerate among the FA particles themselves, resulting in a filler-filler interaction and a poor interface bonding, due to the strong polarity of hydroxide groups on the FA surfaces. Hence, the reduction in the properties may occur at the higher volume of the FA particles.

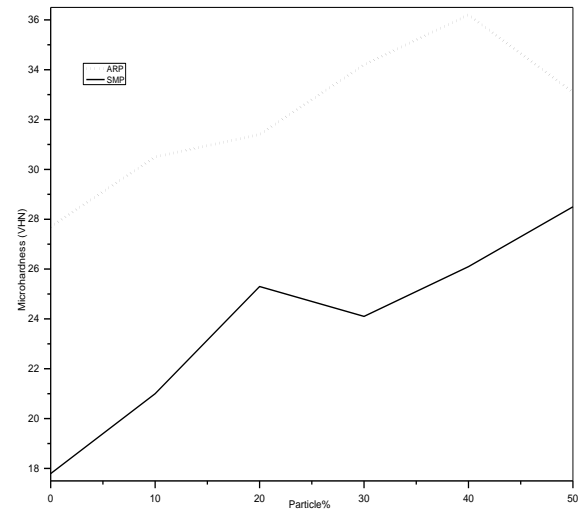


Figure 3. Micro-hardness of the as-received (ARP) and surface-modified (SMP) fly ash particles

The tensile details of the neat and FA-reinforced cured samples are shown in Fig. 4. The tensile strength increased by 8% when there was 20% FA while the lowest ebb of 38% was found when the amounts of FA are 50%. The  $\sigma$ -modulus was increased up to 40% FA with development by 112%. The elongation-at-break was found to decrease as compared to the average value of the neat polyester of 8%. The higher strength was due to the creation of stronger interface interactions between the polyester and FA particles. This leads to greater load transfer between the polyester and the filler and enables greater stress generated in the material before the failure [10]. The decrease of the tensile strength at higher filler contents is observed. The reason was largely because of the interactions between the filler and polyester matrix was impeded resulting in reduced strength of the composites [11].

The presence of the minor traces of the carbon impurities might be a cause of the reduction. The strain at failure decreased with increasing the filler addition of the FA due to the interface interaction, which restricted the flexibility of molecular chain of polyester.

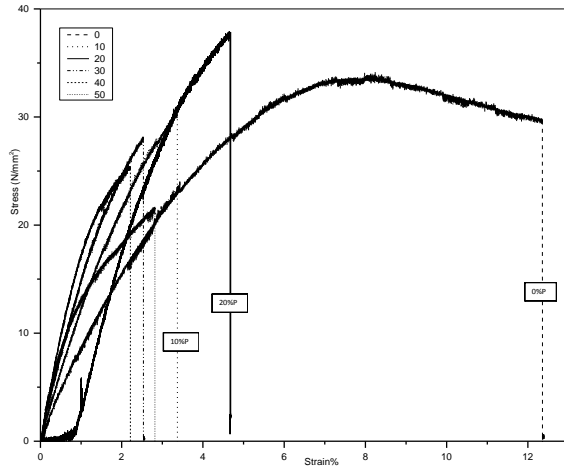


Figure 4. The mechanical properties of FA-UP composite

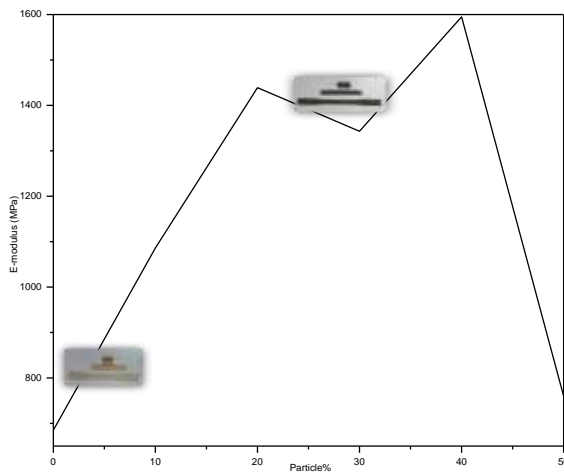


Figure 5. The e-modulus property of the FA-UP composite

The modulus data of the composites are given in Fig. 5. The modulus was increased with FA addition. Moreover, the extent of the increase was greater than the neat polyester. This was because the interaction hardly influences the strength of the modulus [12]. In other words, the modulus is a phenomenon involving the initial strain values that require the lower stress. The higher filler reduced the modulus due to super-saturation of the FA concentrations. Thus, the reduction in the intimate contact area between polyester and FA occurred [10].

Figure 6 depicts the Charpy impact strength of the polyester-FA composites. The figure shows the composites prepared from the surface-modified FA particles and compared to the surface-original FA particles. There was a considerable increase as the FA

content increased. The reduction was seen at 50% FA, which is in accordance with the  $\epsilon$ -modulus. Both the tensile and impact properties indicated that there was an optimum interaction between the matrix and FA components. At 10% FA, the intercomponent bonding was slightly strong. At 20% FA, the increase was observed in all the properties, i.e. hardness, tensile strength, impact strength, modulus and tensile strain. At 30% FA, it is evident from some properties that the intercomponent bonding was lowered. At the points where there were higher amounts of FA particles, the increase in hardness was maintained while a good proportional trend can still be seen in hardness, modulus and impact strength. The impact resistance is the ability of a material to resist breaking under a shock loading. Since it is also defined as the ability to resist the fracture under stress applied at a high speed, it should be noted that the applied stress in the Charpy impact is limited under the yield point.

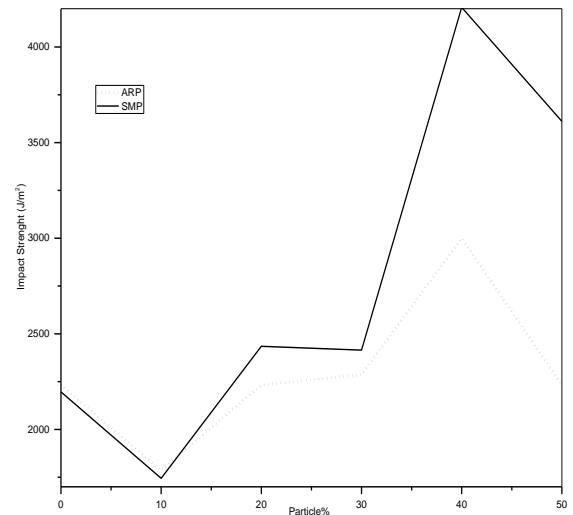


Figure 6. The impact strength of the as-received (ARP) and surface-modified (SMP) fly ash particles

The fracture morphology of the tensile tested specimens of UP-20% FA composite is shown in Fig. 7. It was observed that the fracture surface was not smooth, but slightly rough. The fracture morphology also shows small size voids seen well around the large particles. The void concentration can be increased with FA concentration, thus leads to reducing the strength and elongation at break. The SEM image of the impact-fractured surface of 40% FA (Fig. 7) also revealed that large sized FA particles played a significant role in bringing about the fracture. More voids can be expected at higher concentrations of the FA. Contrary to the impact-fractured sample of 40% FA filled HDPE [12], the evidenced crack formation at the fracture surface cannot be observed. The

decrease in the impact of 50% FA implied that possible cracks were rapidly propagated due to the large voids. Thus, contributing to the overall impact strength of the composites. Hence, the 40% FA represent the optimum composite for both impact and  $e$ -modulus applications. It is mainly due to the lower pore content or higher hardness.

The further study of the SEM images is shown in Fig. 8. The fracture morphology showed that almost all FA particles remained intact in their places. This is the evidence for the existence of good interface bonding between the polyester matrix and FA particles. The SEM images also revealed that small sized FA particles did not play a significant role in bringing about the fracture. It was found that the composites with smallest size FA particles (less than about 3  $\mu\text{m}$ ) proved to be better in enhancing strength and relative elongation [12].

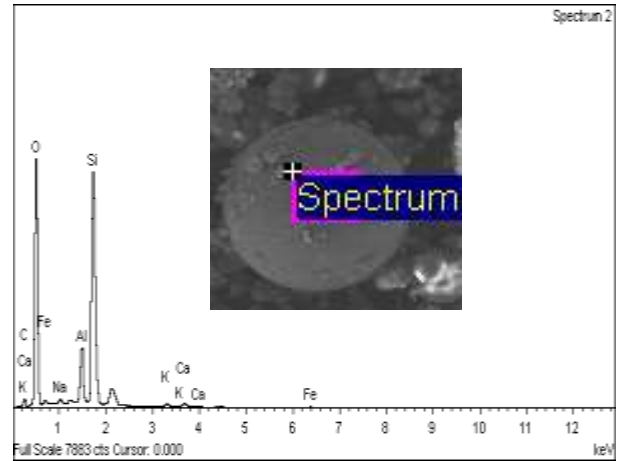
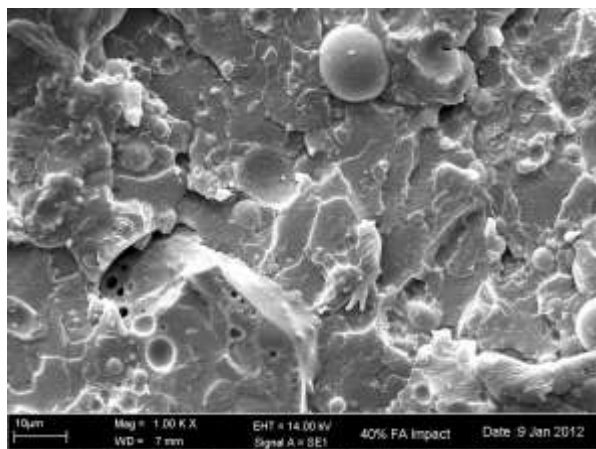
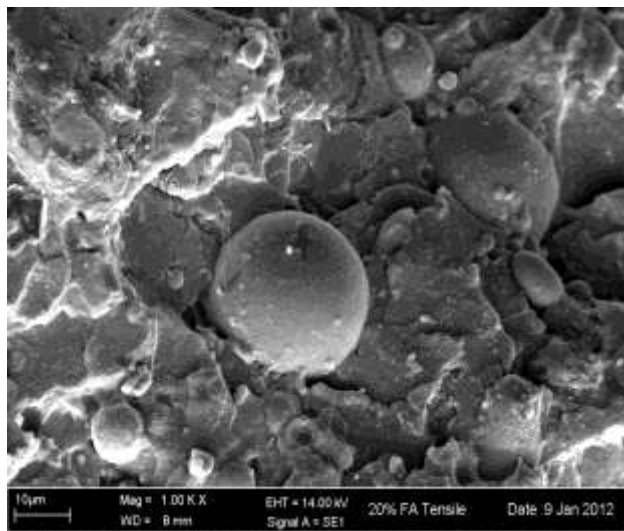
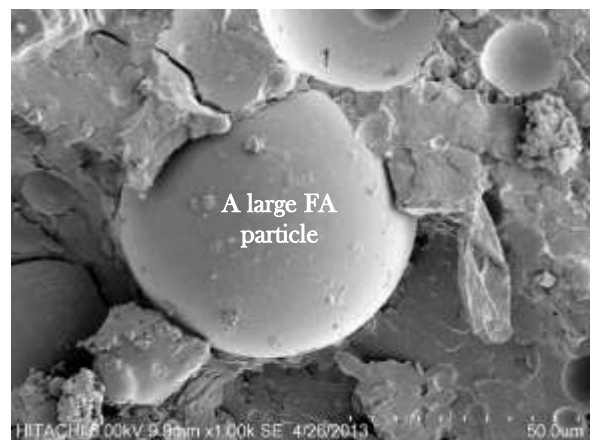


Figure 7. From first to last graph: (1) SEM image of 20% FA-UP tensile test specimen, (2) 40% FA-UP impact specimen, and (3) Fig. 2: SEM-EDX analysis of a chosen particle..



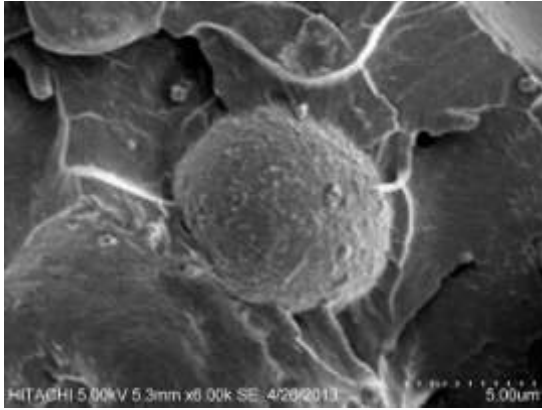


Figure 8: From first to last photo: (1) SEM images of 40 wt.% FA-UP tensile fracture morphology showing a uniform distribution of the particles, (2) spotted large FA particle, and (3) good attachment of small size FA particle

#### 4. Conclusions

The reinforcing FA particles for UP matrix was proven in this study. The different phases of the FA incorporated into the UP matrix were well evidenced by XRD. This amount of FA into UP brought about the increase in hardness,  $\epsilon$ -modulus, tensile and impact strengths. When 30% FA were added to the UP matrix, FA agglomerates might occur within the polyester matrix. However, the amounts of the UP still brought about the improvement in hardness and  $\epsilon$ -modulus. Thus, the composite is an excellent for both impact and  $\epsilon$ -modulus applications because the higher hardness.

#### Acknowledgements

Special thanks are due to Multimedia University Malaysia for facilitating the completion of this project number IP20110411003.

#### References:

- [1] S. Sen, N. Nugay, *Eur. Polym. J.* 37 (2001) 2047-2053
- [2] D.C.D. Nath, S. Bandyopadhyay, S. Gupta, A. Yu, D. Blackburn, C. White, *Appl. Surf. Sci.* 256 (2010) 2759-2763
- [3] M. Rahail Parvaiz, Smita Mohanty, Sanjay K. Nayak, P.A. Mahanwar, *Mater. Sci. Eng. A* 528 (2011) 4277-4286

[4] Yang Yu-Fen, Gai Guo-Sheng, Cai Zhen-Fang, Chen Qing-Ru, *J. Hazard. Mater.* B133 (2006) 276-282

[5] Subhankar Ghorui, N.R. Bandyopadhyay, Dipa Ray, Suparna Sengupta, Tanusree Kar, *Ind. Crops Prod.* 34 (2011) 893-899

[6] K.T. Varughese, B. K. Chaturvedi, *Cem. Concr. Compos.* 18 (1996) 105-108

[7] S. Zahi, *Int. J. Materials Engineering Innovation* 4 (2013) 241-257

[8] S. Zahi, A.R. Daud, *Mater. Des.* 32 (2011) 1337-1346

[9] Colin R. Ward, David French, *Fuel* 85 (2006) 2268-2277

[10] D.C.D. Nath, S. Bandyopadhyay, J. Campbell, A. Yu, D. Blackburn, C. White, *Appl. Surf. Sci.* 257 (2010) 1216-1221

[11] Yoldas Seki, Kutlay Sever, Mehmet Sarikanat, Ali Sakarya, Eren Elik, *Composites: Part B* 45 (2013) 1534-1540

[12] Iftekhar Ahmad, Prakash A. Mahanwar, *Journal of Minerals & Materials Characterization & Engineering* 9 (2010) 183-198

# Numerical simulation of the crystal growth of Ti:Al<sub>2</sub>O<sub>3</sub> material by the $\mu$ -PD Technology

H. Azou<sup>a</sup>, A. Laidoune<sup>a</sup>, D. Haddad<sup>b</sup>, D. Bahloul<sup>a</sup> and F. Merrouchi<sup>c</sup>

<sup>a</sup>Département de Physique, Facultés des Sciences de la Matière, Université de Batna1.

1rue Chahid Boukhlouf Mohamed El-Hadi, 05000 Batna, Algeria.

<sup>b</sup>Département de mécanique, Faculté de l'engineering, Laboratoire (LESEI), Université de Batna2, Algeria.

<sup>c</sup>Département de. Hydraulique, Institut de génie civil, hydraulique et architecture, Université de Batna2.

Received date: September 11, 2016; revised date: December 03, 2016; accepted date: December 11, 2016

## Abstract

In this work we have studied the growth of titanium doped sapphire using the micro-pulling down technique; we established a numerical, two-dimensional finite volume model in cylindrical coordinates with an axisymmetric configuration. The flow, the heat and the mass transfer are modeled by the differential equations of conservation of mass, momentum, energy and species. This problem, which takes into account the convection-diffusion coupling, is discretized using the Finite Volumes Method. Simulation results show that the longitudinal distribution of titanium remains homogeneous along the axis of the sapphire material. The radial mass transfer of titanium increases in the crystal when the pulling rate increases. This important result contributes to strengthen the coupling of the laser beam with the active ions and allows a highest laser output power. The melt/crystal interface for the  $\mu$ -PD technique has a flat shape; this flatness of the interface shape agrees with the experiment observation and is very important since it shows that drawing conditions are very stable. Our model for the  $\mu$ -PD method is in good agreement with experimental results.

**Keywords:** Crystal growth, Fiber crystals, Sapphire, Titanium, micro-pulling down ( $\mu$ -PD), Shaped crystals.

## Nomenclature

**Bi** Biotnumber,  $hR_d/k_m$ .

**C** dimensionless solute concentration.

**C<sub>0</sub>** initial solute concentration.

**Cp<sub>c</sub>** specific heat capacity of the crystal (J/KgK).

**Cp<sub>m</sub>** specific heat capacity of the melt (J/KgK).

**D** diffusion coefficient ( $m^2/s$ ).

**g<sub>0</sub>** gravitational acceleration ( $m^2/s$ ).

**h** heat transfer coefficient ( $w/cm^2 k$ ).

**k<sub>c</sub>** thermal conductivity of crystal ( $w/m k$ ).

**k<sub>m</sub>** thermal conductivity of melt ( $w/m k$ ).

**Ma** Marangoni number  $((\partial\gamma/\partial T) R_d T_m)/(\mu_m \alpha_m)$ .

**Pe<sub>c</sub>** Peclet numbers of the crystal  $U_c R_d/\alpha_m$ .

**Pe<sub>m</sub>** Peclet numbers of the melt  $U_m R_d/\alpha_m$ .

**Pr** Prandtl number  $\nu/\alpha_m$ .

**Ra<sub>T</sub>** thermal Rayleigh number

$g_0 \beta_T (T_{max} - T_m) R_c^3 / \alpha_m \nu$

**Ra<sub>S</sub>** solutal Rayleigh number,  $\frac{g_0 \beta_c C_0 R_c^3}{D} \nu$ .

**R<sub>d</sub>** crucible radius.

**R<sub>c</sub>** crystal radius.

**Sc** Schmidt number,  $\nu_m/D$ .

**T** dimensionless temperature.

**T<sub>a</sub>** ambient temperature.

**t** time.

**u** r-component of velocity.

**v** z-component of velocity.

**r** dimensionless radial cylindrical coordinates.

**z** dimensionless axial cylindrical coordinates.

**1. Introduction**

Because of its exceptional chemical and physical properties [1], sapphire is a very important material used in several military, environmental, medical, and industrial applications [2,3]: optical systems, watch windows, cellular phone glasses, optical fibers, wave guides for surgery, needles for laser therapy and medical power delivery systems [2].

Titanium doped sapphire has excellent mechanical, thermal, and optical properties which allow the development of various systems especially laser devices [4]. Many growing techniques have been used to grow this material such as Czochralski (CZ) [5, 6], Heat exchanger method (HEM) [7] Kyropoulos (KY) [4] and pulsed laser deposition (PLD) [8, 9].

More recently there has been intense interest in using the micro-pulling-down method for the growth of shaped crystals fibers in a wide variety of domains, especially for laser, medical and optical application [10, 11].

The geometry, the shape and the quality of crystals play an important role in the choice of the growing technique [10]. We chose to study the micro pulling down technique because it allows the growth of stable high quality shaped crystals than the other comparable complex techniques [10]. In fact, it allows the control of the thermal gradient, the use of high pulling rates and high possibility to get stable shaped crystals [12]. Furthermore, when the pulling rate is sufficiently high the segregation problem can be avoided [2, 12].

The  $\mu$ -PD technique now has become a major method for growing crystalline fibers of good quality [15] with controlled format imposed by the geometry of the capillary at the bottom of the crucible [10]. Because of the small amount of raw material, the  $\mu$ -PD technique is used for research laboratories [2], especially to search for new materials.

In this work we have performed a numerical simulation of the growing process with the micro-pulling down  $\mu$ -PD technique. The theoretical analysis of this method for the growth of single crystal fibers of Ti doped  $AlO_3$  is conducted using the mass, momentum, energy and solutal concentration conservation laws.

The study of the problem is simplified to an incompressible flow of a viscous fluid in the molten zone governed by the Navier-Stokes, heat transfer and concentration equations under the Boussinesq approximation. We use a two-dimensional axisymmetric model discretized using a Finite Volumes Method (FVM) in cylindrical coordinates system  $(r, z)$ .

The next section summarizes the growth conditions using the micro-pulling down technique. In Section 3 we present the mathematical formulation of our model that is

the governing equations, the boundary conditions and the numerical scheme used in our simulations. Section 4 is devoted to the results and discussion, followed by conclusions in section 5.

**2. Growth conditions**

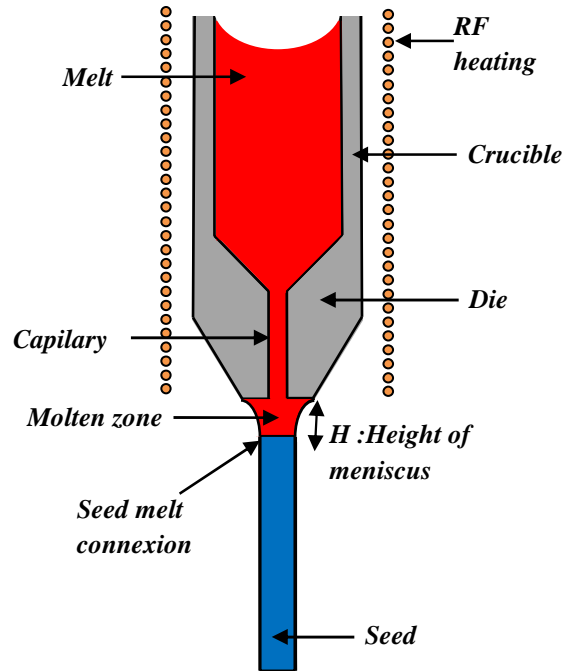


**Fig.1 :** Schematic diagram of domain of  $\mu$ -PD.

The system to be modeled is sketched in Fig.1; the raw material (red color) in the crucible was heated until melting by using RF (Radio frequency) heating furnace [11]. The micro-pulling-down  $\mu$ -PD uses a capillary die for the growth of shaped crystals.

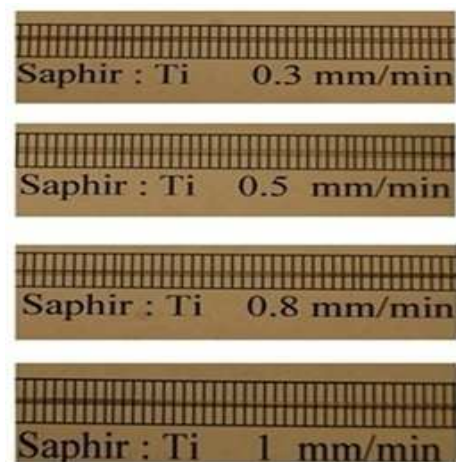


**Fig.2.** Ti doped sapphire fibers.

The growth is generated by the connection of the seed (blue color) with the drop at the bottom of the capillary die in the crucible. In Fig.2, we present titanium-doped sapphire crystal fibers along [0001] direction, for different pulling rates [19].

In order to perform the growth in steady conditions, many growth conditions have to be satisfied: Firstly; In order to grow the fiber with a constant diameter, the growth angle constraint needs to be specified [13]:

$$\frac{dR_m}{dz} = -\tan \phi_0 \tag{1}$$

As shown in Fig. 3,  $R_m$  is the radial distance of the free surface, and  $\phi_0$  is the growth angle determined by crystallographic orientation and specified by the crystal-liquid-vapor triple junction [10].

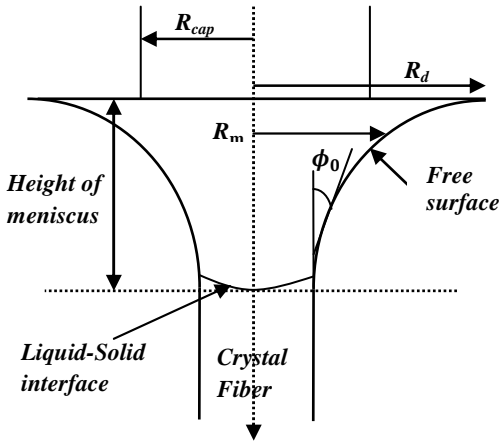


Fig.3: Zoom in the molten zone.

The crystal shape should be controlled by the shape of the meniscus (i.e., the  $\phi = \phi_0$  requirement) [14].

In our case, for sapphire  $\phi = \phi_0 = 17^\circ$  in the growth direction [0001] [12, 15].

The pulling is conducted down with controlled speed; equation (2) describes the relationship between the radius of the capillary, the radius of the crystal and the pulling rate [10].

$$\rho_m v_{cap} d_{cap}^2 = \rho_c d_c^2 v_c \tag{2}$$

This equation states out the mass conservation between the inlet in the capillary and the outlet at the bottom of liquid-solid interface. The fundamental parameters involved in the micro-pulling down method [10] are:

the growth velocity  $v_c$ , the flow velocity at the capillary  $v_{cap}$ , the crucible radius at the bottom  $R_d$ , and the radius of the crystal  $R_c = d_c/2$ ; while  $d_c$  and  $d_{cap}$  are the diameters of the growing crystal and the capillary respectively (fig.4).

The other parameter is the molten zone height; the relationship between these three parameters is theoretically given in [10] by:

$$H = R_c \cos \phi_0 \left[ \csc \left( \frac{R_d}{R_c \cos \phi_0} \right) - \csc \left( \frac{1}{\cos \phi_0} \right) \right] \tag{3}$$

The most important parameter determining the quality and uniformity of the obtained crystals [11] is the shape of the molten zone; where its meniscus profile, is given in [10, 16] by:

$$z(r) = R_c \cos \phi_0 \left[ \csc \left( \frac{R_d}{R_c \cos \phi_0} \right) - \csc \left( \frac{r}{R_c \cos \phi_0} \right) \right] \tag{4}$$

Where r is the radial distance from the growth axis:

$$R_c \leq r \leq R_d$$

### 3. Mathematical formulation

The computational domain is presented in figure 4.

In order to reduce the CPU time we can ignore the melt height  $h_m$ (from  $z = 0$ ) in the crucible [17].

The calculation domain starts at the top of the capillary tube at  $H_{cap}$ , as shown in the schematic diagram of Fig.4. This is a good approximation provided that we include the melt height  $h_m$  into account for meniscus calculation [17].

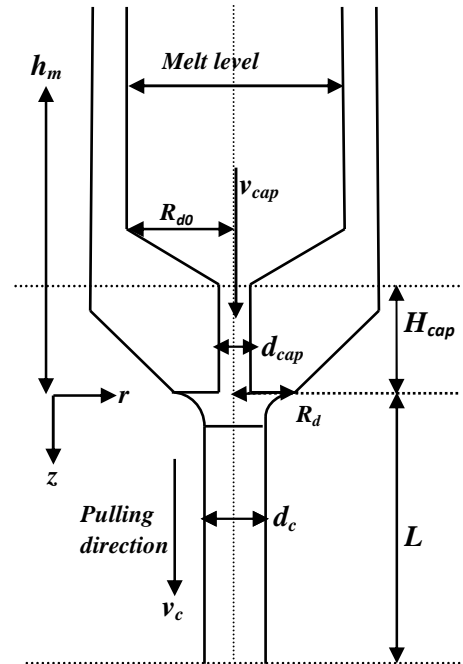


Fig.4: Schematic diagram of the computational domain.

3.1 Governing equations

The melt is assumed incompressible and Newtonian, while the flow is laminar. Dimensionless variables are defined by scaling lengths by  $R_d$ , velocity by  $\alpha_m/R_d$ , temperature by the melting point  $T_m$ , and concentration by  $C_0$ , where  $\alpha_m$  is the thermal diffusivity of the melt [17].

Because of the cylindrical symmetry of the problem, we have used a two dimensional axisymmetric model. The flow, the heat and the mass transfer are modeled by the dimensionless differential equations:

Equation of radial component of the momentum:

$$\frac{\partial u}{\partial t} + u \frac{\partial u}{\partial r} + v \frac{\partial u}{\partial z} = -\frac{\partial p}{\partial r} + Pr \frac{\partial}{\partial r} \left( \frac{1}{r} \frac{\partial}{\partial r} (ru) \right) + Pr \frac{\partial}{\partial z} \left( \frac{\partial u}{\partial z} \right) \quad (5)$$

Equation of axial component of the momentum:

$$\frac{\partial v}{\partial t} + u \frac{\partial v}{\partial r} + v \frac{\partial v}{\partial z} = -\frac{\partial p}{\partial z} + Pr \frac{\partial}{\partial r} \left( \frac{1}{r} \frac{\partial}{\partial r} (rv) \right) + Pr \frac{\partial}{\partial z} \left( \frac{\partial v}{\partial z} \right) - Pr Ra_T T + \frac{Pr^2}{Sc} Ra_s C \quad (6)$$

Conservation equation:

$$\frac{\partial \rho}{\partial t} + \frac{1}{r} \frac{\partial}{\partial r} (r\rho u) + \frac{\partial}{\partial z} (\rho v) = 0 \quad (7)$$

Energy equation:

$$r \frac{\partial T}{\partial t} + \frac{\partial}{\partial r} (ruT) + \frac{\partial}{\partial z} (rvT) = \frac{\partial}{\partial r} \left( r\alpha_i \frac{\partial T}{\partial r} \right) + \frac{\partial}{\partial z} \left( r\alpha_i \frac{\partial T}{\partial z} \right) \quad i = (m, c) \quad (8)$$

Dopant concentration equation:

$$r \frac{\partial C}{\partial t} + \frac{\partial}{\partial r} (ruC) + \frac{\partial}{\partial z} (rvC) = \frac{Pr}{Sc} \left[ \frac{\partial}{\partial r} \left( r \frac{\partial C}{\partial r} \right) + \frac{\partial}{\partial z} \left( r \frac{\partial C}{\partial z} \right) \right] \quad (9)$$

Fig.5 shows the mesh grid which has been used to solve numerically the above equations. The physical domain in axisymmetric cylindrical coordinates (r,z) was subdivided into a finite number of contiguous volumes (CV) of volume V, which are bounded by cell faces located about halfway between consecutive nodal points. This subdivision has been used for tow phase of sapphire (i=m for the melt, i=c for the crystal.)

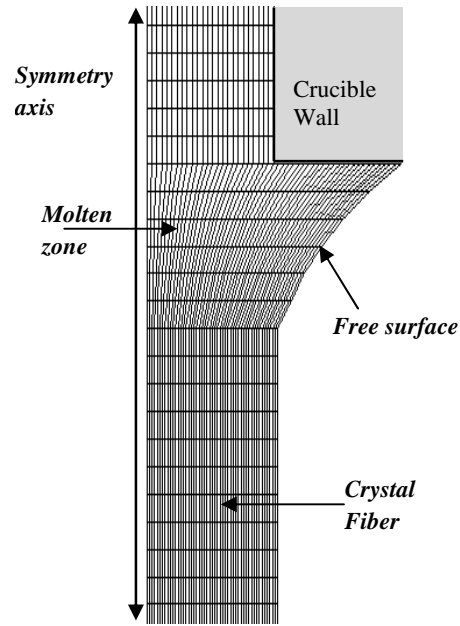


Fig. 5: A portion of a sample mesh for calculation.

3.2 Boundary conditions

It is assumed that the solute is uniformly distributed in the melt reservoir and its concentration is  $C_0$ ; also the solute diffusion in the solid phase is neglected[18]. These governing equations with their associated boundary conditions are discretized by a finite volume method (FVM). We present below a detailed description about the boundary conditions simulations as the reference [17].

3.2.1 Boundary conditions at the symmetric axis

In our two dimensional axisymmetric model the boundary condition at the symmetric axis for the physical quantities is set as follows:

$$\frac{\partial \Phi}{\partial r} = 0$$

In the above equations,  $\Phi$  is the physical propriety (velocities  $\mathbf{u}, \mathbf{v}$ , temperature  $T$ , concentration  $C$ ).

At the other boundaries the conditions were set for each physical quantity as follows:

3.2.2 Temperature boundary conditions

- At the top entrance the temperature was set by the radio frequency generator. It's about  $\Delta T \approx 20$  to  $30 K$  above the melting point of sapphire.

$$T = T_m + \Delta T \quad (10)$$

-At the material surface, the heat transfer from the system to the ambient is controlled by convection according to the energy balance along the material surface:

$$n \cdot k_i \vec{\nabla} T = -Bi(T - T_a) \tag{12}$$

Where  $\mathbf{n}$  is the unit normal vector on the melt or crystal surface pointing outwards;  $k_i$  is the ratio of thermal conductivity of phase  $i$  to the melt; where ( $i = m(\text{melt}), i = c(\text{crystal})$ ) and  $Bi = hR_d/k_m$  is the Biot number. In this study the ambient temperature  $T_a$  is set to be a constant.

- At the end of the fiber  $\mathbf{z} = \mathbf{L}$  using the fixed-temperature boundary condition, i.e.  $T = T_a$ .

3.2.3 Velocity boundary conditions

-The radial and axial velocities at the top entrance are given as follows:

$$\mathbf{u} = \mathbf{u}_0 = \mathbf{0}$$

$$\mathbf{v} = \mathbf{v}_{cap} = \left(\frac{\rho_c}{\rho_m}\right) \left(\frac{d_c}{d_{cap}}\right)^2 \mathbf{v}_c \tag{13}$$

Where  $\mathbf{v}_c$  is the growth velocity, and  $\mathbf{v}_{cap}$  is the flow velocity in capillary channel

-At the wall inside the capillary,

$$\mathbf{u} = \mathbf{0}$$

$$\mathbf{v} = \mathbf{0}$$

- In the free surface, the two components of the velocity are deduced from Marangoni convection; where the tangential stress balance is required:

$$ns: t = Ma(s \cdot \nabla T) \tag{14}$$

Where  $\mathbf{s}$  is the unit tangent vector at the free surface,  $Ma$  is the Marangoni number and  $\mathbf{t}$  the shear stress tensor.

- In the crystal, velocity boundary condition is:

$$\mathbf{v} = \mathbf{v}_c$$

3.2.4 Solute concentration boundary conditions

At the top entrance ( $\mathbf{z} = -\mathbf{H}_{cap}$ ), the solute boundary condition is given by the solute flux balance:

$$\vec{e}_z \cdot \vec{\nabla} C = \left(\frac{Sc}{Pr}\right) Pe_m (C - 1) \tag{15}$$

Where  $\mathbf{e}_z$  is the unit vector along the z axis, and  $\nabla C$  is the gradient of the concentration.

-The Neumann condition is imposed at the melt/crystal interfaces:

$$\vec{n} \cdot \vec{\nabla} C = \left[\left(\frac{\rho_c}{\rho_m}\right) - K\right] \left(\frac{Sc}{Pr}\right) Pe_c C(n \cdot e_z) \tag{16}$$

Where  $K$  is the segregation coefficient according to the phase diagram, and  $\vec{n}$  is the unit normal vector at the growth front pointing to the melt,  $Pe_m = \mathbf{v}_m R_d / \alpha_m$  and  $Pe_c = \mathbf{v}_c R_d / \alpha_m$  are the Peclet numbers of the melt and crystal respectively.

4. Results and Discussion

In this study, we have fixed the concentration of titanium in the melt to 0.1 at% [19].

The physical properties of  $Ti^{3+}$ :  $Al_2O_3$  [15, 18 and 19] and some input parameters [17, 19] for calculations are listed in Table 1:

Table 1

Physical properties

- $Cp_c = 1300 \text{ (J/KgK)}$
- $Cp_m = 765 \text{ (J/KgK)}$ .
- $D = 5 \times 10^{-9} \text{ (m}^2 / \text{s)}$
- $k_c = 17.5 \text{ W/mK}$
- $k_m = 3.5 \text{ W/mK}$
- $\partial\gamma/\partial T = (-3.5) \times 10^{-5} \text{ Nm}^{-1} \text{K}^{-1}$
- $\mu_m = 0.0475 \text{ Kg/ms}$
- $T_m = 2323 \text{ K}$
- $\Delta H = 1.1 \times 10^6 \text{ J/Kg}$
- $\beta_T = 1.8 \times 10^{-5} \text{ K}^{-1}$
- $\rho_c = 3960 \text{ Kg/m}^3$
- $\rho_m = 3500 \text{ Kg/m}^3$
- $K = 1$
- $\phi_0 = 17^\circ$

Input parameters

- $R_c = 0.3 - 1 \text{ mm}$
- $R_{cap} = 0.27 - 0.5 \text{ mm}$
- $R_d = 0.57 - 2 \text{ mm}$
- $C_0 = 0.1 - 0.2 \text{ at\%}$
- $v_c = (0.3, 0.5, 0.8 \text{ and } 1) \text{ mm/min}$

4.1 Effect of the pulling rate

4.1.1 The axial pulling rate

Our simulation focuses on the effect of the pulling rate on the homogeneity of titanium concentration along the growth fiber axis (radial and axial axis). First, we present the axial distribution of  $Ti^{3+}$  concentration in the sapphire crystal fiber for different pulling rates; these results are illustrated in Fig.6.

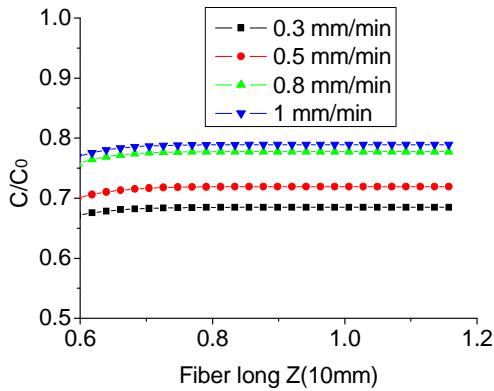


Fig.6: Titanium distribution along the axis of the sapphire fiber a function of pulling rate.

According to these results (Fig.6), we noticed that the longitudinal distribution of the  $Ti^{3+}$  remains homogeneous along the axis of the fiber even for relatively high pulling rates compared to other growth techniques [2].

The high pulling rate is one of the favorable conditions for axial homogeneous dopants distribution for the micro-pulling-down growth technique [12]. This result is in good agreement with experimental results of the dopants axial distribution reported in Fig.7.

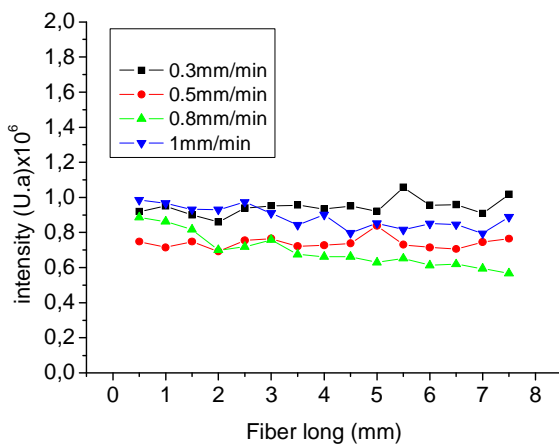


Fig.7: Titanium distribution along the axis of the fiber. Experimental: A. Laidoune.

Experimental results in Fig.7 show the homogeneity of  $Ti^{3+}$  along the longitudinal fiber direction for different pulling rates [19]. This result confirms the validity of our

two-dimensional axisymmetric finite volume model.

4.1.2 The radial pulling rate

In figure 8, we present the radial distribution of  $Ti^{3+}$  for different pulling rates.

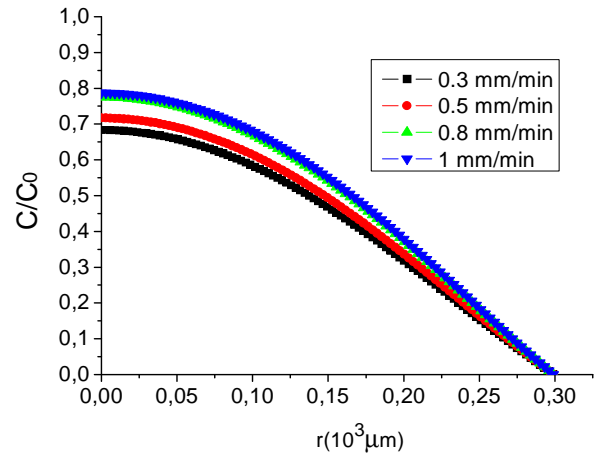


Fig.8: Ti radial distribution for different pulling rate.

According to these results (Fig.8), we observed that the radial distribution of Ti dopants gather around the axis of the fiber. Thus there is no segregation towards the periphery. This result remains true for relatively high pulling rates. Therefore these results confirm that the size and the geometry of the  $\mu$ -PD growth technique helps to avoid the segregation of titanium towards the periphery of the fiber despite the high pulling rates used for this technique compared with other methods [1, 2].

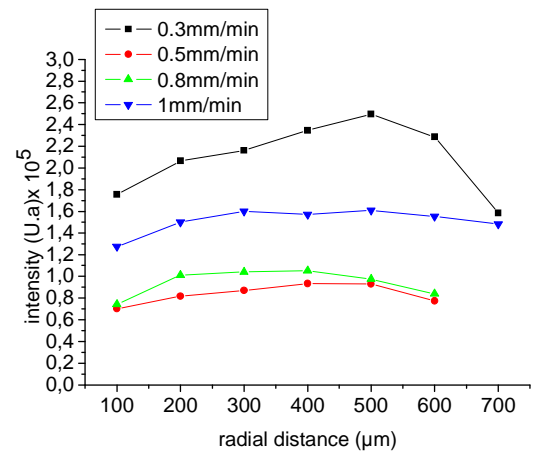


Fig.9: Luminescence measurements showing the titanium radial distribution.

Fig.9 presents the radial micro luminescence results that show the gathering of  $Ti^{3+}$  ions in the core of the fiber than in the periphery; the radial distribution is suitable as an amplifying medium for the design of fiber lasers [19].

4.2.3 The variation of titanium concentration versus the pulling rate

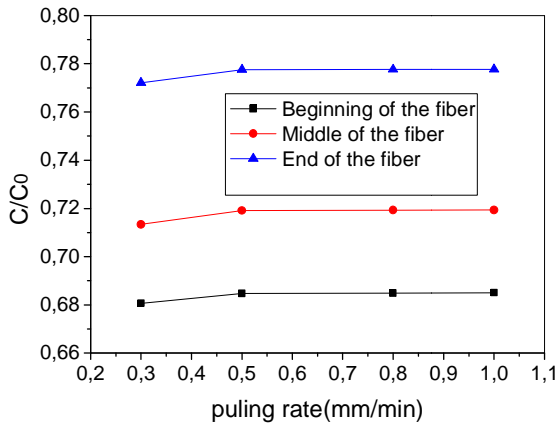


Fig.10: The concentration of titanium in the fiber as a function of the different pulling rate for three parts of the fiber.

Fig.10 shows the longitudinal homogeneity of the concentration of titanium along the fiber axis in good agreement with the experiment results obtained from the luminescence measurements of Fig.11 [19]:

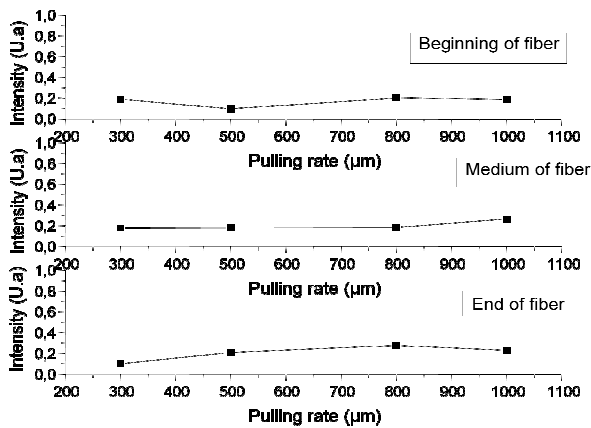


Fig.11: Luminescence measurements showing the concentration of dopants in three parts of the fiber as function of the different pulling rate.

4.2 The melt/crystal interface shape

The quality of the crystals and single crystal fibers is governed by many factors, citing the dynamics of drawing, the thermal transfer, effect of convection, and the geometry of the melt/crystal interface.

The melt/crystal interface shape plays an important role for the quality of the crystal fiber drawn. The shape of this interface is essentially determined by the heat transfer in the growing system [20].

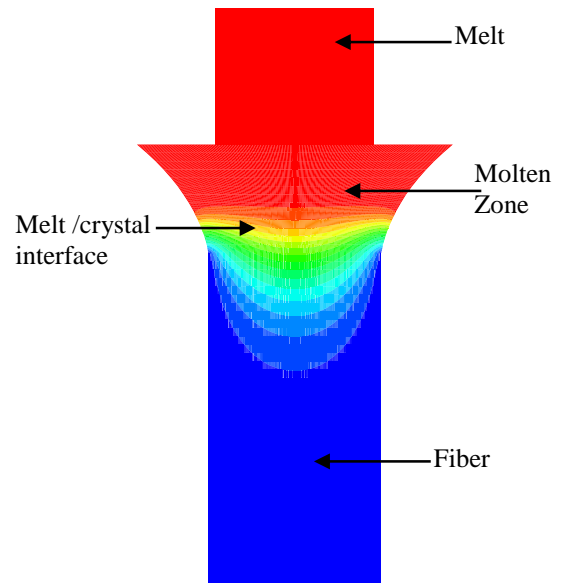


Fig.12: Temperature contour plot showing the melt/crystal interface.

Fig. 12 shows the temperature contour plot (heat transfer) in the growth system. The blue color is the solid and the red color is the sapphire melt. According to these results, the melt/crystal interface for the  $\mu$ -PD technique has almost a flat shape and this is in good agreement with the experiment observation [19]. This flatness of the interface shape is very important since it shows that drawing conditions are very stable.

4.3 Effect of growth angle on the height of the molten zone

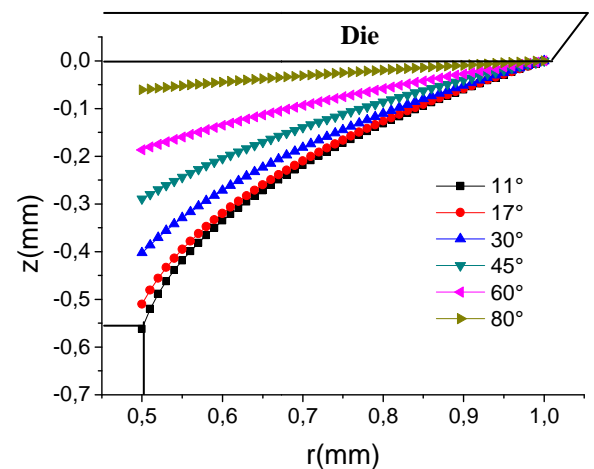


Fig 13: The variation of the height of the molten zone as function of the growth angle.

The meniscus shape is mainly affected by the capillary shape and the melt height [17]. In this part we have studied the effect of the growth angle on the meniscus shape also on the height of the molten zone on the meniscus shape and on the height of the molten zone. Fig.13 shows the calculated meniscus shapes for different growth angle: (11°, 17°, 30°, 45°, 60° 80°).

We noticed that the height of the molten zone decreases when the angle of growth increases. As results the decrease or the increase of the meniscus height causes an increase or decrease in the diameter of the fiber [19], and this affects on the quality of the drawn fiber.

4.4 Effect of the geometry of the  $\mu$ -PD technique on the segregation problem

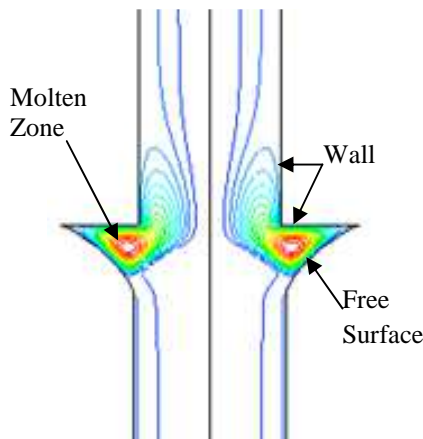


Fig 14: Presentation of streamline in the  $\mu$ -PD technique.

According to Fig 14, we notice that there is no flow near the free surface and the wall (blue color). This is one of the advantages of this method over other growing methods It is related to the small dimensions (mm,  $\mu$ m) involved in the micro pulling process.

So the size of the micro-pulling down avoids and minimizes the segregation problem of the dopants towards the periphery. Because the laser beam passes in the axis of the fiber, this result show that the use of this technique reduces significantly the segregation towards the periphery of the fiber making the large concentration of  $Ti^{3+}$  in the center of the core of the fiber where it is needed.

In fact the experimental and the simulation results show that the micro pulling down geometry helps to avoid the dopants' segregation which is great advantages to pull performed materials single crystals fiber with good optical and thermal properties.

5. Conclusion

In this work we have established a two-dimensional axisymmetric finite volume model (FVM) in cylindrical coordinates to study the growth of  $Ti: AlO_3$  material by the  $\mu$ -PD technique. This study shows:

- With other growing techniques we usually observe the segregation of the dopants towards the periphery. Whereas for the micro pulling down technique we showed that the dopants distribution of  $Ti^{3+}$  is homogeneous whatever the pulling rate and there is no segregation towards the periphery.
- The longitudinal mass transfer (longitudinal distribution of the  $Ti^{3+}$ ) remains homogeneous along the axis of the sapphire fiber even for relatively high pulling rates; this homogeneity gives a material with a good optical and thermal quality for several applications [19]. Our results are in good agreement with experimental results that show that the obtained fibers have a good morphological and optical quality [19].
- The radial mass transfer of titanium increase in the crystal drawn when the pulling rate increases.
- The heat transfer gives information on the shape of the melt/crystal interface; which plays an important role for the optical and thermal quality of the material drawn.
- The size and the geometry of the crucible and the pulling rate minimize the segregation problem of the dopants to the periphery of the fiber. This is due to the fact that the dopants do not have enough time to migrate to the periphery during the growth.
- Our results are in good agreement with the experiment that show that the obtained fibers have a good morphological and optical quality and. This agreement shows the validity of the two-dimensional axisymmetric finite volume model.

Therefore, for the micro pulling down ( $\mu$ -PD) method, the results obtained are important for laser applications. Indeed, for other growth methods such as Czochralski [6], it is not easy to avoid the problem of segregation to the periphery, whereas the micro pulling down promotes the gathering of impurities towards the axis of the fiber making a good overlap with the laser beam when the material or the fiber is used as amplifying medium in a laser.

## References

- [1] Fukuda T., *Advances IN materials Research* 8, 2007.
- [2] THIERRY DUFFAR. © 2010 John Wiley & Sons Ltd.
- [3] Chandra P. Khattak, Frederick Schmid, *Journal of Crystal Growth*. 225 (2001).
- [4] G. Alombert-Goget, K. Lebbou, N. Barthalay, H. Legal, G. Chériaux. *Optical Materials* 36 (2014) 2004–2006.
- [5] H. Li, E.A. Ghezal, G. Alombert-Goget, G. Breton, J.M. Ingargiola, A. Brenier, K. Lebbou. *Optical Materials* 37 (2014) 132–138.
- [6] Reinhard Uecker ; Detlef Klimm ; Steffen Ganschow ; Peter Reiche ; Rainer Bertram ; Mathias Roßberg ; Roberto Fornari. *Proc. SPIE* 5990, *Optically Based Biological and Chemical Sensing, and Optically Based Materials for Defence*, 599006 (October 15, 2005).
- [7] David B. Joyce, Frederick Schmid. *Journal of Crystal Growth* 312 (2010) 1138–1141.
- [8] A. A. Anderson, R. W. Eason, L. M. B. Hickey, M. Jelinek, C. Grivas, D. S. Gill, and N. A. Vainos, *Optics Letters* 22, 1556-1558 (1997).
- [9] L. S. Wu, A. H. Wang, J. M. Wu, L. Wei, G. X. Zhu, and S. T. Ying, *Electronics Letters* 31, 1151-1152 (1995).
- [10] E. A. Ghezal, H. Li, A. Nehari, G. Alombert-Goget, A. Brenier, K. Lebbou, M. F. Joubert, and M. T. Soltani, *Crystal growth & design*. 12 (2012) 4098–4103.
- [11] D.Sangla, N.Aubry, A.Nehari, A.Brenier, O.Tillement, K.Lebbou, F.Balembois., *Journal of Crystal Growth* 312(2009)125–130.
- [12] A. Nehari, T. Duffar, E.A. Ghezal, K. Lebbou. *Cryst. Growth Des.*2014, 14, 6492-6496.
- [13] V.A. TATARCHENKO and G.A. SATUNKIN. *Journal of Crystal Growth* 37 (1977) 285–288.
- [14] T. SUREK, B. CHALMERS and A.I. MLAVSKY. *Journal of Crystal Growth* 42 (1977) 453–465.
- [15] H. S. Fang, Z. W. Yan, and E. D. Bourret-Courchesne. DOI: 10.1021/cg101021t .2011. *CRYSTAL GROWTH & DESIGN* Article. Vol. 11, 121 129.
- [16] V.A. Tatarchenko. *Journal of Crystal Growth* 37 (1977) 272.
- [17] C.W. Lan, S. Uda, T. Fukuda. *Journal of Crystal Growth* 193 (1998) 552–562. June 1998.
- [18] Abdeldjelil Nehari . THESE DE DOCTORAT L'UNIVERSITE DE LYON 2011.
- [19] A. Laidoune. Thèse de doctorat. Université Hadj de Lakhdar - Batna, 2010 Algeria.
- [20] Chung-Wei Lu, Jyh-Chen Chen, Chien-Hung Chen (2010),. *Journal of Crystal Growth* 312; 1074-1079.
- [21] Azoui. H, Laidoune. A, Djamel. Haddad, Bahloul. D. 3ème conférence Internationale des énergies renouvelables CIER - 2015 *Proceedings of Engineering and Technology - PET* pp.228-236 Copyright IPCO-2016.